Exploring Convection and Dynamos in the Cores and Envelopes of Stars

by

Nicholas Andrew Featherstone

B.S., North Carolina State University, 2003

M.S., University of Colorado, 2005

A thesis submitted to the

Faculty of the Graduate School of the

University of Colorado in partial fulfillment

of the requirements for the degree of

Doctor of Philosophy

Department of Astrophysical and Planetary Sciences

2011

This thesis entitled:
Exploring Convection and Dynamos in the Cores and Envelopes of Stars
written by Nicholas Andrew Featherstone
has been approved for the Department of Astrophysical and Planetary Sciences

Juri Toomre

Bradley W. Hindman

Allan Sacha Brun

Mark P. Rast

Philip J. Armitage

Keith Julien

Date

The final copy of this thesis has been examined by the signatories, and we find that both the content and the form meet acceptable presentation standards of scholarly work in the above mentioned discipline.

Featherstone, Nicholas Andrew (Ph.D., Astrophysical and Planetary Sciences)

Exploring Convection and Dynamos in the Cores and Envelopes of Stars

Thesis directed by Profs. Juri Toomre and Bradley W. Hindman

We present theoretical studies in two complementary areas dealing with convection, rotation, and dynamos in A-type stars, and with local helioseismology in the Sun. Our studies begin with the main-sequence A stars (stars of about 2 $M_\odot$) that possess a radiative envelope overlying a convective core. Using 3-D simulations with the Anelastic Spherical Harmonic (ASH) code to study full spherical domains, we examine the effects of a primordial magnetic field on the dynamo action realized in the turbulent core. Dynamo activity realized in the presence of such a field is significantly more efficient than in its absence, yielding magnetic energies that are roughly tenfold those of the kinetic energy associated with the convective motions. Both convective motions and magnetic fields assume a decidedly global-scale topology in this regime, with convective downdrafts from one side of the core streaming freely across the rotation axis, advecting and stretching magnetic fields across distant portions of the core in the process. We examine the topology of these strong magnetic fields and aspects of their generation in this super-equipartition dynamo.

We next develop a 3-D inversion method for helioseismic measurements of horizontal flows obtained using ring-diagram analysis. Helioseismology uses the broad range of acoustic oscillations observed at the solar surface to study properties deep within the Sun. Our inversion method (called ARRDI) incorporates measurements of the wavefield made at multiple horizontal resolutions to discern the subsurface structure of horizontal flows within the star. We adopt a regularized least squares (RLS) approach for these inversions and develop a novel iterative extension to the RLS scheme wherein the flow field across the entire solar disk may be efficiently recovered. We have calculated the set of 3-D sensitivity kernels necessary for the application of our inversion technique to MDI data. We explore the horizontal- and depth-averaging properties of these sensitivity kernels, and find they differ substantially between measurements made at different horizontal resolutions.

After characterizing the errors and averaging properties of our inversion algorithm, we examine the subsurface flows around sunspots. We find that sunspots possess outflows which extend to a depth of 10 Mm. These outflows possess a noticeable two-component structure, characterized by a near-surface moat outflow and another deeper outflow at 5 Mm. Our 3-D inversion procedure should be very useful in interpreting the vast helioseismic data sets now becoming available.

Dedication

For Manissa. For the songs we have sung together as well as those we've yet to sing.

Acknowledgements

Throughout my tenure as a graduate student, Juri Toomre and Brad Hindman have been a consistent source of guidance and encouragement. Our many scientific discussions have helped to shape the themes pursued in this thesis, and their attention to detail has been invaluable in crafting its final presentation. Juri has fostered a research setting within his group wherein the pursuit of such disparate topics as those presented within this thesis can not only be undertaken, but can flourish. Working with Brad, I was introduced to the novel notion of peering beneath the surface of the Sun, and it was under Juri's guidance that I first gained footing in the theoretical exploration of magnetism in the deep interiors of stars. Together, these two have played a pivotal role in my development as a scientist, and words cannot begin to express the debt of gratitude I feel toward them for this.

I am also grateful to Sacha Brun and Matthew Browning who journeyed to Boulder several times each year to help see the A-star work to completion. Their thoughtful suggestions were crucial in deciding upon which avenues of that work to emphasize and which to abandon all together. I thank Deborah Haber for her invaluable assistance as I learned the essentials of ring analysis. I would also like to acknowledge Michael Thompson for his many useful suggestions and contributions to the development of ARRDI, and I thank Aaron Birch for his kernel calculation routines. I gratefully acknowledge the many helpful conversations with Mark Miesch, Benjamin Brown, and Kyle Augustson concerning convection and dynamo theory that have occured over these past few years. Finally, I thank Gwen Dickinson, Pete Ruprecht, and Jim McKown. Their tireless work ensured that my own energies were focused on the science presented in this thesis.

This research has been supported by NASA GSRP awards NNX07AP34H and NNX06AI29H, by NASA Heliophysics Theory Program grants NNX08AI57G and NASA NNG05G124G, by NASA Living with a Star grants NNG05GM83G, NAG5-13520, and NAG5-12491, by NASA Heliophysics Guest Investigator grant NNX08AJ08G, and finally, by NSF grant ATM-0219581. The simulations presented herein were carried out with NSF PACI support of PSC, NCSA and TACC, and by NASA HEC support at Project Columbia.

Contents

Chapter

Tables

Table

Figures

Figure

Chapter 1

Overview of Convection and Magnetism in Stars

It has been known for over a century now that stars are magnetic entities. Magnetism was first detected in the Sun by Hale (1908), with the first nonsolar detection by Babcock (1947) following a few decades later. Magnetic fields are now known to be ubiquitous across the main sequence and indeed across all stages of stellar evolution. They play an active role in stellar formation, affecting molecular cloud collapse and modulating accretion onto protostars through their interactions with the circumstellar disk. On the main sequence, magnetic fields regulate the spin down of stars through their interaction with stellar winds, later serving as seeds for the strong magnetism observed in white dwarfs and neutron stars.

Within main sequence stars, magnetic fields rarely exist in isolation. Whether in the cores of massive stars or in the envelopes of stars more like our Sun, magnetism is inextricably linked to the convective motions of an ionized gas. The interaction of convection and magnetism can lead to some interesting and surprising effects, such as magnetic cycles and explosive events. The latter is of obvious importance to modern society, where solar phenomena such as coronal mass ejections can severely impede communications satellites and disrupt power grids. However, through the periodic emergence of sunspots at the solar surface, the Sun's magnetism has perhaps exterted a more subtle influence on society as well, fascinating ancient sungazers, notably the Chinese, long before the existence of any theory of electromagnetism (e.g., Wittman & Xu 1987).

The methods for understanding magnetism and its generation in stars run the full gamut of theoretical to observational. This thesis delves into both of these areas, beginning with three-

dimensional (3-D) numerical simulations of convection and dynamo action in the cores of A-type stars. The convective cores of these stars lie buried beneath deep radiative envelopes that have long been suspected of harboring intense and large-scale magnetic fields. We explore what implications the presence of such strong, organized fields might have on the core dynamos within these stars before turning to convection in the Sun.

The proximity of the Sun allows us to probe the interplay between its convection and magnetism in great detail through helioseismology. Following our A-star explorations, we develop a local helioseismic technique useful for probing flows around magnetic features in the shallow near-surface layers of the solar convection zone. This technique combines velocity measurements obtained with variable horizontal resolution using ring-analysis helioseismology to yield a self-consistent description of the large and small-scales of convection present in the upper 20 Mm of the solar convection zone. Before beginning, let us proceed with a general discussion of magnetism in stars, followed by a more focused discussion of what helioseismology has revealed about the interaction of magnetism and convection in our own star.

1.1 Stellar Magnetic Field Measurements

Magnetic fields in stars are measured by observing the Zeeman splitting of magnetically sensitive spectral lines. In the simplest case, a magnetic field will split a spectral line into what is known as a Zeeman triplet, comprised of a linearly polarized component at the center of the unsplit line, and two circularly polarized components on either side of line center. The degree of splitting realized by the circularly polarized components is proportional to the strength of the magnetic field. Unfortunately such triplets are difficult to resolve in all but the slowest rotators owing to the competing effect of Doppler broadening of the line resulting from rotation of the star. Some resolution of Zeeman triplets has been achieved using near infrared lines in cool stars such as the M and K dwarfs (e.g., Saar & Linsky 1985; Valenti et al. 1995) and in some slowly rotating Ap stars (Mathys 2001).

When the Zeeman splitting is unresolved, a broadening of the line is observed. Fitting

of the observed line to a model accounting for Doppler broadening, magnetic fields, and other line-formation effects allows the average (i.e., disk-integrated) magnetic flux to be estimated (e.g., Robinson et al. 1980a; Saar 1988). This technique is insensitive to any small-scale tangling present in the magnetic field and has found wide use as a general diagnostic of the field strength in stars, particularly in the cool dwarf stars (e.g., Robinson et al. 1980b) and protostars such as the classical T Tauri stars (Johns-Krull 1997). While measurements of the splitting or broadening of the line provide only an estimate of the magnetic field modulus, more sophisticated techniques enable the recovery of the magnetic field geometry.

The magnetic field orientation, it turns out, is encoded in the polarization properties of the spectral line. The splitting of the circularly polarized components of the line can be used to deduce the intensity-weighted disk-average of the line-of-sight magnetic field. Similarly, the linear polarization allows one to infer the intensity-weighted averaged of the transverse field strength. These simple measures of the field orientation are good for large-scale fields with little variation across the stellar disk and have been applied widely to the persistent fields of the chemically peculiar Ap stars (e.g., Borra & Landstreet 1980; Leroy 1995).

Initial attempts to discern the geometry of stellar magnetic fields began with the large-scale magnetic fields of the Ap stars. The dipolar component of the magnetic field was obtained by observing a changing spectral line over several rotation periods. These variations were fitted to a model of what might be expected from a dipole inclined with respect to the rotation axis (e.g., Preston 1967). Zeeman Doppler Imaging (ZDI; Semel 1989; Brown et al. 1991) and the related technique of Magnetic Doppler Imaging (MDI; Piskunov & Kochukhov 2002) have expanded on this general idea through the use of higher-order multipoles for both the poloidal and toroidal fields in the fitting procedure. They have yielded a much more detailed understanding of the surface toplogies of magnetic fields in a wide variety of stars.

The advantages of surface-field imaging techniques such as ZDI are readily apparent in Figure 1.1 where an F7 star has been imaged three times over the course of three years. The poloidal field is clearly non-axisymmetric in nature and is shown to flip over the course of the three years observed,

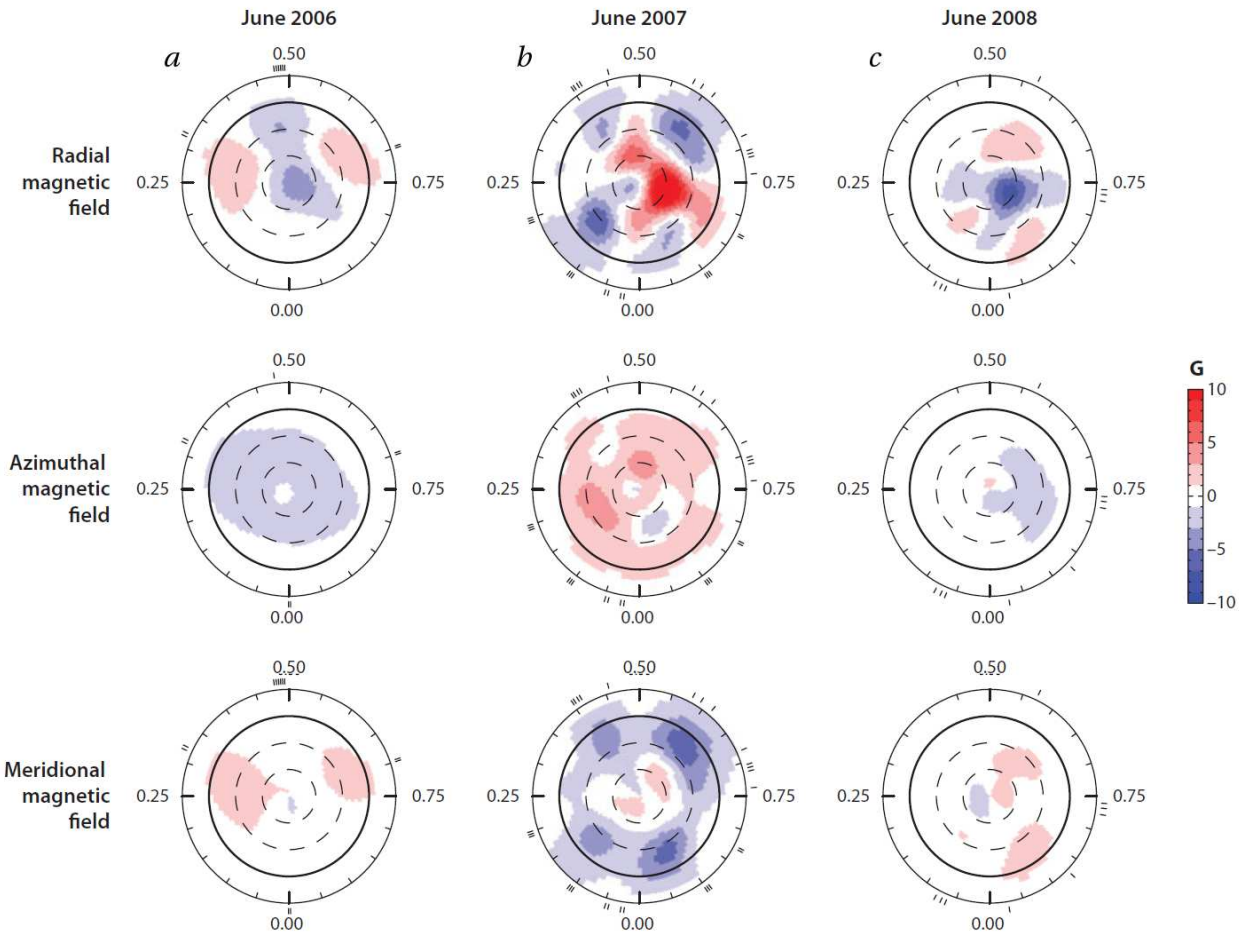

Figure 1.1: Zeeman Doppler Imaging of the dynamo cycle in the F star τ Boo. Polar view of magnetic fields imaged in (a) June 2006 (Catala et al. 2007), (b) June 2008 (Donati et al. 2008) and (c) June 2009 (Donati et al. 2009). Concentric circles indicate lines of latitude. The stellar equator is indicatd by the thick black line and a latitude of $-30°$ by the outer solid line. Both poloidal and toroidal components of the field are seen to reverse between subsequent years, hinting at the presence of a dynamo with a cycle roughly ten times faster than that found in the Sun. (Adapted from Donati & Landstreet 2009)

as does the more axisymmetric toroidal field. The ability to discern the topology of magnetic fields on stars through techniques such as ZDI and MDI holds great promise for observing stellar dynamo behavior. These techniques have also been used to analyze the magnetic fields of the more massive stars, such as the chemically peculiar Ap and Bp stars (e.g., Kochukhov et al. 2004) as well as magnetic fields in the pre-main-sequence (PMS) T Tauri stars (e.g., Donati et al. 2008, 2010;

Hussain et al. 2008).

1.2 Magnetism in Low Mass Stars

Stars across the H-R diagram fall into two broad categories: those with convective cores and those with convective envelopes. Stars with masses less than about 1.5 $M_{\odot}$ (spectral type F and later) have convective envelopes that deepen with decreasing mass, ultimately encompassing the entire stellar radius in the case of the fully convective M-dwarfs. The outer convection zones of these stars exhibit a wide range of solar-like phenomena. Dark star spots that persist on time scales of days have been observed in numerous studies (e.g., Radick 1982; Dorren & Guinan 1982; Richards 1990; Barnes et al. 2004). The absorption signatures of prominence-like clouds of cool plasma, locked into corotation with the star by coronal magnetic fields, have also been observed (Collier Cameron et al. 1989; Donati et al. 2000), suggesting that a magnetic corona may be present in these stars. Cyclic chromospheric emission in solar-like stars observed through calcium H and K has hinted at the presence of dynamo cycles in cool stars (e.g., Wilson 1978; Baliunas et al. 1998). More recently, as shown in Figure 1.1, ZDI has demonstrated the occurrence of a field polarity reversal in an F star star (Catala et al. 2007; Donati et al. 2008, 2009).

The surface magnetism observed in the low-mass stars is thought to result from the presence of a rotationally influenced convective dynamo, as opposed to a primordial field. Indeed, within stars of a given mass, tracers of magnetic activity, such as X-ray flaring and chromospheric HK emission, increase with the stellar rotation rate (e.g., Noyes et al. 1984). This trend of increased magnetic activity ceases for all low mass stars at some mass-dependent rotation rate for all of the low-mass stars, such that increased rotation does not further strengthen the magnetic fields (e.g., Pizzolato et al. 2003; Reiners et al. 2009). Presumably the fields become so strong as to feed back on the convection through some as yet unknown dynamo quenching mechanism.

1.3 Magnetism in Massive Stars

Stars more massive than about $1.5M_{\odot}$ possess deep outer envelopes that are primarily quiescent and radiative in nature. While stars in the $1.5M_{\odot}$-$3M_{\odot}$ range are thought to possess thin convection zones near their surface, driven by the ionization of hydrogen and helium, strong convection is mainly driven deep within the cores of these stars where vigorous burning of hydrogen is accomplished largely through the CNO cycle. Within the stars in this mass range (O,B,A, and early F) magnetism has been observed primarily in the chemically peculiar Ap and Bp stars, but some recent observations have begun to demonstrate the presence of magnetism in the normal O and B stars (e.g., Donati et al. 2006; Bouret et al. 2008). Searches for magnetism in the normal A and early F stars have been both extensive and fruitless (e.g., Shorlin et al. 2002; Bagnulo et al. 2006).

The chemically peculiar Ap and Bp stars are so named for the strong surface abundances they exhibit in Si and many other metals (e.g., Hg, Cr, Eu; Mestel 1999). These stars constitute a small percentage of the total A and B stars, peaking at 10% for the 3 $M_{\odot}$ stars and tapering off to nearly zero at 1.5 $M_{\odot}$ (Power et al. 2008). All known Ap stars of the Si and Sr-Cr-Eu peculiarity classes are observed to be magnetic, with field strengths ranging from 300 G up to 30,000 G (e.g., Babcock 1947; Auriere et al. 2007). However, searches for magnetism in the other pecularity classes (such as the Hg and Mn peculiarity classes) have failed to find magnetic fields (Shorlin et al. 2002).

Imaging of these stars through MDI and ZDI has shown that the different peculiar elemental abundances tend to concentrate in different regions of the star and do not always reflect the geometry of the magnetic field (see Figure 1.2). The observed surface fields are typically large-scale and predominantly poloidal in nature, and when variable, they do so only at the stellar rotation rate (e.g., Mestel 1999; Donati & Landstreet 2009). The large-scale and persistent nature of the observed magnetic fields in the Ap and Bp stars, uncharacteristic of dynamo driven fields, suggests that these fields may be of primordial origin, deriving from a remnant magnetic field amplified during the collapse of the star from its originating molecular cloud.

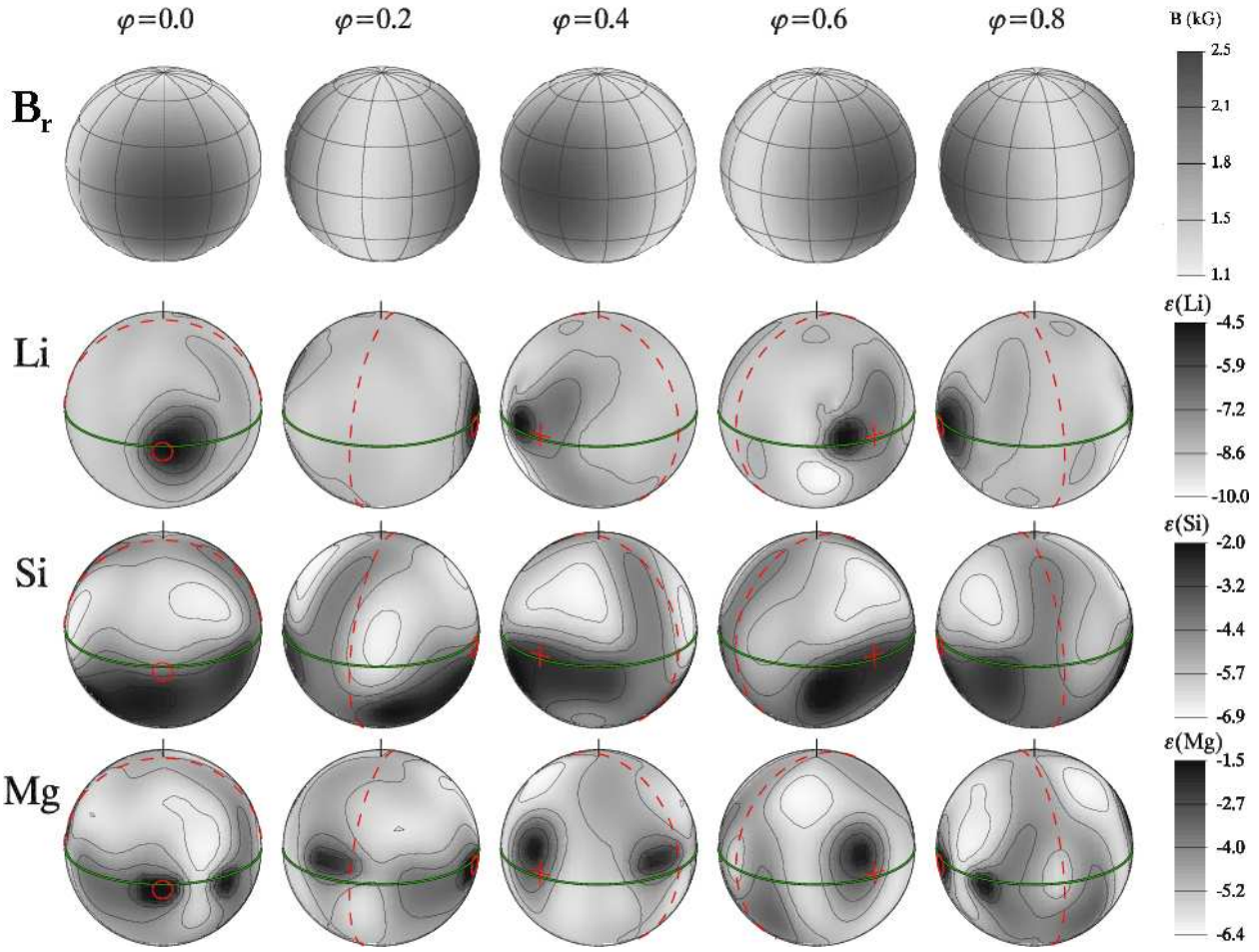

Figure 1.2: Magnetic Doppler Imaging of the rapidly rotating Ap star HR3831. (*upper row*) Radial component of the magnetic field imaged at five intervals spanning one rotation period. Many Ap stars exhibit a relatively simple surface magnetic field topology. Here the field is well approximated with a dipole inclined by 90° with respect to the rotation axis. (*lower rows*) Surface maps of the relative abundances of different elements. $\varepsilon(M) \equiv \log(N_M/N_{total})$. Abundance maps differ between elements. The Li abundance shows a strong correlation with the dipolar field, while other abundances, such as Si and Mg, do not. (Adapted from Kochukhov et al. 2004)

Magnetic fields have been observed in more massive stars with some limited success. Detection of magnetic fields in the normal O and B stars are difficult owing to the intrinsic width and weakness of the magnetically sensitive spectral lines in these stars. Only a handful of B stars (six) have been observed to have magnetic fields (Henrichs et al. 2000; Neiner et al. 2003; Donati et al. 2006c; Petit et al. 2008b), and an even smaller number of O stars, namely three (Donati et al.

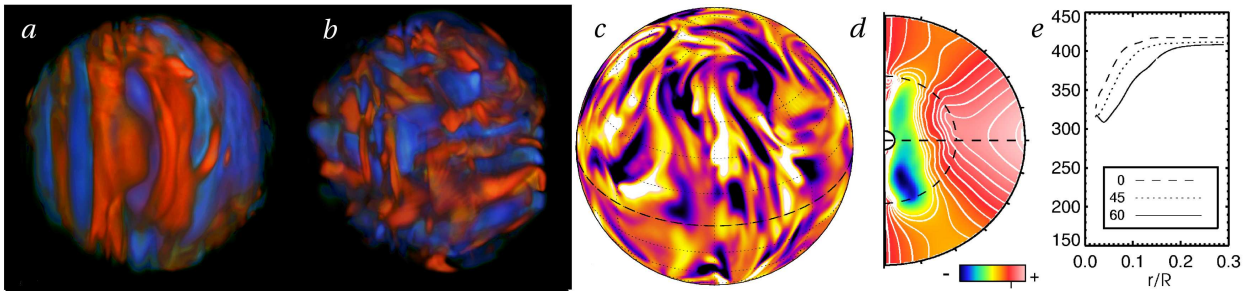

Figure 1.3: Simulations with ASH of core convection in a rotating A-type star, with the core surrounded by stable radiative envelope. (a) Volume rendering of the strong radial magnetic field achieved by dynamo action in the core, and (b) its longitudinal component. (c) Global view of radial velocity at fixed radius near the middle of the core (downflows in blue tones). (d) Azimuthal velocity in cross-section, with dashed lines showing the core-envelope interface and the equator. Dark tones indicate central column of slow rotation. (e) Angular velocity variations with radius. (Adapted from Brun, Browning & Toomre 2005)

2002, 2006b; Bouret et al. 2008). Much like the peculiar Ap and Bp stars, these few normal O and B stars are found to possess persistent, largely poloidal magnetic topologies with field strengths in the kG range. Some notable exceptions do occur, such as with the early B star τ Sco, which was deduced to have a rather complicated twisted toroidal topology thought to originate from the interaction between a primordial surface field and the stellar wind (Donati et al. 2006). The static nature of the fields in the O stars is also suspect since observations by Bouret et al. (2008) hint at the presence of a dynamo driven field in the O star ξ Ori A.

1.4 Seeking to Address Magnetism in A-type Stars

The strong magnetic fields observed on the surfaces of Ap stars are intriguing in part for their persistence in the apparent absence of any regenerative dynamo mechanism operating in their radiative envelopes. Convection in the cores of these stars has long been suspected of harboring strong dynamos, and recent 3-D numerical modeling has enabled a detailed exploration of the dynamo states accessible to these stars (e.g., Browning, Brun & Toomre 2004; Brun, Browning & Toomre 2005). These simulations have revealed that core convection in A-type stars involves highly time-dependent flows with complex, vigorous convection that can penetrate substantially into the

overlying radiative zone (Fig. 1.3). Such motions often span multiple scale heights and serve to couple widely separated portions of the core. Convection tends to drive a prominent column of slow rotation maintained throughout the cores of these stars, though this strong differential rotation is diminished greatly in the presence of magnetic fields. When dynamo action is admitted, strong magnetic fields are generated whose associated magnetic energy is in approximate equipartition with that of the convective motions. Such magnetic fields were found to be largely non-axisymmetric in nature, with the axisymmetric poloidal and toroidal fields contributing little to the overall energy balance.

It is thus entirely likely that intense magnetic fields are generated in the cores of A-type stars but there are difficulties associated with transporting these fields to the stellar surface. Meridional circulations are likely too weak to carry magnetic flux from the core to the surface on time scales shorter than the stellar lifetime (e.g. Charbonneau & MacGregor 2001). Moreover, the transport of dynamo-generated fields through magnetic buoyancy seems unlikely if magnetic fields attain only equipartition levels in the cores of these stars (MacDonald & Mullan 2004). Indeed, no buoyant magnetic fields were realized in the simulations of Brun, Browning & Toomre (2005).

It seems more plausible that the strong magnetic fields of the Ap stars originate instead within the molecular clouds from which these stars have formed. Typical ohmic diffusion times across the radiative envelope are comparable or longer than the stellar lifetime (e.g., Cowling 1945) and so strong magnetic fields amplified during the collapse phase may well persist throughout the main-sequence lifetime of an A star (about 10^9 years). An interesting aspect of the primordial field story involves the 3-D simulations of Braithewaite & Spruit (2004), which found that a randomly organized magnetic field, left to its own devices in a quiescent radiative envelope, will eventually relax into a coherent large-scale field, with a twisted toroidal geometry.

Large-scale magnetic field strengths in the 10 kG range are commonly observed on the surfaces of the Ap stars and, if these fields truly are indicative of an organized subsurface field, equally strong magnetism may well pervade the deep radiative interior. Magnetic field strengths in this range are approaching equipartition levels with respect to the expected convective motions in the cores of

these stars (e.g., Browning, Brun & Toomre 2004). It is thus natural to ask what role a primordial magnetic field, with some threading into the convective core, might play in shaping the behavior of the core dynamo.

We explore this question through 3-D numerical modeling of convection in the interiors of A stars, finding that dynamo action in the presence of a primordial field in the radiative envelope is very different from that operating in its absence. Both convective motions and magnetic fields assume a decidedly global-scale topology in this regime, with convective downdrafts from one side of the star streaming freely across the rotation axis, advecting and stretching magnetic fields across distant portions of the core in the process. Magnetic energies, which were equipartition in the absence of the primordial magnetic field, attain levels that are tenfold that of the associated convective motions. We examine these super-equipartition magnetic states in detail in Chapters 2-4 before then proceeding to helioseismic studies of flows around magnetic features in the Sun.

1.5 Magnetism in the Sun

Our proximity to the Sun of course enables much more detailed observations of its magnetic fields than is achievable in other stars. Magnetism in the Sun is most readily apparent through the appearance of dark sunspots on the solar surface (Figure 1.4*a*). The dark umbra of sunspots are now known to harbor kG-strength fields and are typically cooler than the surrounding plasma by about 1000-2000 K due to the inhibition of convective heat transport in the presence of such strong magnetism. Hosting typical diameters of a few tens of Mm, sunspots can live for weeks to months following their emergence before decaying and forming the small-scale flux which comprises the active regions in which they reside (e.g., Solanki 2003).

Sunspots emerge in concentrated latitudinal bands, and it is the migration of these bands of emergence that is the most easily recognizable signature of the 22-year solar cycle. Emergence occurs at mid-latitudes of $\pm 35^{\circ}$ initially and gradually migrates toward the equator over the course of 11 years. After 11 years, the magnetic dipole of the Sun has reversed, and emergence begins anew at the mid-latitudes. A variety of established symmetries and ordering rules, suggestive of an

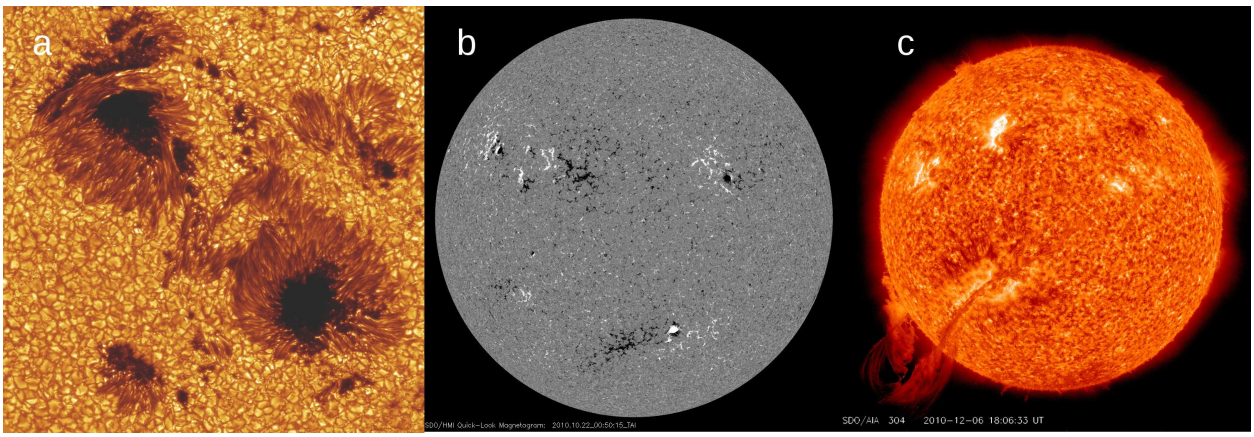

Figure 1.4: The many aspects of magnetism in the Sun. (*a*) Continuum image of a sunspot group near disk center taken with the Swedish Solar Telescope (credit: G. Scharmer & K. Langhans). Strong magnetic fields in the dark umbra of sunspots inhibit local convection (here prominently visible on granular scales). (*b*) Magnetogram of the Sun obtained on 22 Oct 2010 showing magnetic field along the line of sight in white and the opposite polarity in black (obtained with the Helioseismic and Magnetic Imager aboard the Solar Dynamics Observatory [SDO]). A clear preference for polarity of the leading and trailing edges of active regions is evident within each hemisphere and opposite between hemispheres. Magnetism in the leading portion of the active region tends to obey Joy's law, emerging at lower latitudes than in the trailing portion. (*c*) Image of the Sun from 6 Dec 2010 showing the eruption of a large filament, visible above the disk for over two week prior to eruption (obtained with the Atmospheric Imaging Assembly (AIA) aboard SDO).

underlying large-scale dynamo, characterize sunspot emergence. Throughout the cycle, sunspots emerge in pairs of opposite polarity, with the same polarity for all leading spots within the same hemisphere (and the opposite sense in the other hemisphere). This law, known as the Hale polarity law (Hale et al. 1919; Hale & Nicholson 1925), hints at the presence of a large-scale, subsurface toroidal magnetic field generated by such a dynamo. Other phenomena, such as the tilting of sunspots described by Joy's law (Hale et al. 1919), whereby the leading polarity emerges nearer to the equator than the trailing polarity (Figure 1.4*b*), and the equatorward migration of the active region belts over the solar cycle, are similarly suggestive of a large-scale dynamo.

The prevailing picture is that solar active regions originate from subsurface magnetic flux tubes that rise to the solar surface. The advent of helioseismology and the subsequent discovery by it of the tachocline (see §1.6) has suggested that the base of the convection zone is the likely

seat of the solar dynamo. Magnetic flux emerging from the tachocline must then first traverse the solar convection zone, a region of highly turbulent flow, on its way to the solar surface. The effects of convection on emerging magnetism are most visible in the upper convection zone where highly vigorous convection occurs on many horizontal scales, ranging from the solar granulation (1 Mm scale) to the more global-scale flows, often termed solar subsurface weather (SSW), characterized by meandering jet-stream-like patterns. As we discuss in detail in §1.7, flows at all scales are strongly linked with surface magnetic features, and so it is thought that the twisting of magnetic fields by these fluid motions, both in the photosphere and in the subsurface layers, is likely to be the driving force behind solar eruptions such as flaring and coronal mass ejections (Figure 1.4*c*).

1.6 Acoustic Oscillations of the Solar Interior

Understanding the origin of the solar cycle and the associated energetic magnetic events are outstanding challenges to modern solar physics. Serious progress is now being made in studying the solar cycle through 3-D theoretical simulations of convection and magnetism in solar-like stars, with some of these now beginning to exhibit dynamo cycles (e.g., Brown et al. 2010, 2011; Ghizaru, Charbonneau & Smolarkiewicz 2010). On the observational side, helioseismic probing of the solar interior has proven to be a powerful tool for examining magnetism the upper reaches of the convection zone, and has shown potential as a predictive tool for magnetic events.

The solar oscillations manifest as displacements of the solar surface that occur with periods of about 5 min (3 mHz) and were observed by Leighton et al. (1962) using Mount Wilson Doppler measurements. The prevailing interpretation now is that these oscillations arise from standing acoustic modes trapped beneath the photosphere (Ulrich 1970; Leibacher & Stein 1971) and are excited by near-surface turbulent convection (e.g., Goldreich & Keeley 1977; Libbrecht et al. 1986; Goode et al. 1992). When power spectra (in horizontal wavenumber and frequency) are constructed from the observed Doppler data, modal power is found to fall along discrete ridges in frequency-wavenumber space, with power focused at specific frequencies for each horizontal wavenumber (Figure 1.5*a*).

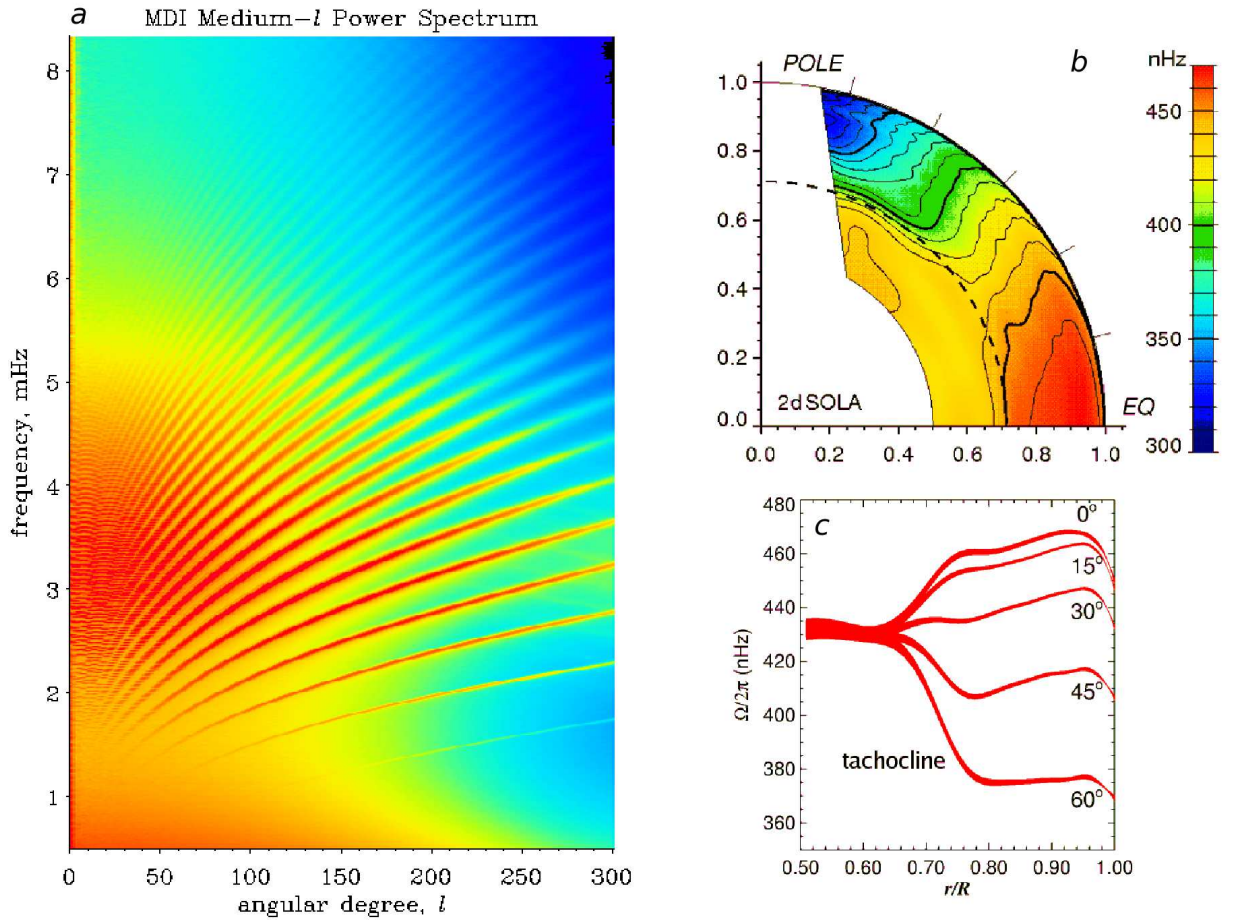

Figure 1.5: Probing solar interior rotation with global helioseismology. (a) Solar power spectrum observed with MDI as a function of frequency and spherical harmonic degree ℓ. High acoustic power is indicated in red tones, and low power by blue tones. Power is concentrated at discrete frequencies specific to each ℓ. (b) Differential rotation of the Sun (angular velocity Ω) as realized through inversion of global-mode frequency splittings. The fast equator is found to rotate once every 25 days, and the slow pole completes one revolution in about 33 days. The differential rotation transitions to solid body rotation in the radiative interior as illustrated more clearly in (c) where radial cuts at various latitudes are shown (Thompson et al. 2003).

A wide variety of techniques have been devised by which the properties of the solar wavefield may be exploited to infer the internal structure and flows within the Sun. They broadly fall into two categories. Global helioseismology employs large-scale and long-lived acoustic modes, capable of circumnavigating the the Sun many times, to deduce properties of the solar interior as a function of radius and latitude (e.g., Deubner & Gough 1984; Gough & Toomre 1991; Christensen-Dalsgaard 2002; Thompson et al. 2003). Local helioseismic techniques, on the other hand, analyze the wavefield over some localized portion of the solar surface to infer the local variation of some quantity (i.e., flow or temperature) beneath that region of the Sun (e.g. Braun et al. 1987; Hill 1988; Duvall et al. 1993; Lindsey & Braun 1997; Gizon et al. 2010).

Global helioseismology has been particularly useful in inferring the interior nature of the solar differential rotation. Inversions of global-mode frequency splittings revealed that the surface differential rotation (expressed in terms of the angular velocity Ω) imprints through to the base of the convection zone. The differential rotation ultimately terminates in a thin layer of shear at the base of the convection zone where a transition to solid body rotation in the radiative interior occurs (e.g., Thompson et al. 1996, 2003; Schou et al. 1998; Figure 1.5b, c). This shearing layer, termed the tachocline (Spiegal & Zhan 1992), has become a common ingredient in solar dynamo modeling due to its likely role in the generation of strong toroidal magnetic fields (e.g., Parker 1993; Charbonneau & MacGregor 1997; Browning et al. 2006). Global helioseismology has also been instrumental in probing other aspects of solar interior structure, such as establishing the base of the solar convection zone and determining the chemical composition of the solar interior. Perhaps most notably, accurate determinations of the temperature in the solar core played a key role in encouraging the intensive search that revealed the existence of neutrino oscillations (see e.g., Christensen-Dalsgaard 2002 for a review).

The nature of global-helioseismic modes means that solar interior properties are averaged in longitude and over both the northern and sourthern hemispheres. Details concerning the subsurface structure of solar magnetic fields and near-surface convection, which manifest on small-scales and which are not axisymmetric or hemispherically symmetric, are thus inaccessible to global techniques.

Local helioseismic techniques do not perform such averaging and allow for full three-dimensional mapping of regions of the Sun, making them much more useful for probing the fine-scale properties of the solar convection zone.

1.7 Probing Solar Magnetism through Local Helioseismology

1.7.1 Local Helioseismic Techniques

Modern local helioseismic studies typically probe flows in the upper convection zone using one of two widely applied techniques. Ring diagram analysis infers the presence of a subsurface flow in some localized region of the Sun by fitting for Doppler shifts induced in waves propagating through that region. An example of the flow mapping achievable with ring-diagram analysis is shown in Figure 1.6 where large-scale, meandering flows are seen to pervade the subsurface layers of the Sun. Time-distance distance methods measure such flows by analyzing the wavefield in physical space, inferring the flow by measuring travel times for wave packets to propagate between two sites on the solar surface. These two methods yield comparable results when compared (e.g., Hindman et al. 2004). However time-distance methods afford higher horizontal resolution, particularly below the solar surface, than do current ring analysis implementations (see §1.8). We discuss these two methods here briefly and provide a detailed desription of the ring analysis method in Chapter 5.

When viewed at a constant frequency, the 3-D power spectrum (in termporal frequency and horizontal wavenumber) associated with a localized region of the solar surface appears as a series of concentric rings (Figure 1.7). Advection of waves by an underlying flow induce a Doppler shift in these rings. Ring-analysis techniques (e.g., Hill 1988; Schou and Bogart 1998, Haber et al. 2002) assess subsurface flows by measuring anisotropies in the shifting of these rings and sound speed variation through their isotropic shifts (e.g., Basu et al. 2004). Measurements of the frequency shifts associated with different horizontal wavenumbers and modal orders average the subsurface flow differently and may be combined through linear inversion to yield a map of the flow both horizontally and with depth.

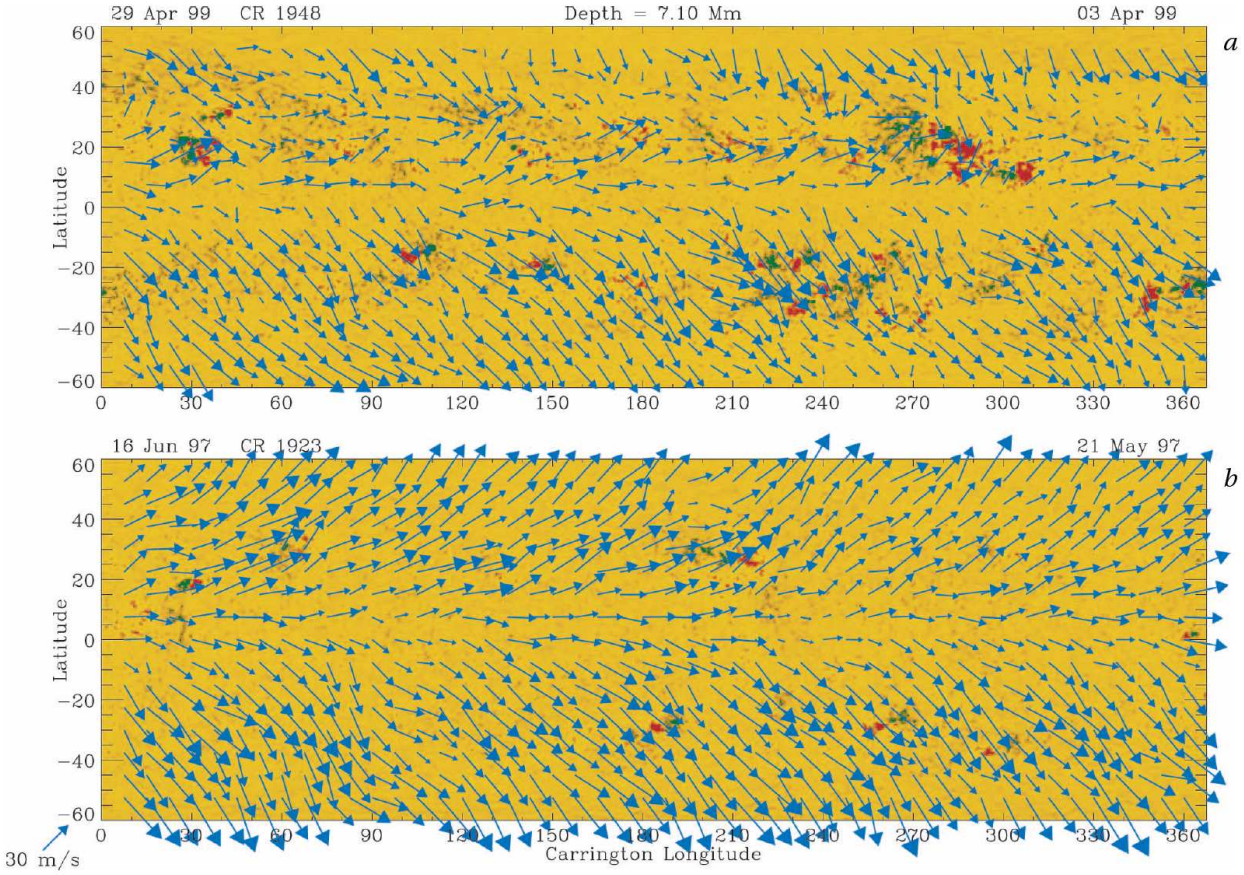

Figure 1.6: Subsurface flows as viewed with ring-analysis helioseismology during (*a*) the magnetically active period spanning 3 April 1999 through 29 April 1999 and (*b*) the relatively inactive period spanning 21 May 1997 through 16 June 1997. Blue arrows indicate subsurface flows at a depth of 7 Mm beneath below the photosphere. Flow vectors at each latitude and Carrington longitude represent a seven-day average over the measured flow at that coordinate. An average magnetogram for this time period is underlaid, with red and green indicating opposite polarities of strong line-of-sight magnetic field, and yellow denoting regions of weak magnetic field. Large, meandering jet stream-like motions are visible which possess a clear poleward component within each hemisphere. The meandering patterns of these flows are much less organized in the 1999 data and seem to be influenced by the strong magnetic features present. (Adapted from Haber et al. 2002)

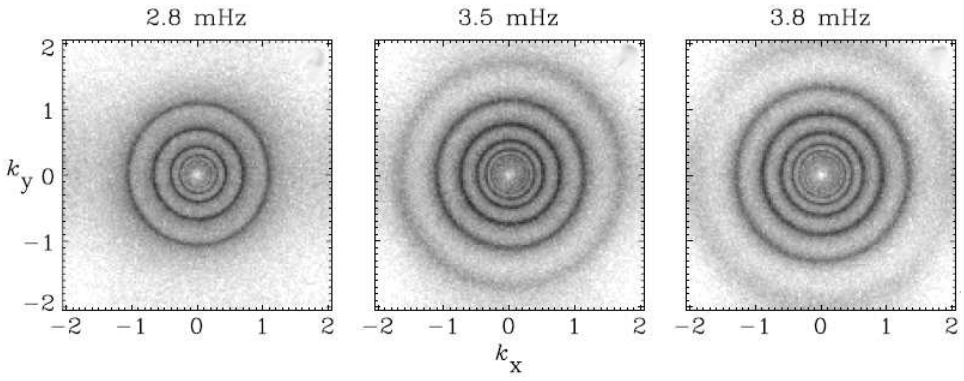

Figure 1.7: Solar power spectrum of a localized patch of the Sun as viewed when cut at three temporal frequencies. Power manifests as concentric rings that expand in horizontal wavenumber (k_x and k_y) with increasing frequency ν. Ring-analysis methods deduce subsurface flows by measuring Doppler shifts induced in these rings when an underlying flow is present. (adapted from Haber et al. 2002)

Time-distance methods make direct use of the surface Doppler signal (rather than its power spectrum) and determine flow velocities by measuring the time required for wave packets to travel a fixed distance across the solar surface (e.g., Duvall et al. 1993; Kosovichev 1996). A background flow produces an anistropy in the travel times for waves propagating in opposite directions, and thermal heterogeneities, which affect the sound speed, produce isotropic travel time shifts. Travel time measurements are typically obtained by constructing the cross-covariance function and fitting it with a Gaussian wavelet whose phase is related to the time lag between the two wave signals (e.g., Kosovichev et al. 1997; Figure 1.8). By Fourier filtering the Dopplergrams to isolate waves with specific radial orders and phase speeds, travel-time maps of waves with varying degrees of depth penetration can be constructed. Point-to-point correlations are often noisy and so travel times are typically constructed using some degree of spatial averaging, either between a point on the surface and a surrounding annulus (Duvall et al. 1996, 1997), or by averaging over all points that have the same horizontal separation lying within some common region of the Sun (Featherstone et al. 2004). These travel times may then be inverted to discern the subsurface flows (e.g., Gizon & Birch 2002; Birch et al. 2004). A detailed review of the time-distance technique is provided by Gizon & Birch

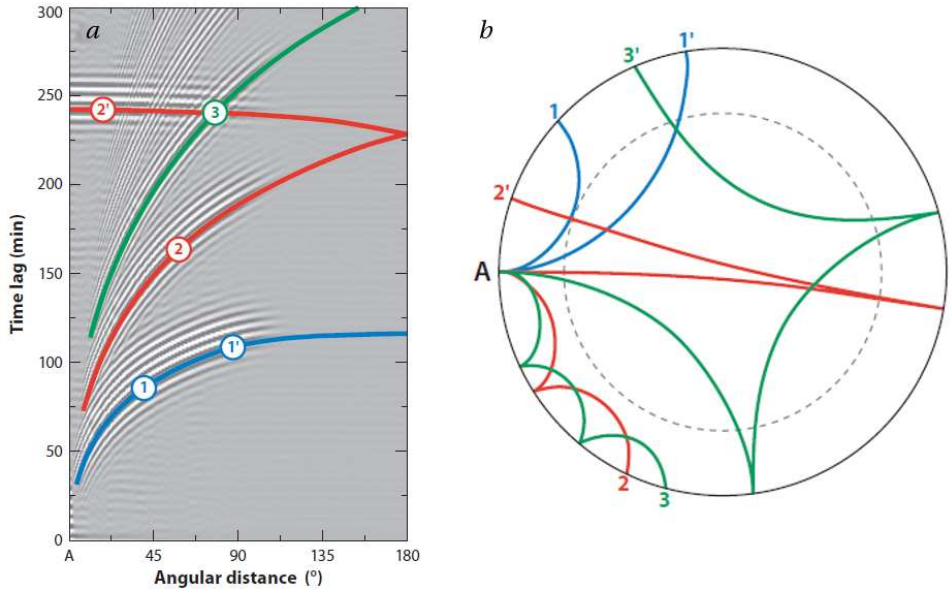

Figure 1.8: Example of the time-distance cross covariance function. (a) Measured point-to-point cross covariance as a function of spatial lag (shown here as angular separation in degrees) and time lag. Broad, ridged bands of power are apparent. The slope of these bands indicates the time required for a wave packet to travel between two points separated by the indicated angular distance. Different bands are denoted by colored and numbered lines and correspond to waves undergoing different numbers of skips when traveling between points. (b) Geometry of the ray paths taken by waves when creating the different bands of power in the cross covariance function. (Adapted from Gizon et al. 2010)

(2005).

We note that ring analysis and time-distance methods are by no means the only local helioseismic methods. One of the early applications of local helioseismology employed a technique known as Hankel analysis (Braun et al. 1987), which examines differences between waves propagating into and out of some point on the solar surface. By looking at the power in incoming and outgoing waves, Braun et al. (1987) found that sunspots were strong absorbers of acoustic power. Hankel analysis has found wide application in the measurement of phase shifts and mode mixing induced by sunspots (e.g., Braun, et al. 1992, Braun 1995). Another form of local helioseismology is acoustic holography (Lindsey & Braun 1997), which uses the wavefield at the solar surface to estimate properties of the wavefield in the interior and has also been applied to the measurement

of phase shifts in waves induced by magnetic fields (e.g., Lindsey & Braun 2005*a*,*b*) The most novel application of acoustic holography (and indeed local helioseismology) is its application to far-side imaging of active complexes in the Sun (e.g., Lindsey & Braun 2000; Braun & Lindsey 2001; González Hernández et al. 2007), making it a powerful predictive tool for active region emergence.

1.7.2 Meridional Circulations

One of the early applications of local helioseismic techniques to global-scale motions was to the study of meridional circulations in the upper convection zone. Known through Doppler measurements to possess a surface velocity of 20 m s^{-1} (Hathaway et al. 1996), these poleward circulations are thought to be a key mediator of angular momentum transport in the solar convection zone. There, along with Reynolds stresses resulting from the turbulent convective motions, the meridional circulations likely play a pivotal role in the establishment and maintenance of the solar-differential rotation (e.g. Brun & Toomre 2002). Rotational shearing in the tachocline, associated with the transition from the differentially-rotating convection zone to the solid body rotation of the radiative interior, is thought to play central role in the development of strong toroidal magnetic fields by the solar dynamo. Measurements of meridional circulations are thus useful both for informing 3-D numerical simulations of dynamo action in the convection zone (e.g., Brun, Miesch & Toomre 2004). Moreover, such measurements also provide important input to flux transport dynamo models (e.g., Dikpati & Charbonneau 1999).

Initial measurements of the meridional circulations using local helioseismic techniques were shown through subsequent time-distance measurements to remain relatively constant in strength down to a depth of 26 Mm (Giles et al. 1997). Further studies using a variety of local helioseismic approaches have confirmed this finding (e.g., González, Hernández et al. 1999, 2000; Duvall & Gizon 2000; Zhao & Kosovichev 2004). Temporal variation of the meridional circulations has been assessed through time-distance (Giles 1999) and ring-analysis studies (Haber et al. 2002). As shown in Figure 1.9, these studies revealed the presence of a deep countercell of meridional circulation in the northern hemisphere. This submerged cell lacked a southern counterpart and varied in

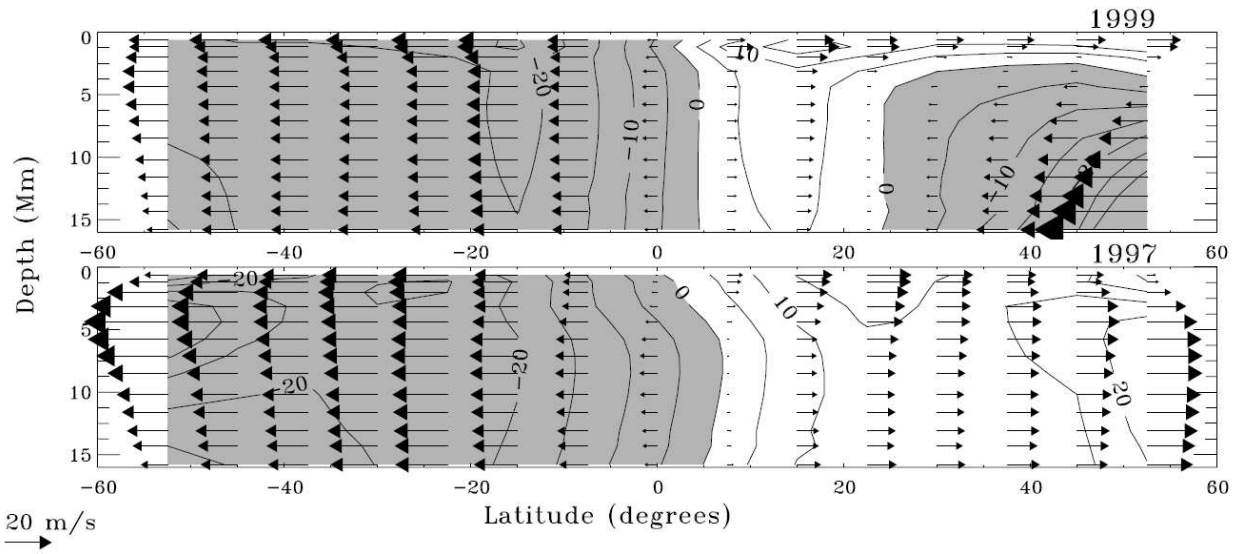

Figure 1.9: Meridional circulations as measured using ring-analysis helioseismology. Flows have been averaged in longitude and in time for the two periods spanning (*lower panel*) 14 April 1997 through 12 July 1997 and (*upper panel*) 7 March 1999 through 26 May 1999. Meridional circulations are poleward within each hemisphere, and the strength of the circulations is relatively constant in depth during 1997. Variability of the circulations is visible in 1999 where the presence of a submerged countercell is apparent in the northern hemisphere. (Adapted from Haber et al. 2002)

strength and sign with respect to the overlying shallow circulation over the course of the years 1998-2001. Subsequent studies (González Hernández et al. 2006) using more deeply penetrating modes also found a submerged countercell, and reported that similar cells appeared periodically with the changing B_0-angle of the Sun. The existence of such multiple circulatory cells within a single hemisphere might thus be an observational artifact (see also Gizon & Birch 2005).

Meridional circulations also vary over the course of the solar cycle. Upon subtraction of the temporal mean from the meridional circulation profile, a surface inflow into the active latitudes becomes visible. This 10 m s^{-1} inflow pattern migrates equatorward, along with the magnetic activity belts, over the solar cycle (Haber et al. 2002; Gizon 2003; Zhao & Kosovichev 2004; González Hernández et al. 2008; Basu & Antia 2010). Time-distance observations extending to greater depths suggest that these inflows transition to similarly migrating diverging flows below about 18 Mm in depth (Chou & Dai 2001; Beck et al. 2002). The correlation between these

variations in meridional circulations and the active region belts has led to investigations into the influence that active-region related flows might have on the meridional circulations and differential rotation.

1.7.3 Flows Around Active Regions

Local helioseismology has been extensively applied to the probing of the flows into and around active regions, since the shearing of magnetic field lines by the flow is likely responsible for driving the magnetic reconnection associated with energetic events such as flaring and coronal mass ejections. Both time-distance and ring analysis have shown that on large-scales (30° in extent), near-surface flows tend to converge on active regions with speeds of about 50 m s^{-1} (Gizon et al. 2001; Haber et al. 2001). When depth inversions are applied, these inflows are shown to transition to outflows of comparable strength around a depth of 10 Mm as in Figure 1.10 (Haber et al. 2002; Zhao & Kosovichev 2004; Komm et al. 2005). Komm et al. (2004) have suggested that the divergence of large-scale flows around active regions can be coupled with mass conservation to compute the vertical velocity of the flow and find 1 m s^{-1} downflows down to a depth of about 10 Mm beneath active regions and upflows below this depth.

Shearing flows tend to pervade active region complexes. Using ring analysis to study flows beneath a quiescent filament, Hindman et al. (2006) reported that near-surface convection (on scales of about 40 Mm) underlying the filament tended to generate an average shear about the neutral line between its magnetic footpoints. On larger scales, Coriolis forces induce vorticity in the surface inflows (cyclonic in the northern hemisphere) that transition to weakly anticyclonic flow in the surrounding quiet Sun (Komm et al. 2007; Hindman et al. 2009). Within an active complex, the outflows associated with individual sunspots tend to be anticyclonic as well (Hindman et al. 2009). Moreover, the active regions themselves revolve faster about the rotation axis of the Sun than their quiet Sun surroundings by about 20 m s^{-1} (e.g., Zhao et al. 2004; Hindman et al. 2009; Komm et al. 2009).

Observations of these shearing flows in active regions have elicited much interest in using

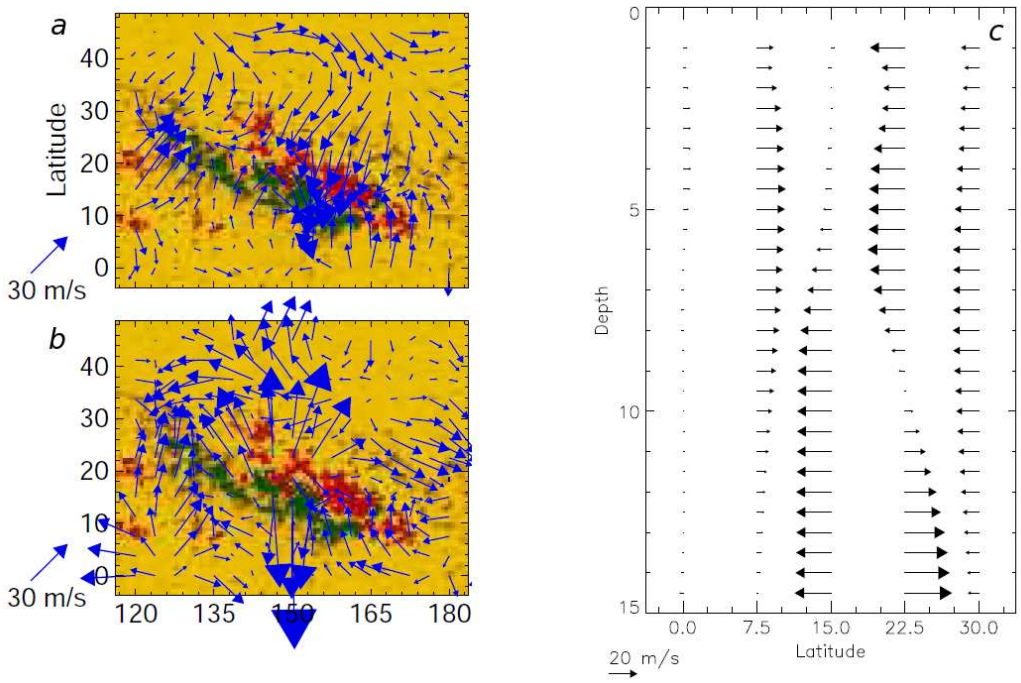

Figure 1.10: Surface inflows into active regions transition to outflows at depth. OLA inversion of 16° ring measurements made around active region NOAA 9433 on 23 April 2001 are shown at depths of (a) 7 Mm and (b) 14 Mm. Underlaid is the magnetogram for that day, with opposite field polarities indicated in red and green. (c) Horizontal flows into and away from the active region as a function of depth and latitude, averaged over the longitudes 142.5° -157.5° and the time period 23 - 27 April 2001. Inflows transition to outflows around a depth of 10 Mm. (Adapted from Haber et al. 2004)

these measurements as a predictive tool for flaring and CMEs. The vertical velocity of active region flows, along with its curl, may be used to construct the associated kinetic helicity. Subsequent ring-analysis studies have sought to use the vertical velocity and kinetic helicity to develop predictive models for magnetic events. The observations of Komm et al. (2008, 2009) hint that the appearance of organized upflows might precede the emergence of large-scale magnetic flux. The measured the kinetic helicity has also been shown to correlate well with both the level of a magnetic activity (i.e. levels of high activity have high kinetic helicity), and the intensity of the X-ray flares arising from the active region (Komm et al. 2005, 2007; Mason et al. 2006)

1.7.4 Active Region Influence on Global-Scale Flows

Given the large-scale inflows into and circulations around active regions, it is natural to ask whether the observed variations in the meridional circulation (Figure 1.11*a*) over the solar cycle are due to migrating active region inflows or are they due to the presence of additional meridional cells (as posited by Zhao & Kosovichev 2004)? Moreover, what effect might active region flows have on the so-called solar "torsional oscillations?" These latitudinal variations in the solar rotation rate are characterized by alternating bands of 10 m s^{-1} slow and fast rotation (Figure 1.11*b*) that migrate equatorward in similar manner to the bands of solar activity. The torsional oscillations were first observed by Howard & Labonte (1980) through Doppler measurements of the surface rotation rate, and examined in recent detail by Ulrich (2010). They have been studied through inversion of global-mode frequency splittings (e.g. Kosovichev & Schou 1997; Schou 1999; Howe et al. 2000) and through local helioseismic studies using time-distance (Giles et al. 1998; Beck et al. 2002; Zhao & Kosovichev 2004) and ring analysis (Basu et al. 1999, Basu & Antia 2000; Haber et al. 2000, 2002). In the vicinity of the active regions, these torsional oscillations manifest as regions of fast rotation equatorward of the sunspot latitudes and slow rotation on the poleward side.

The driving of torsional oscillations has been attributed to a variety of phenomena, including Lorentz forces from migrating dynamo waves, changes in the balance of Reynolds and Maxwell stresses, and the suppression of turbulent viscosity by active regions (see e.g., Shibahashi 2004 for a review). One particularly interesting model is that of Spruit (2003) which proposes that the torsional oscillations originate through downdrafts driven by radiative cooling associated with the small-scale magnetic fields of active regions. Coriolis forces acting on these downdrafts produce a cyclonicity in agreement with observations which (in this model) is then responsible for the faster rotation equatorward of the active belts and the slower rotation on the poleward side. Similarly, the variation of meridional circulation over the solar cycle is appropriately reproduced.

Gizon & Rempel (2008) demonstrated that incorporating such a surface cooling term into a flux transport model can yield meridional and zonal flows in rough agreement with those measured

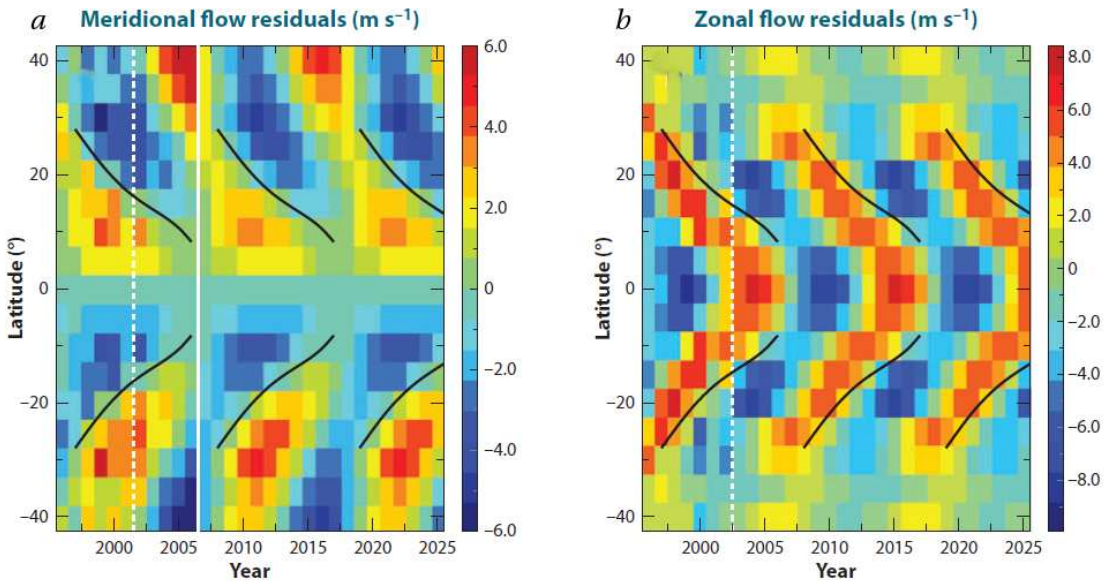

Figure 1.11: Torsional oscillations and meridional flow variations over the solar cycle. Shown are the residuals for (a) meridional circulation and (b) zonal flows obtained after subtracting the time-averaged component of the flow. Meridional flows were measured for the years 1996-2006, and zonal flows during 1996-2002. Flows are extrapolated into the future to better illustrate the patterns present. Thick black curves indicate the mean latitudes of magnetic activity. The migration of the zonal flows and meridional circulations displays a clear linkage to the migration of the active latitude belts. (adapted from Gizon & Rempel 2008; Gizon et al. 2010)

through time-distance. Other approaches to understanding this problem have involved analyses of longitudinal means obtained which incorporate the active regions and those obtained when regions of magnetic activity are masked out. Using f-mode time-distance, Gizon (2003) found that active region flows alone do not fully account for the torsional oscillations (i.e. torsional oscillations occur in quiet Sun as well), but can account for the variations observed in meridional circulations over the solar cycle. However, ring-analysis measurements of quiet Sun meridional circulation obtained using similar magnetic masking indicate that active region inflows cannot fully account for the variation in meridional circulation (González Hernández et al. 2006). The disentanglement of the global-scale flows from active-region flows is thus tricky and the effects of the former on the latter remain unclear, particularly with respect to the meridional circulations.

1.7.5 Flows Around Sunspots

The emergence and migration of sunspots at the solar surface, the tell-tale signature of the 22-year solar cycle, has engendered much interest into their structure and maintenance. Of primary interest is whether sunspots are monolithic flux structures extending deep into the convection zone, or whether they are coherent only in the shallow layers, transitioning to a much more diffuse fibril structure below a depth of 1-2 Mm (e.g., Parker 1979, Schüssler 2005). Moreover, do plasma flows in the vicinity of sunspots possibly help stabilize these magnetic structures, allowing them to persist for days and even weeks? Theory and simulations have long suggested that sunspots must possess a stabilizing, convergent downdraft (e.g., Parker 1979, 1992; Hurlburt & Rucklidge 2000; Hurlburt & DeRosa 2008), but recent 3-D simulations by Rempel (2009) display systematic outflows with depth.

Early measurements revealed the presence of surface outflows around sunspots, now termed moat flows, visible in the movement of surface magnetic features and later through Doppler measurement at the solar surface (Sheeley 1969, 1972; Brickhouse & Labonte 1988). These moat flows were found to be on the order of 1 km s^{-1} and are thought to be driven by pressure gradients resulting from heat buildup below the sunspot where convection is suppressed (e.g., Nye et al. 1988; Solanki 2003). The advent of local helioseismic techniques has enabled further probing of the subsurface nature of these moat flows. Using f-mode time-distance methods, Gizon et al. (2000) were able to confirm the presence of the moat flow in the upper 2 Mm of the convection zone. Deeper probing using the solar p-modes has enabled the persistence of the moat flow with depth to be probed using a variety of helioseismic techniques (e.g., Lindsey et al. 1996; Sun et al. 1997; Braun & Lindsey 2003; Gizon et al. 2009; Featherstone et al. 2011). There are differences concerning the strength and depth to which the moat flows extend, but generally these approaches concur that a radial outflow on the order of 100-200 m s^{-1} persists around a sunspots to a depth of about 10 Mm.

A notable exception to this trend are the p-mode time-distance results of Zhao & Kosovichev

(2001, 2003) and Zhao et al. (2010) which suggest that sunspots possess convergent downdrafts in the upper 3 Mm of the convection zone. The disagreement between such results and other helioseismic studies, particularly the p-mode measurements of Gizon et al. (2009), is puzzling. However, some of the earlier time-distance studies using p-modes did indicate downdrafts in sunspots on the order of 1-2 km s^{-1} in the upper 1 Mm (Duvall et al. 1996; Kosovichev et al. 1996). As noted in Gizon et al. (2009), time-distance measurements are particularly sensitive to the filtering process wherebye waves with a certain radial order and phase speed are isolated before measuring travel times. Different filtering will undoubtedly affect the depth-averaging properties of the different measurements, possibly leading to inconsistent results.

1.8 Achieving 3-D Inversions of Ring-Analysis Measurements

A number of the insights into the dynamics of the upper convection zone have been informed by ring-analysis methods. One goal of this thesis is to improve the capability of ring analyses to assess small-scale and intermediate-scales of subsurface flows. Owing to the lack of fine-scale resolution available at depth in their current inversion methods, ring-analysis studies yield little information on the nature of the deep flows around sunspots. Ring analyses have typically been performed on square regions of the Sun that are either 16° or 2° (in heliographic angle) in size. In the case of 16° measurements, the data are inverted to yield the underlying flow field with depth, and a horizontally uniform flow is assumed, effectively making these 1-D inversions. Ring analyses on 2° regions afford a much finer resolution, but have been restricted to fitting f-mode measurements only, with no inversion performed. These higher resolution measurements are averaged in horizontal wavenumber to yield a representative average over the upper 2 Mm of the convection zone.

Applications of 2° surface measurements to the study of sunspots within active regions and shearing flows beneath filaments (Hindman et al. 2006, 2009) hint at an unexploited potential for ring analyses to probe these flows in similar detail at depth. In principle, such benefits may be gained by performing 1-D inversions on 2° p-mode measurements, similar in nature to the 16° inversions. In practice, noisy power spectra make the fitting of modes penetrating more deeply

than 5 Mm difficult for 2° analysis regions. However, when analysis regions with a somewhat coarser horizontal resolution of 4° are employed, Doppler shifts for modes reaching down to about 10 Mm in depth can be reliably measured.

Ideally a flow map of the subsurface flow should be constructed by self-consistently combining measurements made using different analysis region sizes. The region of the solar disk covered by a single 16° measurement will also be covered by numerous higher-resolution measurements. These 2° and 4° measurements can provide a much more detailed description of the near-surface layers, but say nothing about the flow at depths beyond about 10 Mm. Combining measurements from different analysis regions can be accomplished through a 3-D inversion of the data but it requires the development of 3-D kernels that describe both the vertical and the horizontal sensitivies of the various measurements to a flow.

We have developed a 3-D inversion method capable of combining multiple analysis region sizes in such a fashion and have calculated the 3-D sensitivity kernels necessary for the inversion of existing MDI data. This inversion package, while tested using MDI data, will be implemented into the HMI data pipeline in spring 2011. Collectively termed the ARRDI (Adaptably-Resolved Ring Diagram Inversion) package, these programs enable the self-consistent inversion of ring-analysis fits achieved using an arbitrary combination of modes and analysis regions sizes. We will detail the development of ARRDI beginning in Chapter 5 and turn to the first applications of ARRDI to flows around sunspots and active regions in Chapter 8. We begin now with an exploration of convective dynamos in the deep cores of A stars.

Chapter 2

Primordial Magnetic Fields with Core Dynamos in A-type Stars

We begin with an exploration of magnetism and convection in the cores of A-type stars. Observations of magnetism in the peculiar A-type (Ap) stars indicate the presence of concentrations of magnetic field that extend over large portions of the stellar surface. These patches of magnetic field are thought to coincide with locations where a primordial magnetic field, originating in the formative collapse of the star, extends through the stellar surface. The following three chapters discuss how such strong, organized magnetic fields may influence the dynamo achieved deep within the cores of these stars and are largely a restatement of the work contained in Featherstone et al. (2009)[1] . As the principal architect of the text, I was also responsible for conducting the numerical simulations and performing their subsequent analyses. Throughout this study, my coauthors provided guidance concerning the exploration of the strong dynamo states realized through these simulations.

We devote this chapter to a discussion of the observations of surface magnetic fields in the Ap stars and to theories describing their origin. We close with a discussion of our methodology for examining the interaction between a primordial magnetic field and a core dynamo. In Chapter 3, we focus on how the overall magnetic and kinetic energy balance is modified in the dynamo state realized when a primordial magnetic field and core dynamo are modeled together. The various elements of the flows and magnetic field structures that characterize the super-equipartition state that is realized, in which the magnetic energy can be tenfold greater than the convective kinetic

[1] Featherstone, N.A., Browning, M.K., Brun, A.S. & Toomre, J., 2009, "Effects of Fossil Magnetic Fields on Convective Core Dynamos in A-type Stars", *ApJ*, **705**, 1000

energy, are analyzed there. Chapter 4 is devoted to a more detailed examination of the processes responsible for the generation and maintenance of such strong magnetic fields and closes with reflections on the significance of achieving such super-equipartition dynamo behavior.

2.1 Ap Stars and Magnetism

The unusual chemical abundances of peculiar A-type stars were first noted by Maury (1897), who discovered a strong Si II doublet in the spectrum of α^2CVn. Subsequent observations of this and similar stars over the last century have shown these stars to exhibit strong and variable spectral lines (relative to solar values) in Si and certain other elements (e.g., Sr, Hg). Most, if not all, of the Si and Sr-Cr-Eu pecularity classes possess equally variable and unusually strong magnetic fields (Babcock 1947, Mestel 1999). These magnetic fields are generally thought to be of primordial origin, resulting from the diffusive evolution of the magnetic field threading the initial molecular cloud. However, convection in the cores of these stars may also play a significant role. Our interests concern the nature of the interaction between such a primordial magnetic field and a core-dynamo harbored within the convective interior of an A-type star.

2.1.1 Observations of Magnetic Fields

Observations of magnetic fields in Ap stars are carried out primarily through measurements of the longitudinal (line of sight) field, deduced by measuring the wavelength shifts between spectral lines of opposite circular polarization (Mathys 2001). Typical longitudinal field strengths for the magnetic Ap stars are a few hundred Gauss, but field strengths ranging from 20,000 G down to a lower threshold of $\sim$ 300 G have been observed (Aurière et al. 2007). Some inferences about the nature of the structure of magnetic fields on these stars has been made through complementary measurements of the magnetic field modulus (also termed "the surface field"). However, Doppler broadening makes such measurements possible only for the slowest rotators (Mathys 2001). Observations of the slow rotators suggest a lower cutoff for the mean modulus of about 3,000 G, well above the detectability limit (Mathys et al. 1997, Freyhammer et al. 2008). For stars on which

both the longitudinal field and the field modulus have been measured, the field modulus is typically similar in magnitude to the longitudinal field. A comparable longitudinal field and field modulus hint at the presence of a large-scale ordered field in these slow rotators. A spatially intermittent field would have a much smaller ratio of the longitudinal field to the modulus, as is the case for the Sun, where variations in the line-of-sight field across the solar surface tend to cancel each other out.

Field strengths for the Ap stars, when variable, are observed to vary at the stellar rotation rate (Deutsch 1956, Preston 1971). The Ap stars appear to preferentially rotate more slowly than the normal A-stars, with the possible exception of the early A-stars (Abt 2000, Royer et al. 2007). Within the class of Ap stars, however, there is little or no correlation between magnetic field strength and rotation rate (e.g. Kochukhov & Bagnulo 2006). Such a lack of correlation is contrary to what one might expect from fields generated by a core dynamo. Within the class of Ap stars, rotational periods range from decades to a fraction of a day, with typical periods on the order of a few days (e.g. Borra et al. 1982, Mestel 1999).

The variability and apparent large-scale organization of the magnetic fields observed in Ap stars has led to oblique rotator models (ORM) (Stibbs 1950, Mestel 1999). The ORM envisage a large-scale magnetic dipole, inclined to the rotation axis, frozen into the atmosphere of the star, and dragged along with the star as it rotates. This model is highly idealized and modifications to a simple dipole are often required. The modulus measurements of Mathys et al. (1997) suggest a significant deviation from a purely dipolar geometry, with only one minimum and maximum present during a rotational cycle (as opposed to the two expected for a dipolar field). More recently Kochukhov et al. (2004) showed that the spectrum of 53 Cam was well fit only after employing higher order multipoles (spherical harmonic degree ℓ up to 15).

2.1.2 Possible Primordial Origin of Magnetism

The apparently static nature of the magnetic fields of Ap stars has led to the development of the fossil field theory. As originally pointed out by Cowling (1945) in the context of the Sun,

a typical Ohmic decay time for a global-scale stellar magnetic field is longer than the lifetime of the star. The observed magnetic fields may then be a remnant of an interstellar field threading the cloud of gas from which the star formed. Recent observational surveys suggest that Ap stars exhibit markedly less magnetic flux as they near the end of their main-sequence lifetimes, possibly due to diffusive decay or reorganization of magnetic fields in the radiative zones of these stars (Kochukov & Bagnulo 2006, Landstreet et al. 2008). The fossil theory may also help explain the slow rotation of Ap stars (relative to their nonmagnetic counterparts) through magnetic braking of the star earlier in its lifetime (Mestel 1999). Such braking has been observed in magnetic Ae stars (the pre-main sequence progenitors of Ap stars) which exhibit rotation rates about six times slower than the non-magnetic Ae stars (Alecian et al. 2008).

The structure of a typical fossil field has been a subject of speculation for some time. On the basis of stability arguments, these fields have generally been thought to be comprised of some form of linked poloidal and toroidal fields. Purely toroidal configurations have been shown by Tayler (1973) to be unstable to perturbations of azimuthal order $m = 1$, with the perturbations growing on the time scale needed for an Alfven wave to travel along the magnetic field line. Purely poloidal field has been shown to be unstable to non-axisymmetric perturbations (e.g. Wright 1973, Markey & Tayler 1973, Flowers & Ruderman 1977). The analysis of Braithwaite (2007) suggests that rotation decreases the rate of growth of instability, but does not prevent the onset. Likewise Brun (2007) has studied the role of rotation on the onset of the poloidal instability and found that the most unstable wavenumber m increases with the rotation rate. A stable magnetic field configuration in the radiative zone must necessarily contain more twist than purely poloidal or toroidal configurations afford. Prendergast (1956) showed that such a linked, poloidal-toroidal configuration satisfied the criteria for equilibrium, but stopped short of proving the stability of such a field. More recently, Duez & Mathis (2009) have derived a linear stability analysis of the magnetic field configuration in a barotropic star, confirming the mixed toroidal-poloidal nature of the stable field.

The numerical simulations of Braithwaite & Spruit (2004) and Braithwaite & Nordlund (2006)

for a nonrotating star have shown that a linked poloidal-toroidal field configuration is indeed stable on time scales commensurate with those of the star's evolution, and appears to be the preferred equilibrium condition for an initially random field. They find that a randomly oriented fossil field, present from the time of the star's appearance on the main sequence, will slowly relax into a twisted torus shape. The diffusion of this torus through the radiative zone, into the nonconducting atmosphere of the star (which cannot support a twisted field) results in the appearance of a largely poloidal field at the stellar surface. They estimate this diffusion time to be around 2×10^9 years, a time somewhat longer than the main sequence lifetime of the star. The appearance and subsequent diffusion of this fossil field may also help to explain the observed middle-aged nature of the magnetic Ap stars (Kochukhov & Bagnulo 2006).

2.1.3 Dynamic Origins for Fields

The cores of A-type stars (roughly the inner 15% by radius), along with a thin shell at the surface, are known to be convective, and such core convection has long been suspected of achieving dynamo action (Krause & Oetken 1976). Brun, Browning & Toomre (2005 hereafter BBT05) have investigated this possibility through 3-D numerical simulations and found that the cores of A-stars sustain vigorous dynamo action, with typical field strengths reaching near equipartition values with the convective kinetic energy. Core dynamos may have bearing on the surface fields observed in Ap stars through the production of magnetically buoyant structures. This possibility has been investigated through simulations by MacGregor & Cassinelli (2003) for more massive O and B stars, demonstrating that flux tubes may rise to the stellar surface in a time significantly less than the star's main sequence lifetime. However, MacDonald & Mullan (2004) have pointed out that the inclusion of realistic compositional gradients into the model of MacGregor & Cassinelli would severely hinder the rise of flux tubes, ultimately requiring a very high field strength if a magnetic structure is to reach the stellar surface. Given that these fields are assumed to be produced by dynamo action in the core, their strengths would need to be well in excess of equipartition values, possessing magnetic energies at least ten times greater than the convective kinetic energy.

Convection may also play a role in the early evolution of these stars' magnetic fields. The fully convective Hayashi phase that A-stars are thought to undergo on their journey to the main sequence holds the potential for magnetic dynamo action. Fully convective dynamos have been found, for instance by Dobler et al. (2006) and in 3-D modelling of M-type stars (Browning & Basri 2007; Browning 2008). Surveys of Ae stars by Alecian et al. (2008) reveal the existence of observable magnetic fields in these stars following the Hayashi phase (but prior to the development of a convective core). Either these fields must have been present prior to a Hayashi phase and survived, or were generated by the convective motions present during that epoch. Dynamo activity during a Hayashi phase thus seems likely and may augment or alter any primordial magnetic fields.

Separately, the field instabilities noted in §1.2 could lead to dynamo action through interaction with prominent differential rotation, as suggested by Spruit (2002), though some complications with this mechanism have been raised by Zahn et al. (2007). The dynamo scenario envisioned by Spruit is unlikely to be operating in main-sequence Ap stars, since the surfaces of these stars are observed to be rotating as solid bodies. This mechanism may, however, have had a role in field generation at earlier epochs.

2.1.4 Interaction of Core Dynamo with Fossil Field

While a primordial magnetic field seems to be the likely source for the surface magnetism observed on Ap stars, convection may also be implicated. Whether during the Hayashi phase early in the star's lifetime, or during the main sequence phases, convection and associated dynamo action may have a role in the magnetic fields that are observed. This leads to several basic questions. What is the nature of the interaction between a primordial field and one generated contemporaneously by a core dynamo? Does a strong fossil magnetic field help or hinder dynamo action, and does the dynamo have any significant effect on the configuration of the fossil field? Kinematic modeling by Moss (2004) suggests that a sufficiently strong exterior field could hinder the dynamo action in the core. Although instructive, this axisymmetric model does not capture the complex 3-D processes likely to be occurring within the core.

We are thus motivated to turn to detailed modeling of the coupling of a fossil field and convective core dynamo within an A-type star. The nonlinear 3-D simulations used here allow us to assess both the growth and equilibration of the magnetic fields, and also the feedback of such fields on the nature of flows within the core. Our results provide some insights into the interaction between an exterior fossil field and the stellar core dynamo, demonstrating that the presence of a fossil field holds out possibilities for enhanced dynamo action.

2.2 Simulation Elements

2.2.1 Anelastic MHD Approach

Our numerical simulations are carried out using the anelastic spherical harmonic (ASH) code which is described in detail in Clune et al. (1999) and in Brun et al. (2004). ASH is a pseudo-spectral code designed to perform efficiently on massively parallel supercomputers and solves the 3-D magnetohydrodynamic (MHD) equations in a rotating spherical shell. The anelastic approximation assumes that fluid motions are subsonic and that perturbations to thermodynamic variables are small compared to their mean, horizontally-averaged values at a given depth in the fluid (Gough 1969, Gilman & Glatzmaier 1980). Within the anelastic approximation, the thermodynamic variables are linearized about their spherically symmetric and evolving mean state with density $\bar{\rho}$, pressure $\bar{P}$, temperature $\bar{T}$, and specific entropy $\bar{S}$. Fluctuations about this state are denoted as ρ, P, T, and S. In the uniformly rotating reference frame of the star, the MHD equations are expressed as

$$\nabla \cdot (\bar{\rho}\boldsymbol{v}) = 0, \tag{2.1}$$

$$\nabla \cdot \boldsymbol{B} = 0, \tag{2.2}$$

$$\bar{\rho}\left[\frac{\partial \boldsymbol{v}}{\partial t}+(\boldsymbol{v}\cdot\nabla)\boldsymbol{v}+2\boldsymbol{\Omega}_0\times\boldsymbol{v}\right]=-\nabla P+\rho\boldsymbol{g} \\ +\frac{1}{4\pi}(\nabla\times\boldsymbol{B})\times\boldsymbol{B}-\nabla\cdot\mathcal{D}-[\nabla\bar{P}-\bar{\rho}\boldsymbol{g}], \tag{2.3}$$

$$\bar{\rho}\bar{T}\frac{\partial S}{\partial t}+\bar{\rho}\bar{T}\boldsymbol{v}\cdot\nabla(\bar{S}+S)=\nabla\cdot[\kappa_r\bar{\rho}c_p\nabla(\bar{T}+T) \\ +\kappa\bar{\rho}\bar{T}\nabla(\bar{S}+S)]+\frac{4\pi\eta}{c^2}|\boldsymbol{j}|^2 \\ +2\bar{\rho}\nu\left[e_{ij}e_{ij}-\frac{1}{3}(\nabla\cdot\boldsymbol{v})^2\right]+\bar{\rho}\epsilon, \tag{2.4}$$

$$\frac{\partial \boldsymbol{B}}{\partial t}=\nabla\times(\boldsymbol{v}\times\boldsymbol{B})-\nabla\times(\eta\nabla\times\boldsymbol{B}). \tag{2.5}$$

The velocity $\boldsymbol{v}$ expressed in spherical coordinates is $\boldsymbol{v}=(v_r,v_\theta,v_\phi)$ relative to a frame rotating at constant angular velocity $\boldsymbol{\Omega_o}$, $\boldsymbol{g}$ is the gravitational acceleration, $\boldsymbol{B}=(B_r,B_\theta,B_\phi)$ is the magnetic field, $\boldsymbol{j}=c/4\pi(\nabla\times\boldsymbol{B})$ is the current density, c_p is the specific heat at constant pressure, κ_r is the radiative diffusivity, η is the effective magnetic diffusivity, and $\mathcal{D}$ is the viscous stress tensor given by

$$\mathcal{D}_{ij}=-2\bar{\rho}\nu\left[e_{ij}-\frac{1}{3}(\nabla\cdot\boldsymbol{v})\delta_{ij}\right], \tag{2.6}$$

where e_{ij} is the strain rate tensor, and ν and κ are effective eddy diffusivities. We have chosen to represent the energy generation by nuclear burning of the CNO cycle with a volumetric heating term $\overline{\rho}\epsilon$ (see §2.2.3 below for details). This set of equations is closed by assuming the thermodynamic fluctuations satisfy the linear relations

$$\frac{\rho}{\bar{\rho}}=\frac{P}{\bar{P}}-\frac{T}{\bar{T}}=\frac{P}{\gamma\bar{P}}-\frac{S}{c_p}, \tag{2.7}$$

assuming the ideal gas law

$$\bar{P}=\mathcal{R}\bar{\rho}\bar{T}, \tag{2.8}$$

where $\mathcal{R}$ is the gas constant. In this MHD context, the anelastic approximation also filters out the fast magneto-acoustic modes. Alfven modes, as well as the slow magnetosonic modes are retained.

The divergence-free nature of the mass flux and of the magnetic field is maintained through the use of a toroidal-poloidal decomposition whereby

$$\bar{\rho}\boldsymbol{v} = \nabla \times \nabla \times (W\boldsymbol{e}_r) + \nabla \times (Z\boldsymbol{e}_r), \tag{2.9}$$

$$\boldsymbol{B} = \nabla \times \nabla \times (C\boldsymbol{e}_r) + \nabla \times (A\boldsymbol{e}_r). \tag{2.10}$$

The streamfunctions W and Z, as well as the magnetic potentials C and A, are functions of all three spatial coordinates and time; $\boldsymbol{e}_r$ is the radial unit vector.

This set of equations in the six variables W, Z, C, A, S, and P requires 12 boundary conditions to be well posed. We have chosen to impose the following boundary conditions throughout the simulation:

(1) Impenetrable top and bottom surfaces in the deep shell: $v_r = 0$

(2) Stress-free top and bottom: $(\partial/\partial r)(v_\theta/r) = (\partial/\partial r)(v_\phi/r) = 0$

(3) Constant entropy gradient at top and bottom: $\partial\bar{S}/\partial r = \text{constant}$, $\partial S/\partial r = 0$

(4) Perfect conductor top and bottom: $B_r = (\partial/\partial r)(B_\theta/r) = (\partial/\partial r)(B_\phi/r) = 0$

These conditions ensure that no mass or angular momentum is lost from the system via either radial momentum flux or torques arising from viscous or magnetic stresses at the upper and lower boundaries of the deep spherical shell being studied. Emergent flux through the top and the bottom remains constant in time, but differs between the two boundaries to account for energy generation in the core. The leakage of magnetic energy from the domain is prevented by forcing the Poynting flux to vanish at the boundaries. Other boundary conditions, especially for the magnetic fields, could be imposed, but at this stage these appear to be the most neutral, particularly at the lower boundary where strong magnetic fields are generated.

2.2.2 Implementation of ASH

Seeking to deal with full spherical global domains, ASH is a large-eddy simulation (LES) code, with subgrid-scale (SGS) descriptions for dynamics occurring on scales below the spatial resolution of the simulations. We have chosen to focus on the larger scales of flow, believing that they are most likely to be responsible for establishing the mean properties of core convection and dynamo action. In the solar context, this approach has been reasonably successful in making contact with helioseismic deductions of the solar interior differential rotation (Brun & Toomre 2003, Miesch, Brun & Toomre 2006, Miesch et al. 2008), and has been shown in the A-star context (BBT05) to produce sustained dynamo action. Here we treat the SGS terms most simply as enhancements to the kinematic viscosity as well as to the thermal and magnetic diffusivities. Much as in BBT05, we have defined our eddy viscosity and diffusivities to be a function of the mean density alone (and hence radius), independent of horizontal position or time. Specifically, we have taken these quantities to be proportional to $\overline{\rho}^{-1/2}$.

ASH's numerical implementation involves expanding all variables in spherical harmonics $Y_l^m(\theta, \phi)$ in the horizontal directions and Chebyshev polynomials in the radial direction. To gain higher resolution at the interface between the convective and radiative zones, and thus to better resolve the penetrative convection occuring in this region, we have employed a stacked Chebyshev scheme. In doing so, we have split the computational domain into two separate regions (radially) and performed separate Chebyshev expansions for each region. The spherical harmonic expansion is truncated at degree ℓ_{max}, with all azimuthal orders m retained in a triangular truncation, ensuring that we have uniform resolution over spherical surfaces. For our simulations, we have taken $\ell_{max} = 170$, corresponding to 256 mesh points in the latitudinal direction (N_θ), with the longitudinal mesh having N_ϕ=2N_θ, and in radius $N_r = 49 + 33 = 82$. The time evolution of our simulations is computed using an implicit, second-order Crank-Nicolson scheme for the linear terms and an explicit second-order Adams-Bashforth scheme for the advective, Coriolis and Lorentz terms. The computational demands of these calculations are substantial, and thus the ASH code has been

optimized to run on massively parallel supercomputers, using the message passing interface (MPI) to communicate between different computational nodes.

2.2.3 Modeling the A-type star

We have chosen to model the inner 30% by radius of a main-sequence A-type star of $2M_\odot$ rotating at four times the mean solar rate of $\Omega_0 = 414$ nHz. The mean rotation period is thus about seven days. The emerging luminosity of this star is $19L_\odot$. The inner 2% of the star by radius has been excluded to avoid the coordinate singularity at $r = 0$. This model consists of a convective core occupying the inner 15% by radius of the star with an overlying radiative zone extending to the outer radius of our computational domain. The density contrast across the full domain is 21.5, and that across the convective core is 2.04.

All models presented here were initialized using the statistically mature case C4m of BBT05. The convection and associated dynamo action involved complex flows and magnetism that were continuously evolving and rebuilding structures, but the overall system had equilibrated in terms of its time-averaged properties such as energies and differential rotation. Case C4m was evolved from a one-dimensional stellar structure model (at an age of 500 My) computed with the CESAM stellar evolution code (Morel 1997) using realistic microphysics and employing a classical mixing-length formalism to describe the convection. A necessary modification to this model was the softening of the entropy gradient in going from the convective core to the radiative zone. The stark contrast in entropy between these two regions would otherwise result in the driving of high frequency internal gravity waves which would severely limit the time steps. The principal input parameters are the same for the simulations presented here as for their progenitor case. As in BBT05, the energy generation term ϵ was implemented as $\epsilon = \epsilon_0 \overline{T_6}^8$, with $\epsilon_0 = 6.0 \times 10^{-9}$ erg g^{-1}s^{-1}. Furthurmore, we have taken the thermal diffusivity κ to be 4.0×10^{12} cm^{2}s^{-1} at the top of the domain. Similarly there the SGS viscosity is $\nu = 1.0 \times 10^{12}$ cm^{2}s^{-1} and the magnetic diffusivity is $\eta = 2.0 \times 10^{11}$ cm^{2}s^{-1}. Thus our effective Prandtl number Pr=0.25, and our magnetic Prandtl number is Pm=5.0. These values were chosen to achieve a high magnetic Reynolds number Rm at reasonable computational

cost and to facilitate comparison with BBT05. Using rms velocities and magnetic field strengths at mid-core and a length based on the core depth, the Reynolds number Re for our primary case A following equilibration is 136, and the corresponding magnetic Reynolds number Rm is 680. The associated Rossby number for this case is Ro=6×10^{-3}.

2.2.4 Imposing a Fossil Magnetic Field

All simulations here have been initialized by superimposing external magnetic fields of varying geometries onto the existing field structure of case C4m of BBT05 at a time corresponding to day 2,000 of that simulation. Our choices for the initial magnetic configuration in each case have been motivated by stability considerations and the need to sort out the role that the toroidal and poloidal components of the imposed magnetic field have in the overall response.

We have chosen a mixed poloidal-toroidal magnetic field (case A), a poloidal field (case B), and a purely toroidal magnetic field (case C) for our initial external field configurations. To disentangle the effects of spatial scale of the field, we have also examined external field configurations with higher-order multipolar structure (lacking a toroidal component) in which each hemisphere receives zero net magnetic flux across the interface between the convective core and the radiative zone.

The toroidal field for cases A and C was defined as

$$B_\phi = A \exp\left(-\frac{(\boldsymbol{r}-\boldsymbol{r_0})^2}{2\sigma^2}\right), \tag{2.11}$$

where r_0 lies along the equator at $0.225R$, σ is taken to be $2r_0$, and the amplitude A is taken to be 30 kG.

Our mixed field case A included the same functional form for B_ϕ but with an added poloidal field consistent with a current threading through the center of the magnetic torus. The strength of the poloidal field was adjusted so that the ratio of energy in the poloidal field to that in the toroidal field was 1:9, as suggested by the results of Braithwaite & Nordlund (2006). Placing such a mixed field into C4m resulted in only a 10% increase to the total magnetic energy of that system. The

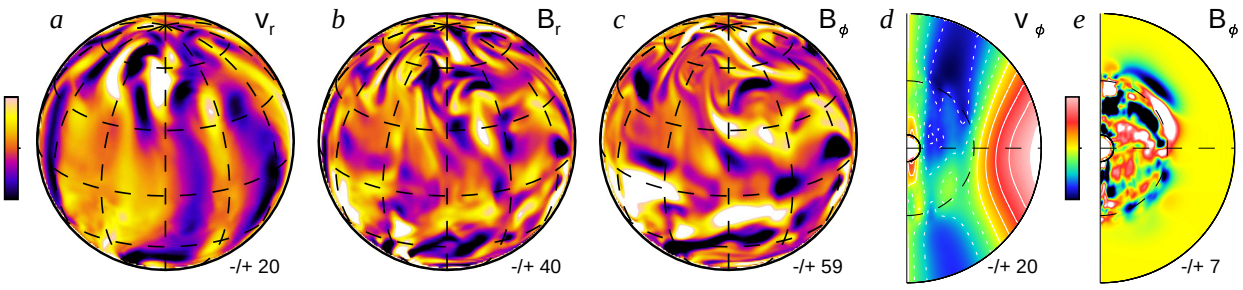

Figure 2.1: Flow and magnetic field properties of the core convection dynamo in the progenitor case C4m. (a) Snapshot of radial velocity at mid-core (r=0.10R), showing some columnar alignment of wavering rolls with rotation axis (upright). Regions of upflow are shown in light tones, downflows in dark tones; ranges in m s^{-1}. (b) Companion snapshot of radial magnetic field at mid-core, with stronger field roughly coincident with downflows. Positive fields denoted by light tones, negative by dark; ranges in kG. (c) Azimuthal magnetic field B_ϕ at mid-core with some extended ribbon-like structures running east-west. (d) Mean zonal velocity $\langle v_\phi \rangle$ in radius and latitude possessing a central column of slower rotation. Prograde flow shown in red tones, retrograde in blue tones; ranges in m s^{-1}. (e) Mean azimuthal magnetic field $\langle B_\phi \rangle$, with complex structure evident and exhibiting no preferred sense in either hemisphere. Positive field in red tones, negative in green/blue; ranges in kG.

purely toroidal and purely poloidal cases were also studied for comparison. In those cases, the field geometry and strength was identical to that component in the mixed field case. Due to stability considerations, it is the mixed field case A that appears to be the most physically relevant. As such, we have focused the bulk of our computational efforts and analyses on that case.

2.3 Core Dynamo in Progenitor

Some key aspects of the progenitor dynamo simulation case C4m are summarized in Figure 2.1 illustrating the typical flows and fields achieved at one instant in time. These flows have been sampled at mid-core ($r = 0.1R$) and are displayed on spherical shells. In addition, we have sampled the differential rotational profile and mean fields realized in this system (Figs. 1d and 1e), where the azimuthal velocity v_ϕ and magnetic field B_ϕ have been averaged over longitude and displayed as a function of radius and latitude.

Case C4m of BBT05 involves highly time-dependent flows with complex, vigorous convection that penetrated substantially into the overlying radiative zone. These flows are characterized by

convective motions spanning multiple scale heights that serve to couple widely separated parts of the computational domain. These convective motions give rise to a nearly adiabatically stratified core slightly prolate in shape. The prolate shape owes to the greater effect of the Coriolis force on radial velocities at the lower latitudes (see discussion in BBT04). Surrounding the convective core is a further region of overshooting, roughly spherical in shape, which does not substantially modify the stable stratification of the radiative zone. A striking change in case C4m compared to its own hydrodynamic progenitor is the significant suppression of the differential rotation in the core. The hydrodynamic case has a prominent column of slow rotation maintained primarily by Reynolds stresses arising from the convection that transport angular momentum equatorward and radially outward. These counteract viscous stresses that transport angular momentum poleward and radially inward.

The addition of a seed dipole magnetic field to that hydrodynamic case to yield case C4m, as discussed in BBT05, resulted in a marked change to the differential rotation of the system. The dynamo action achieved by this system produces Maxwell stresses that tend to transport angular momentum poleward, opposing the Reynolds stresses and ultimately disrupting the differential rotation. There remains a weak column of slower (retrograde) rotation (Fig. 2.1). The persistent dynamo action realized in this simulation yields nearly equipartition magnetic energies, with those about 90% of the kinetic energy. The magnetic energy in this system is largely comprised of fluctuating (non-axisymmetric) fields, with the axisymmetric poloidal and toroidal fields contributing little to the overall energy balance. Both the magnetic fields and flows in case C4m are highly intermittent in time, with no evident preferred field polarity.

The addition of a twisted dipolar magnetic field, consistent with the expected geometry of a primordial field, to case C4m leads to remarkable changes in the core dynamo. Magnetic fields achieved in the core become super-equipartition in nature, with an associated energy roughly tenfold that of the convective motions. We turn now to a detailed exploration of this dynamo state in the following chapter.

Chapter 3

Surprising Implications of a Primordial Magnetic Field

3.1 Modified Dynamo Action

A preliminary assessment of the dynamo action achieved in our 3-D simulations is provided by examining the evolving global energy balances achieved in each case. The energy associated with the kinetic energy (KE) is defined as

$$KE = \frac{1}{2}(\overline{\rho} + \rho)(v_r^2 + v_\theta^2 + v_\phi^2), \tag{3.1}$$

and magnetic (ME) energy as

$$ME = \frac{1}{8\pi}(B_r^2 + B_\theta^2 + B_\phi^2). \tag{3.2}$$

The azimuthal velocity v_ϕ is taken relative to the rotating frame. We find it useful to examine a number of decompositions of ME. To facilitate contact between our work and previous dynamo modeling, we are often interested in mean fields and flows and the fluctuations about those means. We thus adopt the following notation for the fluctuating (non-axisymmetric) velocities

$$\boldsymbol{v'} = ((v_r - \langle v_r \rangle)\boldsymbol{e}_r + (v_\theta - \langle v_\theta \rangle)\boldsymbol{e}_\theta + (v_\phi - \langle v_\phi \rangle)\boldsymbol{e}_\phi. \tag{3.3}$$

Angular brackets denote averages in azimuth (longitude). The fluctuating magnetic field vector $\boldsymbol{B'}$ is defined likewise. The magnetic energy is further decomposed into those portions associated with the mean toroidal fields (MTE), the mean poloidal fields (MPE) and the fluctuating nonaxisymmetric fields (FME). We define these quantities as

$$MTE = \frac{1}{8\pi}\langle B_\phi \rangle^2, \tag{3.4}$$

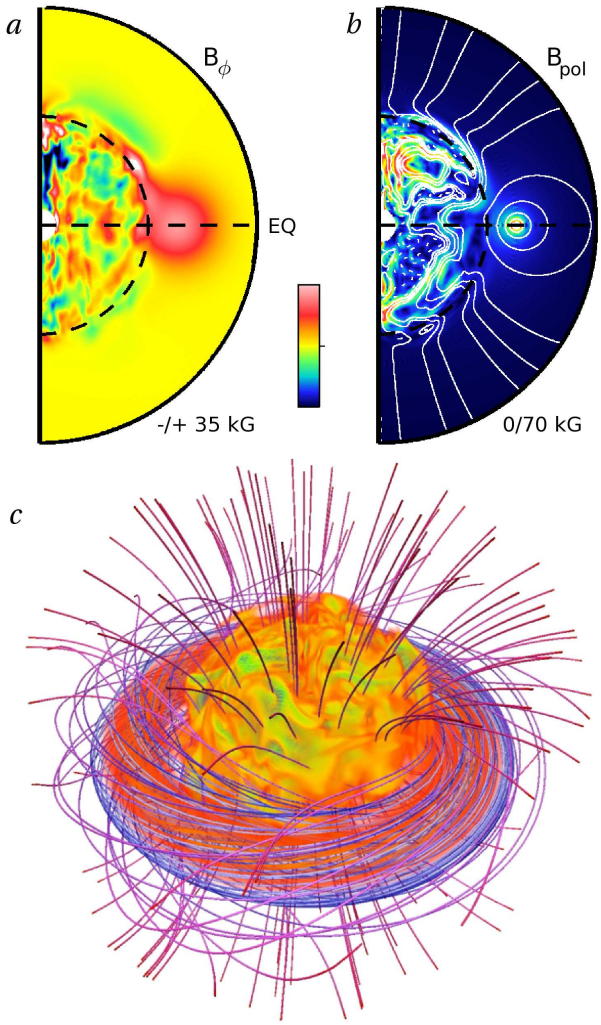

Figure 3.1: Superimposing a fossil field into the progenitor case to initiate case A. (a) Azimuthally-averaged B_ϕ at the initial instant and (b) the companion poloidal field. White lines denote poloidal field lines, and the underlay the poloidal field modulus. (c) Magnetic energy density shown volume rendered, with the imposed field forming the outer torus of moderate field strength. Field lines correspond to those of the fossil field only.

$$MPE = \frac{1}{8\pi}(\langle B_r \rangle^2 + \langle B_\theta \rangle^2), \tag{3.5}$$

and

$$FME = \frac{1}{8\pi}[(B'_r)^2 + (B'_\theta)^2 + (B'_\phi)^2]. \tag{3.6}$$

We also find it useful to distinguish between the magnetic energy in the fluctuating ϕ component of the field (FTE) and that in the fluctuating r and θ components (FPE), with

$$FTE = \frac{1}{8\pi}(B'_\phi)^2 \tag{3.7}$$

and

$$FPE = \frac{1}{8\pi}[(B'_r)^2 + (B'_\theta)^2]. \tag{3.8}$$

The superposition of our twisted fossil magnetic field into case C4m, involving the introduction of both toroidal and poloidal components, and denoted here as the mixed-field case A, is shown in Figure 3.1 at the outset. Magnetic field has been added primarily into the radiative zone, but there is some threading of the field near the equator into the convective core. There ensues a notable departure of behavior in our mixed-field system from that of the progenitor case C4m. This is readily apparent in the systematic evolution of kinetic and magnetic energies (Figs. 3.2*a*, 3.3). The KE, ME, and MTE shown here have been averaged over the full computational domain. We have also studied the early response of the system to either the introduction of the external purely poloidal field (case B, Fig. 3.2*b*) or of a purely toroidal field (case C, Fig. 3.2*c*). Variations in ME and KE occur on the dynamical time scale (i.e. the overturning time of roughly 100 days) in each case. It is evident that the toroidal field has little effect, whereas the purely poloidal field leads to a more rapid early growth in ME than the mixed-field case A. This suggests that the presence of a poloidal component, and not the twist (helicity) of the external field, is an important ingredient leading to significant growth in overall ME. However, since it has been argued that neither a purely toroidal nor a purely poloidal field would survive in the radiative exterior, we shall hereafter concentrate on the stable mixed-field case A.

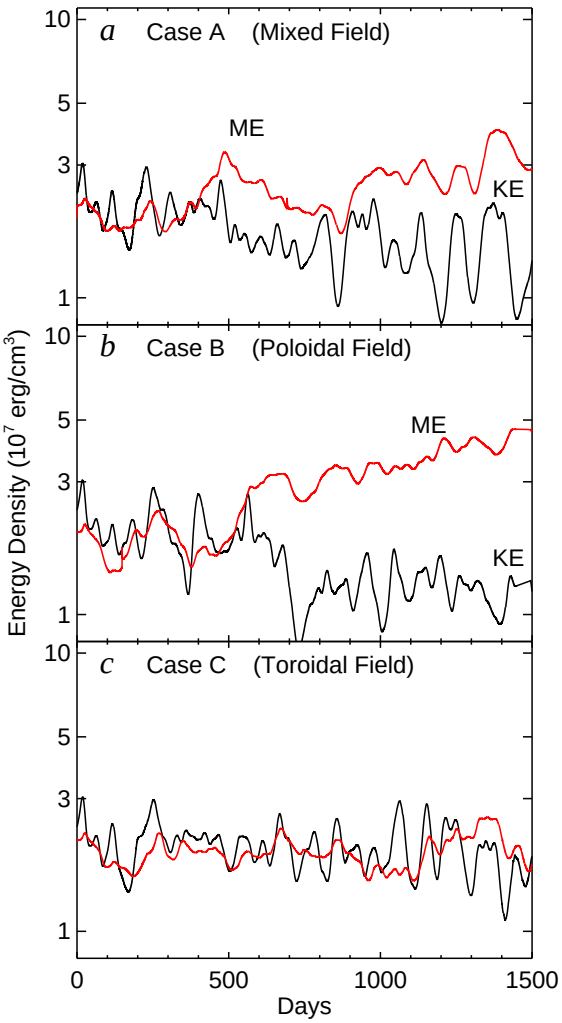

Figure 3.2: Separating the role of flux and helicity. (a) Temporal evolution of the mixed-field case A. Volume-averaged magnetic energy ME is shown in red and KE in black. (b) Temporal evolution for the poloidal field case B. (c) Evolution of the purely toroidal field case C. Cases A and B exhibit a tendency for transition to super-equipartition. Case C exhibits no such behavior, suggesting that the inclusion of a poloidal magnetic field spurs the transition.

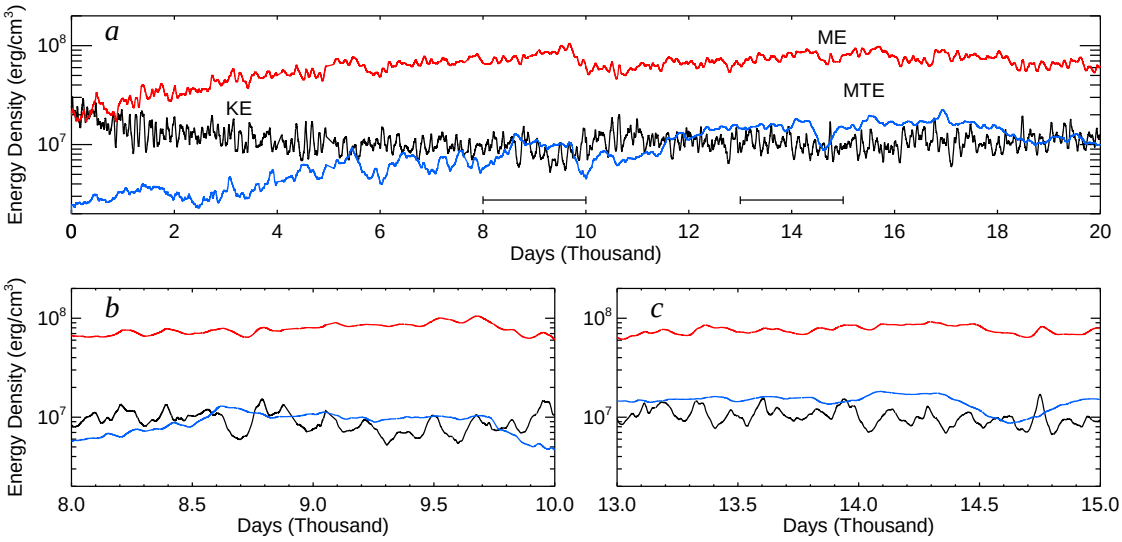

Figure 3.3: Temporal evolution of overall energy densities (volume-averaged) in case A after imposition of an external mixed magnetic field. *(a)* Full evolution sequence over 20,000 days (or about 2,900 rotation periods), revealing that the magnetic energy ME (red) has grown in strength to become about ten-fold greater than the kinetic energy KE (black). The mean toroidal field magnetic energy MTE (blue) has also increased prominently in strength, attaining in *(b)* roughly equipartition levels with KE in the close-in view starting at 8,000 days, and *(c)* slightly super-equipartition behavior in the interval starting at 13,000 days.

3.1.1 Temporal Evolution of Energies in Case A

The full evolution of case A is shown in Figure 3.3. Following the imposition of our fossil magnetic field (constituting only about a 10% increase in ME), the overall ME (volume integrated) of case A undergoes a phase of gradual growth. This growth of ME continues for approximately one magnetic diffusion time across the core radius (∼7,000 days), at which point the system reaches a saturation level of ME/KE ∼10. Over the roughly three diffusion times (and many hundreds of dynamical times) we have evolved this case, the ratio ME/KE is highly intermittent in time, varying on time scales of a few hundred days. It reaches a peak of about 16 near day 10,000, followed by a rapid decline to more typical values. Such behavior is in marked contrast to that of the progenitor case C4m where approximate equipartition of magnetic and kinetic energies was maintained throughout the simulation.

The energy balance here is achieved through a roughly fourfold rise in ME, along with a

twofold decrease in KE. The growth of ME is accompanied by a similar growth of axisymmetric (mean) toroidal fields (MTE) which generally account for about $10-20\%$ of the total ME, much as in the progenitor solution. A steady rise in MTE continues until approximate equipartition with respect to KE is reached. By contrast, the energy in the axisymmetric poloidal fields (not shown) comprises about 5% of the total ME on average. Axisymmetric toroidal fields undergo a brief phase of super-equipartition of their own near 15,000 days. Such equipartition and super-equipartition behavior of the mean fields is examined in expanded temporal detail in Figures 3.3*b*,*c* respectively. Here KE and ME both vary on time scales of one to two hundred days. By contrast, MTE varies on time scales of 500 to 1,000 days and follows the long term trends in ME. Shorter trends in ME are due largely to non-axisymmetric (fluctuating) magnetic fields within the core which vary on time scales commensurate with the convection. The axisymmetric fields are stored largely within the lower radiative zone where flows are much more quiescent. Diffusive processes play a more dominant role in the evolution of the magnetic field there, resulting in slower evolutionary trends for MTE. The variation in KE in the two extracted closeups of the time series (Figs. 3.3*b,c*) is modest despite the different MTE, in large part because the bulk of kinetic energy for this system is convective and concentrated within the core. Convective motions and axisymmetric fields thus interact largely near the convective core and radiative zone interface, which includes the region of overshooting.

3.2 Dynamics of Super-Equipartition State

The spatial structuring in the velocity and magnetic fields within the super-equipartition states realized by dynamo action in case A is relatively complex in order to avoid strong Lorentz forces that would otherwise seek to quench the flows. We now examine the nature of such structures and their implications for the overall dynamics.

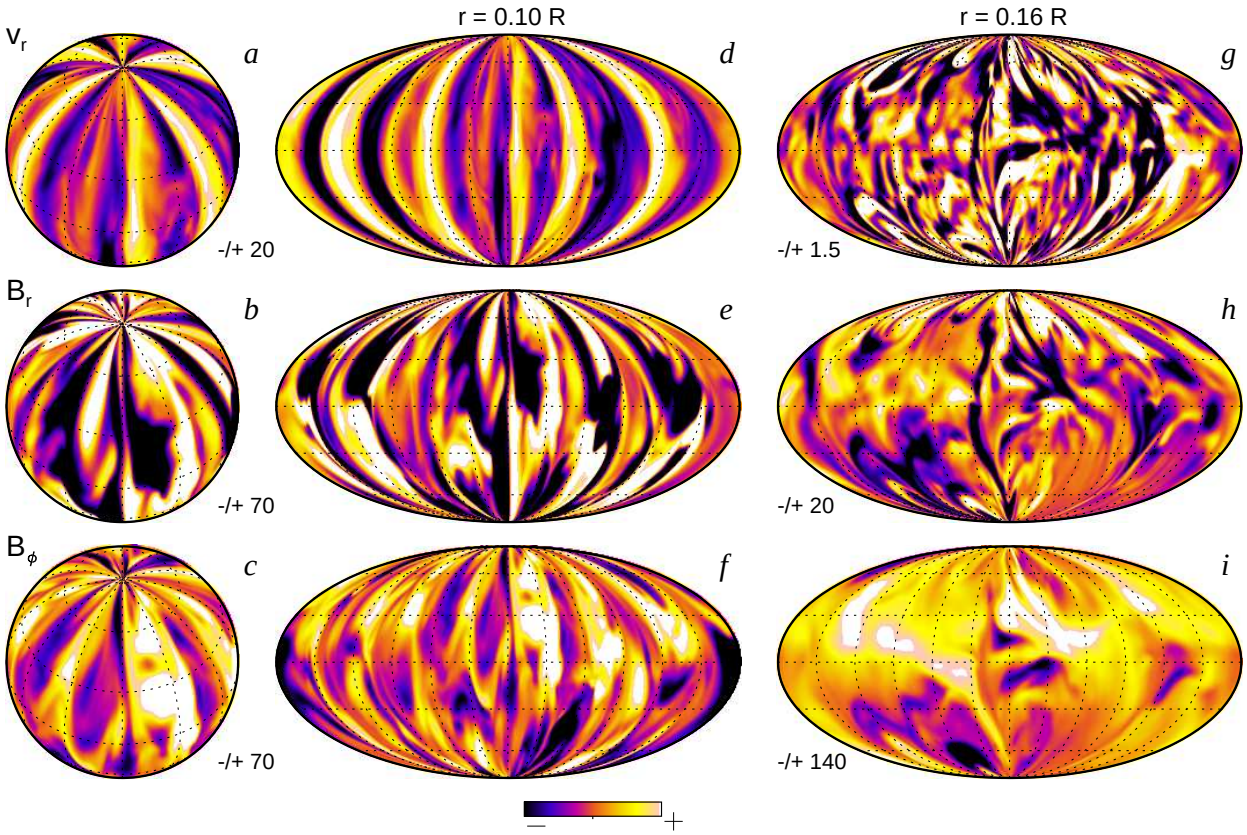

Figure 3.4: Snapshot of radial velocity v_r (upper panels) and the two magnetic field components B_r and B_ϕ (middle and lower panels) for the mixed-field case A at about day 15,000. The tilted orthographic views (left column) and Mollweide projection are sampled at mid-core (r=0.10R; left and center columns), and in the region of overshooting near the core and radiative zone interface (r=0.16R; right column). Using a common color table, velocity ranges are indicated in m s^{-1} and magnetic field sense and strength in kG; yellow tones are positive, dark violet negative.

3.2.1 Overall Properties

Strong magnetic fields generated in our mixed-field case A are present fairly uniformly throughout the convective core. The convection continues to exhibit broad upflows and downflows spanning much of the convection zone, with smaller scale motions present in the region of overshooting. A snapshot of the evolving flows and magnetic fields is shown in Figure 3.4, sampling radial velocities and both radial and azimuthal magnetic field components both at mid-core (r=0.10R) and in the overshooting region (r = 0.16R) at around day 15,000. Velocities and magnetic fields at mid-core are shown in both orthographic view (with the north pole tilted into view), and also rendered in Mollweide projection, with the full spherical surface thus visible. In the latter rendition, lines of latitude are denoted by horizontal lines (equator at middle), and those of longitude by curved lines. The radial velocity patterns (Fig. 3.4*a,d*) indicate roll-like motions roughly aligned with the rotation axis and involving about four to six rolls. These rolls extend from pole to pole, maintaining their coherence across both hemispheres. Such behavior contrasts with that of the progenitor where convective rolls tend to waver in latitude (Fig. 2.1*a*). Flows in case A exhibit somewhat smaller amplitudes than those of the progenitor case. Typical convective velocities (based on rms velocity at mid-core) for case A are $\sim$20 m s^{-1} versus $\sim$29 m s^{-1} before the external field was imposed. The radial velocity pattern in the region of overshooting (Fig. 3.4*g*), compared to mid-core, involves smaller scales and less alignment, consistent with intermittent upward penetration by plumes, which involve roughly tenfold weaker velocities.

The accompanying radial magnetic fields for case A at mid-core (Figs. 3.4*b,e*) and in the region of overshooting (Fig. 3.4*h*) exhibit similar patterns to that seen in the convective flows. These magnetic structures are less spatially intermittent than their counterparts in BBT05. Azimuthal magnetic fields display similar behavior (Figs. 3.4c, f, i) and exhibit much less banding within the core than that observed in the progenitor case. Typical magnetic field strengths at mid-core are roughly 80 kG, or about 20% higher than those present prior to imposing the fossil field. Regions of prominent azimuthal and radial fields exhibit approximate antisymmetry about the equator. The

simplified magnetic geometry within the core in case A is suggestive of a columnar, helical magnetic field topology unlike that seen in the progenitor case C4m.

Near the edge of the convective core, some rotational shearing still exists in the transition from weak differential rotation in the core to nearly solid body rotation in the radiative exterior. The strong B_ϕ (Fig. 3.4*i*) fields trace out the boundaries of the largest convective rolls. Shearing and stretching in the overshooting region allow these structures to grow into ribbons of field that wrap their way poleward around the cylindrical convective rolls. Magnetic field strengths within the centers of these ribbons are about 200 kG.

3.2.2 Complex Interplay of Flows and Field Structures

The intricate configurations of the strong magnetic fields realized in case A are clarified by Figure 3.5 showing 3-D volume renderings of the magnetic energy and tracings of the magnetic field lines, sampling the same time instant as in Figure 3.4. Magnetic energy throughout the convective core and the region of overshooting is presented in Figure 3.5*a*. The regions of strong magnetic energy density (denoted by green/orange tones) reach from equator to pole in long helical arcs. Toroidal structures are visible here as well, with magnetic energy tending to wrap around convective columns parallel to the rotational axis rather than the entire core. These impressions are accentuated in magnetic field line tracings (Fig. 3.5*b*), showing complex wrappings around the convective cells. Other volume renditions involve a narrow slice in the equatorial plane, sampling again the magnetic energy density (Fig. 3.5*c*) and the kinetic energy density (Fig. 3.5*d*). Here we view the equatorial plane as if from the north pole. The strong flux ropes (about 200 kG in strength) extend throughout much of the core, tracing out the pattern of the most prominent convective rolls found there. Regions of blue indicate strong ($\sim$ 300 kG) regions of magnetic field. These strong fields are part of extended helical arcs (Fig. 3.5*b*). The accompanying kinetic energy rendition (Fig. 3.5*d*) reveals that the strongest fields are laterally displaced from the fastest flows, recognizing that otherwise Lorentz forces may tend to suppress the flows unless the velocity and magnetic exhibit some measure of alignment (see §4.1).

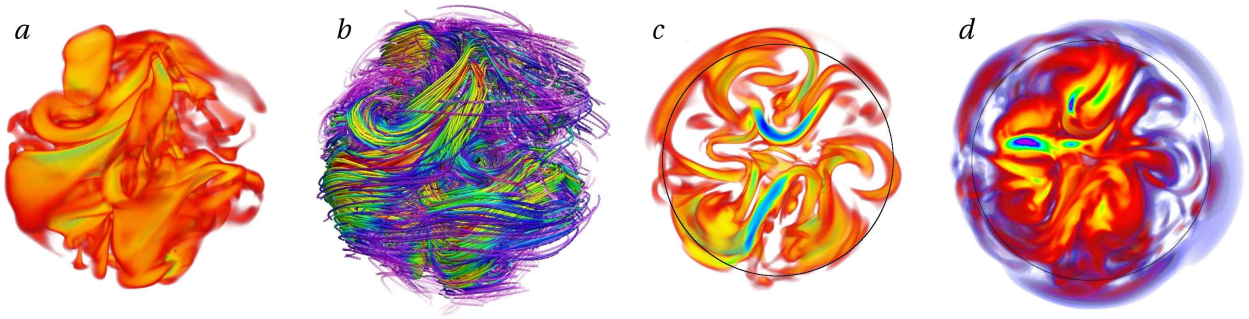

Figure 3.5: Volume rendering of magnetic stuctures (with rotation axis vertical) near day 15,000 accompanying Fig 3.4. (a) Magnetic energy density realized in the convection zone and region of overshooting; yellow/green tones indicate high values, and red tones low values. (b) Magnetic field lines traced throughout the convection zone. Yellow/red tones correspond to high field strengths, violet/blue tones to low. Strong flux ropes coincide with regions of high magnetic energy. (c) Magnetic energy density rendered in the equatorial plane viewed as if from the north pole, with greatest energy levels shown in blue/green. (d) Companion kinetic energy density rendered in the equatorial plane showing that the fastest flows are positioned adjacent to the sides of the regions of strongest field, with blue/green again highest energy density.

These dynamic structures in magnetic energy evolve on time scales of about 100 days. A sense of these intricate changes is provided by Figure 3.6 by sampling the evolution of magnetic fields in the equatorial plane over a 350 day interval. Here close inspection reveals that magnetic structures are seen to rise radially, stretch, and ultimately dissipate. At times large bundles of magnetic flux cleave into each other, forming tubular structures that encircle much of the convection zone at the equator.

3.2.3 Statistical Properties of Super-Equipartition State

Topological differences in magnetic fields and flows between case C4m and case A may be further characterized through probability distribution functions (pdf) of $\boldsymbol{v}$ and $\boldsymbol{B}$, as shown in Figure 3.7 for the velocity and magnetic field at mid-core. Magnetic fields (Fig. 3.7b,d) peak at higher values and exhibit a noticably greater range of variability in case A than in case C4m. This broadening, related to the spatial intermittency, may be quantified by measuring the kurtosis $\mathcal{K}$ (the fourth moment) of these curves. A large value of $\mathcal{K}$ indicates a broad distribution, and a low value indicates a narrow one. We find that $\mathcal{K}$ for B_r has transitioned from a value of 4.4 in case C4m

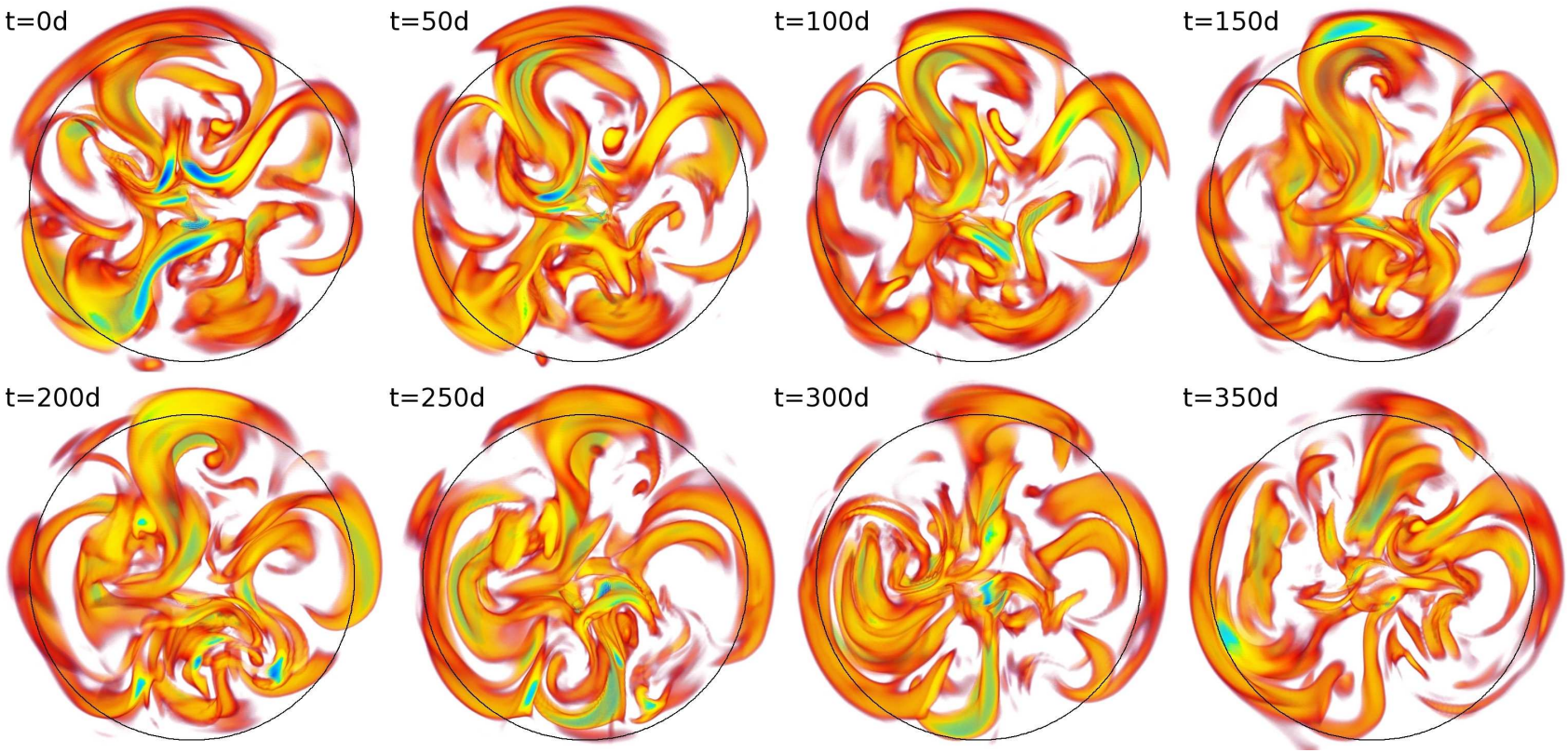

Figure 3.6: Sequence of views showing the evolution of magnetic energy density in narrow volume renderings of the equatorial plane, starting from day 15,000 (as in Fig. 3.5*c*). Green/yellow tones denote high values, red tones low values. Magnetic features stretch, strengthen, and at times join with those created by adjoining convective rolls.

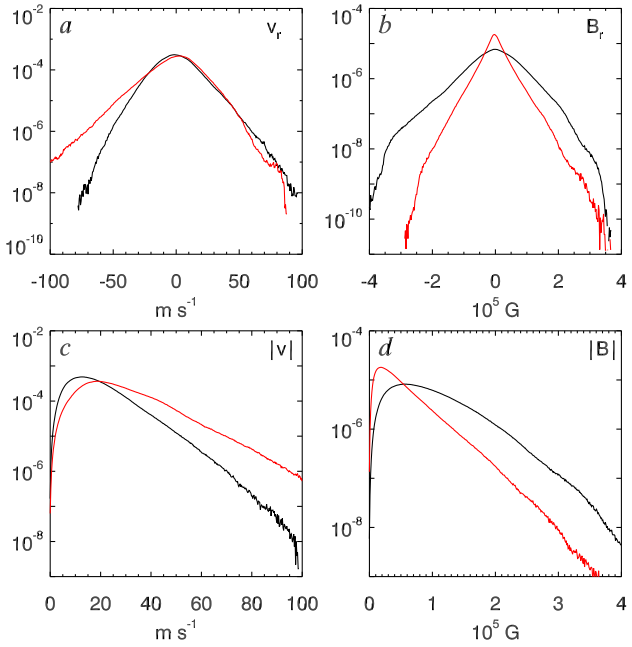

Figure 3.7: Time-averaged pdf's for case A (black) and case C4m (red) of velocities (V_r and $|V|$) and magnetic fields (B_r and $|B|$) sampled on a spherical surface at mid-core (r=0.10R). Case A is characterized by narrower velocity distributions and broader magnetic field distributions than case C4m.

to 6.7 in case A. The convective core of case A is thus pervaded more uniformly by strong magnetic field than in case C4m. The converse is true for the the velocity distributions (Fig. 3.7*a*,*c*), which are narrower and peak at lower values in case A relative to case C4m. Correspondingly the $\mathcal{K}$ for v_r has transitioned from 4.4 in C4m to 4.1 in case A. The most vigorous downflows in case A are somewhat weaker than those in case C4m which exhibits a more prominent negative tail in v_r.

3.3 Growth of Axisymmetric Helical Fields

The super-equipartition state achieved in case A involves the generation of strong axisymmetric (mean) magnetic structures well beyond that achieved in the absence of an external fossil field. Figure 3.8 shows the profiles with radius and latitude of the mean toroidal and poloidal magnetic fields for the greater part of the overall evolution. Two prominent twisted structures of opposite helicity have developed near the equator for our mixed case. Both torii persist on time scales of

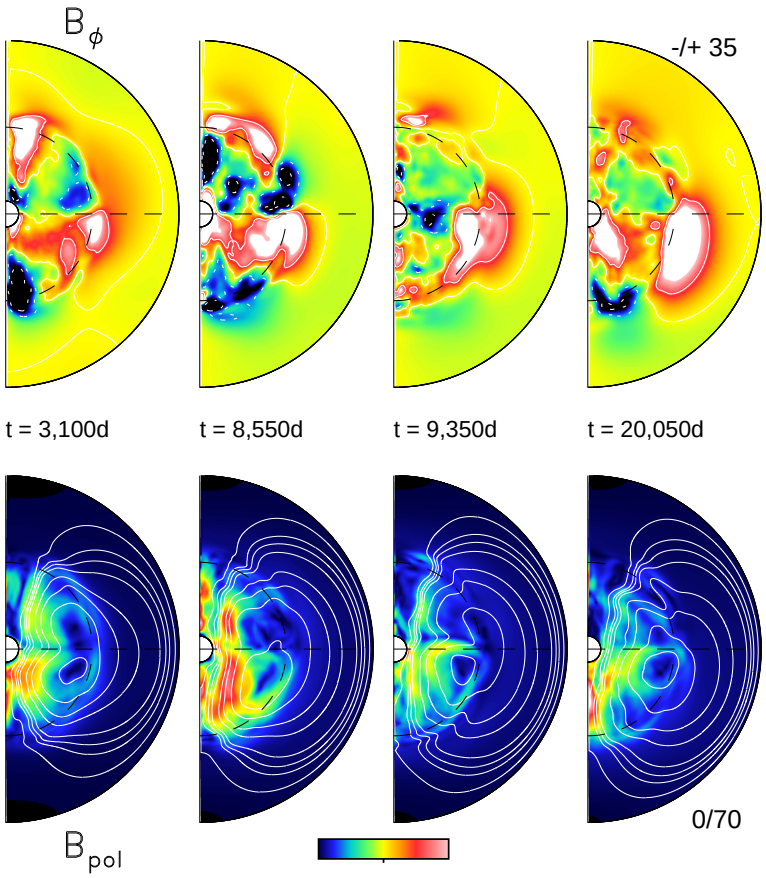

Figure 3.8: Temporal evolution of the mean toroidal (*upper*) and poloidal (*lower*) magnetic fields for case A. Each sample involves azimuthal averages, accompanied by a 100 day temporal average (centered about the indicated times). Helical structures of opposite polarity wax and wane over the course of the 17,000 days sampled. Magnetic field strength is shown in color; contours indicate poloidal field lines for B_{pol}, and zero field strength for B_ϕ. Units in kG.

order the diffusion time, but the northern, negatively signed torus tends to vary in strength more than its southern counterpart, disappearing completely after about day 10,000. These oppositely signed toroidal tubes with a common, enveloping poloidal component have typical field strengths of a few tens of kG, with peak mean field strengths of around 100 kG near their centers. For comparison, overall peak field strengths of 350 kG are achieved within the core. Evolution of the system for multiple diffusion times leads to the emergence of a single positively signed toroidal flux structure in the radiative envelope.

The prominent equatorial torii that develop mainly in the radiative exterior at low latitudes reside in a region previously characterized by strong rotational shear. The energy initially in the differential rotation (DRKE) is insufficient to account for the bulk of the magnetic toroidal energy (MTE) contained in these structures, since the DRKE comprised only about 10% of the total KE initially. Values of MTE near the end of the simulation (then comparable with KE) are roughly five times the initial value of DRKE. Rather than reflecting field structures that truly encircle the convective core, the torii of Figure 3.8 represent the mean of a more complicated magnetic geometry as seen in Figure 3.6. Thus while an Ω-effect is certainly at work on the poloidal fields in this region, non-axisymmetric motions are responsible for the bulk of the mean field generation here. We discuss these generation mechanisms further in §4.1.

3.4 Nature of Differential Rotation

The coupling of convection with rotation tends to redistribute angular momentum so that differential rotation is established, yet the structure and amplitude of such rotational shearing flows is difficult to predict. Browning, Brun & Toomre (2004) explored the differential rotation established by core convection in the purely hydrodynamic version of our A-type star. The convection yields a slow column of differential rotation throughout the core. With the inclusion of magnetism, and the realization of dynamo activity as in case C4m, this differential rotation is considerably weakened, but the slowly rotating (retrograde) central column of fluid (Fig. 2.1*d*) is retained. The radiative zone close to the equator exhibits a prograde mean zonal flow $\langle v_\phi \rangle$.

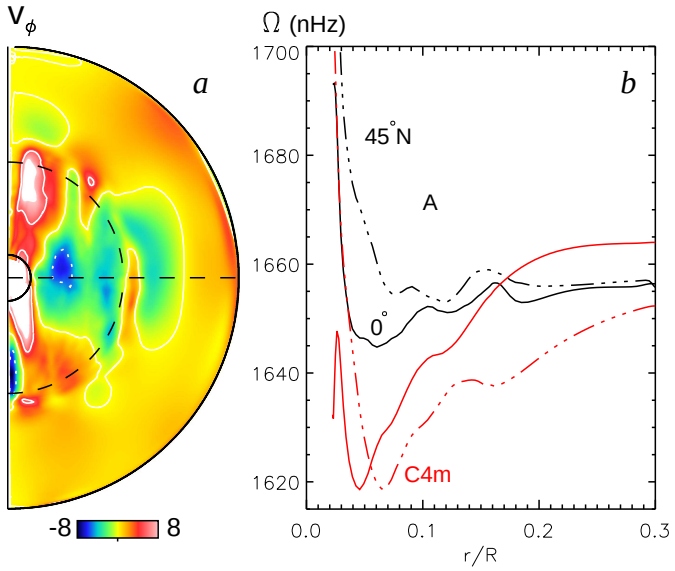

Figure 3.9: Differential rotation realized in Case A. (a) Zonal velocity v_ϕ averaged over longitude and over 200 days around day 15,000. (b) Radial cuts of mean angular velocity Ω at low (0°) and mid latitudes (45°N) for case A (black) and case C4m (red). The radiative zone is in a state of near solid body rotation for case A. The system frame rate Ω_0 is 1,655 nhz.

Imposing mixed or poloidal external magnetic fields alters the differential rotation until the radiative zone is nearly in solid body rotation (Fig. 3.9a,b). The slow central column of retrograde flow in the progenitor case is largely absent, replaced by a region of slightly prograde rotation close to the rotation axis. Magnetic torquing resulting from correlations between the imposed poloidal field, and the subsequently developing toroidal fields, transports much of the angular momentum from the radiative zone (seen as the faster v_ϕ in Fig. 2.1d) into the convective core. Radial and latitudinal shear throughout much of the domain is diminished at late times, particularly near the core and radiative zone interface. A weak retrograde jet has formed coincident with the location of the large helical magnetic structures (evident in B_ϕ in Figure 3.8) formed close to the interface. The super-equipartition state arising from the imposition of a mixed magnetic field has thus significantly diminished the differential rotation present in the progenitor case.

Weak departures from solid body rotation in the outer radiative envelope of case A are generally columnar in nature, with lines of constant Ω cutting across field lines in the radiative envelope. There the angular momentum transport is dominated by magnetic torques and meridional

circulations. Magnetic torques realized in case A are much stronger relative to case C4m owing to the large axisymmetric fields realized in the radiative envelope of case A. However, transport of angular momentum by meridional circulations prevents a pure state of isorotation as suggested by Ferraro's law (Ferraro 1937) along magnetic field lines, ultimately maintaining a differential rotation similar in nature (but weaker in amplitude) to that achieved primarily through meridional circulations and viscous transport in the progenitor case C4m.

Before proceeding, we note that our perfect conductor boundary conditions, which force magnetic field lines to close within the domain may also play some role in sustaining the nearly solid-body rotation observed in the radiative zone. The progenitor case C4m employed a radial magnetic field boundary condition which may have favored the columnar differential rotation realized in that case. The closing of our magnetic field lines within the domain will necessarily disrupt a tendency toward such columnar differential rotation in the radiative zone. In the super-equipartion regime, the core dynamo has a tendency to build strong horizontal magnetic fields at the lower boundary, and a perfect conductor lower boundary condition is more appropriate for case A. The appropriate boundary condition for the outer boundary is less clear. Were the strong toroidal fields generated at the core-radiative zone interface to become magnetically buoyant, adopting a radial magnetic field boundary condition at the top of the domain may become problematic as the (likely toroidal) field is forced to change its geometry over the last few grid points. However, we have not yet observed the buoyant rise of magnetic field in case A, and we note that it may thus be interesting to examine what effects of a radial magnetic field boundary condition at the outer boundary may have on the differential rotation achieved in the radiative zone.

3.5 Distribution of Magnetic Energy

Magnetic energy in case A is largely contained within the convective core of the A-type star. However, convective overshoot, meridional circulations, and diffusion serve to transport some magnetic field into the overlying radiative zone. We now examine several components of the magnetic energy and their distribution throughout the computational domain. Various time-averaged mag-

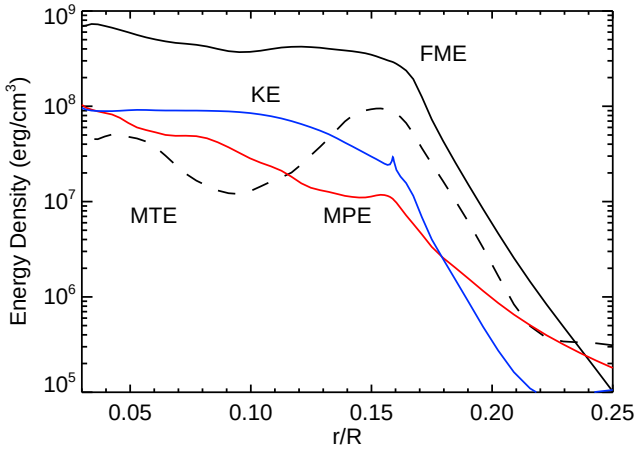

Figure 3.10: Variation with proportional radius of horizontally-averaged kinetic and magnetic energy densities for case A. Profiles are averaged over 100 days near day 15,000. The penetrative convective core boundary is roughly at r=0.16R.

netic and kinetic energy densities are shown as a function of radius in Figure 3.10. These quantities have been averaged over the full sphere at each radius and then temporally averaged over the interval spanning 15,000 to 15,100 days. Magnetic fields are super-equipartition compared to the kinetic energy throughout the core and the region of overshooting owing largely to fluctuating magnetic fields (FME). The mean field energies MTE and MPE are largely sub-equipartition throughout the core. However, the mean toroidal fields peak to super-equipartition values near the interface, owing to the development of large toroidal bands of magnetic field there. Magnetic energies of all types fall off substantially outside of r$\sim$0.16R, the approximate outer edge of the region of overshooting. Magnetic energies in the remainder of the radiative zone are achieved largely through diffusive processes. The energy balance both inside and outside the core is detailed in Table 1. All energies are quoted relative to the average KE in each region.

3.6 Growth of Large-Scale Magnetic Structure

The addition of our fossil field has led to the development of larger-scale magnetic structures than those present in the progenitor simulation. Figure 3.11*a* depicts the time-averaged magnetic

TABLE 1
Magnetic to Kinetic Energy Ratios

Region	Convective Core	Radiative Envelope
ME/KE	7.38	5.18
FME/KE	6.36	3.75
MTE/KE	0.64	1.22
MPE/KE	0.38	0.21

Table 3.1: Time and volume averaged magnetic energies compared to kinetic energies. Temporal averaging covers days 15,000 to 15,100 as in Fig. 3.10. Volume averaging is carried out over the convective core ($r \leq 0.15R$) and over the radiative envelope ($r > 0.15R$).

energy spectrum (with spherical harmonic degree ℓ) soon after the imposition of an external field in case A. Shown also is the spectrum for a more mature stage ($\sim$ day 15,000) during the simulation after super-equipartition magnetic fields have developed. Individual spectra were created using spherical shells at mid-core and averaged over about 200 days in each case. Magnetic energy has increased on scales as small as spherical harmonic degree $\ell = 60$, but the larger scales ($\ell \leq 10$) exhibit the most growth. The mixed external field has thus led to the growth of the large-scale components of the magnetic field, while leaving the energy in the smaller structures relatively unchanged. Moreover, these structures are largely non-axisymmetric, with axisymmetric structures comprising only about 20% of the magnetic energy on average.

The accompanying kinetic energy spectra are shown in Figure 3.11b . As the dynamo reaches super-equipartition levels, kinetic energy decreases by a factor of about two across much of the spectrum. This trend reflects the overall decrease of kinetic energy shown in Figure 3 and the transition of the system to a less turbulent state.

The growth of large-scale magnetic structure is also apparent in volume renderings of the magnetic energy in Figure 3.12, showing snapshots of the magnetic energy density just prior to inserting the external field and during the super-equipartition phase (day 15,000). The rendering of the full convective core conveys a good sense of the helical convection in the core. The ribbons of magnetic energy seen at early times (Fig. 3.12c) have become noticebly wider in the super-equipartition regime (Fig. 3.12d). Similar morphology is apparent in renderings of ME in the

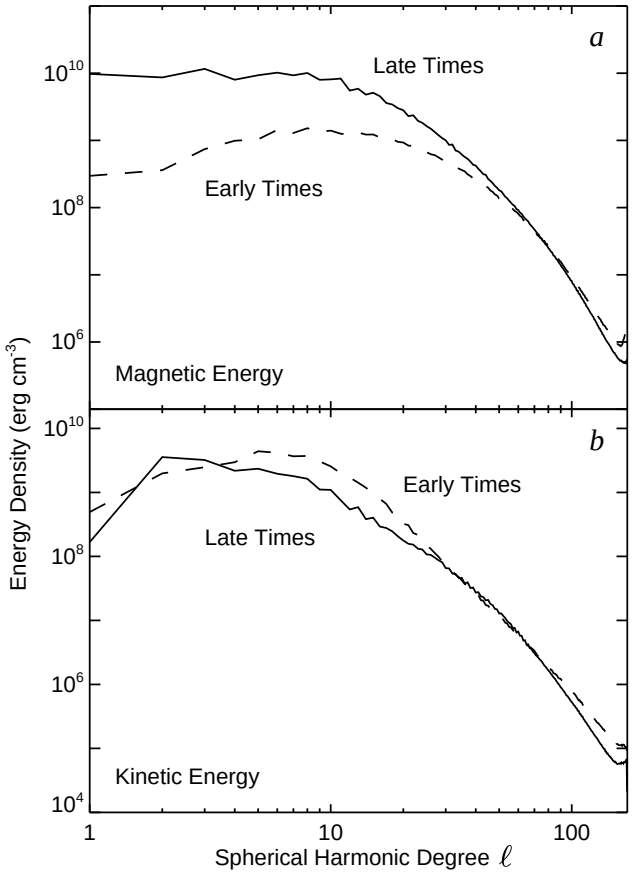

Figure 3.11: Magnetic and kinetic energy spectra sampled at mid-core in case A for early and late times. (a) Time-averaged initial ME spectrum (dashed line) and the spectrum realized after 15,000 days (solid line). (b) Accompanying KE spectra. The imposition of mixed fields in case A has yielded a dynamo with more prominent global-scale magnetic fields than in progenitor case C4m.

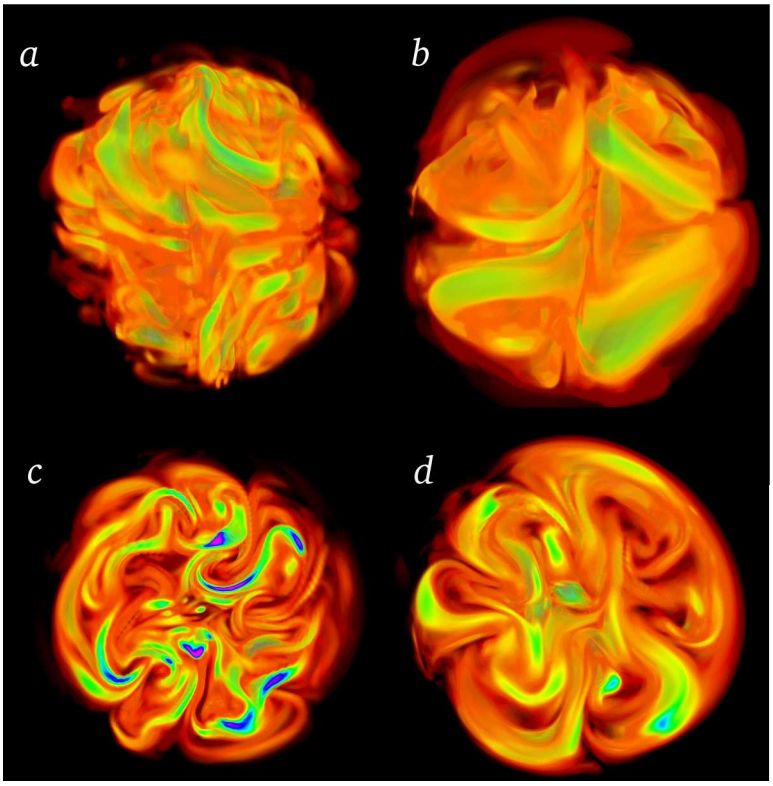

Figure 3.12: Volume rendering of magnetic energy density viewing the entire convection zone (a) prior to the insertion of the fossil field, and (b) 15,000 days later. The rotation axis is vertical. Structures are noticably larger in scale in the later super-equipartition regime. Companion images of magnetic energy density viewing the equatorial plane from the north, showing (c) progenitor state and (d) mature super-equipartition state.

equatorial plane. The early time (Fig. 3.12c) exhibits much smaller-scale fields than the later time (Fig. 3.12d). The shift in peaks of KE and ME in the energy spectra of Figure 3.11 suggests that the dynamo now running in case A is much more global-scale in nature than that in the progenitor case C4m. We turn now to a detailed examination of the mechanisms by which case A sustains such a large-scale, super-equipartition state.

Chapter 4

Maintaining the Strong Dynamo

4.1 Sustaining a Super-Equipartition State

The super-equipartition state achieved here in which magnetic energy ME is tenfold greater than the convective kinetic energy KE is quite remarkable, for one might anticipate that the feedback from the Lorentz forces would prevent this. In contrast, progenitor case C4m was nearly in equipartition by this measure. So how does case A achieve and sustain such strong magnetic fields? The shift towards larger-scale convective motions and magnetic field structures suggests that a more global field/flow topology is necessary for this state. The high magnetic field strengths realized in case A might be anticipated to yield Lorentz forces that react back on the flow, ultimately quenching the flows that generate such fields through an α-quenching process (Cattaneo & Hughes 1996). For our energy balance to survive, the flows must organize themselves in a fashion that minimizes these Lorentz forces while still maintaining sufficient induction to balance the dissipative processes present in the system (which also serve here to provide some field reconnection). This may be accomplished by separating regions of strong flow from those of strong magnetic field, or by some tendency to align $\boldsymbol{j}$ and $\boldsymbol{B}$ and thereby lessen Lorentz force feedbacks. We turn now to a discussion of these issues and of the dominant mechanisms responsible for magnetic field generation in case A.

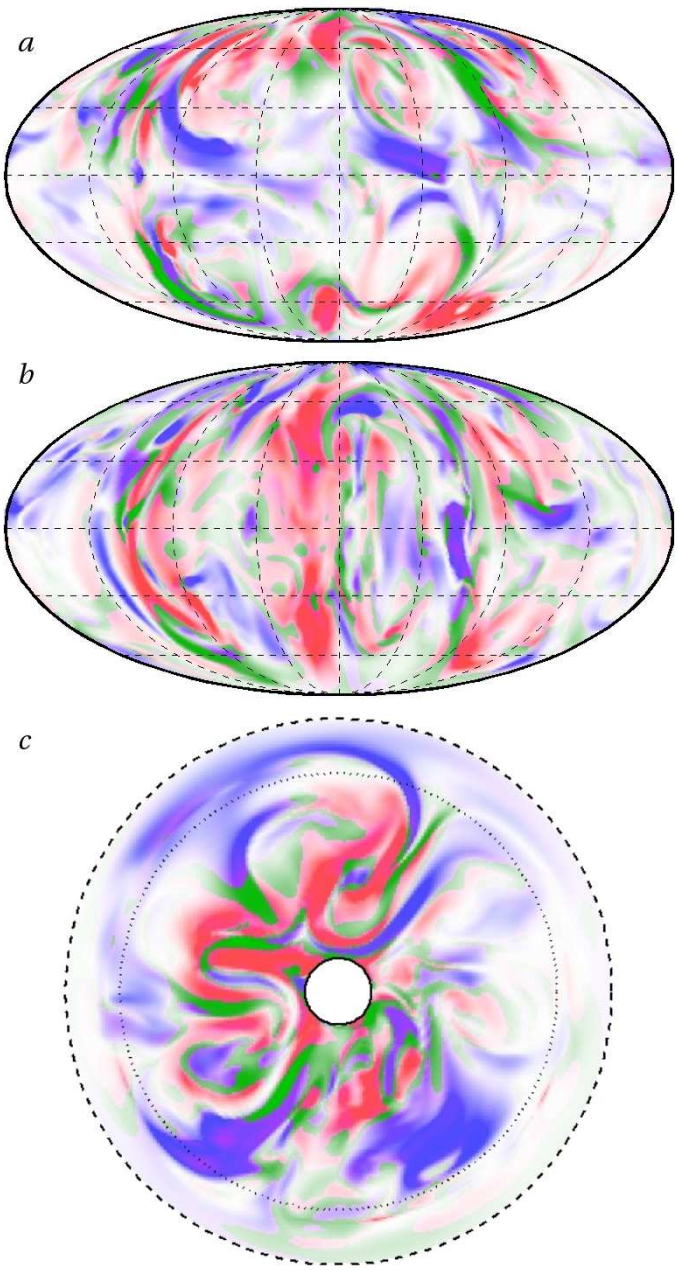

Figure 4.1: Dual rendering of kinetic energy (red) and magnetic energy (blue) near day 15,000. Regions where both quantities are strong (relative to their respective rms values) appear in green. (*a*) Mollweide view at the interface between the core and the radiative zone (r=0.15R), and (*b*) at mid-core, (r=0.075R). (*c*) Partial view of the equatorial plane from the pole. The dotted line denotes the edge of the convective core, and the outer dashed line r=0.19R, capturing a portion of the radiative zone (including the region of overshooting).

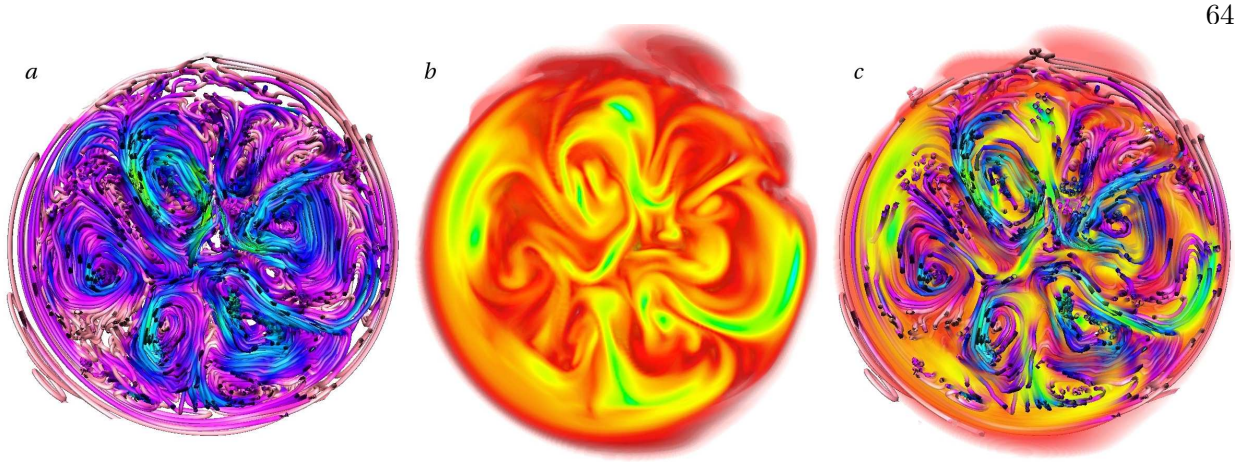

Figure 4.2: Comparing partitioning of fast flows and strong fields in a snapshot sampled in the equatorial region. (a) Instantaneous flow tangent lines (day 9,000). Coloring in blue/green indicates the fastest speeds ($\sim$30 m s^{-1}) and regions of violet/pink that of weaker flows ($\sim$5 m s^{-1}). Six prominent rolls are present. (b) Patterns of stronger magnetic energy are similar to those of the faster flows though somewhat displaced. Regions of bright green denote $\sim$250 kG fields, reddish regions $\sim$30 kG fields. (c) Flow lines and magnetic energy density rendered together. Regions of fast flow and strong fields exhibit notable alignment.

4.1.1 Surviving Lorentz Feedbacks

We can assess the nature of alignment and displacement of field and flow by examining their large-scale organization as illustrated in Figure 4.1. Here instantaneous snapshots of magnetic energy and kinetic energy near day 15,000 are overlaid at two depths and in an equatorial cut. Regions of strong ME are shown in blue, strong KE in red, and regions where both are strong (relative to their rms values) are shown in green. Clearly the patterns in KE are similar to those seen in ME. However, some of the features are laterally displaced, with arcs of ME running adjacent to arcs of KE. Some patches of overlap are visible as well, particularly in Figure 4.1c which suggest that some strong magnetic structures merge with fast velocity structures. For such overlapping regions to survive, Lorentz forces must not be strong enough locally to disrupt the flow. This, in turn, implies some alignment of $\boldsymbol{j}$ and $\boldsymbol{B}$. The current density $\boldsymbol{j}$ depends, through Ohm's law, on both the electric field and on the alignment of flows and fields (through $\boldsymbol{v} \times \boldsymbol{B}$). Minimizing the Lorentz force locally thus typically implies some alignment of $\boldsymbol{v}$ and $\boldsymbol{B}$.

The large-scale alignment of flows and fields may be explored through volume renderings

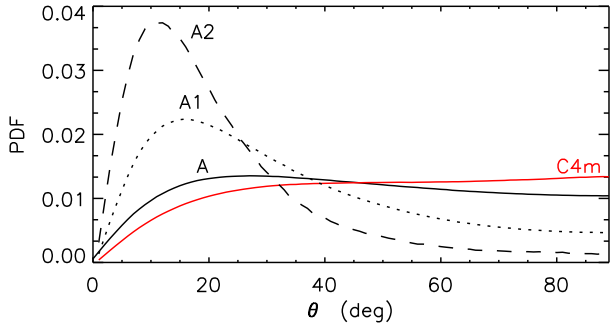

Figure 4.3: Probability distribution functions (pdfs) of the relative angle θ between $\boldsymbol{v}$ and $\boldsymbol{B}$ measured throughout the convective core for cases A (black) and C4m (red), averaged over about 50 realizations spanning 100 days. Flows and magnetic fields exhibit more alignment in the super-equipartition regime of case A than in case C4m. The alignment of flow and magnetic fields in case A is more pronounced in regions of strong flow and field, shown by plotting pdfs only for sites where local values of both $\boldsymbol{v}$ and $\boldsymbol{B}$ exceed their rms values (labeled A1) or twice those values (A2).

as in Figure 4.2*a* where instantaneous streamlines are depicted in the equatorial region. The corresponding magnetic energy density (Fig. 4.2*b*) and a combined rendering of these two quantities (Fig. 4.2*c*) are illustrated as well. The large, cloverleaf-type patterns in the magnetic energy density are typically tangent to the local magnetic field vector. Rendered in the same image, the two patterns trace each other closely, with alignment most evident in regions of strong magnetic field. Another measure of the alignment of flows and magnetic fields is achieved by examining the relative angle θ between $\boldsymbol{v}$ and $\boldsymbol{B}$ throughout the core. Figure 4.3, examining probability distribution functions (pdfs) of that angle, shows that our evolved case A typically exhibits more alignment than the progenitor case C4m. By weighting these by the local KE and ME, thus concentrating on regions of fast flow and strong field, the alignment becomes more pronounced. This may be seen by forming pdfs where both $\boldsymbol{v}$ and $\boldsymbol{B}$ exceed a threshold of either just their rms values (curve A1) or twice those values (A2). For the latter, the pdf peaks at $\theta \sim 10°$, compared to sampling all sites which yields a broad maximum centered on 25°.

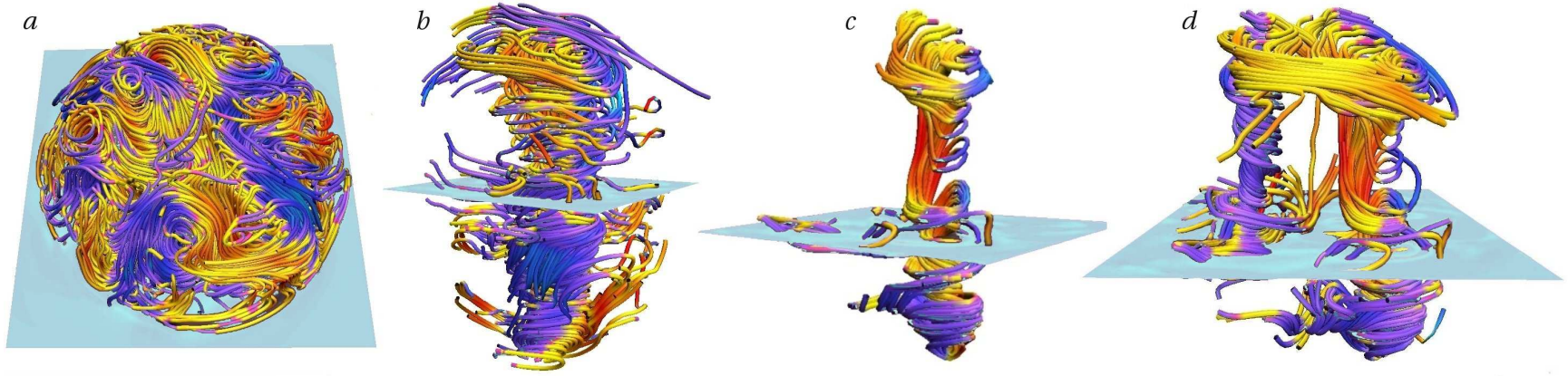

Figure 4.4: Columnar convection for case A visualized using instantaneous streamlines near day 15,000. Streamlines are colored by velocity component along the rotation axis v_z. Blue (yellow) tones indicate northward (southward) motion; equatorial plane indicated by light blue. (a) View of convective core from the north. The core is typically dominated by four to six prominent rolls. (b) Individual columnar cell from the roll complex. The columnar motion extends across the equatorial plane. Tilting of the orbits due to the spherical boundary of the core is visible. (c) Interior view of the same roll. Many rolls in this system possess an axial flow. Such flows freely cross the equatorial plane as seen here. (d) Rendering of that roll along with a neighboring roll. Axial flows tend to link neighboring rolls near the edge of the convective core.

4.1.2 Global Connectivity of Structures

Figure 4.2 showing an equatorial cut has emphasized that the core is typically occupied by four to six cylindrical convective rolls, with their axes primarily aligned with the rotation axis, as suggested by Figure 3.4*d*. The geometry and connectivity of the flows in this system play a significant role in how the strong magnetic fields are built and sustained. Turning to analysis of flow streamlines shown variously in Figure 4.4, we see that the rolls typically possess a narrow core, with a prominent upward or downward velocity (say v_z) along the rotation axis. Within each roll, surrounding the fast core is a broader region of circular flow in a plane nearly perpendicular to the rotation axis. As these convective motions overshoot into the radiative zone, buoyancy forces brake the radial component of the flow. The resulting tilt of the roll motions reflects the slope of the intersection of the roll with the edge of the convection zone and is similar to that observed in simulations of rotating spherical shells with rigid boundaries (e.g., Busse 2002). These outer regions of the rolls exhibit a weaker v_z than in the fast core of the roll, though of the same sense, thus yielding helical flow lines.

It is quite striking that the fast axial core flow in one roll can often be seen to connect near the radiative interface to the core flow (of the opposite sense) in an adjacent roll. The axial core flows extend along with the overall roll structure across the equator, though there are some examples in which the sense of the axial flow changes at the equator. These axial core flows can thus serve to effectively connect the two hemispheres, in addition to linking neighboring rolls.

The coupling of the rolls is also evident in the time sampling of both streamlines and magnetic energy density shown in equatorial cuts in Figure 4.5. Close study shows that there are frequent events in which streaming flows extend across the full domain, thereby coupling opposite sides of the convective core. It appears that the genesis of such streaming flows comes from two counter-rotating rolls on one side of the convective core (yielding a zone of converging flow toward the rotating axis) becoming correctly phased with another set of rolls on the opposite side that are driving some flow away from the axis. Such large-scale flows appear to be crucial to establishing the largest

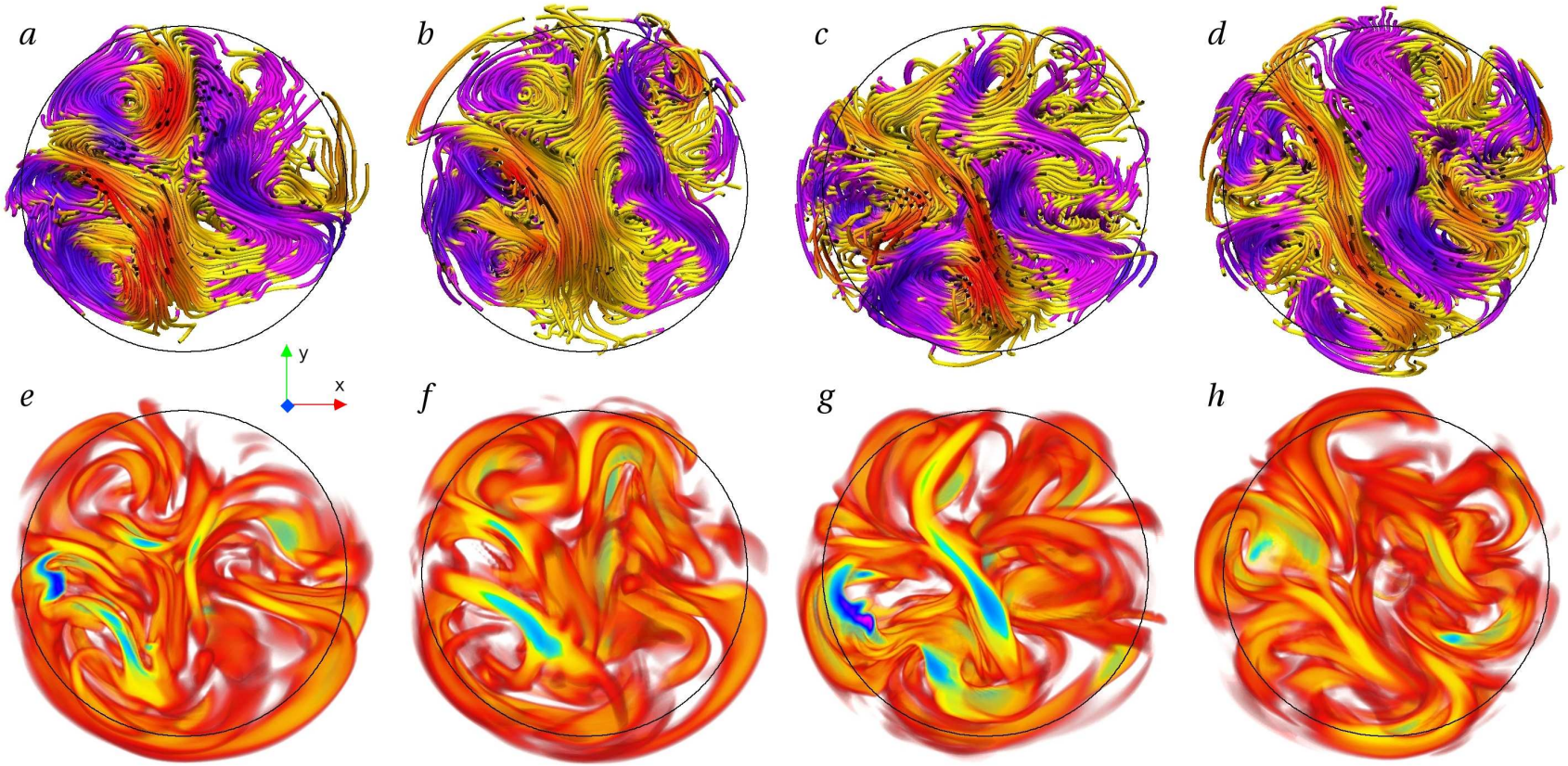

Figure 4.5: Sampling the evolving flow streamlines (*a*-*d*) and accompanying magnetic energy density (*e*-*h*) close to the equatorial plane in four time instants each separated by about 50 days (starting at day 9,000). Violet tones indicate positive motions in the y-direction, and yellow tones negative motions. Regions of strong ME are shown in yellow/green tones.

magnetic structures built by the dynamo action. As these streaming flows couple distant portions of the core, they stretch and advect the fields into the configurations seen in the the evolving ME patterns. Figure 4.5 shows that broad swathes of magnetic field extending across the convective core are nearly coincident with the fast core crossing flows. Thus it appears that attaining global-scale magnetic field within a core that possesses little differential rotation, yet senses Coriolis forces significantly, relies on the large-scale connectivity among the evolving system of rolls.

Although the convective rolls are fairly complex and variable in time, the more prominent rolls maintain their coherence for a few tens of rotation periods. The prominent axis-crossing motions serve to connect rolls on opposite sides of the core, stretching magnetic field from one roll to another as they do so. The resulting magnetic field structures thus thread through multiple rolls, connecting across the rotation axis and along the periphery of neighboring cells. The topology has thus become much more global in scale, resulting in the notable spectral change seen in Figure 3.11.

4.1.3 Details of Magnetic Field Generation

As the magnetic energy in case A is manifest predominantly in the fluctuating (non-axisymmetric) magnetic fields, we focus on the generation of FME here. The generation of energy in the fluctuating fields may be computed by taking the dot product of the induction equation with the fluctuating magnetic field $\boldsymbol{B'}$. Contributions to the generation of FME arise from correlations between fluctuating flows and fields with both their fluctuating and mean counterparts. However, while mean flows and magnetic fields contribute to the generation and destruction of FME, we find that the primary balance is struck between terms involving shearing, diffusion and advection associated with the fluctuating components of the flow and magnetic field so that

$$\frac{\partial(FME)}{\partial t} \approx 0 \approx \frac{1}{4\pi}\boldsymbol{B'}\cdot[\underbrace{(\boldsymbol{B'}\cdot\nabla)\boldsymbol{v'}}_{\text{shearing}} \underbrace{-\nabla\times(\eta\nabla\times\boldsymbol{B'})}_{\text{diffusion}} \underbrace{-(\boldsymbol{v'}\cdot\nabla)\boldsymbol{B'}}_{\text{advection}}] \tag{4.1}$$

holds approximately. We examine the contributions of these individual terms to the generation and dissipation of the constituents of FME (namely FPE and FTE) in Figure 4.6.

The local enhancement and diminishment of FPE by advection (Fig. 4.6*a*) reflects the columnar nature of the rolls. Orbital motions about the axes of these rolls efficiently carry FPE from regions of generation (via shearing as in Fig. 4.6*b*) to the rest of the core. Generation of FPE occurs primarily near the rotation axis and near the outer boundary of the core. The noticably weak columnar region of generation at mid-core is roughly coincident with the location of the roll axes. Orbital motions of the rolls are largely parallel to the equatorial plane throughout most of the core. As buoyancy brakes the radial component of these motions in the region of overshooting, the resulting motions tend to conform to the spherical boundary of the core. The ensuing tilting of the orbits (see Fig. 4.4) sets up a region of shear between the rotation axis and the outer core that serves to generate field parallel to the core boundary. Additional generation of field in the outer core also occurs through shearing in the azimuthal direction that serves to convert B_ϕ into B_r and B_θ there. Generation of FPE near the rotation axis, somewhat stronger than that seen in the outer core, is accomplished primarily through generation of B_r due to shearing of B_ϕ. The close proximity of inflows and outflows of the columnar rolls near the rotation axis sets up regions of strong shearing of radial flows (see Fig. 4.5*a,c*) that efficiently stretches the strong azimuthal field generated in this region into radial field. Core-crossing flows in particular, such as that prominently visible in Figure 4.5*d*, have a similar effect in this region.

The effect of advection on FTE (Fig. 4.6*d*) is similar to that seen with FPE in that circulations generally carry energy away from the region of strong generation near the rotation axis (Fig. 4.6*e*) to the outer core where less generation is occurring. Generation of FTE occurs primarily near the rotation axis as well. The convergence of multiple rolls at the rotation axis sets up gradients of v_ϕ in the direction perpendicular to the rotation axis, resulting in strong shear in this region. Moreover, core-crossing motions such as in Figure 4.5*d* will effectively shear radial field orthogonal to these motions, generating azimuthal field in the process. An additional effect, not included in the decomposition of Figure 4.6, is the action of mean shear near the rotation axis (see Fig. 3.9*a*)

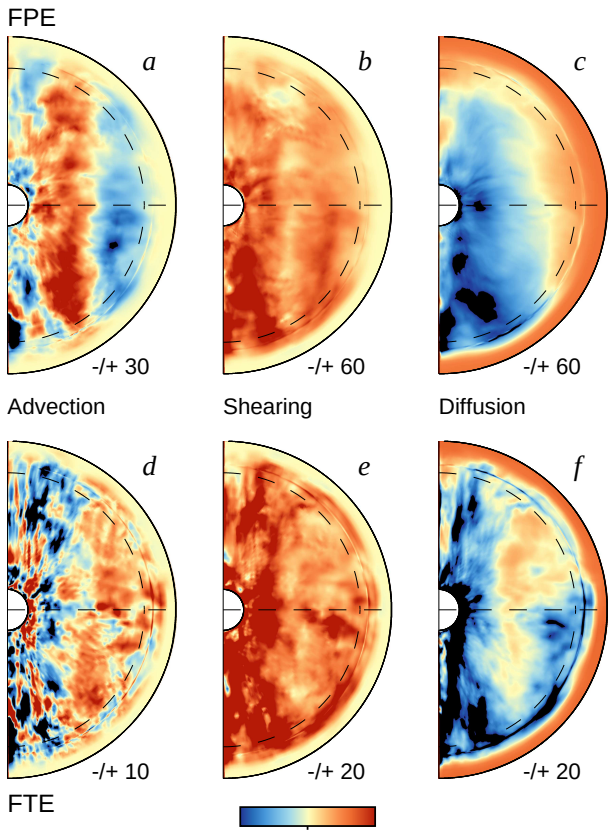

Figure 4.6: Generation and dissipation of fluctuating magnetic energy for case A. (*top row*) Generation of FPE from (*a*) advection, (*b*) shearing and (*c*) diffusion. (*bottom row*) Generation of FTE likewise from (*d*) advection, (*e*) shearing and (*f*) diffusion. Generation terms are shown in erg cm^{-3} s^{-1} and have been averaged in azimuth and in time over 200 days near day 15,000.

acting on the non-axisymmetric B_r and B_ϕ. Very near the rotation axis, the generation of FTE through this shearing effect is comparable to that due to the non-axisymmetric flows. We note that no similarly strong effects of mean flows on generation of FPE is observed. An additional region of strong generation of FTE is present at the outer boundary of the convective core. In contrast to FPE, the geometry of this region is largely spherical in nature owing to the transition from relatively strong azimuthal flows in the core to a region of nearly solid body rotation in the radiative zone.

The effects of diffusion on FPE and FTE (Figs. 4.6*c*,*f*) is strongest near the rotation axis and weakest in the outer core where advection mitigates the effects of generation more readily. The net effects of diffusion in the regions of generation is thus to destroy FTE and FPE. Beyond the region of overshooting, however, diffusive processes serve to carry energy from the outer edge of the convective core into the radiative zone where generation of magnetic field is minimal.

4.2 Multipolar External Fields

We have thus far investigated the effects of an external field involving only a dipolar ($\ell = 1$) magnetic field. However, measurements of magnetic fields in Ap stars suggest that the surface fields of these stars involve multipolar components with spherical harmonic degrees greater than $\ell = 1$. It is appropriate to examine the effects of more complex magnetic topologies on the system. Does the scale of the imposed magnetic flux matter, and if so, how? We have thus examined two additional external fields configurations, with $\ell = 2, m = 0$ and $\ell = 4, m = 0$. In each case, the strength of the fossil field was adjusted so that the integrated unsigned magnetic flux across the convective core boundary was identical to that in the mixed-field case A. Unlike the mixed-field case, neither of these two cases possessed a net flux of magnetic field through either hemisphere. Moreover, here there was no magnetic flux linking the northern and southern hemisphere of the star across the equator.

We show the evolution of the energies for these two cases in Figure 4.7. In each a transition to super-equipartition is evident. However, the growth of the $\ell = 2$ case (Fig. 4.7*a*) is faster than

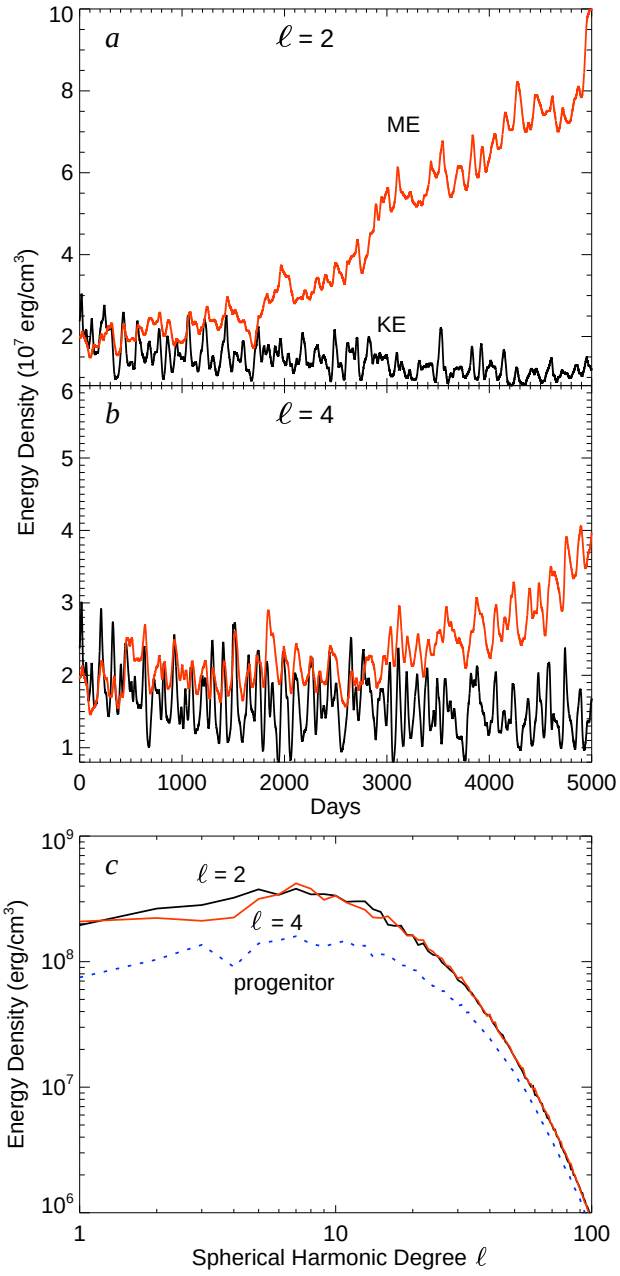

Figure 4.7: Multipolar cases. (a) Temporal evolution of the quadrupolar $\ell = 2$ case. Volume-averaged ME is shown in red and KE in black. (b) Evolution for the ℓ=4 multipolar case. (c) Spectra at mid-core for both cases at day 4000. ℓ=2 is shown in black, and ℓ=4 in red. The progenitor case is shown in blue (dotted) for reference.

that of the $\ell = 4$ case (Fig. 4.7*b*). Each of these exhibit growth that is in turn slower than the dipolar cases. The mechanisms that cause the growth clearly have a dependence on length-scale. Magnetic energy spectra for these cases (Fig. 4.7*c*) are qualitatively similar to those of the mature mixed-field case A. In both instances, larger-scale fields have grown more than the smaller-scale fields.

Evolution of the axisymmetric fields for the $\ell = 2$ and $\ell = 4$ cases are shown in Figures 4.8 and 4.9 respectively. The effects of weak differential rotation (Ω-effect) initially operating in the radiative zone are evident in snapshots of the toroidal fields. Such banded toroidal structures give way to those produced by processes in the core as the initial poloidal field component diffuses away and the differential rotation subsides. In each case, the imposed magnetic flux is reprocessed by the core until a roughly dipolar field configuration is realized within the core. Continued pumping of this field into the radiative zone, combined with diffusion of the imposed fossil field placed there, leads ultimately to a magnetic field geometry which is largely dipolar in the radiative zone in both cases. This behavior suggests that linkage of the initial fossil field to that inside the core is not crucial to achieving a super-equipartition state. Rather, it seems that the scale over which magnetic field lines are able to connect distant regions of the core may be key.

4.3 Conclusions and Perspectives

Our work has revealed that a remnant primordial field linking the convective core and the radiative envelope of an A-type star may significantly impact the dynamics of convection within the core. By placing a modest fossil field into the radiative zone involving a 10% increase in the total magnetic energy, the dynamo responds by a five-fold increase in the overall magnetic energy in the system. With an accompanying two-fold decrease in convective kinetic energy, the dynamo is now in a super-equipartition state with the ratio of ME/KE of order ten. The bulk of the magnetic energy (about 85%) achieved through the resulting dynamo action is contained in the fluctuating (non-axisymmetric) magnetic fields, with about 10% in mean (axisymmetric) toroidal fields and about 5% of the energy contained in the mean poloidal fields.

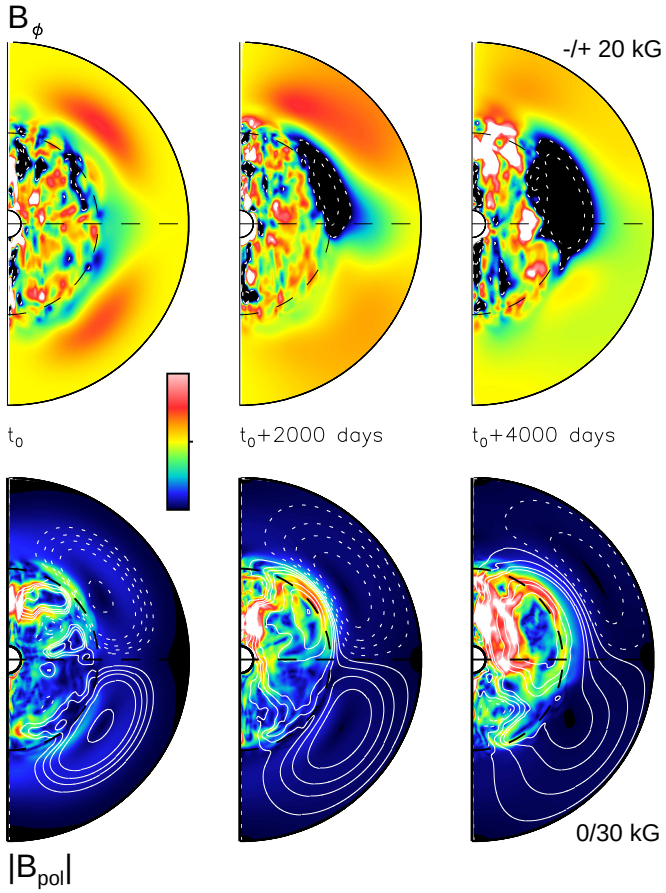

Figure 4.8: Mean field evolution for the quadrupolar $\ell = 2$ case. (*upper row*) Azimuthally-averaged B_ϕ at three instants in time spanning 4,000 days. (*lower row*) Corresponding mean poloidal fields. White lines denote poloidal field lines. Solid lines are counterclockwise, and dashed lines are clockwise. The colored underlay indicates the strength of the mean poloidal field modulus.

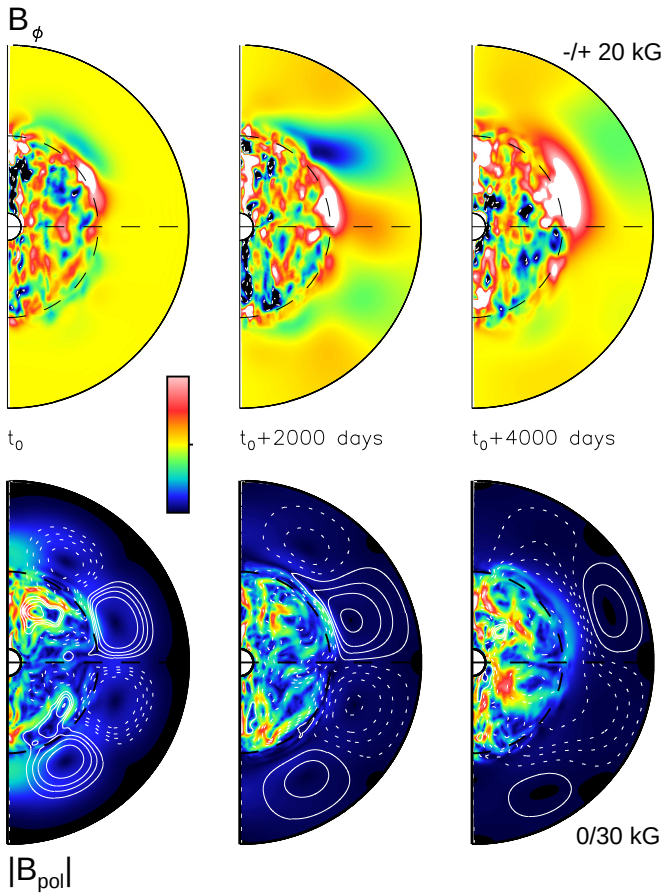

Figure 4.9: As in Fig. 4.8 showing the $\ell = 4$ multipolar case. (*upper row*) Azimuthally-averaged B_ϕ at three instants in time spanning 4,000 days. (*lower row*) Corresponding mean poloidal fields. Magnetic fields in the $\ell = 4$ case also evolve toward a dipole in the radiative zone.

The mean magnetic fields built in this regime are substantial, with peak mean toroidal field strengths of around 10^5 G (about one-third of the peak fluctuating fields found in the core). The mean toroidal fields typically manifest as large, oppositely signed torii encircling the convective core just above and below the equatorial plane. These bands wax and wane in strength over time, but maintain their approximate anti-symmetry about the equatorial plane. The mean poloidal fields in case A exhibit a prominent dipolar component with strengths of around 2×10^4 G near the edge of the core. While the strength of the poloidal field is variable in time, we have observed no flip of the dipole moment in the roughly three magnetic diffusion times spanned by the simulation.

We have examined the sensitivity of the super-equipartition transition to the structure of the imposed mean field as well. Toroidal external fields with some threading through the core have no effect. Rather, the transition requires an external field with a poloidal component. Systems with smaller-scale poloidal fields ($\ell = 2$ and $\ell = 4$) take longer for a transition to occur but reach end states similar to case A and case B ($\ell = 1$). All of these systems are characterized by super-equipartition between the magnetic and kinetic energy, diminished differential rotation throughout the core, and a tendency to develop a mean poloidal field configuration that is dipolar in nature. The sign of the dipole moment for the $\ell = 2$ case is the same as that of case A, but that for the $\ell = 4$ case is oppositely directed, suggesting that the external field may bias the system in some fashion.

4.3.1 Sustaining the Strong Field Dynamo

The maintenance of such strong magnetic fields is an intricate matter, particularly in light of the strong Lorentz forces that potentially accompany them. Organization of flows in a fashion that minimizes Lorentz feedbacks is thus crucial to this balance. The velocity configuration in case A is characterized by four to six prominent convective rolls aligned with and extending along the rotation axis. Convective motions in these rolls are largely perpendicular to the rotation axis except in the roll center. There pressure gradients induced by tilting of the roll orbits at the spherical boundary of the convective core induce flows along the roll axis. Some of these axial flows originate

and terminate at the equatorial plane, while others flow freely between the two hemispheres (Fig. 4.4). The substantial reduction in differential rotation in this system has allowed for axis crossing streaming flows. When rolls phase properly, inflow (i.e. toward the rotation axis) from one roll may cross the rotation axis, merging with the outflow of another roll.

The convective state achieved in case A thus exhibits motions that are much more global in nature (Fig. 3.11) than case C4m, and the core is in general more topologically connected as a result, particularly through the intermittent core-crossing motions. The magnetic fields of case A follow a similar trend, exhibiting a much more global-scale field topology than in case C4m. Magnetic structures typically wrap around the boundaries of the convective columns in large arching helical bands of field. Moreover, core crossing flows display a clear magnetic signature (Fig. 4.5), with large bundles of magnetic flux stretching across the core, linking rolls on opposite sides of the core.

We find that the coexistence of our convection with these strong magnetic fields relies on a greater coalignment of the flows and magnetic fields than that achieved in case C4m. Magnetic field structures tend to mimick patterns visible in streamline renditions of the flow-field, suggestive of a guiding effect of the magnetic field on the flow. However, regions of strong field are typically separate from (albeit often adjacent to) regions of strong flow. This is particularly true of the fast axial flows in the center of the convective columns. We find these regions to be largely devoid of magnetic energy.

Our primary case A bears some similarities to phenomena observed in geodynamo modeling. In the absence of magnetic fields, convection in those models also exhibits a strong tendency for Taylor columns aligned with the rotation axis (e.g. Roberts & Glatzmaier 2000). As with our case A, the convection within their cells is helical, with axial flows setting up circulations linking neighboring columns at high latitudes and near the equatorial plane. In the presence of magnetism, this convection maintains its columnar nature, and the associated helical motion serves to create an efficient α-effect as magnetic field is stretched and twisted around the convective rolls (e.g. Olsen et al. 1999). Super-equipartition is found in these models as well, with typical values of ME/KE of 10-20, but with some reaching as high as 10^3 (Kuang & Bloxham 1999, Glatzmaier et al. 1999).

This regime, referred to as the strong field regime, involves comparable Lorentz and Coriolis forces. As the inner 35% of the Earth's core is solid, geodynamo models have an inner sphere that flows may not cross. Dynamics closer to the rotation axis than the tangent cylinder associated with this inner sphere can be considerably different than that occurring within the outer convective rolls. Olson et al. (1999) for example note the presence of thermally driven upwellings along the rotation axis in the tangent cylinder that tend to modify the mean poloidal field, effectively lowering the poloidal flux through the core boundary at the poles. We observe no such effects in our A-star simulations as the tangent cylinder is much less pronounced, with flows crossing the rotation axis freely above and below our small inner cutout.

The force balance achieved in geodynamo models typically involves some balance between the Lorentz, Coriolis, and buoyancy forces (Christensen & Aubert 2006). Such a force balance was not present in the progenitor C4m which was largely geostrophic in nature. However, the super-equipartition state realized in case A does exhibit such a triple force balance in the direction parallel to the rotation axis. Pressure plays a stronger role in the horizontal, where the predominant balance is between pressure, Coriolis, and Lorentz forces.

Inertial forces are weak in geodynamo models. Due to the rapid rotation of the Earth and the relatively weak convective velocities achieved, geodynamo models are much more rotationally constrained than our A-star models. A typical Rossby number, which measures the inertial force relative to the Coriolis force, is about 10^{-5} in the geodynamo versus about 10^{-3} for our A-star. We find the inertial term in case A, while diminished relative to the progenitor case C4m, to be non-negligible in our simulations, typically contributing to the force balance at the 10% level.

Saturation in geodynamo models can involve the advection (driven by the axial circulations within the rolls) of poloidal field into the centers of anticyclonic rolls. Equilibration between Lorentz and Coriolis forces is achieved in these rolls through an outward directed Lorentz force that counteracts the inward Coriolis force (Sakuraba & Kono 1999, Olson et al. 1999), a phenomenon that we do not observe in our super-equipartition cases. Instead for our case A, the magnetic fields exhibit a tendency to encircle the rolls, leaving the roll centers relatively devoid of magnetic field.

The encircling field has the net effect of squeezing individual rolls. For a given intersection of two rolls pervaded by magnetic flux, Lorentz forces may work in tandem with the Coriolis force on one side of the intersection and against it on the other. The similarities of our super-equipartition dynamos to the geodynamo are nevertheless striking. It seems that by imposing a modest external field we have enabled our system to transition toward the strong-field dynamo regime.

4.3.2 Possible Field Emergence

We have demonstrated that the presence of a fossil field may induce the core dynamo of an A-star to transition to a more laminar but stronger dynamo state. From an observational standpoint, however, it is prudent to ask what implications such a state may have for magnetic fields at the surface. While we have not observed the rise of buoyant magnetic structures in this simulation, we do find that more efficient generation of mean fields at the edge of the convection zone has led to the development of 10^5 G fields there. Even stronger fields may be required for structures to become buoyant and eventually reach the surface, as has been considered when studying such possibilities for the more massive O and B stars (MacGregor & Cassinelli 2003; MacDonald & Mullan 2004). They suggest that fields with super-equipartition strengths would be needed to achieve field emergence. It is thus of some interest that we have found similar strong-field dynamo states for our less massive A-type stars.

We have yet to ascertain if our core dynamos have attained the upper limit for magnetic field strengths. Indeed, periods of brief super-equipartition are apparent even with the mean fields in Figure 3.3. What sets the strength and temporal extent of these phases is unclear, and may rely on fortuitous phasing of the convective rolls and magnetic field near the core boundary. Moreover, the development of sufficiently strong flux tubes may rely on adopting much lower diffusivities in the radiative zone, such as through hyperdiffusivity. Our eddy diffusivity parameterization for the SGS motions in this region may simply be too diffusive to allow the buildup of 10^6 G or greater fields.

Such considerations encourage detailed studies of what is required for magnetic structures

to become unstable and reach the surface in these A-stars. Our simulations have revealed that a distinctly super-equipartition state can be achieved by the core dynamo, yet judging from the complexities realized with geodynamos, there may well exist a wide range of strong field states that have yet to be explored.

Chapter 5

Helioseismic Ring Analyses with 3-D Inversions

5.1 Introduction

The local helioseismic technique of ring analysis (Hill 1988) has yielded many valuable insights into the nature of flows in the upper convection zone and their interaction with magnetism there. Ring analyses assess subsurface velocities below a localized region of the Sun by measuring the Doppler shifts in the resonant acoustic modes induced by the presence of a flow. Different modes average the subsurface flow differently in depth, and frequency splittings measured using different modes can be inverted in depth to determine the depth dependence of the flow. By tiling the solar disk with a number of overlapping analysis regions, a solar flow map in longitude, latitude, and depth may be constructed. In their current formulation, ring analyses employ only one tiling size in the generation of such flow maps. We have developed a novel method for generating these flow maps by self-consistently incorporating measurements made using tiles with multiple horizontal resolutions.

Mapping the surface of the Sun using ring analysis measurements has already begun to reveal the intricate nature of flows in the upper convection zone. One of the most notable examples is the presence of evolving large-scale meandering flows, now known as solar sub-surface weather (SSW), that exhibit a clear interaction with magnetic features through their inflows and outflows (e.g., Haber et al. 2002). The vortical nature of these flows in the presence of active regions has been a subject of particular interest due to their likely role in the twisting and shearing of magnetic field, thought to lead to eruptive events such as flaring and coronal mass ejections (Haber et al.

2004; Komm et al. 2005, 2009, Hindman et al. 2006, 2009). When applied to the measurement of meridional circulations, ring analysis has shown that these global-scale motions also possess a clear linkage to magnetic activity, varying in strength and location over the course of the solar cycle (Haber et al. 2002; González Hernández et al. 2008; Basu et al. 2010).

The rich potential for ring analysis to illuminate the variation of flows in the upper convection zone has been only partially exploited, however, owing to the single resolution and 1-dimensionality of the applications thus far. In a ring analysis study, a single analysis region size, or tile size, is chosen, and the disk is tiled with a number of these analysis regions, overlapping one another by roughly half their horizontal extent. The resulting flow maps are constructed with a horizontal resolution determined by that tiling size, and at each position on the disk, a given measurement represents a fairly uniform horizontal average over this tile. The choice of tiling size is determined by the scientific objective. Small analysis regions permit the measurements of the shallowest modes and afford finer horizontal resolution. Measurements from larger tile sizes employ longer-wavelength, more deeply penetrating modes, and sample depths of the convection zone inaccessible to the smaller tilesizes, albeit with lower horizontal resolution. Thus, for the study of deep meridional circulations (e.g., González, Hernández et al.(2000) a tile size of 30° might be selected, while for studies of the detailed interactions between flows and magnetic fields in the upper convection zone, a tile size of 2° might be used (e.g., Hindman et al. 2006). Thus when high resolution is chosen, it is done so at the expense of depth sensitivity and vice versa.

Many applications of ring-analysis stand to benefit if deep mapping of the subsurface flow can be accomplished alongside high resolution mapping of the near-surface layers. Studies that examine the small-scale nature of convection along with its large-scale means stand to benefit most. As we discuss in detail in §5.2, 2° measurements have larger errors than the lower resolution 16° measurements, primarily owing to the smaller amount of spatial averaging involved in computing the 2° power spectra. Power spectra are a nonlinear data product, and it is unlikely that the noisy 2° measurements will yield the same large-scale mean as the 16° measurements when spatially averaged to the larger scales. Moreover, the incorporation of measurements from multiple tile

sizes can lead to a natural progression of horizontal resolution with depth. One might then assess how the surface inflows observed near active regions transition into outflows at depth and how the small-scale supergranular patterns around active regions establish the larger-scale surface inflow (e.g., Haber et al. 2004; Hindman et al. 2009). Searches for the solar giant cells of convection may also benefit through a better understanding of the depth dependence of the observed north-south alignment of supergranules, thought to arise from the organizing effect of deep-seated, larger-scale motions (Lisle et al. 2004; Featherstone et al. 2006). Moreover, a detailed, unified description of subsurface vorticity would undoubtedly benefit attempts to predict active region flaring using ring analysis which is currently accomplished with low-resolution 16° measurements (e.g., Komm et al. 2010; Maurya & Ambastha 2010)

The self-consistent incorporation of multiple resolutions of ring-analysis measurements into a unified solution describing the solar flow can thus be highly advantageous, but it is nontrivial. For a given analysis-region size, complementary measurements are produced using different radial mode orders with different spatial wavenumbers. These measurements represent unique spatial averages over the solar subsurface flows, and velocity maps obtained from fits to the different modes will necessarily disagree with one another. Moreover, the same modes from different tile sizes will have different horizontal averaging functions. A simple averaging together of results from different analysis regions sizes is thus impossible. To that end, we have developed a 3-D inversion technique which we have termed Adaptable Resolution Ring Diagram Inversions (or ARRDI), that allows us to simultaneously invert data from a number of different modes and region sizes to obtain a self-consistent map of the horizontal flow over the full disk of the Sun and for a range of depths. We proceed now with a detailed discussion of the measurement technique in §5.2, followed by a discussion of the calculation of the sensitivity kernels §6.1. The inversion algorithm is discussed in §7.1, and its averaging properties in §7.2, followed by a comparison of the results realized using our new method and previous methods in section 8.1.

5.2 Ring-Analysis Technique

5.2.1 Obtaining Doppler Measurements

Modern Doppler measurements of the entire solar surface are generally obtained through one of two world-class observatories. For space-based observations, local helioseismic techniques rely primarily on the Michelson Doppler Imager (MDI; Scherrer et al. 1995) aboard the Solar and Heliospheric Observatory (SOHO). MDI measures Doppler shifts and line-of-sight magnetic field using five narrow filters spanning the wings and core of the Ni 6768 Å line. Using a CCD array with 1024×1024 pixels, MDI generates Dopplergrams and magnetograms with a 4" resolution (1.45 Mm per pixel at disk center in the Sun) at a 1 min cadence. The primary drawback to observations made aboard SOHO, which is positioned at the Earth-Sun L_1 Lagrange point, concerns telemetry limitations to the data transfer. Full-resolution Dopplergrams are returned for only two to three months of every year, and lower resolution Doppler data is transferred during the remainder of the year.

The data transfer limitations of MDI can be partly overcome through measurements made using Doppler data from the Global Oscillations Network Group (GONG; Harvey et al. 1996), comprised of six ground-based telescopes sited around the world, with a combined duty cycle of around 90%. GONG employs 1024x1024 CCD arrays to generate full-disk Dopplergrams of the Sun using the same Ni line as MDI. Dopplergrams are generated with a 2.5" resolution and 1 min cadence, and line-of-sight magnetograms are captured every 20 min.

Helioseismic investigations in the near future will rely heavily on spaced-based observation with the Helioseismic and Magnetic Imager (HMI; Kosovichev et al. 2007). HMI is aboard the Solar Dynamics Observatory (SDO) and will return full-disk Dopplergrams and *vector* magnetograms with 1" resolution at a 45 s cadence using a 4096×4096 ccd array. Measurements of Doppler shifts and magnetic fields obtained using this instrument will use the FeI line at 6173 Å, which is more magnetically sensitive (i.e. higher Lande factor) and thus better suited for the generation of vector magnetograms than the Ni line used in MDI and GONG. The ring-analysis inversion package

described in Chapter 5 has been developed for integration into the HMI data pipeline.

5.2.2 Measuring Flows with Ring Analysis

Our ring-analysis measurements are made using Doppler-velocity data obtained with the Michelson Doppler Imager (MDI) aboard the Solar and Heliospheric Observatory (SOHO). Each analysis operates upon a sequence of images constructed by tracking a square patch of the Sun, 16° in size, for 1664 min (27.7 hr) with a 60 s cadence. The tracking slides the analysis region across the solar surface at the Snodgrass (1984) differential rotation rate corresponding to the central latitude of the patch. This tracking largely removes the prominent signal associated with the surface differential rotation of the Sun, allowing us to sample the smaller-scale convective patterns of interest. In total, 189 such patches, overlapping their nearest neighbors by 7.5° are used to tile the solar disk, covering the central portion of the disk within 60° of disk center. As it is tracked, the data is remapped to a Cartesian grid using Postel's projection. This projection has the property that great circles passing through the center of the analysis region are remapped as straight lines, and distances along those lines are preserved, thus minimizing distortions in the power spectrum and enabling the measurements to be made at higher latitudes than would otherwise be possible (Haber et al. 1995; Bogart et al. 1995).

The tracked mosaic of 16° regions is then further subdivided into similarly overlapping mosaics of 4° and 2° tiles. The pixel resolution of the MDI instrument is 0.125° at the solar equator. The horizontal dimension for these different tiles is thus a power of 2 (in pixels) in each case, enabling their efficient computation through fast Fourier transforms. Alternative tiling schemes could also be employed involving intermediate sized tiles of 8° (for example), but we have found that the higher resolution 4° measurements provide good depth coverage down to about 10 Mm. Beyond this depth our primary interests have concerned the large-scale flows around active regions, which we find to be well sampled using 16° measurements. Higher resolution tiles, such as 1° and 0.5° could also be employed, but fitting frequency shifts in these smaller power spectra is difficult, owing in part broadening of the ridges in frequency as we discuss further in §6.1.3, and may require

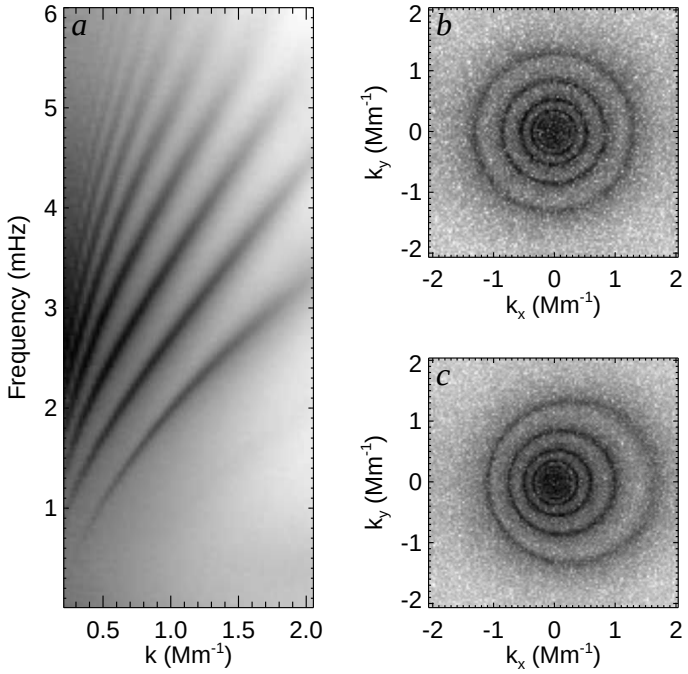

Figure 5.1: Structure of a typical solar power spectrum. (a) Example of a 16° power spectrum as a function of frequency and horizontal wavenumber. Power has been averaged over angle in wavenumber space, with regions of high power indicated by dark tones, and low power by light tones. Power is concentrated along curved ridges. (b) When cut at a constant frequency, these ridges appear as concentric rings, shown here at 3 mHz. (c) Subsurface flows produce a shift of these rings about their centers, as demonstrated here using a 1.5 km s^{-1} eastward flow.

the development of alternative fitting algorithms. For the time being, we thus proceed with a set of measurements made at the 16°, 4° and 2° resolutions.

Each tracked data cube is apodized spatially and temporally. The temporal window function smoothly tapers the duration to 1612 min, while the spatial window function is circularly symmetric and reduces the analysis region to disks that are 15°, 3.75°, and 1.875° for the 16°, 4°, and 2° tiles respectively. Power spectra (in space and time) are then computed from the apodized images. Such power spectra possess curved ridges of power in wavenumber and frequency, which when cut at a constant frequency appear as concentric rings of power (Fig. 5.1). Flows passing beneath one of these patches of the Sun produces a Doppler shift in the wavefield, causing these rings to shift about their centers. As described in Schou et al. (1998), at each total wavenumber k in the power spectrum, we fit the observed power P about a single ridge of power to a model that accounts for

the frequency splittings produced by an underlying flow,

$$P = \frac{A\Gamma}{(\omega - \omega_n + \mathbf{u}\cdot\boldsymbol{k})^2 + \Gamma^2} + \frac{b}{k^3}. \tag{5.1}$$

Here A is the amplitude of the mode, Γ is the half width, ω_n is the resonant frequency of the mode, and b is a smoothly varying background. The wavenumber vector $\boldsymbol{k}$ is given by

$$\boldsymbol{k} = k_x\hat{\boldsymbol{e}}_x + k_y\hat{\boldsymbol{e}}_y, \tag{5.2}$$

where $\hat{\boldsymbol{e}}_x$ and $\hat{\boldsymbol{e}}_y$ are unit vectors in the east-west and north-south directions respectively. Similarly, the velocity vector $\mathbf{u}$ is given by

$$\mathbf{u} = \mathrm{u}_x\hat{\boldsymbol{e}}_x + \mathrm{u}_y\hat{\boldsymbol{e}}_y, \tag{5.3}$$

where u_x and u_y represent a spatial average over the underlying horizontal flow in the east-west and north-south directions. A single velocity measurement $\mathbf{u}$ is thus characterized by 5 parameters: it's location on the solar disk (i.e., the central longitude ϕ and latitude λ of the analysis region), the size T of the analysis region, the mode order n, and the wavenumber k. For the remainder of this chapter, we adopt the notation $\mathbf{u}_i$ as shorthand for

$$\mathbf{u}_i \equiv \mathbf{u}(k_i,\ n_i,\ T_i,\ \phi_i,\ \lambda_i), \tag{5.4}$$

with the subscript i denoting a unique combination of these measurement parameters. By generating a set of measurements $\mathbf{u}_i$, we can then construct a flow map over the solar disk for each mode and tile-size combination.

5.2.3 Interpretation of the Fitted Velocities

Combining the different measurements $\mathbf{u}_i$ into a unified description of the solar subsurface flow, which we call $\boldsymbol{v}$, is nontrivial in that different modes average the horizontal flow differently with depth. The details of this averaging are described for each $\mathbf{u}_i$ by a sensitivity kernel tensor $\mathbf{K}_i$ such that

$$\mathrm{u}_{x,i} = \sum_j \int \mathrm{K}_{xj,i}(\boldsymbol{r}) v_j(\boldsymbol{r}) d\boldsymbol{r} \tag{5.5}$$

and

$$\mathrm{u}_{y,i} = \sum_j \int \mathrm{K}_{yj,i}(\boldsymbol{r}) v_j(\boldsymbol{r}) \boldsymbol{dr}, \tag{5.6}$$

where $\boldsymbol{r}$ is the position vector, and where we have adopted the shorthand

$$\int \boldsymbol{dr} \equiv \int_{-\infty}^{\infty} \int_{-\infty}^{\infty} \int_{-\infty}^{\infty} dx\ dy\ dz \tag{5.7}$$

to indicate an integral taken over all space. In practice, the off-diagonal elements of the kernel tensor $\mathbf{K}$ are small in relation to the diagonal elements (i.e. $\mathrm{K}_{xy} \leq 0.05\ \mathrm{K}_{xx}$) and are insensitive to a horizontally uniform flow (see Birch et al. 2007). We thus proceed by neglecting these off-diagonal elements, thereby yielding the more succinct form of Equations (5.5) and (5.6),

$$\mathrm{u}_{x,i} = \int \mathrm{K}_{xx,i}(\boldsymbol{r}) v_x(\boldsymbol{r}) \boldsymbol{dr}, \tag{5.8}$$

and

$$\mathrm{u}_{y,i} = \int \mathrm{K}_{yy,i}(\boldsymbol{r}) v_y(\boldsymbol{r}) \boldsymbol{dr}. \tag{5.9}$$

A set of measurements $\mathbf{u}_i$ thus defines a system of integral equations that may be inverted to solve for the underlying flow field $\boldsymbol{v}$. Such inversions have previously been carried out using the 16° data but not for the 2° and 4° data. Rather, for these data sets, surface flow maps have been generated using High-Resolution Ring Analysis (HRRA). As noted in Hindman et al. (2006), the small range of wavelengths accessible to the small-tile measurements suggests that the different measurements using only the f-mode ridge sample the upper convection zone in a similar manner. An average in wavenumber over f-mode measurements is thus a sensible representation of the upper convection zone. Flow maps with 2° and 4° resolution generated using HRRA make no use of p-mode data, however, and thus do not provide a similarly high-resolution description of deeper flows.

Traditionally, the inversion of 16° measurements has been accomplished through the use of linear inversion methods wherein the velocity solution at the jth point in the inversion grid, $\mathbf{v}_j$, may be written as a linear combination of the data. Specifically,

$$\mathrm{v}_{x,j} = \sum_i a_{x,\,ji}\, \mathrm{u}_{x,i}, \tag{5.10}$$

where the weights $a_{x,ji}$ are determined through the inversion procedure. Combining Equations (5.8) and (5.10), we see that

$$\mathrm{v}_{x,\,j} = \int C_{x,\,j}(\boldsymbol{r}) v_x(\boldsymbol{r}) \boldsymbol{dr}, \tag{5.11}$$

with

$$C_{x,\,j}(\boldsymbol{r}) = \sum_i a_{x,\,ji}\ K_{xx,i}(\boldsymbol{r}). \tag{5.12}$$

The function $C_{x,\,j}$ is known as the averaging kernel and describes how the solution $\mathbf{v}_j$, when constructed according to Equation (5.10), samples the underlying flowfield.

Two different approaches to building the $C_{x,\,j}$'s have been applied to the 16° measurements. The first of these, Regularized Least Squares (RLS; e.g., Craig & Brown 1969; Haber et al. 2000) finds a solution v_j that fits the measurements well, while sacrificing the best possible fit to maintain some desired degree of smoothness of the solution. Inversions utilizing Optimally Localized Averages (OLA) have also been applied extensively to the analysis of 16° data (e.g. Haber et al. 2004). In an OLA scheme, a set of $a_{x,ji}$'s is generated that minimizes the difference between the averaging kernel $C_{x,j}$ and some desired target function (typically a Gaussian in depth) while keeping the error associated with v_j below some desired value. The solution v_j found through an OLA inversion may not best fit the data, but it can yield results that are easier to interpret. For example, Haber et al. (2004) have shown that the use of an OLA inversion method can result in averaging kernels that lack the negative sidelobes in depth that often occur in RLS averaging kernels.

As applied to ring analysis, both RLS and OLA inversions have traditionally been 1-D in nature, yielding a solution as a function of depth beneath each tile. These inversions have employed horizontally invariant sensitivity kernels, whose structure in depth has been taken to be the kinetic energy density of the associated mode (e.g., Haber et al. 2002). A particular limitation of these methods is that a 1-D inversion performed for a particular tile makes no use of information from neighboring tiles that sample a common portion of the solar disk. This can be overcome through the development of 3-D sensitivity kernels for *all* tile sizes that describe both the horizontal and depth sensitivity of a measurement to a subsurface flow. We will discuss the calculation of such 3-D kernels

shortly, but turn first to a characterization of the ring-analysis measurements themselves.

5.2.4 Characterization of the Data and its Errors

Subsurface flow maps realized through linear inversion of ring-analysis measurements are intimately linked to both uncertainties in the individual measurements as well as to variations in the density of measurements across the disk. A characterization of the measurements and their errors will thus facilitate a better understanding of the inversion results. For ring-analyses, the fitted velocities are those which minimize the difference between the data and the fitting function of Equation 5.1. These fitted parameters thus correspond to a minimum in parameter space about which a Taylor expansion is performed to determine the local curvature of this minimum. This curvature (in the u_x or u_y direction) is then taken as a representative error for our measurement. Using ring-analysis measurements generated for the 72 days spanning 1 March 2001 through 26 May 2001, we have calculated average errors and data filling factors both mode by mode and by position on the disk for each of the three analysis-region sizes.

The presence of magnetic fields, which may suppress convection and produce asymmetries in the wavefield, can also make the fitting of power spectra difficult by introducing perturbations in the power spectrum not accounted for in Equation (5.1). For instance, active regions tend to absorb acoustic power (e.g., Braun 1995), leading to a suppression of power in portions of the power spectrum corresponding to waves travelling away from a region of strong magnetic field. Effects such as this can significantly alter power spectra for the 4° and 2° regions, which are generally noisier than their 16° counterparts owing to the smaller amount of Dopplergram data that is averaged in the power spectrum computation. Moreover, even in the absence of a magnetic field, the frequency linewidths increase with decreasing region size, leading to broader, less well defined power ridges for the smaller analysis regions. These enhanced uncertainties in the fidelity of the power spectrum translate into greater uncertainties in the measurements as the analysis-region size is decreased.

Figure 5.2 illustrates the sensitivity of 2° measurements to a magnetic field using data from 27 March 2001. The unsigned magnetic flux density, degraded to the resolution of the 2° data, is

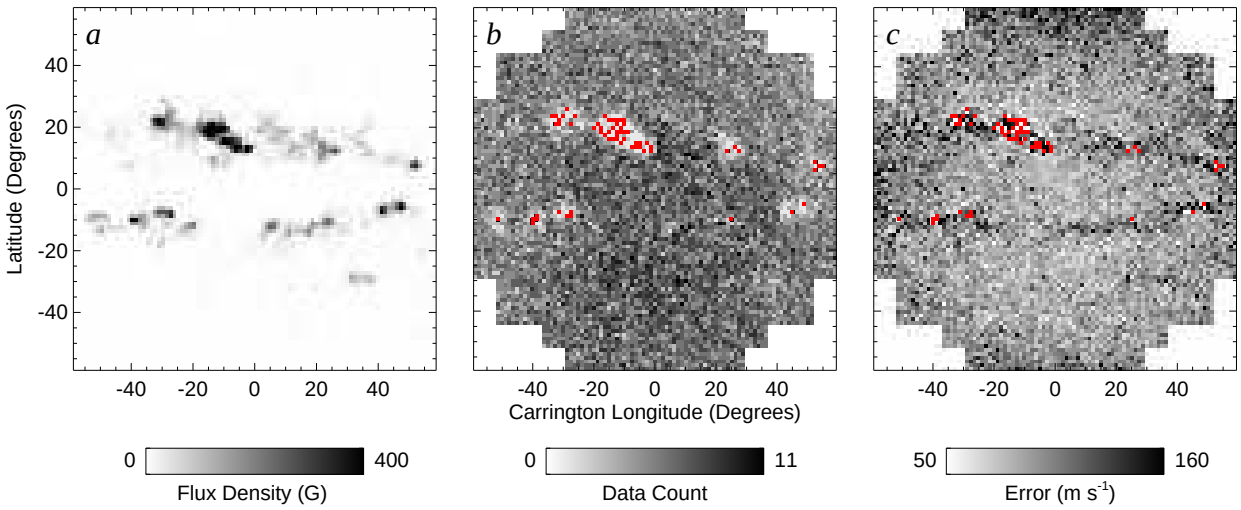

Figure 5.2: The effect of magnetic field strength on ring-analysis errors for 2° measurements from 27 March 2001. (*a*) Magnetic flux density degraded to the resolution of the 2° measurements. Dark tones denote high field strength, and light tones low field strength. (*b*) Data measurement count, averaged over all attempted modes. High and low values indicated as in (*a*). Positions where no successful measurement was made are indicated in red. (*c*) Ring-analysis errors averaged over all attempted modes. Coloring as in (*b*). Regions of high field strength correlate with higher error and a lower measurement success rate.

shown in Figure 5.2*a*. Regions of strong flux density tend to have a lower number of successful measurements (Fig. 5.2*b*). As indicated by the red coloring in Figure 5.2, regions of particularly strong magnetic field are often devoid of velocity measurements. The average measurement errors (Fig. 5.2*c*) are often high in regions of strong magnetic field, with the imprint of the active region belts clearly visible in the associated error mapping.

This general trend persists for the 4° measurements as well. In Figure 5.3*a* we show the disk- and mode-integrated error, averaged in time over 72 days, relative to the magnetic field strength. Magnetograms for each day have been degraded to the resolution of the different analysis-region sizes, as reflected in the fact that the 16° measurements do not possess corresponding fields strengths as high as those associated with the 4° and 2° measurements. Measurement errors are relatively insensitive up to field strengths of $\sim$ 50 G. The measurement success rate drops accordingly as power spectra become more difficult to fit in the presence of strong magnetic fields (Fig. 5.3*b*).

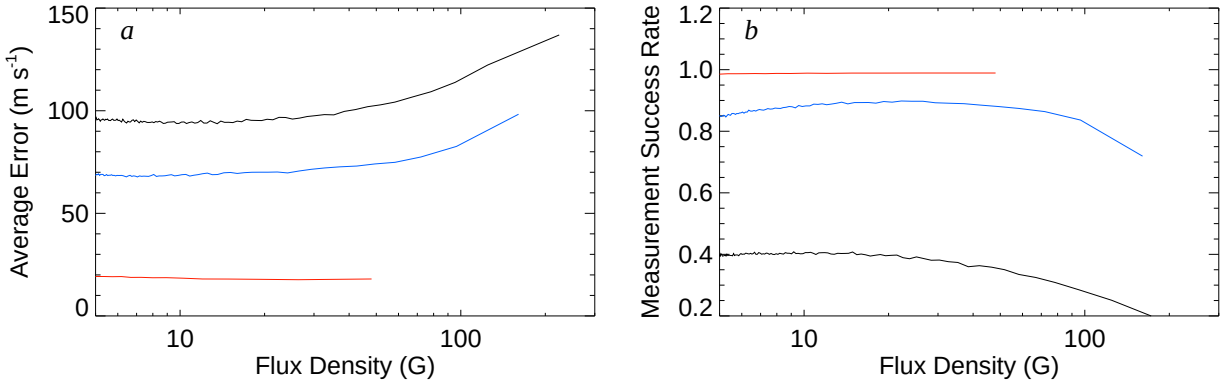

Figure 5.3: Average effects of magnetic field strength on measurements made using different analysis-region sizes. (*a*) Measurement error (averaged over all modes and positions on the disk) versus magnetic flux density for the 16° (red), 4° (blue), and 2° (black) measurements. 16° measurements are relatively insensitive to the magnetic field strength. 4° and 2° measurements exhibit higher uncertainties in regions of strong field and lower measurement success rates.

We note that even in the presence of weak magnetic field, only about 40% of 2° measurements are successful.

Measurement errors exhibit considerable variation between modes as well. We plot the time- and disk-averaged measurement errors for each mode in Figure 5.4 where each symbol-color combination denotes an average error for a particular tile size and mode order. Errors are plotted relative to the lower turning point of their associated modes. In this case, the lower turning point for each mode (where the phase speed and the sound speed are equivalent) has been determined using the sound speed profile from solar model S (Christensen-Dalsgaard et al. 1996). The evanescent f modes have no lower turning point, and so their errors have been plotted relative to the e-folding depth of each mode. Plotting in this manner is advantageous in that it provides a sense of the effective penetration depth of the different measurements as well as the typical uncertainties at those depths.

This information can be particularly useful when deciding on how the horizontal resolution of our inversion grid should change with depth. For example, the deepest penetrating 2° measurement (triangles) is for a p_1 mode (red) with a lower turning point of 6 Mm. However, the error is quite high for 2° measurements beyond a depth of about 3 Mm. We might then expect an inversion

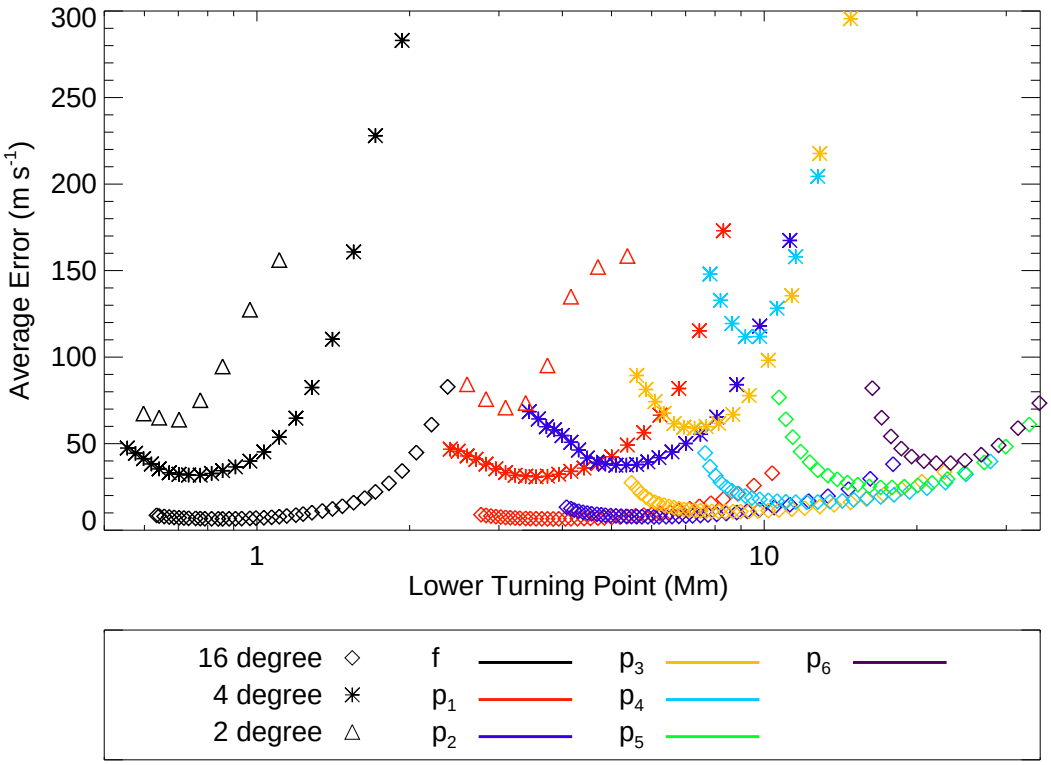

Figure 5.4: Average ring-analysis errors as realized with MDI data. A representative error for each tile size, frequency, and horizontal wavenumber combination was generated by averaging errors from 72 days of ring measurements made using MDI dopplergrams from 1 March 2001 through 26 May 2001 over the full solar disk. Tile size and mode order are indicated using the coloring and symboling scheme indicated. Errors have been plotted as a function of the lower turning point of the associated mode. Errors are lowest for the 16° tiles. Within a given tile size, errors are lowest at mid-ridge and increase with increasing radial mode-order.

algorithm that is aware of the errors to emphasize the 2° measurements when building the solution near the surface and down to depths of 3-4 Mm. Below this depth, the 4° data will likely be favored, and a natural degradation of the inversion's horizontal resolution can occur. Morever, our deepest measurements occur in the 16° dataset and only sample the upper 35 Mm of the solar convection zone, thus setting a lower limit on the depths which we may hope to probe.

Figure 5.4 shows that within any combination of analysis-region size and mode order, the errors exhibit a systematic variation with lower turning point. For a give mode order, the lower turning point is inversely proportional to wavenumber. Errors thus become high at the lower and upper ends of a particular ridge, with a minimum somewhere in between. At mid-ridge, the frequency is closer to 3 mHz, where the solar power spectrum peaks. At the ends of the ridges, the power is then lower than the mid-ridge and background noise can make the power spectrum more difficult to fit. This effect is compounded at the high-wavenumber end of the ridge where frequency linewidths become larger, and the power becomes more spread out in frequency space, thus reducing the ratio of signal to noise.

The time- and disk-averaged data-filling factor for the different modes is plotted in Figure 5.5 using the same symbols as Figure 5.4. The 16° measurements demonstrate a near 100% success rate irrespective of their associated errors. The 4° and 2° measurements, however tend to possess high filling-factors where errors are low and vice versa. Thus, in addition to having high errors beyond about 3 Mm, few 2° measurements are typically available for an inversion algorithm to make use below this depth. We see from Figures 5.4 and 5.5 that, when choosing a horizontal resolution for our inversion grid, we might degrade it twice relative to the surface: once below 3 Mm and again below about 11 Mm where the 4° measurement success begins to decline. Before we discuss the specifics of our inversion algorithm any further, however, we turn to an examination of the development of the sensitivity kernels and their variation with the measurement parameters.

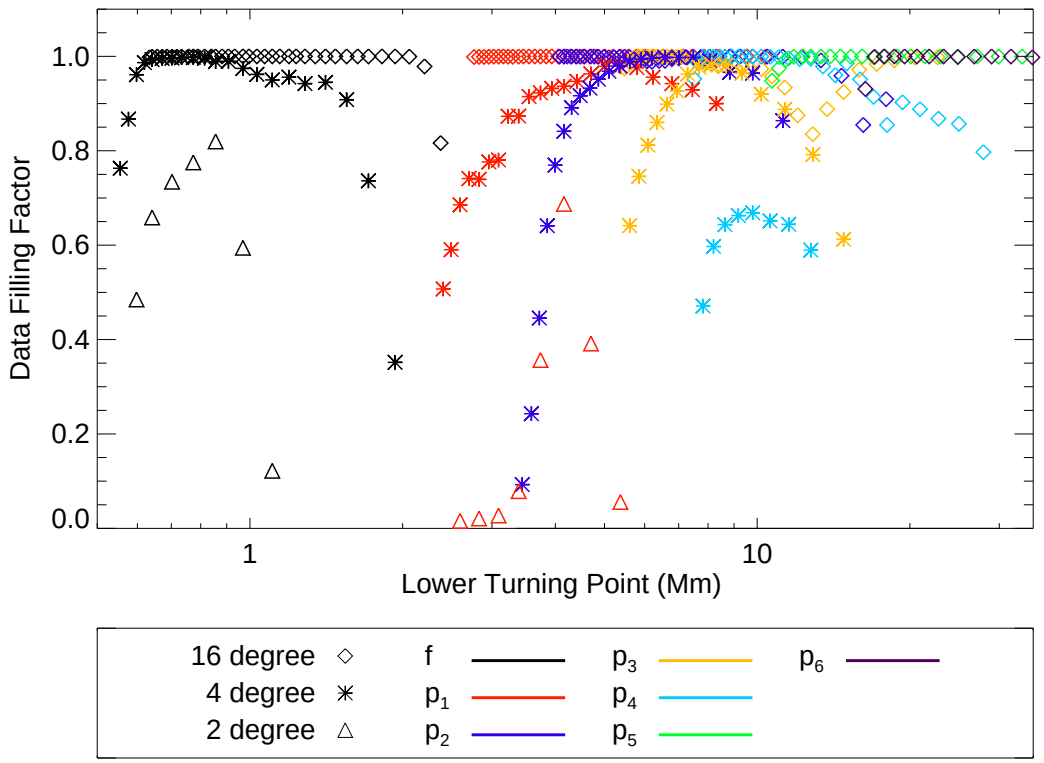

Figure 5.5: Data filling factor over the solar disk for ring-analysis measurements for different modes and different tile sizes. Tile size and mode order are indicated as in Figure 7.4. Measurements attempted for the 16° data are generally successful, with some data dropouts occuring at high n. Success rates for the 4° and 2° measurements behave similarly to the errors, with mid-ridge and low n measurements faring the best.

Chapter 6

Properties of the Sensitivity Kernels

6.1 Development of the Sensitivity Kernels

We now outline the procedure by which a ring-analysis measurement $\mathbf{u}_i$ can be related to a horizontal flow $\boldsymbol{v}$ beneath that corresponding patch of the sun through the sensitivity kernel $\mathbf{K}_i$ by

$$\mathrm{u}_{x,i} = \int \mathrm{K}_{xx,i}(\boldsymbol{r}) v_x(\boldsymbol{r}) \boldsymbol{dr} \tag{6.1}$$

and

$$\mathrm{u}_{y,i} = \int \mathrm{K}_{yy,i}(\boldsymbol{r}) v_y(\boldsymbol{r}) \boldsymbol{dr}. \tag{6.2}$$

The general framework for the calculation of sensitivity kernels has been established in Gizon & Birch (2002) and Birch et al. (2004), and its application to ring-analysis kernels is described in Birch et al. (2007). Our aim here is to present a synthesis of these three papers so that a complete description of the model and calculation is readily available when we discuss the properties of the resulting sensitivity kernels in §6.1.3.

Given that we already have two velocity variables defined ($\mathbf{u}$ and $\boldsymbol{v}$), we choose to work in the fluid displacement vector $\boldsymbol{\xi}(\boldsymbol{r}, t)$ when describing waves in the solar interior. The surface velocity projected along the line of sight, our primary observable, and which we choose to call ϕ, is then given by

$$\phi(\boldsymbol{x}, t) = A(\boldsymbol{x}, t) \left[\hat{\boldsymbol{\ell}} \cdot \dot{\boldsymbol{\xi}}(\boldsymbol{x}, z_{\mathrm{obs}}, t) \right]. \tag{6.3}$$

Here z_{obs} is the height at which the measurements are made, $\hat{\boldsymbol{\ell}}$ is a unit vector directed along the line of sight, $\boldsymbol{x}$ is the horizontal position vector, and the overdot on $\boldsymbol{\xi}$ denotes a time derivative.

The function A describes the spatial and temporal windowing function applied to some patch of the sun before a power spectrum is constructed and a ring-analysis velocity measurement performed.

The observed power spectrum P is then given by

$$P(\boldsymbol{k},\omega) = \phi(\boldsymbol{k},\omega)\phi^*(\boldsymbol{k},\omega), \tag{6.4}$$

where we have adopted the convention that a function written explicitly in terms of ω and k denotes the temporal and horizontal Fourier transform, namely

$$\phi(\boldsymbol{k},\omega) \equiv \int\int \phi(\boldsymbol{x},t)e^{-i\omega t}e^{i\boldsymbol{k}\cdot\boldsymbol{x}}\,d\boldsymbol{k}\,d\omega. \tag{6.5}$$

In the presence of a flow, a perturbation to the power spectrum, δP, is introduced such that

$$P(\boldsymbol{k},\omega) = P_0(\boldsymbol{k},\omega) + \delta P(\boldsymbol{k},\omega), \tag{6.6}$$

where the subscript "0" to indicates quantities in the absence of a flow. The presence of a flow similarly produces a perturbation $\delta\phi$ to the surface velocity field so that, to first order in $\delta\phi$, δP is given by

$$\delta P(\boldsymbol{k},\omega) = \delta\phi(\boldsymbol{k},\omega)\phi_0^*(\boldsymbol{k},\omega) + \delta\phi^*(\boldsymbol{k},\omega)\phi_0(\boldsymbol{k},\omega) = 2\mathrm{Re}\left[\delta\phi(\boldsymbol{k},\omega)\phi_0^*(\boldsymbol{k},\omega)\right] \tag{6.7}$$

Ring-analysis techniques derive a velocity from δP by fitting the power spectrum at a specific k and n as described in Equation (5.1). The fitting described in §5.2 is nonlinear, however, and if we wish to perform a linear inversion, a linear approximation to our fitting technique is needed to compute the sensitivity kernels. Birch et al. (2007) have demonstrated that a linear fitting method given by

$$\mathbf{u}_i = \int_{\omega_0-\Delta\omega_i}^{\omega_0+\Delta\omega_i}\int_0^{2\pi} \boldsymbol{W}_i(\boldsymbol{k}_i,\omega)\delta P(\boldsymbol{k}_i,\omega)k_i\,d\theta\,d\omega, \tag{6.8}$$

with weights $\boldsymbol{W}_i$ defined by

$$\boldsymbol{W}_i \sim \frac{\hat{\boldsymbol{e}}_i}{P_0(\boldsymbol{k}_i,\omega)^2}\frac{\partial P_0(\boldsymbol{k}_i,\omega)}{\partial\omega}, \tag{6.9}$$

yields results that agree well with our nonlinear fitting method for measured velocities up to 400 m s^{-1}. Here $\hat{\boldsymbol{e}}_i$ is a unit vector in the directon of $\mathbf{u}_i$, $\Delta\omega_i$ indicates the frequency range that is used

when fitting a ridge of radial order n_i at a particular wavenumber k_i, and θ indicates the angle the wavenumber vector $\boldsymbol{k}$ makes with respect to the k_x-axis so that

$$\boldsymbol{k}_i = k_i \cos\theta \hat{\boldsymbol{e}_x} + k_i \sin\theta \hat{\boldsymbol{e}_y} \tag{6.10}$$

The only quantity in Equation (6.8) that depends on the presence of a flow is δP. Computing the linear sensitivity of a measurement $\mathbf{u}_i$ to the underlying flow $\boldsymbol{v}$ requires finding an expression for δP of the form

$$\delta P(\boldsymbol{k}, \omega) = \int \boldsymbol{v}(\boldsymbol{r}) \cdot \boldsymbol{f}(\boldsymbol{r}, \boldsymbol{k}, \omega) d\boldsymbol{r}, \tag{6.11}$$

where $\boldsymbol{f}(\boldsymbol{r}, \boldsymbol{k}, \omega)$ is some as yet to be determined function. Combining Equations (6.8) and (6.11) then yields (for a measurement in the x-direction),

$$u_{x,i} = \int v_x(\boldsymbol{r}) \mathrm{K}_{xx,i}(\boldsymbol{r}) d\boldsymbol{r}, \tag{6.12}$$

with the sensitivity kernel $\mathrm{K}_{xx,i}$ given by

$$\mathrm{K}_{xx,i}(\boldsymbol{r}) = \int_{\omega_0 - \Delta\omega}^{\omega_0 + \Delta\omega} \int_0^{2\pi} \boldsymbol{W}_{x,i}(\boldsymbol{k}\ , \omega) f_x(\boldsymbol{r}, \boldsymbol{k}_i\ , \omega) k_i \, d\theta \, d\omega. \tag{6.13}$$

Computation of the sensitivity kernel $\mathrm{K}_{xx,i}$ thus requires a model for the wave field in the absence of a flow, ϕ_0, and for the perturbations to that wave field introduced by a steady flow. We turn now to the development of such a prescription of the solar wave field which may then be used to calculate $\boldsymbol{f}(\boldsymbol{r}, \boldsymbol{k}, \omega)$.

6.1.1 Modeling the Solar Wavefield

Our ring-analysis measurements are made using modes with a number of different horizontal wavelengths, the largest of which (obtained with 16° data) is ~ 0.03 of the solar radius. As even the largest wavelengths considered are quite small compared to the solar radius, we adopt a plane-parallel treatment of the solar interior for our model, neglecting any effects of sphericity. We begin by considering perturbations about an adiabatic background state in hydrostatic balance and look for wave solutions in the displacement $\boldsymbol{\xi}$. We denote thermodynamic background state (horizontally

invariant) variables by an overbar and perturbations about this state by a prime symbol, such that the density ρ is given by

$$\rho(x,\ y,\ z) = \bar{\rho(z)} + \rho'(x,\ y,\ z), \tag{6.14}$$

and so too for the pressure P. Here z denotes the depth, and x and y should be associated with the east-west and north-south directions respectively. Upon carrying out this linearization and neglecting the presence of any large-scale flows, the momentum equations become

$$\bar{\rho}\ddot{\boldsymbol{\xi}} = -\boldsymbol{\nabla}P' + \rho'\boldsymbol{g} + \bar{\rho}\partial_t(\Gamma\boldsymbol{\xi}) + \boldsymbol{S} \tag{6.15}$$

and

$$\bar{\rho}\boldsymbol{g} = \boldsymbol{\nabla}\bar{P}. \tag{6.16}$$

The continuity equation is given by

$$\rho' = -\boldsymbol{\xi}\cdot\boldsymbol{\nabla}\bar{\rho} - \bar{\rho}\boldsymbol{\nabla}\cdot\boldsymbol{\xi}, \tag{6.17}$$

and energy equation by

$$P' = -\boldsymbol{\xi}\cdot\boldsymbol{\nabla}\bar{P} + \bar{c}^2(\rho' + \boldsymbol{\xi}\cdot\boldsymbol{\nabla}\bar{\rho}). \tag{6.18}$$

Here $\mathbf{g}$ denotes gravity, γ is the ratio of specific heats, and c the local sound speed. We use solar model S (Christensen-Dalsgaard et al. 1996) to describe the background stratification and neglect the variation of gravity with depth since the modes we consider sample the upper 30 Mm of the Sun (see Figure 5.4). The function $\boldsymbol{S}$ describes the excitation of waves by near-surface turbulent convection, and the operator Γ describes their damping.

We adopt phenomenological models of the damping and source functions that have been tuned to reproduce the observed power spectra. For the damping, we adopt the model of Birch et al. (2004), which has been tuned mode-by-mode to reproduce the frequency linewidths of high-degree ($kR_\odot \geq 300$) modes as measured by Korzennik et al. (2004) using MDI data. As noted in Gizon & Birch (2002), a prescription for the source function itself is never needed, but rather one for its covariance. Following Birch et al. (2004), we assume a vertical momentum source whose

covariance M has the form

$$M(\boldsymbol{k}, z', z) = e^{-(\omega T_{\rm src})^2} \delta(z - z_{\rm src}) \delta(z' - z_{\rm src}). \tag{6.19}$$

This form of the source covariance, along with a source depth $z_{\rm src}$ of 100 km and source correlation time $T_{\rm src}$ of 68 sec were found by Birch et al. (2004) to yield model power spectra that matched well with observations. We have assumed that the sources are uncorrelated spatially, resulting in the independence of M on the horizontal wavenumber $\boldsymbol{k}$. Our ring-analysis measurements employ modes with wavelengths as small as 4.5 Mm which is still much larger than the measured correlation length for solar granulation of 450 km (Title et al. 1989), making the spatially uncorrelated approximation reasonable.

These four equations can be combined into a single operator $\mathcal{L}$ describing the response of $\boldsymbol{\xi}$ to the source $\boldsymbol{S}$,

$$\mathcal{L}\boldsymbol{\xi} = \bar{\rho}\ddot{\boldsymbol{\xi}} - \boldsymbol{\nabla}[\gamma \bar{P} \boldsymbol{\nabla} \cdot \boldsymbol{\xi} + \boldsymbol{\xi} \cdot \boldsymbol{\nabla} \bar{P}] + (\boldsymbol{\nabla} \cdot \boldsymbol{\xi}) \boldsymbol{\nabla} \bar{P} + \boldsymbol{\xi} \cdot \boldsymbol{\nabla}(\boldsymbol{\nabla} \bar{P}) + \bar{\rho} \partial_t (\Gamma \boldsymbol{\xi}) = \boldsymbol{S}. \tag{6.20}$$

When a large-scale flow $\boldsymbol{v}$ is present, the effects of advection must be included in Equation (6.15), and a perturbation to the wave operator $\delta\mathcal{L}$ becomes

$$\delta\mathcal{L}\boldsymbol{\xi} = 2\bar{\rho}\boldsymbol{v} \cdot \nabla\dot{\boldsymbol{\xi}}, \tag{6.21}$$

which generates a corresponding perturbation to the wave field $\delta\boldsymbol{\xi}$. Denoting the absence of a flow by the subscript "0", Equation (6.20) becomes

$$(\mathcal{L}_0 + \delta\mathcal{L})(\boldsymbol{\xi}_0 + \delta\boldsymbol{\xi}) = \boldsymbol{S}_0, \tag{6.22}$$

where, for simplicity, we have neglected the effect of advection on $\boldsymbol{S}$. Expanding into zero- and first-order contributions, Equation (6.22) becomes to lowest order,

$$\mathcal{L}_0\boldsymbol{\xi}_0 = \boldsymbol{S}_0, \tag{6.23}$$

and to first order,

$$\mathcal{L}_0\delta\boldsymbol{\xi} = -\delta\mathcal{L}\boldsymbol{\xi}_0 \equiv \delta\boldsymbol{S}. \tag{6.24}$$

We see from Equation (6.24) that the advection of the zero-order wavefield serves as the source function for the perturbed wavefield, and have denoted this quantity by $\delta\boldsymbol{S}$ accordingly. The solutions $\boldsymbol{\xi}_0$ and $\delta\boldsymbol{\xi}$ can be constructed from the same set of vector Greens function $\boldsymbol{G}_j$ for the operator $\mathcal{L}_0$, which we define as

$$\mathcal{L}_0\boldsymbol{G}_j(\boldsymbol{x}-\boldsymbol{s},t-t_s)=\hat{\boldsymbol{e}}_j\delta_D(\boldsymbol{x}-\boldsymbol{s})\delta_D(t-t_s). \tag{6.25}$$

Here δ_D is the Dirac delta function. The Green's function $\boldsymbol{G}_j$ represents the velocity resulting from an implusive force at location $\boldsymbol{s}$ and time t_s in the $\hat{\boldsymbol{e}_j}$ direction. We construct the $\boldsymbol{G}_j$'s through a summation over the normal modes of the system described by Equations (6.15)-(6.18) as detailed in Birch et al. (2004). The zero-order solution $\boldsymbol{\xi}_0$ (and so too the zero-order power spectrum) can be constructed from the Greens function of the operator $\mathcal{L}_0$,

$$\boldsymbol{\xi}_0(\boldsymbol{r},t)=\sum_j\int_{-\infty}^{\infty}\int_{-\infty}^{\infty}\boldsymbol{G}_j(\boldsymbol{r}-\boldsymbol{r'},t-t')S_j(\boldsymbol{r'},t')\boldsymbol{dr}'dt'. \tag{6.26}$$

From Equations (6.24) we see that advection acting on the zero-order wavefield serves as the source for the perturbed wavefield, so that

$$\delta\boldsymbol{\xi}(\boldsymbol{r},t)=\sum_j\int_{-\infty}^{\infty}\int_{-\infty}^{\infty}\boldsymbol{G}_j(\boldsymbol{r}-\boldsymbol{r'},t-t')\delta S_j\boldsymbol{dr}'dt'. \tag{6.27}$$

The perturbed wavefield $\delta\boldsymbol{\xi}$ is linearly related to the steady flow $\boldsymbol{v}$ through $\delta\boldsymbol{S}$, and so we now have the pieces in place to construct the function $\boldsymbol{f}(\boldsymbol{r},\boldsymbol{k},\omega)$ of Equation (6.11) and the sensitivity kernel $K_{i,x}$.

6.1.2 Assembly of the Sensitivity Kernels

We now proceed with construction of the sensitivity kernels by rewriting δP in terms of $\boldsymbol{\xi}$ by combining Equations (6.3) and (6.7) to yield

$$\delta P(\boldsymbol{k},\omega)=-2\mathrm{Re}[\omega^2\delta\tilde{\xi}_z(\boldsymbol{k},\omega,z_{\mathrm{obs}})\tilde{\xi}^*_{0,z}(\boldsymbol{k},\omega,z_{\mathrm{obs}})]\equiv\int\boldsymbol{v}(\boldsymbol{r})\cdot\boldsymbol{f}(\boldsymbol{r},\boldsymbol{k},\omega)\boldsymbol{dr}, \tag{6.28}$$

where $\hat{\boldsymbol{\ell}}$ is assumed to be in the $\hat{\boldsymbol{e}}_z$ direction for simplicity. We have further adopted the convention that an overhat on a quantity indicates its convolution with the apodization function A so that

$$\tilde{\xi}_z(\boldsymbol{k},\omega)=\int\int A(\boldsymbol{k}-\boldsymbol{k}',\omega-\omega')\,\xi_z(\boldsymbol{k}',\omega')\,\boldsymbol{dk}'\,d\omega'. \tag{6.29}$$

Taking the Fourier transform of $\delta\xi_z$, we find

$$\delta\xi_z(\boldsymbol{k},\omega,z_{\rm obs}) = \sum_j \int G_{z,j}(\boldsymbol{k},\omega,z_{\rm obs}-z)\delta S_j(\boldsymbol{r},\omega)e^{i\boldsymbol{k}\cdot\boldsymbol{x}}\boldsymbol{dr}, \tag{6.30}$$

and combing Equation (6.24) with Equation (6.30), we have

$$\delta\tilde{\xi}_z(\boldsymbol{k},\omega,z_{\rm obs}) = \int \boldsymbol{v}(r)\cdot\tilde{\boldsymbol{F}}(\boldsymbol{r},z_{\rm obs},\boldsymbol{k},\omega)\boldsymbol{dr}, \tag{6.31}$$

where

$$\boldsymbol{F}(\boldsymbol{r},z_{\rm obs},\boldsymbol{k},\omega) = -2\sum_j \bar{\rho}(z)\, e^{i\boldsymbol{k}\cdot\boldsymbol{x}}\,\hat{G}_{z,j}(\boldsymbol{k},\omega,z_{\rm obs}-z)\,\boldsymbol{\nabla}\xi_{j,0}(\boldsymbol{r},\omega). \tag{6.32}$$

The function $\boldsymbol{f}$ is then simply

$$\boldsymbol{f}(\boldsymbol{r},z_{\rm obs},\boldsymbol{k},\omega,z_{\rm obs}) = -2{\rm Re}\left[\omega^2\,\tilde{\xi}^*_{z,0}(\boldsymbol{k},\omega,z_{\rm obs})\tilde{\boldsymbol{F}}(\boldsymbol{r},z_{\rm obs},\boldsymbol{k},\omega)\right], \tag{6.33}$$

with the sensitivity kernel for a measurement in the $\hat{\boldsymbol{e}}_x$ direction to a horizontal flow v_x given by

$${\rm K}_{xx,i}(\boldsymbol{r}) = \int_{\omega_0-\Delta\omega}^{\omega_0+\Delta\omega}\int_0^{2\pi} W_{x,i}(\boldsymbol{k}_i\ ,\omega)f_x(\boldsymbol{r},\boldsymbol{k}_i\ ,\omega)k_i\,d\theta\,d\omega. \tag{6.34}$$

Many properties of this complex formulation for $\mathbf{K}$ are better understood by examining its 3-D structure, as we next do in §6.1.3. However, there are two important points to note concerning Equation (6.33). First, the effect of advection manifests in this formulation through the presence of the gradient operator which operates on the zero-order wavefield. Second, the sensitivity kernel depends on the apodizing function A through the presence of $\tilde{\xi}_z$ in both $\boldsymbol{f}$ and in the weights W_i (which themselves depend on the zero-order power spectrum). Thus the spatial and temporal windowing needed to construct our power spectra can lead to substantial averaging of modal power in spectral space. A measurement made at a particular wavenumber k_i will thus sample the underlying flowfield differently as the analysis region becomes smaller. We turn now to a more complete discussion of these effects and of the general 3-D structure of the sensitivity kernels.

6.1.3 Structure of the Sensitivity Kernels

The 3-D structure of sensitivity kernels corresponding to 16° measurements of the 3 mHz f and p_1 modes has been examined by Birch et al. (2007). These kernels were found to be

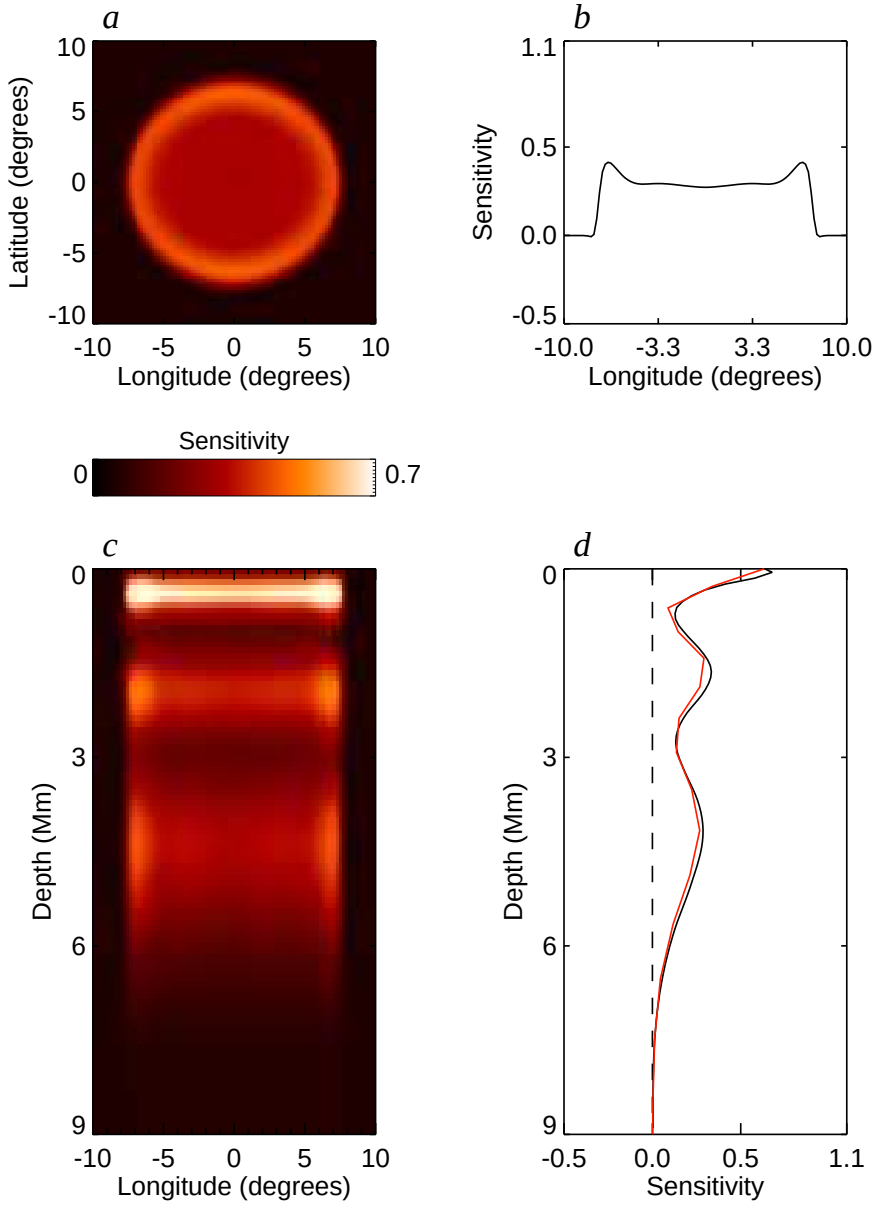

Figure 6.1: Sample sensitivity kernel for a 16° measurement with radial order $n = 2$ and horizontal wavenumber $k = 1.1$ Mm^{-1} ($\ell = 765$). (a) Horizontal cross section of the kernel at a depth of 4.5 Mm. Bright orange tones indicate high sensitivity, and dark tones low. (b) Horizontal cut through the kernel center at 4.5 Mm. (c) Vertical cross-section cut through the kernel center. (d) Vertical cut through the center of the kernel (black) along with kinetic energy density of the associated mode (red). Depth dependence of the sensitivity kernel largely mirrors that of the mode whose measurement it represents.

horizontally smooth, with a vertical structure reflecting the kinetic energy density of the measured mode. Our inversion technique requires a kernel set corresponding to a wide range of wavenumbers ($200 \leq \ell \leq 1100$), radial orders up through $n = 6$, and including kernels for three tile sizes: 2°, 4° and 16°. We have found that the inversion kernels have properties that vary significantly between tile sizes and along a given radial order ridge. As an awareness of some of these features is useful in interpreting the inversion results, we turn now to a detailed discussion of the sensitivity kernel structure.

We first note an important limitation in the calculation of our kernels. As indicated in Equation (6.3), our ring-analysis sensitivity kernels should vary with the central latitude and longitude of the observed patch of the sun. The sensitivity kernel calculation is highly time-consuming, however, requiring approximately $n + 1$ days to compute a single sensitivity kernel for a measurement made for radial mode order n using a modern desktop computer. The computation of a full kernel set (using 3 observation tile sizes and modes through p_6) for measurements made at just one position on the solar disk requires about one month of computing time using 8 cores. The kernel calculation code is written in MATLAB and is not optimized to run on parallel architectures. Computing a full kernel set for each location on the disk currently require many months running on a handful of cores. We have thus taken $\hat{\boldsymbol{\ell}}$ to be directed in the $\hat{\boldsymbol{z}}$ direction, as would be appropriate for a measurement made at disk center (and assuming a plane-parallel geometry), and treat our sensitivity kernels as though they have no variation across the solar disk.

An example of a typical 16° kernel is shown in Figure 6.1. This particular kernel is for a measurement with radial order $n = 2$ and horizontal wavenumber $k = 1.1$ Mm^{-1}. The vertical structure of the kernel is well approximated by the kinetic energy density of the associated mode (as computed using our model). Horizontally, the structure and extent of the sensitivity kernel is largely determined by the analysis-window size. The horizontal variation of sensitivity across the kernel is minimal with the exception of a noticable rim of enhanced sensitivity at the outer edge of the kernel. These edge effects originate from Gibbs ringing at the edges of the apodization window. As noted in Birch et al. (2007), this rim becomes more enhanced as the frequency range over which

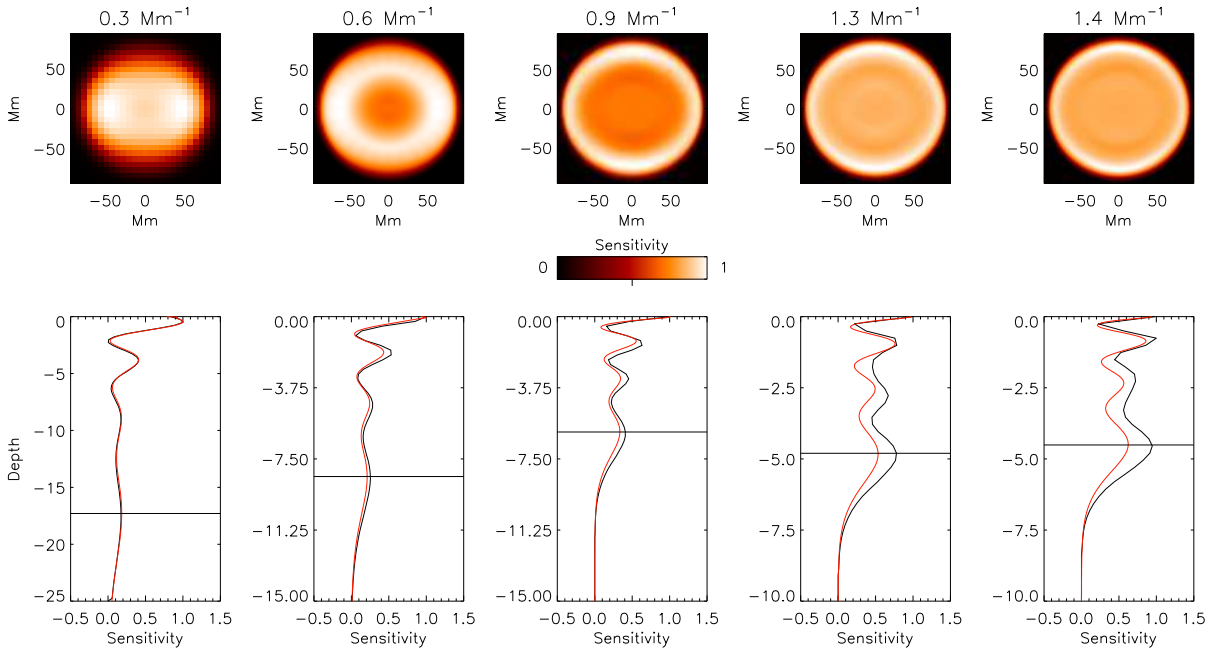

Figure 6.2: Variation of sensitivity kernel structure with horizontal wavenumber. (*upper row*) Horizontal cuts of the sensitivity kernels for several wavenumbers along the p_3 ridge along with (*lower row*) vertical cuts through the center of the sensitivity kernel (black). At high wavenumbers, the kernels develop enhanced rings of sensitivity along the edges. Vertical sensitivity also begins to depart from the kinetic energy density (red) at high wavenumbers.

the fit is carried out is increased. As the frequency range available to the kernel calculation is increased, power from a wider range of modes is available for the reconstruction of the apodization function profile, and the edges become sharper.

Our standard ring measurement technique encompasses a range of frequencies extending from mode center to 40% of the way to the next ridge on either side of the line center. Most sensitivity kernels that we have computed thus exhibit an enhanced sensitivity near the edges as seen in the horizontal structure of Figures 6.1 *a*,*b*. This basic horizontal structure exhibits little variation with depth (Figure 6.1*c*), and the 16° kernels are thus nearly separable. The frequency spacing between neighboring ridges in the power spectrum increases with horizontal wavenumber, and so too does our fitting range. At higher wavenumbers, the sensitivity kernel is constructed from an increasingly wider range of smaller length-scale modes, leading to more prominent rims at high wavenumber. This effect is visible in Figure 6.2 (top row) where we show cross-sections of sensitivity kernels for p_3 measurements.

The vertical structure of the 16° sensitivity kernels also exhibits some variation with wavenumber, developing noticable departures from the kinetic energy density of the mode at the higher wavenumbers (lower row, Fig. 6.2). The reason for this behavior lies with the finite nature of the observing window (i.e. the spatial apodization) whose effect is to blend power in horizontal wavenumber by an amount inversely proportional to the size of the analysis region. This effect is illustrated in Figure 6.3 where we have plotted our model power spectrum at 3 mHz along with the Fourier transform of the 2° and 16° apodization windows. The averaging in wavenumber resulting from a 16° measurement tends to smear power across a distance only slightly larger than the width of a ridge. For the 2° measurements, this effect is much larger and can blend power from several distinct ridges. This effect is exacerbated at higher wavenumbers where the slope of a power spectrum ridge goes as $\sim k^{-\frac{1}{2}}$ and the ridge flattens out, and an averaging over some fixed range in wavenumber will average more power. The broadening of the sensitivity peaks at depth with increasing wavenumber in Figure 6.2 is thus a reflection of the fact that a ring-analysis measurement taken at a specific wavenumber is in fact sensitive to both shallower and more deeply

penetrating modes.

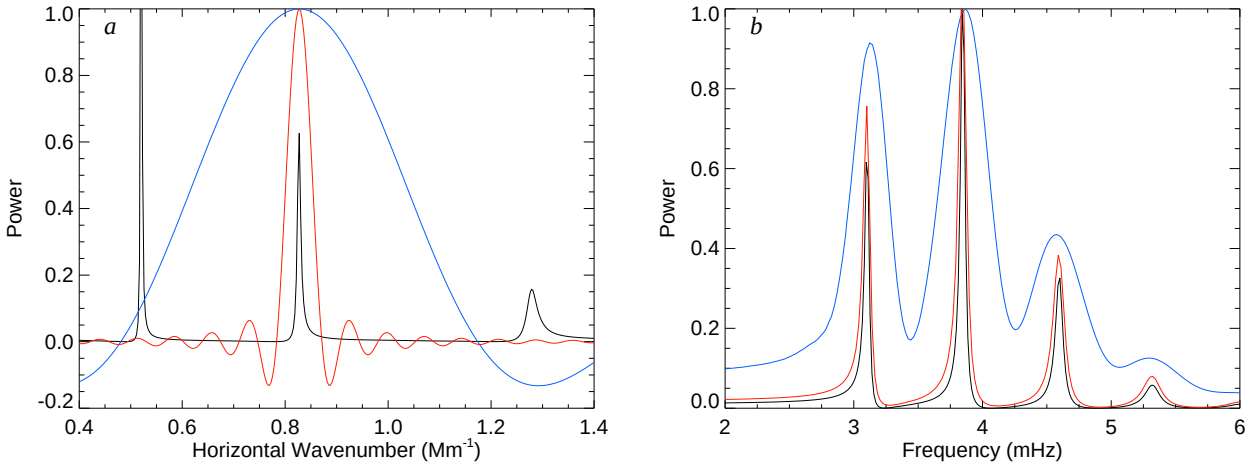

Figure 6.3: Effects of a finite observing region on the observed power spectrum. (a) Model power spectrum at 3 mHz (black) along with the Fourier transform of the window functions for 2° measurements (blue) and 16° measurements (red). Substantial averaging of power in wavenumber occurs for small analysis regions. (b) Model power spectrum (black) cut at horizontal wavenumber $k = 1.39$ Mm^{-1} ($\ell = 967$) after convolving with a circular apodization window for the 2° (blue) and 16° (red) measurements. Averaging in wavenumber leads to an effective smearing of power in frequency.

As indicated in Figure 6.3, for 2° measurements the apodization leads to substantial averaging of power in wavenumber. A representative sensitivity kernel for the 2° measurements is shown in Figure 6.4. This kernel is for the same radial order and wavenumber as that shown in Figure 6.1 (p_2, $k = 1.1$ Mm^{-1}) but exhibits a vertical structure very different from the kinetic energy density and possesses lobes of negative sensitivity near the surface. Negative sidelobes near the surface such as this can result from a measurement being sensitive to power from shallower modes. For example, the observed p_2 ridge is actually constructed by some average that includes (among other modes) both p_2 and p_1 modes. A near surface flow in the x-direction might shift the p_1 ridge towards p_2 on the positive k_x-direction, but away from it negative k_x-direction. After averaging in wavenumber, the observed p_2 ridge could peak at a lower frequency in the positive k_x-direction, but remain unaffected in the negative k_x-direction. This asymmetric shift in the central frequency of the ridge between the two sides of the power spectrum, induced by a shallow flow in the positive x-direction,

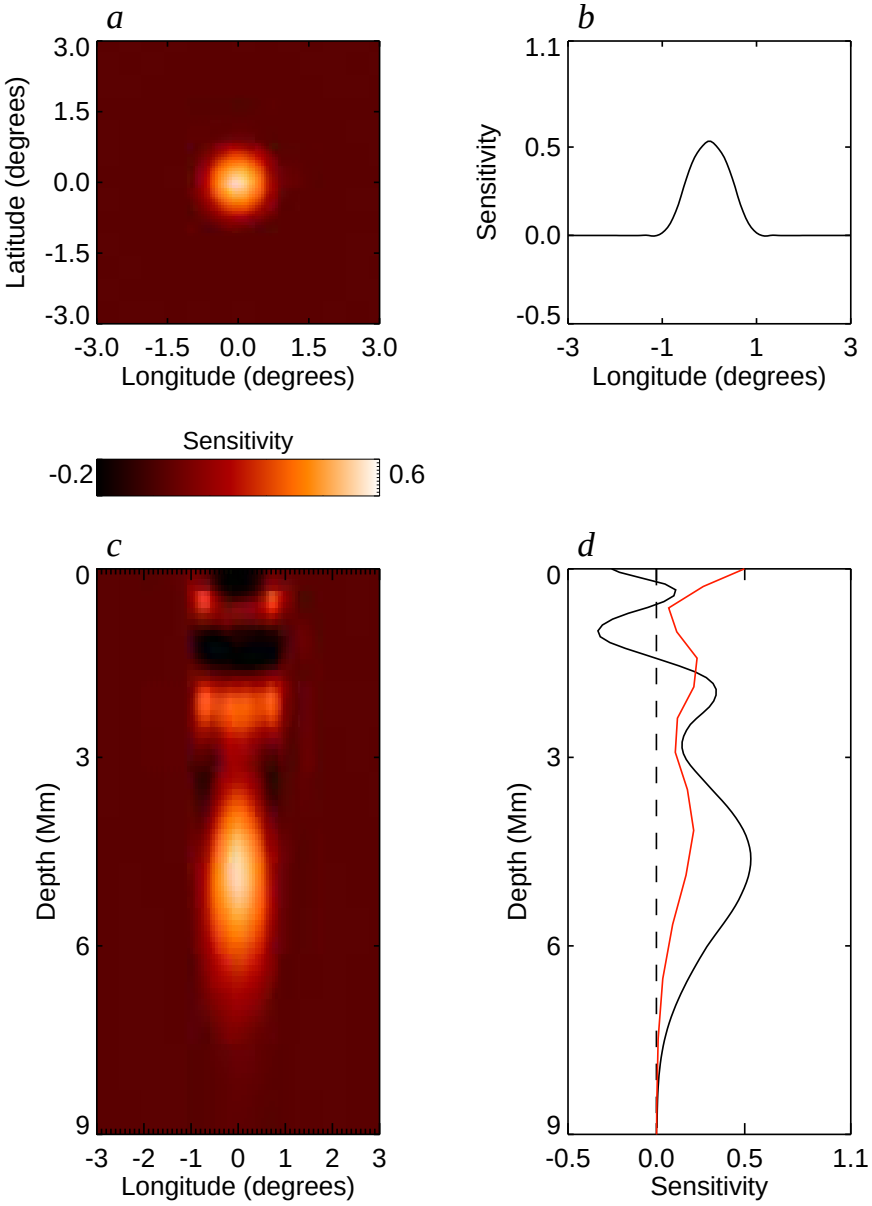

Figure 6.4: Sample sensitivity kernel for a 2° measurement with radial order $n = 2$ and horizontal wavenumber $k = 1.1$ Mm^{-1} ($\ell = 765$). (a) Horizontal cross section of the kernel at a depth of 4.5 Mm. Bright orange tones indicate high sensitivity, and dark tones low sensitivity. (b) Horizontal cut through the kernel center at 4.5 Mm. (c) Vertical cross-section cut through the kernel center. (d) Vertical cut through the center of the kernel (black) along with kinetic energy density of the associated mode (red). Owing to apodization effects, the kernel structure can deviate considerably from the kinetic energy density of the mode for the 2° analysis regions.

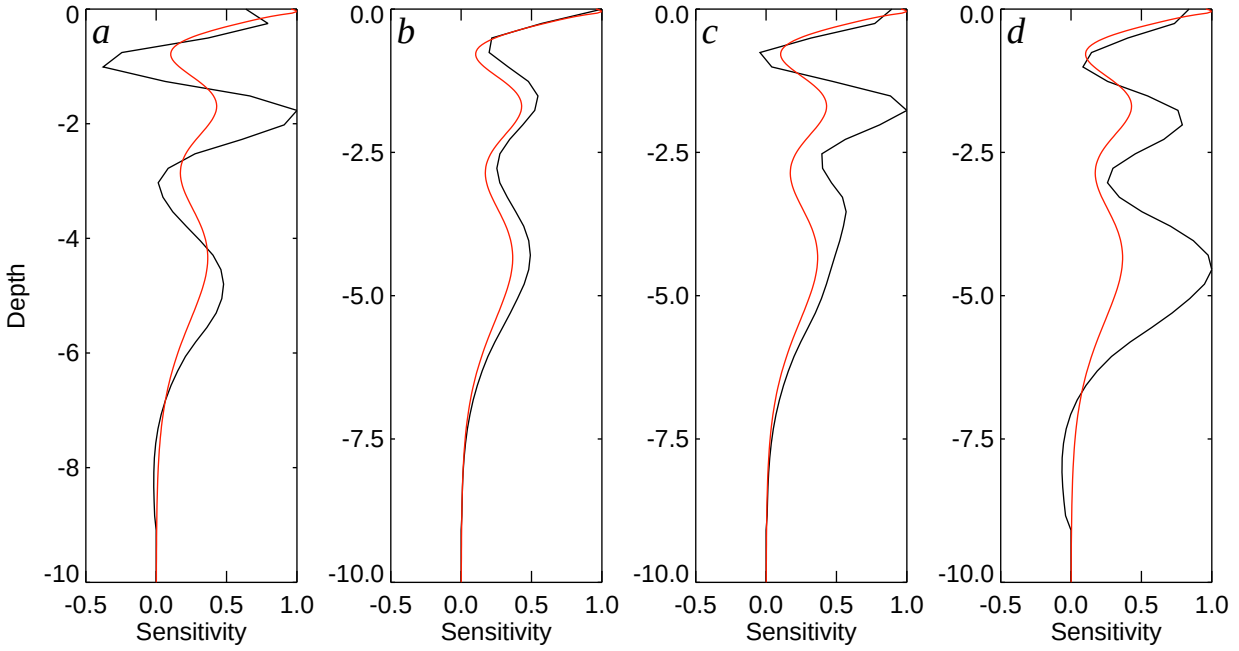

Figure 6.5: Variation of the vertical structure of a 2° sensitivity kernel for the p_2 mode with horizontal wavenumber of 0.26 Mm^{-1} ($\ell = 181$). Horizontally integrated sensitivity is shown in black, and the accompanying kinetic energy density (normalized to 1) is shown in red. The kernel has been computed using a zero-order wavefield with (a) all modes present, (b) only p_2 modes, (c) p_2 and p_1 modes, and (d) p_1, p_2, and p_3 modes present. Averaging in wavenumber, arising from the finite spatial extent of the observations, can mix power from different mode orders, substantially altering the vertical structure of the sensitivity kernels for the 2° measurements.

would be interpreted as a flow in the negative x-direction by our measurement technique.

We can illustrate this effect on the vertical structure of our 2° kernels by removing various mode orders from the zero-order solution. In Figure 6.5, we show a 2° p2 kernel calculated by (a) including all modes, (b) by removing all modes but the $n = 2$ mode, by (c) including only $n = 2$ and $n = 1$ modes, and by (d) including $n = 1, 2$ and 3 modes. The vertical structure of the kernel clearly reflects the kinetic energy density of the target mode when no other modes are present, and shows varying degrees of departure from this structure as additional modes are included. It is unavoidable that any measurement technique, ring analysis or otherwise, that employs a power spectrum constructed from a finite data set will inherently incorporate such mode-averaging effects into the measurements. These effects, while potentially undesired, are not necessarily a weakness

of the technique, provided that the sensitivity kernels account for their existence, as we have done here.

Chapter 7

Attaining 3-D Inversions of Ring Analysis Data

7.1 Elements of the Inversion Procedure

With sensitivity kernels in hand, we now turn to the inversion of the measurements. Our ring analysis technique involves measurements made at numerous wavenumbers and overlapping regions of three sizes on the solar disk. In total, one 26 hour period of observation with MDI can produce data sufficient to make approximately 3×10^5 ring measurements. We have found that inverting about one-ninth of the solar disk at once is computationally tractable. A single inversion can in principle thus involve roughly 3×10^4 measurements. As discussed in §5.2, this collection of measurements defines a system of integral equations describing the flow field,

$$\mathrm{u}_i = \int K_i(\boldsymbol{r}) v(\boldsymbol{r}) \boldsymbol{dr}, \tag{7.1}$$

that must be solved simultaneously. For brevity, we have here dropped the use of the subscripts x and y under the assumption that the x-velocity measurement $\mathrm{u}_{x,i}$ is assumed to be independent of a flow in the y-direction, v_y, and vice versa. Equation (7.1) may then apply to either measurement direction without loss of generality. Discretizing Equation (7.1) leads to a set of linear equations

$$\mathrm{u}_i = \sum_j \mathrm{K}_{ij} \mathrm{v}_j \mathrm{dr}_j. \tag{7.2}$$

In order to simplify the representation of the linear system, we employ a 1-D decomposition of our 3-D inversion grid, using the index j as shorthand for a single location in the solution grid so that

$$\mathrm{K}_{ij} \equiv K_i(x_j,\ y_j,\ z_j). \tag{7.3}$$

Here dr_j denotes the corresponding volume weights used to evaluate the integral. Adopting the convention that matrices are indicated with Roman font, 1-D matrices by lower case letters, and 2-D matrices by upper case letters, we can write

$$\mathrm{u} = \mathrm{A}\mathrm{v}, \tag{7.4}$$

with

$$\mathrm{A}_{ij} = \mathrm{K}_{ij}\mathrm{dr}_j. \tag{7.5}$$

7.1.1 Regularized Least Squares Approach

Given N measurements, we can then in principle invert A to solve for the solar flow field at N points. However, an additional complication lies in the inherent error in the measurements caused by uncertainties in the measurement procedure so that Equation (7.4) becomes

$$(\mathrm{u} + \delta\mathrm{u}) = \mathrm{A}(\mathrm{v} + \delta\mathrm{v}). \tag{7.6}$$

Spurious errors δu in u can lead to departures δv from the true solution v. Depending on the kernel structure, an erroneous measurement u_i can "pollute" the entire solution v, rather than just a single value v_j. Moreover, the presence of errors can lead to inconsistencies between measurements with overlapping sensivity kernels, effectively rendering the matrix singular. We thus require additional information to stabilize the solution. Regularized Least Squares (RLS; c.f. Craig & Brown 1969) is one such approach that involves both our estimate of the errors on u and our intuition concerning the expected structure of the solution, namely that it should be smooth to some degree. Rather than solving Equation (7.4) directly, the RLS approach seeks a trade-off between a good fit of the solution to the data and the smoothness of the solution by minimizing the functional

$$\Psi = \sum_i \frac{1}{\sigma_i^2}\left(\mathrm{u}_i - \int K_i(\boldsymbol{r})v(\boldsymbol{r})\boldsymbol{dr}\right)^2 + \lambda\int |\mathcal{D}v(\boldsymbol{r})|^2\boldsymbol{dr}. \tag{7.7}$$

Here, the σ_i's are the estimated errors on the measurements. The operator $\mathcal{D}$ can be any functional describing the smoothness of the solution. In our case, we take $\mathcal{D}$ to be the gradient operator

$$\mathcal{D}v \equiv \boldsymbol{\nabla}v. \tag{7.8}$$

Other smoothing operators are possible as well (the second derivative is often employed), but we have chosen the first derivative for simplicity and owing in part to the complexity of the 1-dimensional data representation of the three-dimensional grid. Here λ is a scalar parameter used to tradeoff between the goodness of fit and the smoothness of the solution. The discretized form of Equation (7.7) becomes

$$\Psi = \sum_i \frac{1}{\sigma_i^2} \left(\mathrm{u}_i - \sum_j \mathrm{A}_{ij} \mathrm{v}_j \right)^2 + \lambda \sum_j \left(\sum_k \mathrm{D}_{jk} \mathrm{v}_k \right)^2, \tag{7.9}$$

with D indicating the discretized form of the gradient operator $\mathcal{D}$. We can find the solution v that minimizes Ψ by differentiating Ψ with respect to v_j. Adopting the shorthand that

$$\mathrm{B}_{ij} \equiv \frac{\mathrm{A}_{ij}}{\sigma_i}\ ,\ \mathrm{d}_i \equiv \frac{\mathrm{u}_i}{\sigma_i}, \tag{7.10}$$

we find an equation for v of the form

$$(\mathrm{B}^{\mathrm{T}}\mathrm{B} + \lambda \mathrm{D}^{\mathrm{T}}\mathrm{D})\mathrm{v} \equiv \mathrm{M}\mathrm{v} = \mathrm{B}^{\mathrm{T}}\mathrm{d}. \tag{7.11}$$

The solution v is then given by

$$\mathrm{v} = \mathrm{M}^{-1}\mathrm{B}^{\mathrm{T}}\mathrm{d}, \tag{7.12}$$

and the solution may be obtained by inverting the matrix M. As the dimension of the kernel matrix B is $n_{solution} \times n_{measurements}$, the dimension of M is $n_{solution} \times n_{solution}$, where $n_{solution}$ is the number of points in the solution grid and $n_{measurements}$ likewise indicates number of observations. We obtain the inverse of the matrix M using the parallel algorithms available through the Scalapack Fortran package. These inversion routines employ an LU-decomposition whose computation time scales as $n^3_{solution}$, and it becomes important to carefully select the horizontal and vertical resolution of the inversion grid when solving for the flow beneath large patches of the sun. The selection of an appropriate gridding scheme is discussed further in section 7.2.

The matrix M contains the associated kernels, weighted by their errors, for all measurements included in the inversion. We select which measurements to include in M by defining an inversion region of arbitrary spatial extent and then assemble M using all measurements whose associated

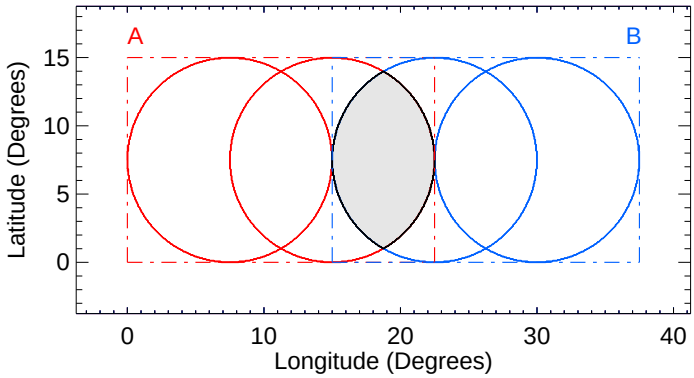

Figure 7.1: Illustrating the need for a modified RLS inversion to bring adjacent inversion regions into agreement. Inversion regions "A" and "B" are indicated by the red and blue dashed-dot lines respectively. Solid circles denote the bounds of 16° measurements. A standard RLS inversion carried out in region "A" cannot account for the overlapping information from region "B" (shaded in gray).

sensitivity kernels lie entirely within that region. This approach can be problematic in light of the overlapping nature of our measurements.

For example, suppose we wish to carry out an inversion of two adjacent regions comprised of two overlapping 16° measurements each. This situation is illustrated in Figure 7.1 where two regions are indicated in red (region "A") and blue (region "B"), and the bounds of the two 16° measurements (which are apodized to 15°) for each region are indicated by the circles. The 7.5° overlap between adjacent measurements leads to a similar overlap between the two inversion regions. Information from the measurement centered at 15° longitude in "A" cannot be included directly in the inversion for region "B" because the associated sensitivity kernel would extend beyond the bounds of the inversion region "B". Depending on the noise characteristics of the measurements, the solution for "A" may not agree with that from "B" in the region of overlap.

This disagreement can be problematic when analyzing flows that span multiple subregions. One solution to this problem is to simply invert the measurements for the full disk at once. However, our experience has shown that the inversion of a square subregion greater than 45° in size can require memory in excess 32 GB. Moreover, inversions for such large regions can take in excess of 1 day to compute. Such computations can be difficult to accomplish using a modern desktop with a typical

core count (4-8) in some time period less than the observing time. To this end, we have devised an iterative method for bringing inversion results from overlapping subregions of the disk into close accord with one another. As the resulting flowmap results from a quilting-together of its individual subregions, we refer to this technique as a stitched inversion and turn now to a description of its implementation.

7.1.2 Stitched Inversions

The stitched inversion method approximates the solution to the standard RLS problem (Eq. 7.7) by subdividing the inversion domain into several smaller subdomains and inverting for their underlying flows as would normally be done. A second set of inversions is then carried out iteratively where the mismatch between adjacent regions in their overlapping interval is penalized through an additional regularization term.

Let us assume there are N subregions of the solar disk whose underlying flows we wish to self-consistently obtain by inversion to yield a full-disk solution. Let the subscript α denote an individual subregion with $\alpha = 1, 2...N$ and the index n denotes the iteration from which the solution results so that $\mathrm{v}_{\alpha n}$ is the solution for subregion α at the nth iteration. An initial solution, $\mathrm{v}_{\alpha 0}$ for each subregion is first obtained by solving our standard RLS equation

$$\mathrm{M}_\alpha \mathrm{v}_{\alpha 0} = \mathrm{B^T}_\alpha \mathrm{d}_\alpha. \tag{7.13}$$

Subsequent solutions $\mathrm{v}_{\alpha n}$ are generated by introducing an additional regularization term $R_{\alpha n}$ to Equation (7.13). This term penalizes the difference between the new solution $\mathrm{v}_{\alpha n}$ and the previous solution $\mathrm{v}_{\alpha n-1}$ at points where the different subregions overlap. We take $R_{\alpha n}$ to be

$$R_{\alpha n} = \Lambda \sum_{\beta \neq \alpha} \sum_j (\mathrm{v}_{j,\alpha n} - \mathrm{v}_{j,\beta\, n-1})^2, \tag{7.14}$$

where Λ is an adjustable regularization parameter, and the sum in j is taken over all points common to regions α and β. Adding $R_{\alpha n}$ to the least squares Equation (7.13) and carrying out the usual

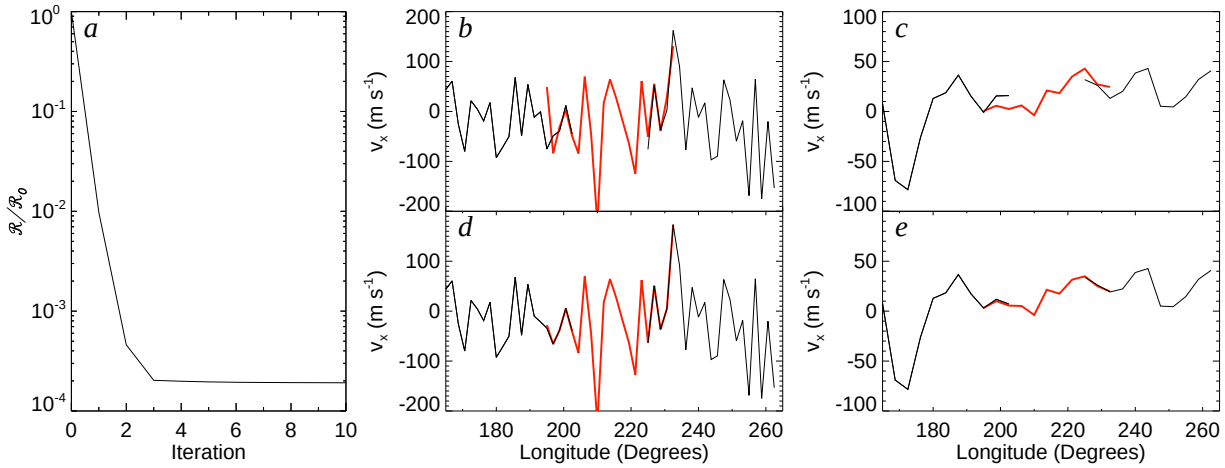

Figure 7.2: Convergence properties from a full-disk inversion using the iterative stitching method. In this case, the flow field for most of the solar disk was reconstructed using 9 square sub-regions 37.5° in horizontal extent overlapping, by 7.5° with their nearest neighbors. (a) Stitching regularization $\mathcal{R}$-value integrated over the full disk (relative to its value after the zero-order inversion). Convergence is achieved within three to five iterations. (b, c) Non-stitched horizontal velocity at one latitude for three overlapping sub-regions (central region colored in red) at 0.5 Mm and 9 Mm in depth respectively. (d, e) Horizontal flow for these same subregions resulting from the converged iterative stitching procedure. Good agreement in the region of overlap is reached at both depths following convergence.

differentiation with respect to v_j leads to a new set of equations

$$\mathrm{Q}_\alpha \mathrm{v}_{\alpha n} \equiv (\mathrm{M}_\alpha + \Lambda \sum_{\beta \neq \alpha} \mathrm{N}_{\alpha\beta}) \mathrm{v}_{\alpha n} = \mathrm{B}^{\mathrm{T}}{}_\alpha \mathrm{d}_\alpha + \Lambda \sum_{\beta \neq \alpha} \mathrm{N}_{\beta\alpha} \mathrm{v}_{\beta\, n-1}. \tag{7.15}$$

Here the $\mathrm{N}_{\alpha\beta}$'s are diagonal matrices whose elements are defined as

$$\mathrm{N}_{jj,\,\alpha\beta} = \begin{cases} 1 & \text{if coordinate } j \text{ in region } \alpha \text{ also occurs in region } \beta \\ 0 & \text{otherwise.} \end{cases}$$

Other prescriptions for $R_{\alpha n}$ are possible. In particular, one might weight $R_{\alpha n}$ by the errors on $\mathrm{v}_{\alpha\, n-1}$ from the previous iteration. However, the formulation of Equation (7.14) yields matrices Q_α that are independent of the iteration n. We are thus required to perform only two matrix inversions for each region: the initial inversion of the matrix M, Equation (7.13), and the inversion of the matrix Q, Equation (7.15). Subsequent solutions are generated by updating the right-hand side of Equation (7.15) and multiplying by Q_α^{-1}.

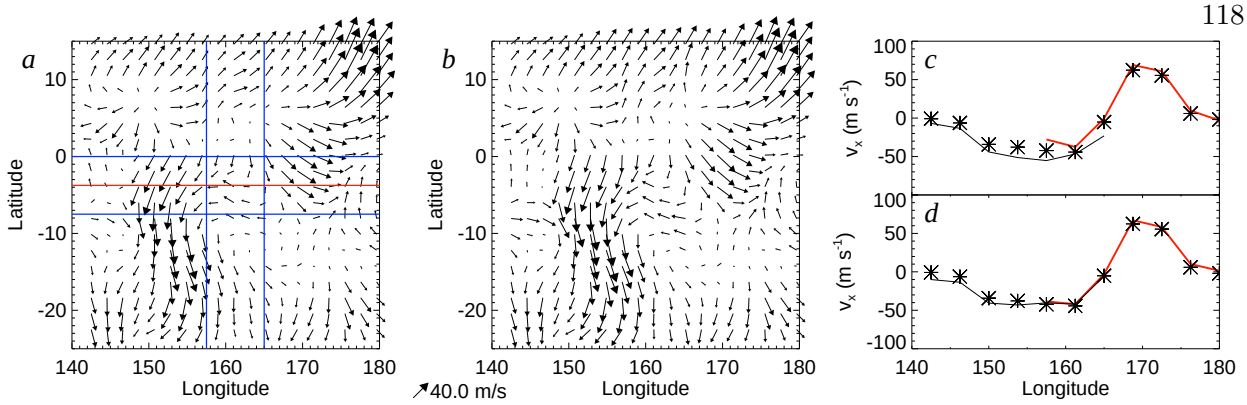

Figure 7.3: Comparision between an iterative stitched inversion (a) and its companion full inversion (b) at a depth of 9Mm (with horizontal resolution interpolated by a factor of two). Blue lines denote boundaries of the four overlapping subregions used in the iterative inversion. Each square subregion was 22.5° in horizontal extent. (c) Sampling of results along the latitude line indicated in red in panel (a) for the full inversion (black symbols) and zero-order results for two overlapping sub-regions of the iterative inversion (black and red lines). (d) Same as in c, but displaying the results for the two sub-regions after the stiched solution has converged. Following the iterative inversion, flows in both regions show good agreement with the full inversion.

In practice the solutions converge quickly, typically requiring three to five iterations. In Figure 7.2 we illustrate the convergence properties for a full disk inversion carried out using this technique. The disk was tiled with nine 37.5° subregions with nearest neighbors overlapping by 7.5°. An integrated $R_{\alpha n}$ for all nine regions was calculated over 10 iterations, with convergence evident around the fourth iteration. Figure 7.2b, d illustrates the pre- and post-convergence properties of the solution. Solutions from neighboring regions typically agree well at the surface following the zero-order inversion. Solutions in the upper layers are determined largely by the 2° measurements. Unlike the 16° measurements, very few of these smaller measurements are omitted near the edges of the inversion and neighboring inversions contain redundant information near the surface. At the 9 Mm depth, however, the missing information from the 4° and 16° measurements is important and neighboring inversions agree well only after the iterative procedure has converged.

We are unable to invert an entire disk to check the validity of this technique. However, we have tested our iterative results on a smaller scale by decomposing a 37.5° region into four 22.5° regions overlapping by 7.5°. A comparison between the results for the iterative stitched

inversion relative to the full inversion at 9 Mm in depth is shown in Figure 7.3. The two flow fields show good agreement with one another. A plot of v_x at constant latitude (see red line Fig. 7.3*a* and Figs. 7.3*c, d*) shows that good agreement both between neighboring regions and the full inversion is reached once the procedure has converged.

7.2 Averaging Properties of the Inversion Algorithm

The solution values v_j are linearly related to the measurement values u_i so that each solution point v_j may be written as

$$\mathrm{v}_j = \sum_i \mathrm{a}_{ji}\mathrm{u}_i, \tag{7.16}$$

where the coefficients a_{ji} are found through Equation (7.12) with

$$\mathrm{a}_{ji} = \frac{1}{\sigma_i^2}\sum_\ell \mathrm{M}^{-1}_{j\ell}\mathrm{A}_{i\ell}. \tag{7.17}$$

The solution is thus a weighted sum of the data whose details depend on the measurements errors and the inverse matrix M^{-1}. The error on the solution, ϵ_j, can be written in similar fashion in terms of the measurement errors σ_i as

$$\epsilon_j^2 = \sum_i \mathrm{a}_{ji}^2 {\sigma_i}^2. \tag{7.18}$$

Note that the a_{ji}'s do not depend on the measurements themselves, only upon the measurement errors and the sensitivity kernels. Inversions made using different measurement values, but with identical errors and identical mode sets, will yield a result by averaging the raw data in exactly the same manner. Interpretation of the results generated using the 3-D inversion procedure requires an understanding of the a_{ji}'s and the localized averaging of measurements they represent. We thus devote the next section to describing in detail the averaging properties of our inversion algorithm.

7.2.1 Data Combination Properties of the Inversion Algorithm

We can gain a sense of how the inversion scheme combines data by using the set of average MDI errors described in §5.2.4 in an inversion. We have carried out an inversion of a $15^\circ \times 15^\circ$ region

with a horizontal resolution of 0.9375° and a grid extending to 25 Mm in depth, assembling the inversion matrix M by assuming that all modes are fit with an uncertainty given by the average error for that mode. We find that a convenient parameterization of the relative contribution of the different data points to the solution is given by the quantity $\mathcal{A}_j$, which we define as

$$\mathcal{A}_j(n,k,T) \equiv \frac{\sum_i \delta_D(T-T_i\,,\ k-k_i\,,\ n-n_i\,)\,\mathrm{a}_{ji}^2}{\sum_i \mathrm{a}_{ji}^2}. \tag{7.19}$$

The quantity $\mathcal{A}_j$ is thus a measure of the disk-integrated contribution, mode-by-mode, of the different measurements to the solution point v_j.

The mode-by-mode contribution, $\mathcal{A}_j$, for the solution v_j at the horizontal center of the inversion domain and at four different target depths is illustrated in Figure 7.4. For a given target depth in the inversion grid, the principle contribution to the result generally comes from modes whose lower turning points are within one Mm or so of that depth. The associated analysis region size (indicated by the different symbols) of the highest $\mathcal{A}_j$'s are typically those that offer the finest available horizontal resolution at that depth. Near the surface, the solution is comprised primarily of 2° f-mode measurements. The influence of the 2° measurements extends to approximately 3 Mm, with the 4° measurements beginning to contribute appreciably beyond this depth. Such behavior is to be anticipated in light of Figure 5.4, where we see that the 2° errors begin to rise sharply beyond about 3 Mm, thus making the 4° data at that depth more favorable to the RLS scheme. The modes employed in the 4° measurements in turn penetrate only as deeply as 13 Mm (not shown). At the depth of 15 Mm then, the 16° measurements are primarily responsible for forming the solution. The changing contributions from the different tile sizes means that the horizontal resolution of the inversion solution naturally degrades with depth (even in the absence of varying horizontal resolution of the inversion points with depth). This natural change in resolution is evident upon inspection of the averaging kernels resulting from the inversion.

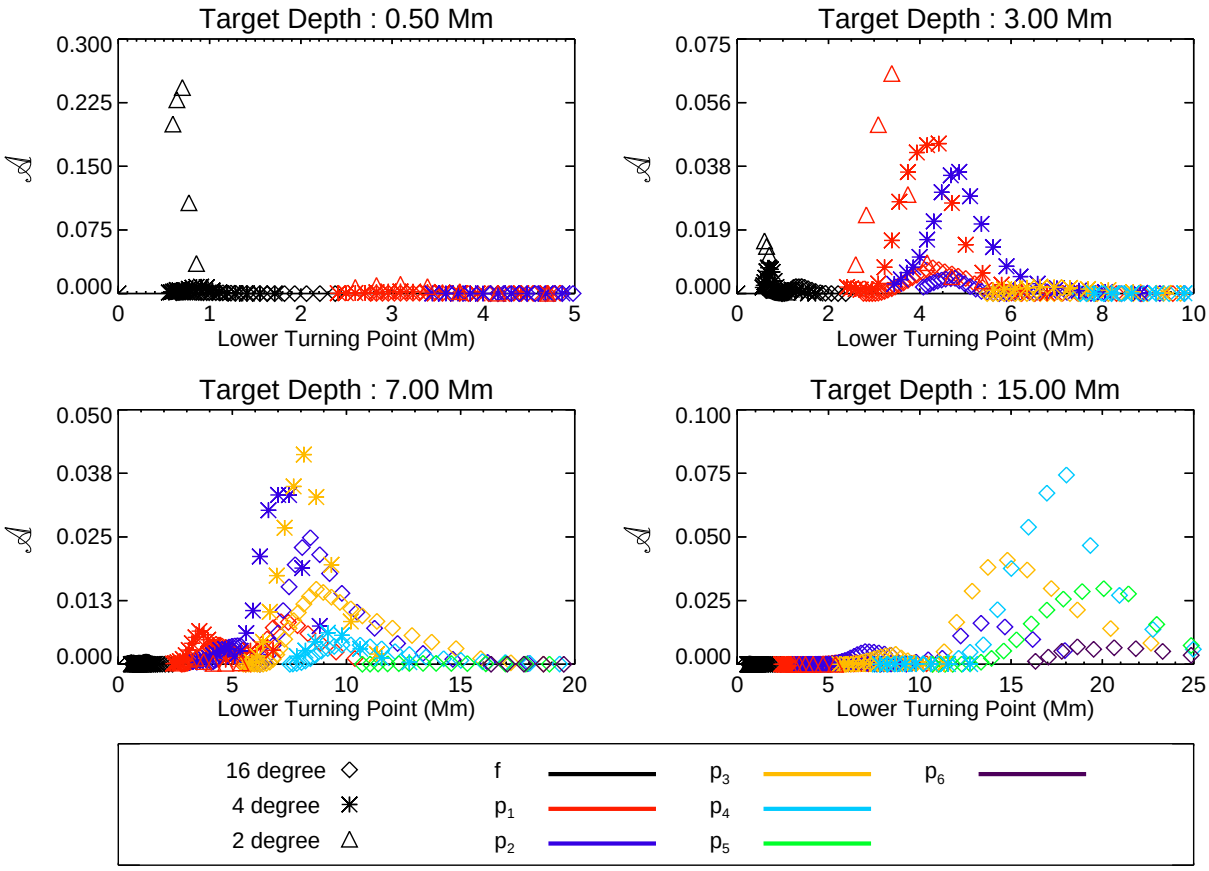

Figure 7.4: Depth-averaging properties of the inversion scheme. The $\mathcal{A}_j(n,\, k,\, T)$'s for a solution point at the horizontal center of the inversion grid, at four target depths, are plotted as a function of the lower turning point of the contributing modes. Tile sizes are indicated by distinct symbols, and different radial orders by the indicated colors. At target depths close to the surface, 2° measurements with a shallow lower turning point are largely used to construct the solution. At mid depths, 4° measurements dominate with contributions from the 2° and 16° data. Deeper in the convection zone, 16° measurements comprise the bulk of $\mathcal{A}_j$.

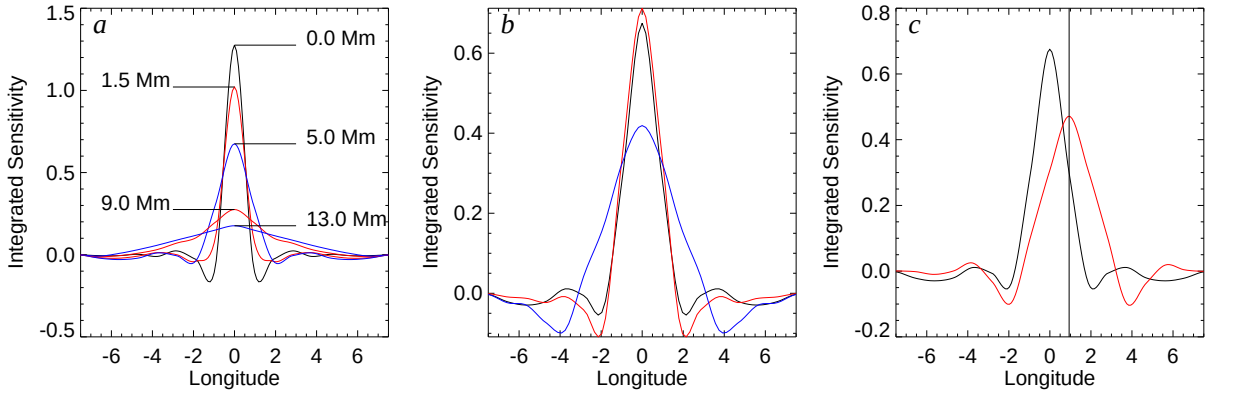

Figure 7.5: Horizontal structure of the averaging kernels. (*a*) Variation of the horizontal structure with target depth. (*b*) Horizontal averaging kernel structure for a target depth of 5 Mm using an inversion grid with horizontal resolution at that depth of 0.9375° (black line), 1.875° (red line), and 3.750° (blue line). The averaging kernels achieved are substantially degraded when the horizontal resolution of the inversion is below that of the measurements. (*c*) Kernel structure for an inversion point lying between two measurements (red). The kernel is much broader than one that is achieved when the inversion point coincides horizontally with a measurement (black). The vertical black line indicates the target longitude.

7.2.2 Averaging Kernels

The averaging kernels for a given solution point are generated from the a_{ji}'s as described by Equation (5.12). Thus, as the $\mathcal{A}_j$'s begin to favor measurements from one tile size over another, the effective width of the averaging kernels changes accordingly. We examine the horizontal structure of the averaging kernels in Figure 7.5*a*. Near the surface, these averaging kernels are roughly 2° in width, with negative sidelobes on either side of the maximum. These sidelobes arise from the inversion subtracting measurements on either side of the target longitude and latitude, and adding those measurements that fall onto the target location. This results in a narrower central peak, but one with small negative sidelobes on either side. At mid-depths, the averaging kernels are roughly 4° in width, with smaller negative sidelobes. Beyond 13 Mm, the horizontal structure is reflective of the 16° measurements.

The horizontal structure of the averaging kernels also depends on the horizontal resolution of the inversion grid. As the resolution is degraded, sensitivity kernels are binned accordingly in the horizontal direction, effectively resulting in a spatial uncertainty in their associated measurements.

We examine the effect of varying the horizontal resolution in Figure 7.5*b*, where we plot horizontal averaging kernels for the solution point at the domain center and a depth of 5 Mm. The averaging kernel realized when adopting a horizontal resolution of 1.875° at this depth is indicated in black and that for a grid with 0.9375° resolution in red. At this depth, the 4° measurements are the predominant contributors to the averaging kernel. These observations are spaced apart by 1.875°. The coarser grid thus has the same horizontal resolution as the measurments, and the finer grid has one interpolating point between measurements. The averaging kernel resulting from the finer grid is less sharply peaked about the solution point than that resulting from the coarser grid, but possesses less pronounced sidelobes on either side of the central peak. However, the differences between the two are small.

The finer horizontal mesh also allows for the reconstruction of the flow at a point halfway between two measurements. The averaging kernel for such an interior solution point at a depth of 5 Mm is shown in Figure 7.5*c* (red). The adjacent averaging kernel for a solution point coinciding with a measurement is shown in black. With no 4° measurement centered at the target longitude, the averaging kernel formed is essentially an average of those for the two measurements made on either side of the solution point. The resulting kernel is thus much broader than one targeted at the location of a 4° measurement, and yields information that is more easily obtained through simple interpolation of the lower resolution inversion results. When using our current tiling scheme, the benefits of adopting a higher horizontal resolution than the measurements themselves can provide at a given depth are thus minimal and unlikely to outweigh the computational costs associated with increasing the number of solution points.

We explore the depth structure of various averaging kernels in Figure 7.6*a*. The averaging kernels tend to peak near their target depth, decaying below that point. Side lobes of positive sensitivity near the surface are apparent for many of the kernels sampled, increasing in strength as the target depth approaches the surface. These kernels also become wider at deeper target depths.

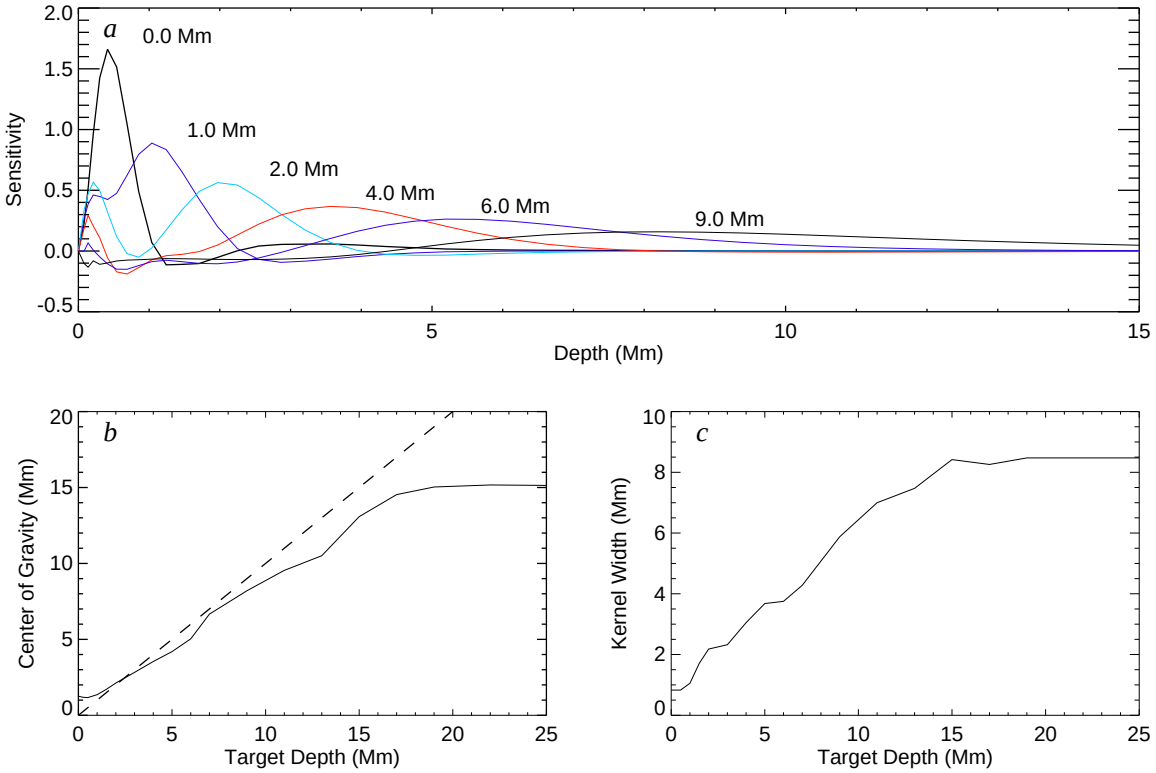

Figure 7.6: Depth properties of the averaging kernels. (a) Sampling of the vertical structure of the averaging kernels. (b) Center of gravity (solid line) achieved at different target depths. For reference, a slope of one is indicated by the dashed line. (c) Kernel width at the different target depths. Averaging kernels become less localized with increasing depth. It is difficult to create well localized averaging kernels below a depth of 15 Mm when using the observations described in §5.2.

We quantify the vertical location of the kernel by the center of gravity, z_{cg}, which we take to be

$$z_{cg} = \frac{\int |C(\boldsymbol{r})| \; z \, \boldsymbol{dr}}{\int |C(\boldsymbol{r})| \; \boldsymbol{dr}}, \tag{7.20}$$

with z the depth below the surface. The center of gravity for averaging kernels at the different target depths is shown in Figure 7.6b. We see that the center of gravity is generally somewhat less than the target depth (except near the surface). Moreover, beyond 15 Mm the inversion is unable to build kernels centered more deeply. The vertical width of the kernels (which we define as the distance between the 0.25 and 0.75 percentile points) increases steadily with depth as well. Kernels are about 1 Mm in width near the surface, and about 8 Mm in width beyond the 15 Mm depth.

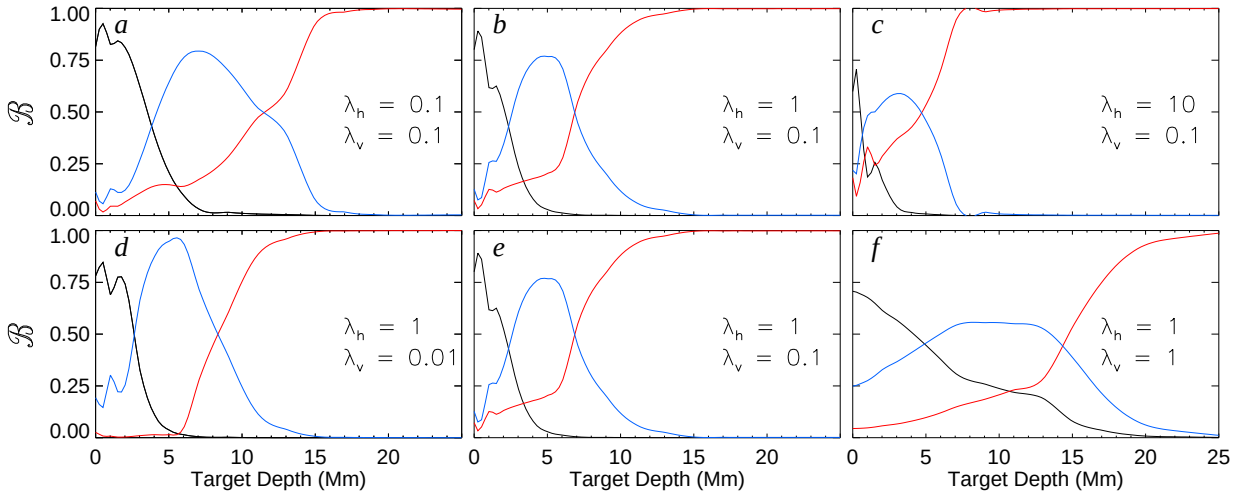

Figure 7.7: Variation of the tile-size contribution parameter $\mathcal{B}(T,\, z)$, with changing regularization in (a-c) the horizontal direction and (d-f) the vertical direction. 2° measurements are indicated in black, 4° data in blue, and 16° data in red. Changing the regularization alters the range of depths over which measurements from the different tiling sizes are emphasized by the inversion algorithm.

7.2.3 Effects of Regularization

The inversion results are dependent on the value assumed for the regularization tradeoff parameter λ. It can be convenient to apply one value of λ, hereafter λ_h, to the horizontal portion of the regularization operator $\mathcal{D}$, and a separate value to the vertical part, hereafter λ_v. As the regularization is increased, the solution becomes smoother, and the averaging kernels broader. Consequently, data is combined differently as the degree of regularization is varied. Some insight into effects of varying the regularization can be gained by examining the parameter $\mathcal{B}$, given by

$$\mathcal{B}(T, z) \equiv \sum_j \left(\frac{\sum_i \delta_D(T - T_i)\, \delta_D(z - z_j)\, \mathrm{a}_{ji}^2}{\sum_i \delta_D(z - z_j)\, \mathrm{a}_{ji}^2} \right), \tag{7.21}$$

which measures relative contribution of measurements obtained from the three different analysis-region sizes to the solution at each depth.

The variation of $\mathcal{B}$ with changing horizontal regularization is demonstrated in Figure 7.7a-c, and with changing vertical regularization in Figure 7.7d-e. As vertical regularization is increased, the solution becomes more averaged in depth, and the regions of contribution for the different tile sizes become less distinct. For sufficiently large vertical regularization, the influence of the

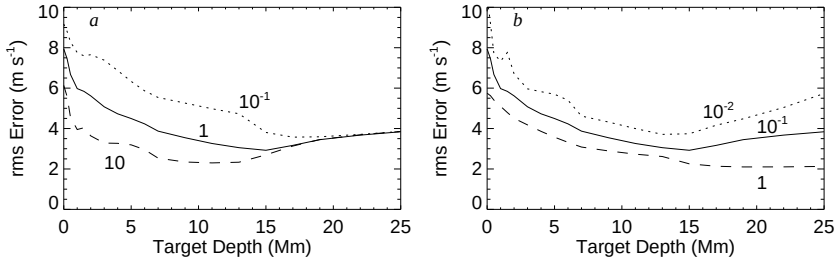

Figure 7.8: Variation of 3-D inversion errors with changing horizontal and vertical regularization (a) Variation of rms error with depth using an $\lambda_v = 0.1$ and different horizontal regularizations of $\lambda_h = 10$ (dashed), $\lambda_h = 1$ (solid) and $\lambda_h = 0.1$ (dotted). (b) Inversion errors realized using a $\lambda_h = 1.0$ and different vertical regularizations of $\lambda_v = 1$ (dashed), $\lambda_v = 0.1$ (solid), and $\lambda_v = 0.01$ (dotted). As regularization is increased, the inversion scheme averages over more data and the resulting errors tend to decrease. Errors at all depths are typically less than 10 m s^{-1}.

2° measurements is felt down to 15 Mm, even though the deepest lower turning point associated with any of the 2° measurements is 5 Mm. The most noticable effect of increasing the horizontal regularization is to increase the usage of the 4° and 16° measurements at increasingly shallower depths. These effects can be better understood through examination of the associated averaging kernels.

The effect of these different regularization parameters on the inversion errors is illustrated in Figure 7.8, and their effect on the averaging kernels is shown in Figure 7.9. Increasing regularization in either direction generally decreases the inversion errors. This is accomplished by averaging over more data, which in turn leads to broader averaging kernels as can be seen in Figure 7.9. There we see that increasing the horizontal regularization leads to increased horizontal width in the averaging kernels. As the horizontal regularization is increased, the inversion scheme seeks to horizontally smooth the solution. This is accomplished near the surface, for instance, by forming the solution at one location by averaging 2° measurements over a broader range in longitude and latitude. Further smoothing is accomplished by incorporating more 4° and 16° measurements into the near-surface solution, as is apparent in the top row Figure 7.7. A similar pattern is followed at the mid-depths where fewer 4° measurements and more 16° measurements are incorporated into the solution as the horizontal regularization is increased.

Vertical regularization works similarly. As the vertical regularization increases, the averaging kernels broaden in depth. The horizontal structure of the averaging kernels shows little change, however, as λ_v is varied by a factor of one hundred. Averaging of the data is thus performed over a wider range of modes as vertical regularization is increased, but not over a wider spatial extent on the disk. This averaging over modes is why the 2° data is used at 15 Mm for $\lambda_v = 1$ as shown in Figure 7.7. There, the solution at depth is smoothed vertically in part by incorporating the shallow modes accessible only to the 2° measurements.

With no known flow to compare our results against, the choice of regularization parameters is unfortunately somewhat arbitrary, even after consideration of the data-combination and averaging-kernel implications. While the errors do vary with the regularization, they are not incredibly sensitive to it, remaining largely within the 5-10 m s^{-1} for all parameter combinations explored here. We choose to adopt values of $\lambda_h = 0.1$ and $\lambda_v = 0.1$ (Fig. 7.8*a*, dotted line), basing this choice on the reasonably focused kernels they provide in the horizontal and in the vertical. This choice also produces flowmaps that compare well with 1-D inversion of the 16° measurements, as discussed in the next section. Morever, for this parameter combination, the deepest effects of the 2° and 4° measurements roughly correspond with the lower turning points of their most deeply penetrating modes.

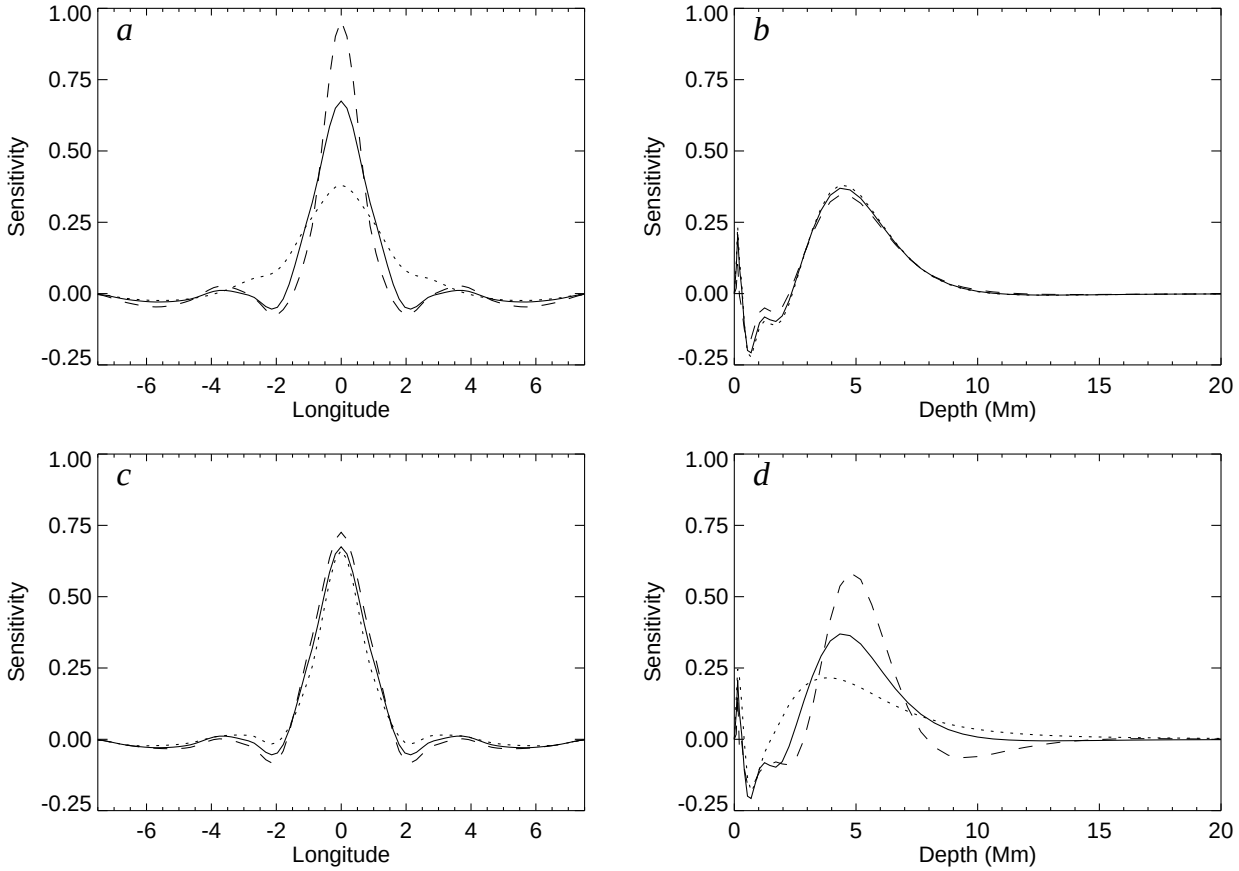

Figure 7.9: Sensitivity of the averaging kernels to variations in the regularization for an averaging kernel targeted at the 5 Mm depth. (*a,b*) Variation of the (*a*) horizontal and (*b*) vertical structure of the averaging kernel with changing horizontal regularization. λ_v has been taken to be 0.1. λ_h of 0.1, 1.0, and 10.0 are indicated by dashed, solid and dotted lines, respectively. (*c,d*) Variation of the (*c*) horizontal and (*d*) vertical structure of the averaging kernel with changing vertical regularization and λ_h of 1.0. λ_h of 0.01, 0.1, and 1.0 are indicated by dashed, solid and dotted lines, respectively. Variations in λ_v change the vertical structure of the averaging kernels while leaving the horizontal structure relatively unchanged. Similarly, λ_h primarily affects the horizontal structure of the averaging kernels.

Chapter 8

Exploring Convection and Magnetism with ARRDI Inversions

8.1 Comparison of ARRDI Results with Prior Assessments

Prior to the development of our 3-D inversion algorithm, flow maps generated from ring-analysis measurements have relied on 1-D (depth) RLS or OLA inversion of the 16° data (e.g., Haber et al. 2004), and on f-mode fits from 2° and 4° measurements (e.g. Hindman et al. 2006). As ARRDI combines all three levels of data in a self-consistent fashion, we should see points of similarity between solutions generated using 1-D inversions and those generated using ARRDI. This is particularly true at key depths where the 3-D inversion tends to emphasize some small subset of the data when constructing the solution. A comparison between solutions generated using 3-D and 1-D techniques will thus serve to highlight its advantages over and differences relative to the previous schemes. We devote this section to a comparison of the ARRDI results with those generated using f-mode fits and 1-D OLA inversions. We employ MDI data from 24 April 2001 for these comparisons. The presence of a particularly large and long lived active complex, NOAA AR 9433, in this dataset allows us to compare flows in regions of both quiet and active sun.

As discussed in §7.2.3, we adopt regularization parameters $\lambda_h = 0.1$ and $\lambda_v = 0.1$ for this comparison. In depth, our inversion grid extends from the surface to a depth of 25 Mm, with 0.5 Mm resolution in depth near the surface transitioning to 3 Mm resolution near the bottom of the grid. Horizontal resolution is 1.25° near the surface and transitions to 3.75° at depth. A complete list of target depths and their horizontal resolution is given in Table 8.1. Horizontally, we tile the full disk with a 3×3 matrix of square 45° regions overlapping by 7.5° in longitude and latitude and

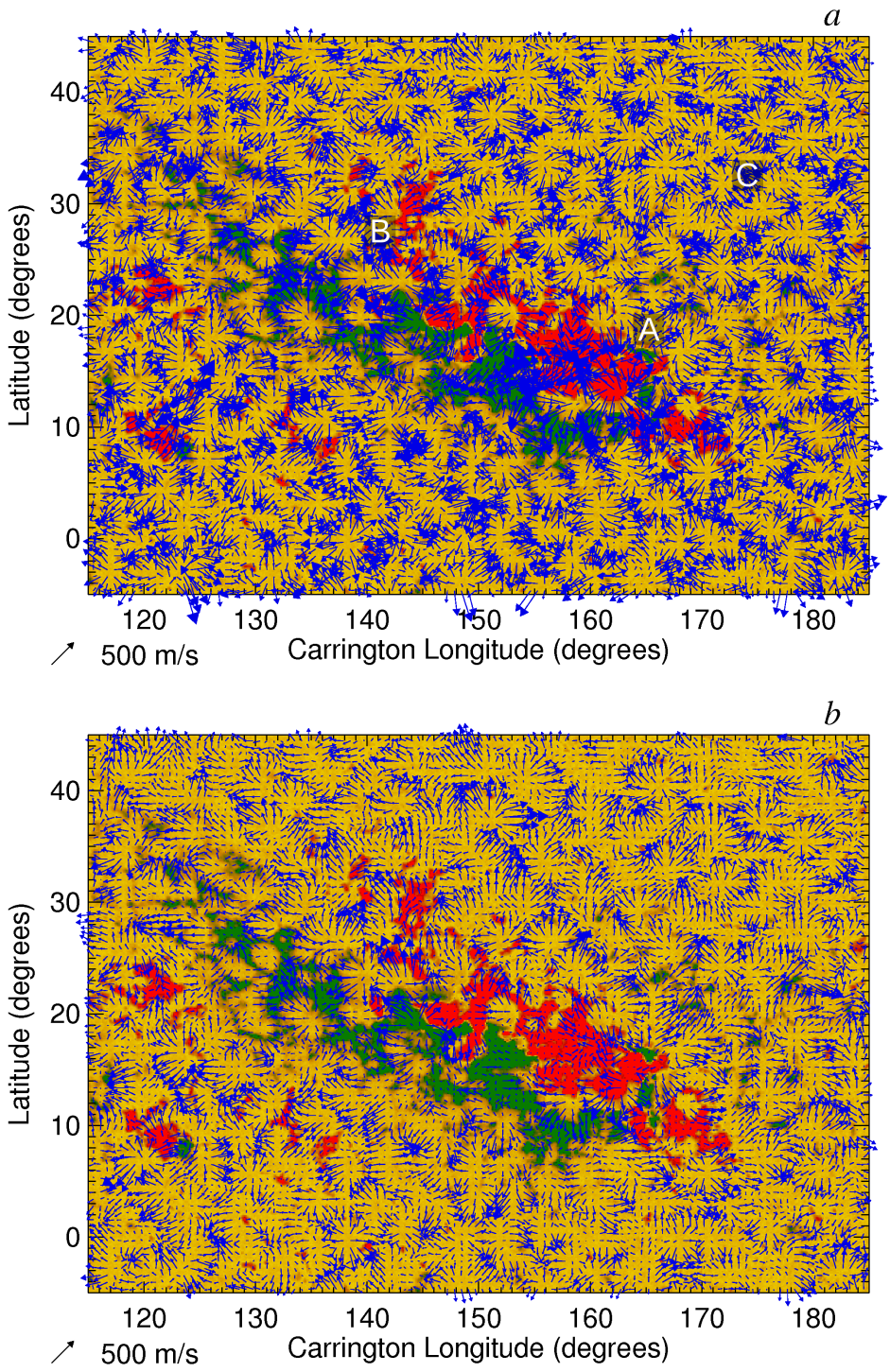

Figure 8.1: Comparison of the ARRDI results to 2° f-mode fits using data from 24 April 2001. (a) 3-D inversion solution at 1 Mm and (b) solution resulting from 2° f-mode fits averaged in wavenumber. Cellular structures are similar in the two flow maps, though the inversion results exhibit higher velocities (possibly due to negative sidelobes in the sensitivity kernels). White lettering indicates locations of the smaller target regions shown in Figs. 8.2 (and at other depths in Fig. 8.4).

TABLE 8.1
Inversion Grid

Target Depth (Mm)	Horizontal Resolution (degrees)
0.0	1.25
0.5	1.25
1.0	1.25
1.5	2.50
2.0	2.50
3.0	2.50
4.0	2.50
5.0	2.50
6.0	2.50
7.0	2.50
9.0	2.50
11.0	3.75
13.0	3.75
17.0	3.75
19.0	3.75
22.0	3.75
25.0	3.75

Table 8.1: Target depths and horizontal resolution of the inversion grid for the 3-D inversions of the April 24, 2001 data.

combined with the stitching algorithm.

8.1.1 Surface Comparisons with the 2° data

In the upper 2 Mm of the convection zone, the f-mode measurements dominate the data (see Figure 5.4). At a depth of 1 Mm, where our horizontal resolution is 1.25°, we thus expect our 3-D inversion to emphasize the 2° f-mode data in generating the solution. The ARRDI -generated flow map at 1 Mm is shown in Figure 8.1*a*. An average magnetogram from that period is underlayed, with regions of strong positive magnetic field indicated in red, regions of strong negative field in green, and weak field in yellow. Velocity vectors are indicated by blue arrows. Convective patterns associated with the largest supergranules ($\sim$ 3° in size) are clearly visible at this depth and tend to possess boundaries that trace out regions of strong magnetic field. For comparison the flow field generated using 2° f-mode fits is shown in Figure 8.1*b*, where we have averaged together the measured velocities over all wavenumbers fit along the f-mode ridge.

Convective patterns in the 2° fits are similar to those in the ARRDI flow map, but amplitudes are noticably lower by about 33% for the fitted velocities. Averaging over the seven wavenumbers fit along the f-mode ridge to generate the 2° map is primarily responsible for this effect. Moreover, each individual 2° data measurement has a sensitivity kernel that is 2° in width horizontally. Surface flows realized through the 3-D inversion can in principle build a narrower horizontal average through the appropriate combination of neighboring measurements as discussed in §7.2, leading to an amplification of the flows recovered through inversion relative to those obtained by averaging f-mode fits.

A more detailed comparison of the two flowmaps is given by Figure 8.2 where we focus on one quiet and two active sun regions labeled A-C in Figure 8.1. In Region A, there are several locations indicated by small blue dots (i.e. zero length arrows) where no f-mode fits were obtained. The ARRDI flowmap is able to reconstruct the flow at these locations using other mode orders, tile sizes, and where necessary, the horizontal regularization. This leads to an interesting effect in Figure 8.1*b*, where the supergranules bordering the active complex appear to possess stronger flows moving *away* from the active region than they do *into* it. In many instances, this is due to the absence of velocity fits rather than an actual decrease in velocity amplitude. Such an effect is not apparent in the ARRDI results. Regions B and C highlight the similarities of the two results for both active and quiet Sun in detail. When data dropouts are not a factor, areas of convergence and divergence correlate well between the two flowmaps, with only small differences between the two. The correlation between these two data sets can be quantified using the Spearman rank correlation coefficient ρ. A value of 1.0 for this coefficient indicates perfectly correlated data, -1.0 indicates perfectly anti-correlated data, and zero indicates no correlation. We find the correlation coefficient for flows in the east-west direction, ρ_{ew}, to be 0.77 and that for flows in the north-south direction, ρ_{ns}, to be 0.74.

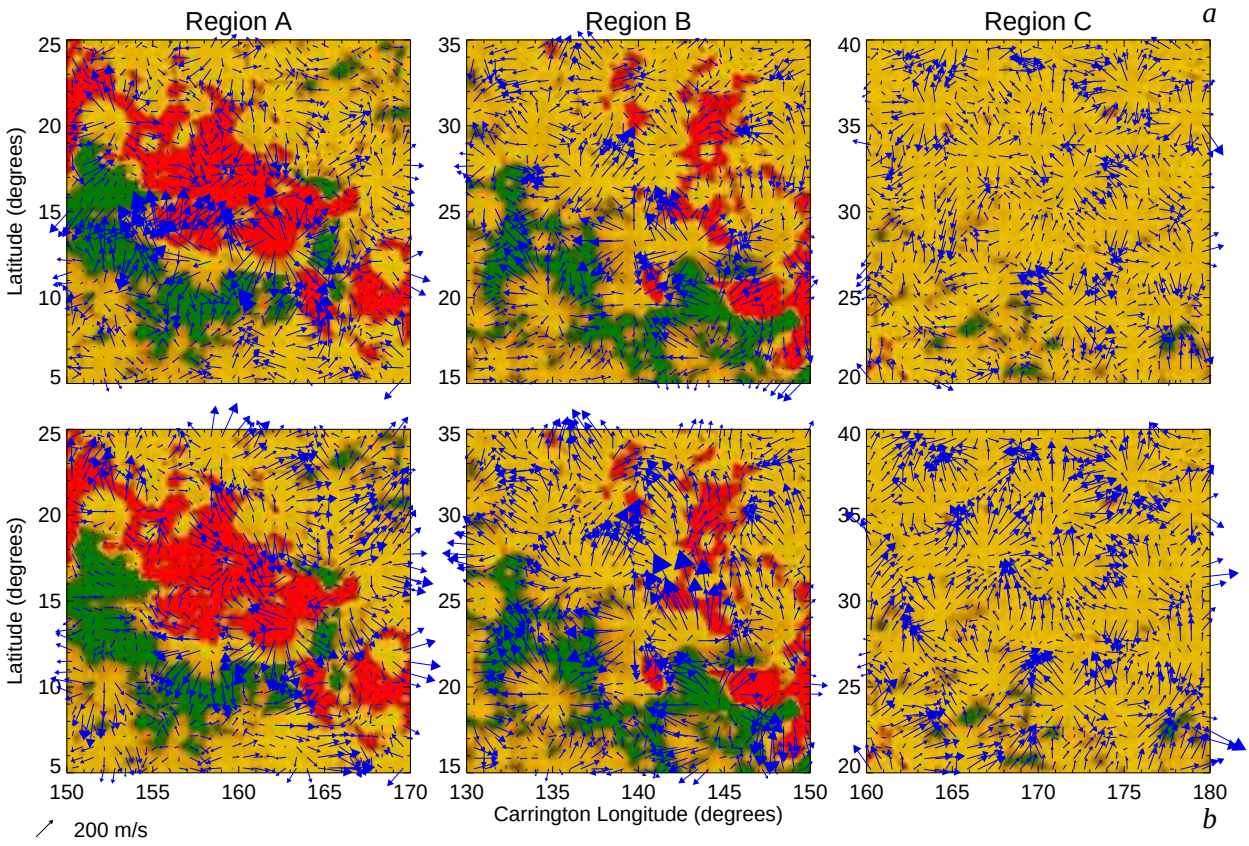

Figure 8.2: Closeups of the regions of interest indicated by white lettering in Figure 8.1 for the (*a, upper row*) ARRDI results and the (*b, lower row*) 2° f-mode fits. Detailed examination of the flow structures in quiet sun (Region C) reveals good agreement between the two datasets. In more active regions (such as A,B), data dropouts are present in the 2° f-mode data set (visible as small blue dots). The 3-D inversion uses 4° and 16° degree data to reconstruct the solution where there is an absence of 2° data.

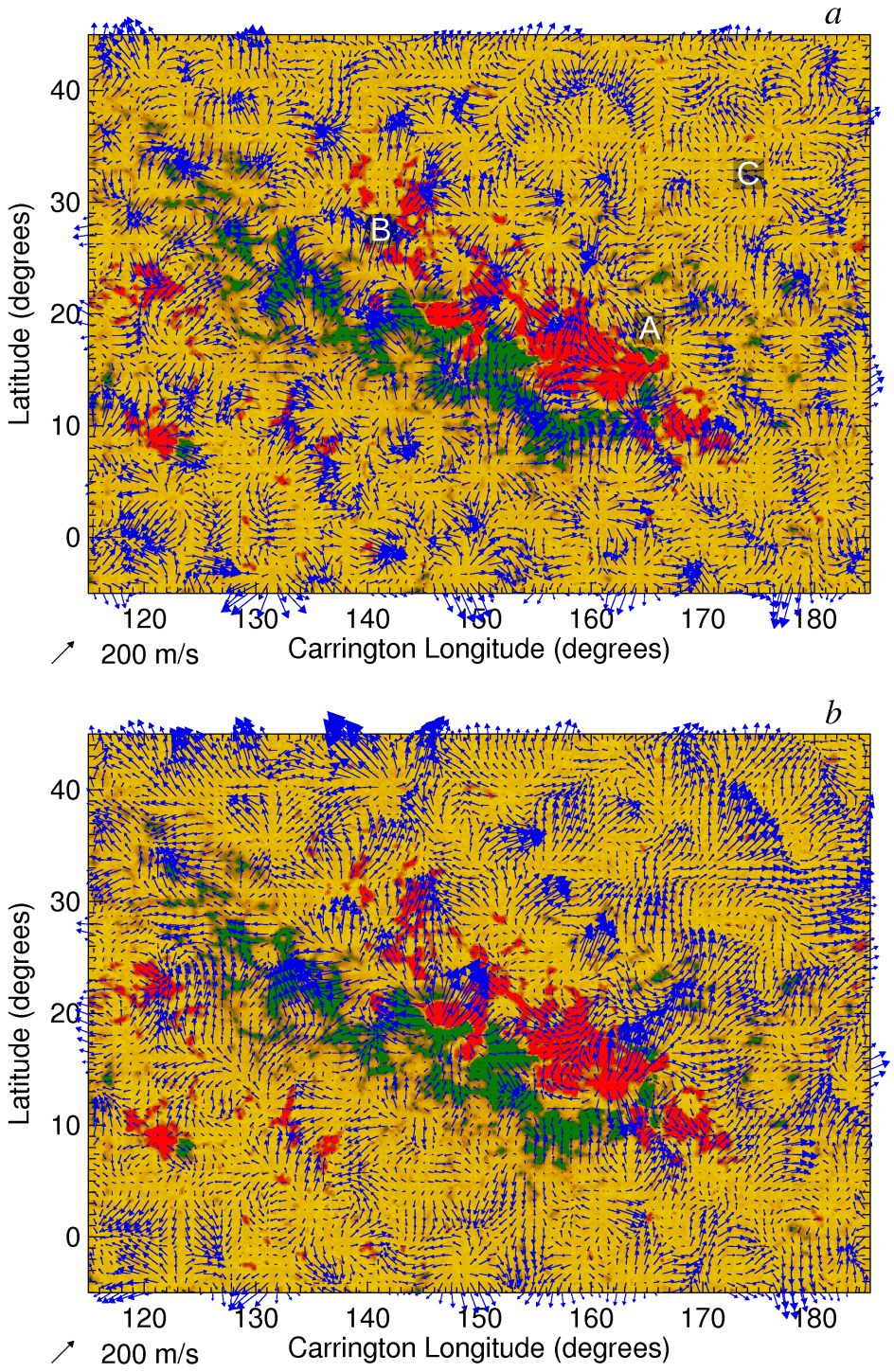

Figure 8.3: Comparison of ARRDI solution to fitted data a depth of 4 Mm using ring-analysis measurements taken on 24 April 2001. (a) Flows as realized through 3-D inversion.(b) Flows as realized by averaging in wavenumber over velocity fits from 4° p_1 measurements. As in Figure 8.1a, White lettering indicates locations of the smaller target regions shown in Figure 8.4. Unlike the comparisons at 1 Mm, flow structures exhibit comparable magnitudes between the two data sets, but differing morphologies.

8.1.2 Comparisons at Depth: Flowmaps and Their Relation to the 4° and 16° Data.

As discussed in §7.2, at the mid-depths of the inversion, the solution is heavily influenced by the 4° measurements. In particular, Figures 7.4*b* and 5.4 suggest that at the 4 Mm depth, the 4° p_1 measurements are primarily responsible for the construction of the solution. In Figure 8.3, we compare the ARRDI flowmap at 4 Mm with one generated by averaging the 4° p_1 measurements over all horizontal wavenumbers. Such a comparison can be more deceptive than those using the f-modes as the solution at this depth cannot be attributed to any one radial mode order. For instance, the 2° p_1 and 4° p_2 measurements may contribute non-negligibly to the solution at 4 Mm as well. Nevertheless, the overall patterning of the convection agrees well between the two flow fields, albeit with some notable exceptions.

One of the more prominent differences between the two flow maps occurs in Region C, shown in detail in Figure 8.4. The presence of the strong northward flow visible in the data is not replicated by the inversion procedure. In this instance, the ARRDI results are much weaker in amplitude and somewhat smaller scale in nature. Agreement between the fits and the inversion results is better in Regions A and B, where the differences are largely associated with the manner in which adjacent regions of converging flow join to one another. However, we note that the 3-D inversion does not see the prominent outflow from the sunspot in Region A (upper right). The Spearman correlation rank coefficients for these two datasets are found to be $\rho_{ew} = 0.54$, and $\rho_{ns} = 0.55$. This is somewhat lower than the f-mode comparisons, but some differences such as this are to be expected as ARRDI incorporates measurements made from modes besides p_1 when generating a solution.

At greater depths we see that the ARRDI results agree well with the 16° OLA inversions. The resulting flow maps are compared at a depth of 14 Mm in Figure 8.5. For the ARRDI results, we have plotted the flow at the target depth of 17 Mm where the center of gravity in depth for the averaging kernels obtained is 14 Mm (see Figure 7.6). The outflow around the active region is replicated well by the 3-D inversion, as are the large-scale westward flows that pass by the northern and southern boundaries of the complex. Velocity amplitudes are somewhat larger in the 3-D results

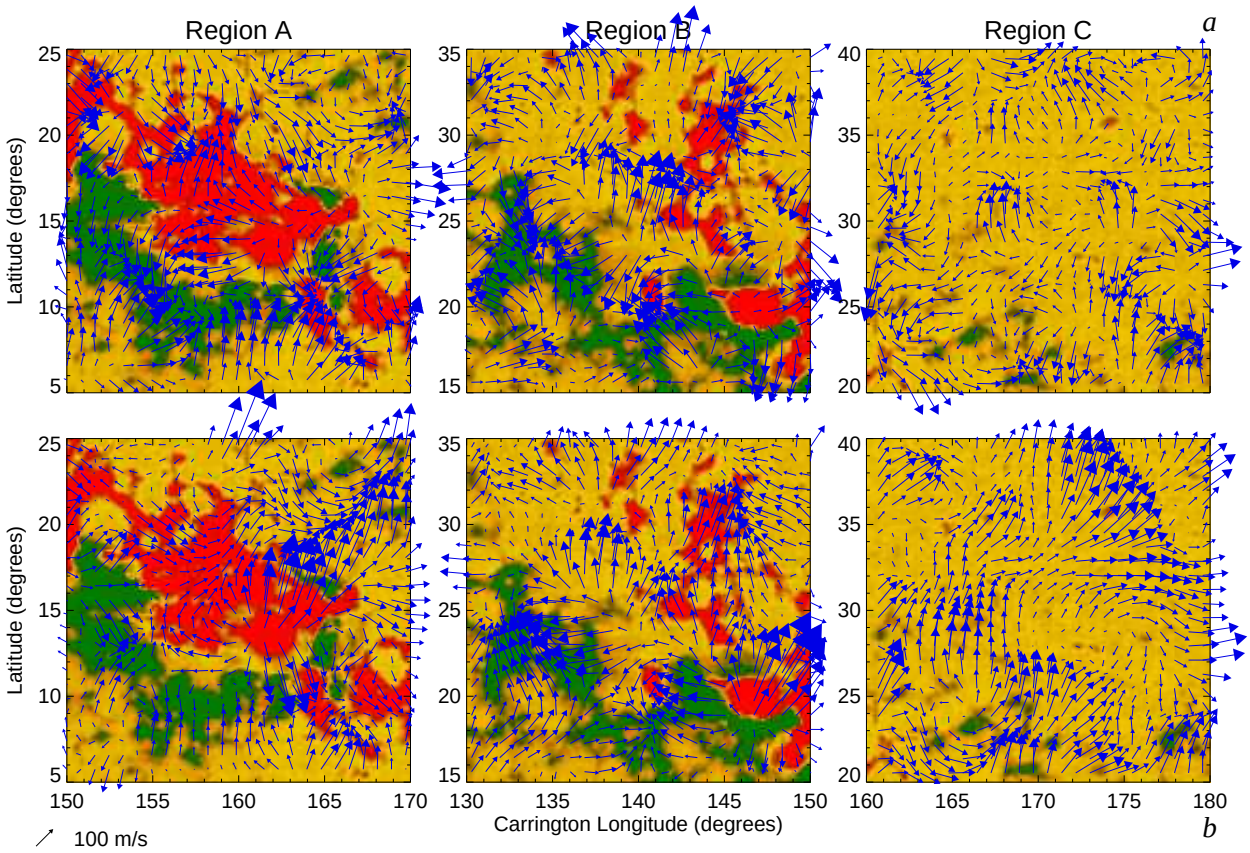

Figure 8.4: Closeups of the regions of interest indicated by white lettering in Figure 8.3 for the (*a, upper row*) 3-D inversion results and the (*b, lower row*) 4° p_1-mode fits. Noticable differences exist between the two analyses, such as the absence in the 3-D inversion of the strong northward outflow from the sunspot in Region A.

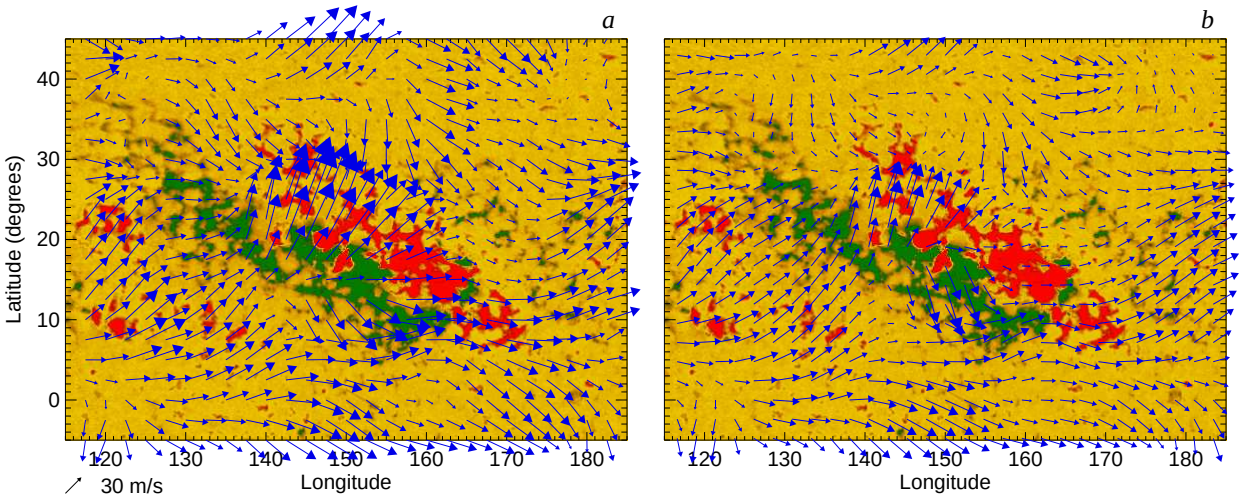

Figure 8.5: Flowmaps at a depth of 14 Mm resulting from (a) the ARRDI algorithm and (b) 1-D OLA inversion of 16° MDI ring data from 24 April 2001. Both solutions exhibit similar outflows around the active complex, suggesting that the 3-D solution at depth is largely determined by the 16° data. The 3-D inversion solution exhibits somewhat stronger flows at this depth, much as in the near-surface solutions of Figure 8.1.

than in the 1-D inversions, and the ARRDI flowmap exhibits smaller scale horizontal structure than that achieved through the 1-D inversions. Here, as with the 2° comparisons, the 3-D inversion has used the horizontal overlap of the measurements to build narrower horizontal averaging kernels, yielding a flowmap with effectively higher resolution and larger resulting velocities. The correlation coefficients here indicate good correlation between the 16° 1-D inversions and the ARRDI results, with $\rho_{ew} = 0.71$, and $\rho_{ns} = 0.80$.

8.1.3 Establishment of Large-Scale Means

The discussion thus far has focused mainly on how the flow fields compare on the smaller and more vigorous scales of convection. What about the large-scale means of these flows? In particular, how do the flow fields obtained through 3-D inversion compare with the 16° scale at that depth when averaged appropriately? In Figure 8.6a, we examine the large-scale means of the ARRDI results at 1 Mm by smoothing the resulting flow map to the 16° scale. We have similarly smoothed the flow map resulting from averaging in wavenumber over the 2° f-mode fits. While

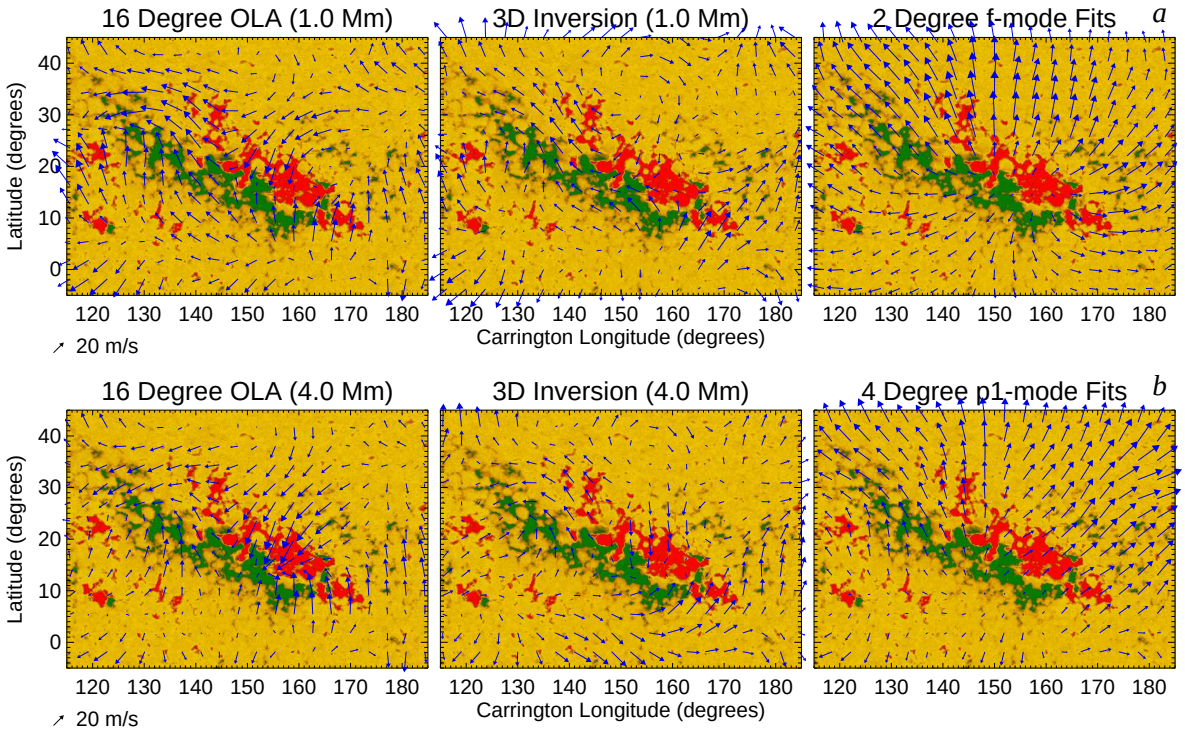

Figure 8.6: Establishment of the large-scale mean flows. (*upper row*) Flowmaps at 1 Mm resulting from 1-D OLA inversions of 16° data, ARRDI results smoothed to the 16° resolution, and smoothed 2° f-mode fits, all using data from 24 April 2001. Inflows into the active complex are reproduced when the ARRDI results are smoothed to the scale of the 16° data. Similar smoothing of the 2° f-mode fits produces an outflow. (*lower row*) Flows obtained at a depth of 4 Mm from 1-D OLA inversion of 16° data, ARRDI results smoothed to 16° resolution, and smoothed p_1 mode fits obtained with 4° data. Similar inflow structures are present in the 1-D and 3-D inversion results. The 4° fits exhibit similar outflows to the 2° fits. Despite the similarities in small-scale structure between the 2° and 4° fits and the ARRDI results, the large-scale means seem to be established by the 16° data.

the non-smoothed ARRDI results agreed relatively well with the 2° f-mode fits at this depth, the large-scale means do not. The 2° fits display a strong outflow at this scale whereas the inversion results clearly show an inflow. This is no doubt due in part to the lack of strong supergranular inflows into the active region and the absence of 2° data at some locations in the active complex. The smoothed 3-D inversion results agree well with the 1-D 16° OLA inversions at this depth, and reproduces the general sense of the inflow into the active region.

Similar behavior in the results is apparent in Figure 8.6*b* where we examine the solutions at 4 Mm and compare with the fits to the 4° p_1 data (which have not been inverted). Once more the fitted data possesses a strong outflow feature when smoothed to the 16° scale that is not shared by the 3-D inversion results. The inflow into the active region found in the ARRDI solution is somewhat weaker than in the 16° results, but is present, as is the northeasterly outflow emanating from the trailing edge of the active complex.

The large-scale means resulting from the ARRDI inversion are thus determined primarily by the 16° measurements, while the small-scale structure generally reflects that of the higher resolution measurements. From examination of Figure 5.4, we see that the typical errors for the 2° and 4° measurements in the upper 4 Mm of the convection zone are on the order of 60 m s^{-1} and 40 m s^{-1} respectively. A mean flow with an amplitude of 20 m s^{-1} such as that of Figure 8.6 is thus well within the errors of the high resolution measurements. The errors on the 16° measurements are substantially smaller, however, with a typicaly value of 10 m s^{-1} at these depths. A reversal of the situation would not work. If the large-scale flows of the solution were set by the 2° or 4° measurements, their 20 m s^{-1} outflow would not agree with the 16° measurements to within their errors. The flowmaps resulting from ARRDI thus represent a multi-scale solution to the inversion problem (Eq. 7.1) that is self-consistent to within the errors of the measurements.

8.2 Sunspot Outflows

Comparisons between 3-D inversions with ARRDI and previous ring-inversion procedures suggest that the ARRDI algorithms yield sensible results. As such we devote the remainder of this chapter to an exploration of ARRDI's potential through its application to flows around sunspots. We focus on sunspots viewed with MDI during January 2002. As with the 2001 data used for comparisons in the previous section, the Sun was highly active during this period, and a number of active regions and sunspots were visible on the disk. One particularly circular sunspot in active region NOAA AR 9787 was observed during this time, and its axisymmetry makes it well suited for the study of average outflows. Outflows around the sunspot in NOAA AR 9787 have been mapped at depth using time-distance by Gizon et al. (2009), and so analyses of this dataset enables the direct comparison between inversion results obtained with ARRDI to those obtained through time-distance.

Our ring-analysis measurements were obtained by tiling the solar disk each day with a mosaic of 16° analysis regions overlapping by 7.5° as described in §5.2. Each of these 16° analysis regions was then further splintered into a similarly structured mosaic of 2° and 4° regions overlapping by 0.9375° and 1.875° respectively. The tiling resolution of these measurements is thus somewhat higher than those used for our initial assessment of ARRDI. We have adjusted the horizontal resolution of our inversion grid accordingly, adopting a horizontal resolution of 0.9375° at the surface. In order to ensure that we gain the full resolving power of the 2° measurements, we maintain this high-resolution down to a depth of 3 Mm before degrading to the resolution appropriate for the 4° measurements. Details of the inversion grid are provided in Table 8.2.

8.2.1 Ubiquitous Sunspot Outflows at Depth

A sampling of the flows and magnetism present during the period spanning 11 Jan 2002 through 25 Jan 2002 (Carrington Rotation 1985) is shown through synoptic mapping of the flows at a depth of 5 Mm in Figure 8.7. This map has been generated by combining full-disk stitched

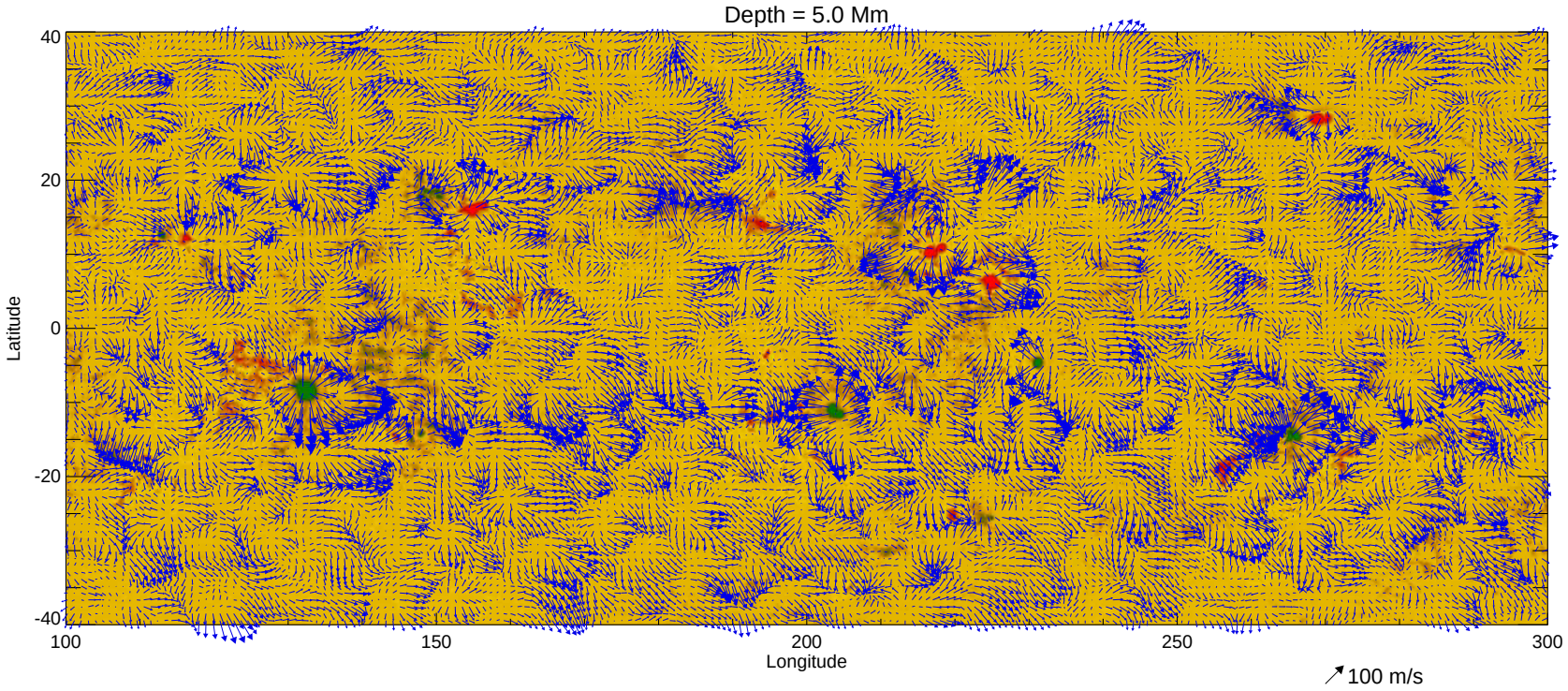

Figure 8.7: Synoptic map of Carrington rotation 1985 spanning the period 11 Jan 2002 through 25 Jan 2002 at a depth of 5 Mm as measured using ARRDI. Daily flowmaps obtained using full-disk stitched inversions were averaged in time over the this period. Each flow vector represents a seven-day average of the flow at that latitude and Carrington longitude. Sunspots, visible as dark green and red spots on the map, are home to strong 100 m s^{-1} outflows. The torsional oscillations are visible at this depth as strong longitudinal flows in the activity belts.

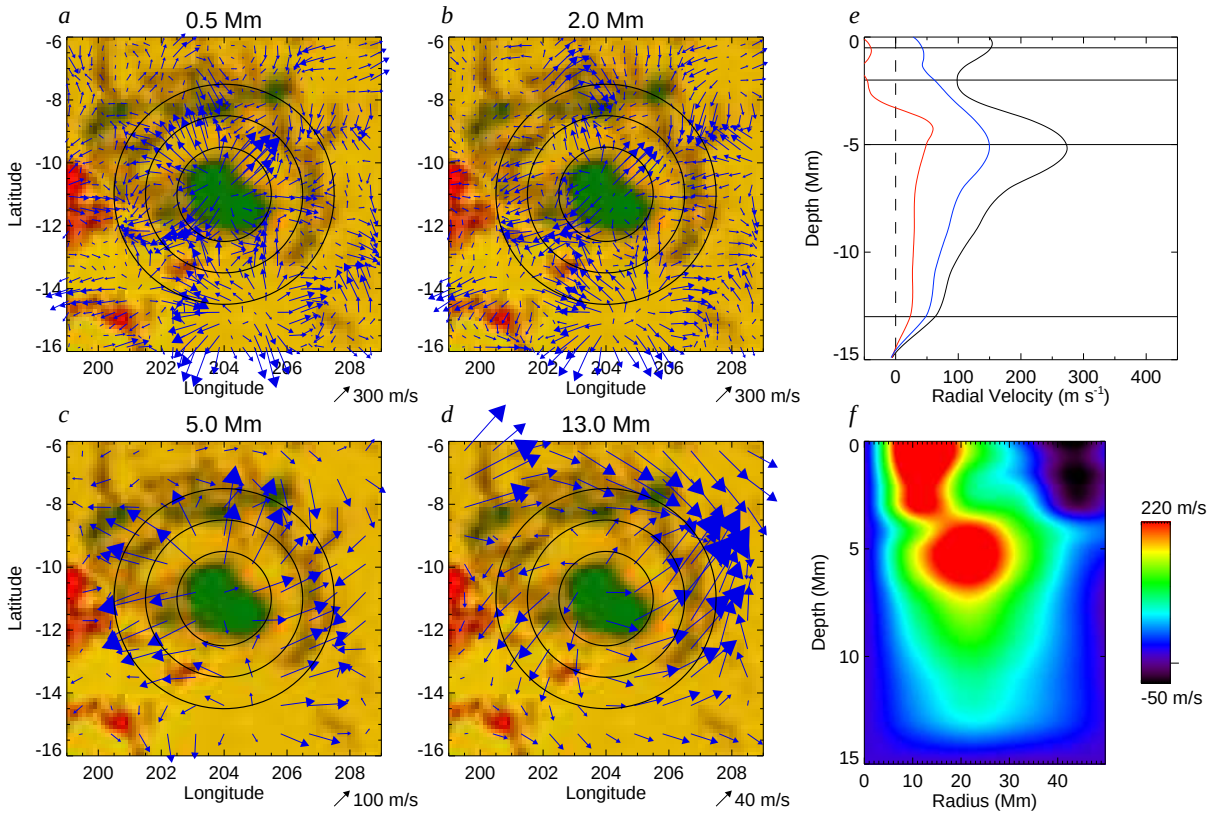

Figure 8.8: The depth variation of a sunspot outflow. (*a-d*) Horizontal flow beneath NOAA AR 9783 on 17 Jan 2002 at four representative depths as determined with ARRDI. Concentric circles indicate radii of 18, 30, and 42 Mm relative to the sunspot center. (*e*) Depth variation of the radial outflow (shown positive), averaged in angle around the sunspot center, is indicated at radii of 18 Mm (black), 30 Mm (blue), and 42 Mm (red). Solid horizontal lines correspond to the depths indicated in *a-d*. (*f*) 2-D view of the sunspot outflow with radius and depth. 150 m s^{-1} outflows are visible at the surface and diminish in strength around 3 Mm. Outflows increase to 350 m s^{-1} around 5 Mm before decaying steadily with depth. The sunspot outflows decay steadily with distance at all depths. A near-surface inflow is visible at the perimeter of the surface moat flow. Flow fields have been interpolated by a factor of two in all cases for ease of viewing.

TABLE 8.2
Inversion Grid For Sunspot Inversions

Target Depth (Mm)	Horizontal Resolution (degrees)
0.0	0.9375
0.5	0.9375
1.0	0.9375
1.5	0.9375
2.0	0.9375
3.0	0.9375
4.0	1.875
5.0	1.875
6.0	1.875
7.0	1.875
9.0	1.875
11.0	1.875
13.0	1.875
17.0	3.75
19.0	3.75
22.0	3.75
25.0	3.75

Table 8.2: Target depths and horizontal resolution of the inversion grid for the 3-D inversions of sunspots from CR 1985.

inversions for each day and averaging the flowmap from multiple days at each Carrington longitude. The Carrington grid rotates 15° per day, and when viewed in this manner, each vector represents a 7-day average of the flow. Flows with a horizontal scale of 4° are most readily visible in this flow map, and a distinctive feature of sunspots at this depth (visible as dark concentrations of red or green in the magnetogram), are their 100 m s^{-1} outflows.

A detailed view of the subsurface outflow beneath a typical sunspot (in NOAA AR 9783) from this rotation is illustrated in Figure 8.8. Flow maps at four representative depths ranging from the near-surface down to 13 Mm are shown in Figures 8.8*a*-*d*. Reference circles are plotted at radii of 18 Mm, 30 Mm, and 42 Mm with respect to the sunspot center, and the radial outflows (averaged in angle about the sunspot) are plotted in Figure 8.8*e*. Near the center of the sunspot, 100-200 m s^{-1} outflows are present at all depths, diminishing in strength with distance from the sunspot center. In these near-surface layers, the most distinctive convective patterns are roughly 3° (36 Mm) in horizontal extent, and so it is likely that we are sampling the largest supergranular

cells of convection. These cells extend across the outer reference circle at 42 Mm, contributing to the net inflow observed in the upper 4 Mm at that radius (Fig. 8.8*e*, red line).

An interesting feature of the NOAA AR 9783 sunspot is the apparent presence of two components to the subsurface outflow. This is most visible in Figure 8.8*f* where the average outflow is shown with depth and radius. The outflow is characterized by a near-surface component which decays with radius much more quickly than a deeper component which peaks around 5 Mm. The transition between these two flow components occurs around 2 Mm. We see from Figure 8.8*b* that flows at this depth are similar in morphology to those near the surface, but that they are weaker overall than the near-surface flows. The presence of a deep outflow, more expansive in radius than the surface moat flow, seems to be a robust feature of the sunspots in this time interval. Further examples of this behavior are provided in Figure 8.9. The deep outflow is not always stronger than the surface moat flow at the 18 Mm radius in these examples, but it is the dominant component of the flow at a distance of 30 Mm in most instances.

The weakening of the surface outflow occurs at a depth where reliable fitting of the 2° measurements becomes difficult. It is thus somewhat unclear if this diminishment is real or is in fact an artifact of the effective transition in the horizontal resolution of the measurements from 2° to 4° at this depth. We also note that the transition region between the two components lies close to the depth where the horizontal resolution of our inversion is degraded by a factor of 2. However, we have run several inversions varying the location of this transition and find similar results. Thus while we cannot rule out the existence of an averaging effect resulting from the measurement procedure, it seems unlikely that this two component structure is an artifact of the inversion grid resolution.

8.2.2 Temporal Evolution of Sunspot Outflows

These subsurface outflows exhibit time variability as their associated sunspot evolves as well. The time-evolution of the sunspot in NOAA AR 9783 is illustrated in Figure 8.10. Flow vectors at a depth of 7 Mm overlay a magnetogram in the upper row of Figure 8.10 and the radial outflow is

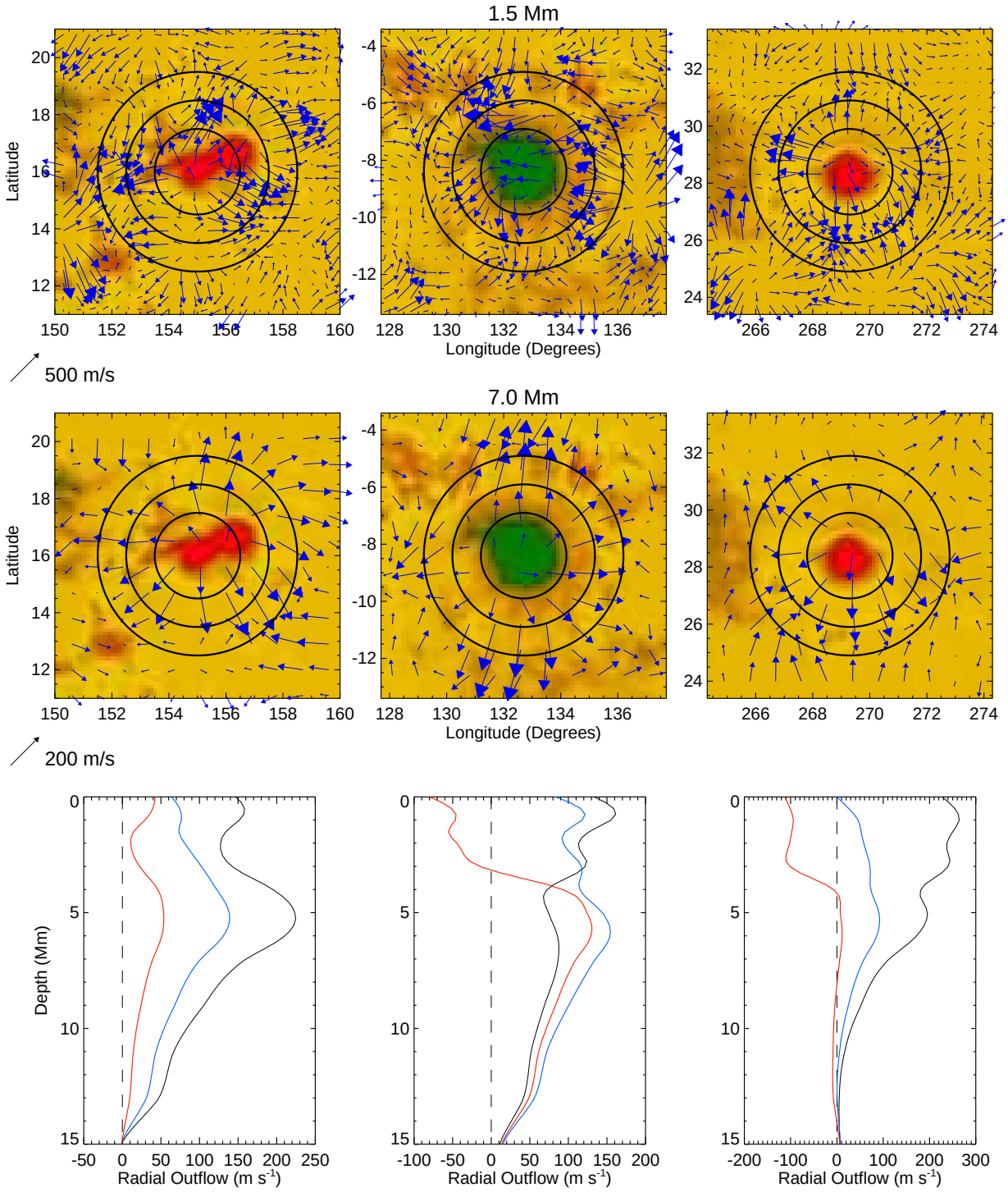

Figure 8.9: Sampling sunspots outflows in CR 1985 for three sunspots as they crossed the central meridian of the disk. Outflows at radii of 18, 30, and 42 Mm are indicated as in Fig. 8.8. Zero outflow is indicated by the dashed line. (*left column*) Flows beneath NOAA AR 9788 on 22 Jan 2002 possess surface and deep outflows similar in nature to that of NOAA AR 9783 in Fig. 8.8, with a diminishment near the 3 Mm depth. While many of the spots we have examined possess these dual outflows, not all do so. (*central column*) The sunspot NOAA AR 9787 (23 Jan 2002) exhibits a less simple outflow structure, and (*right column*) that of NOAA AR 9779 (13 Jan 2002) decays more or less steadily with depth.

plotted for each day in the lower row. This particular sunspot exhibits a fairly persistent outflow as it rotates across the disk. The near-surface and deep components of this flow wax and wane with time, as does the near-surface inflow which is always visible at the 42 Mm radius. With the possible exception of the first day in the series, the deep outflow persists at greater distances than the near-surface outflow for all days.

We have also used ARRDI to follow the evolving flow of a much shorter lived sunspot, this one in NOAA AR 9788 , as it emerges near the western limb and disrupts just before rotating off the eastern limb. A seven-day time series of the emergence and disruption is provided in Figure 8.11 where vector maps illustrate the flows at 5 Mm in depth. Some hint of an outflow is present on 19 Jan just as the spot emerges, with a much more prominent outflow developing on the second day (20 Jan). The development of the outflow appears to emanate from the surface and the interior of the spot before developing into the more familar two-component structure on the third day. This two-component structure persists for a total of three days before the sunspot begins to decay, with the decay of the surface moat flow apparently preceeding that of the deeper outflow (24 Jan).

8.2.3 Sunspot Outflows as Revealed through ARRDI and Time-Distance Inversions

The sunspot in NOAA AR 9787 was the focus of time-distance investigations reported on in Gizon et al. (2009). Outflows measured with ARRDI beneath NOAA AR 9787 will thus allow a comparison between these two techniques. We have averaged the radial outflows beneath the sunspot in NOAA AR 9787 over the six days spanning 20 Jan 2002 through 25 Jan 2002. A similar temporal averaging of the outflows beneath this spot was performed in Gizon et al. (2009). The time-distance analyses were performed using the f-mode ridge, and the p_1 through p_4 ridges. Center-to-quadrant travel times were then measured and inverted using an OLA scheme to recover the east-west and north-south flows. These were in turn averaged in azimuth about the sunspot to yield the radial outflow. Further details can be found in Gizon et al. (2009).

The results of the time-distance inversions at four depths are shown in Figure 8.12*a*, along with those measured using moving magnetic features (MMF, dashed line). Results obtained from

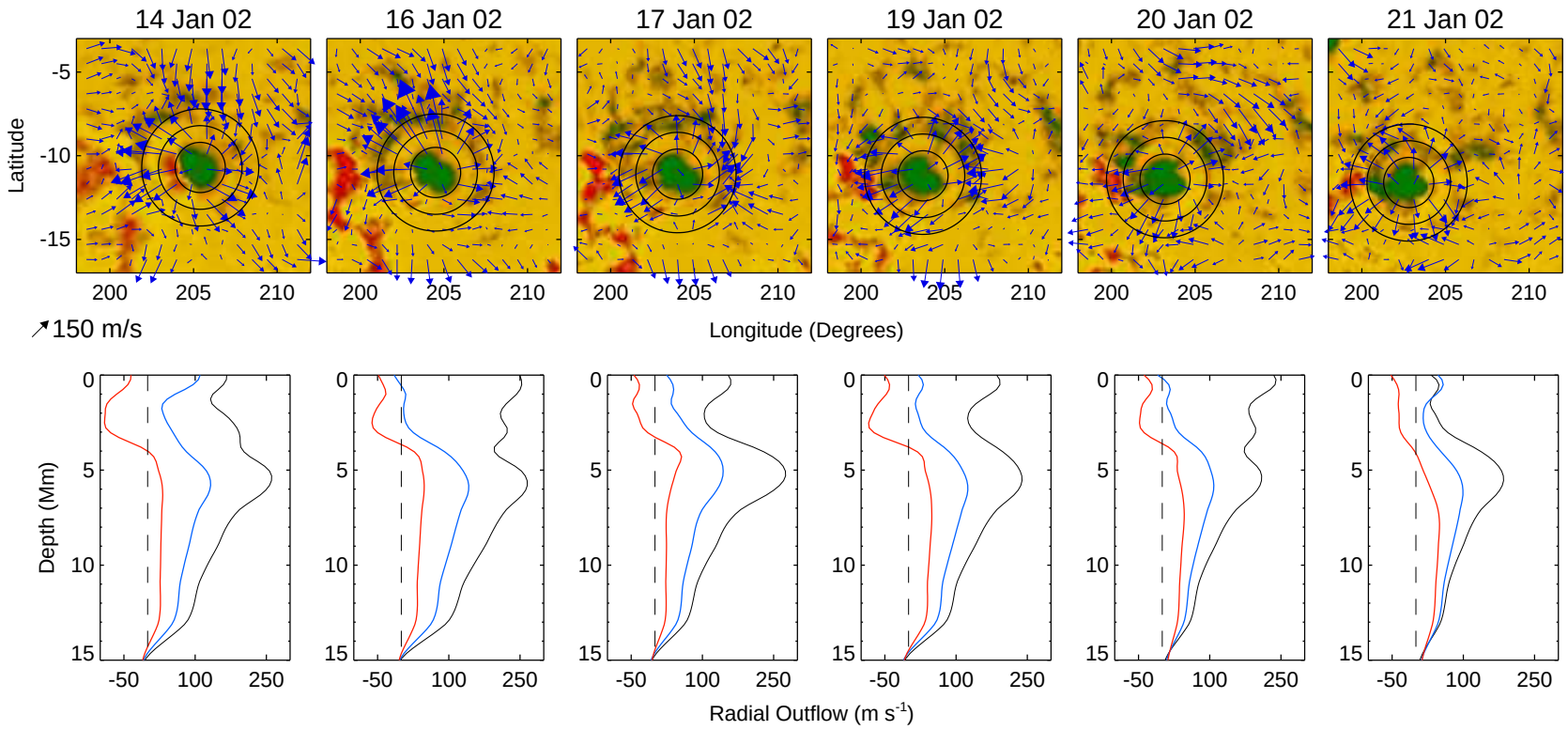

Figure 8.10: The slow evolution of a persistent sunspot. (*upper row*) Horizontal flow beneath NOAA AR 9783 at a depth of 7 Mm as determined using ARRDI. Concentric circles indicate radii of 18, 30, and 42 Mm relative to the sunspot center. (*lower rower*) Radial outflow averaged in angle about the sunspot center for radii of 18 Mm (black), 30 Mm (blue), and 42 Mm (red). A zero outflow is indicated by the vertical dashed line. This particular sunspot exhibits a surface moat flow and a deeper outflow during all six days over which it was observed. The deep outflow at 6 Mm attains an amplitude of 250 m s^{-1} before declining steadily with time. The surface flow waxes and wanes in strength over the course of six days, diminishing in strength during the last day in the series.

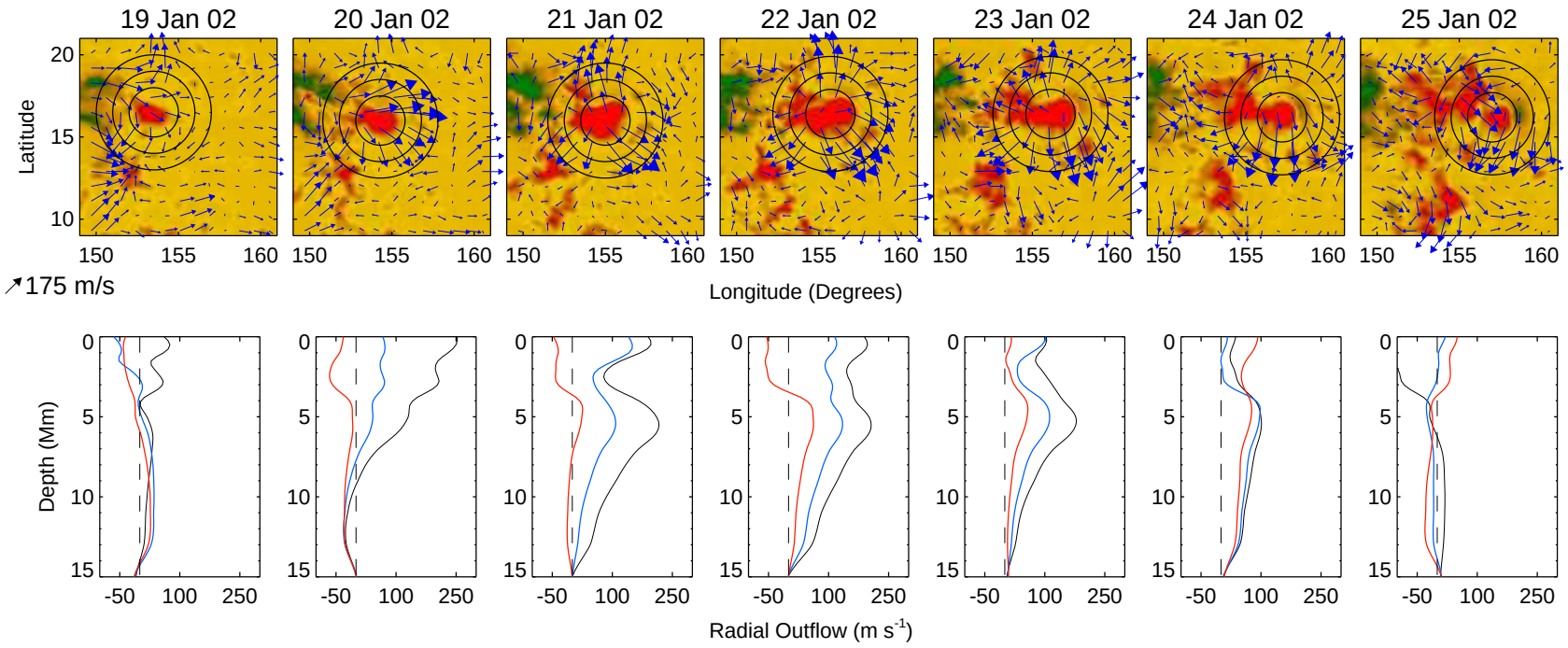

Figure 8.11: Emergence and disruption of a sunspot. (*upper row*) Flows beneath NOAA AR 9788 at a depth of 5 Mm as determined with ARRDI. As with Fig. 8.10, concentric circles are plotted at 18, 30, and 42 Mm from the sunspot center. (*lower rower*) Average radial outflows at each of the radii, with 18 Mm indicated in black, 30 Mm in blue, and 42 Mm in red. No significant outflows are apparent initially. Strong outflows develop on 20 Jan that decrease in strength with depth. A two-component structure is attained on 21 Jan, and the sunspot persists for three days before decaying. Outflow profiles during the final three days suggest that the surface moat flow dissipates prior to the disappearance of the deeper outflow at 5 Mm.

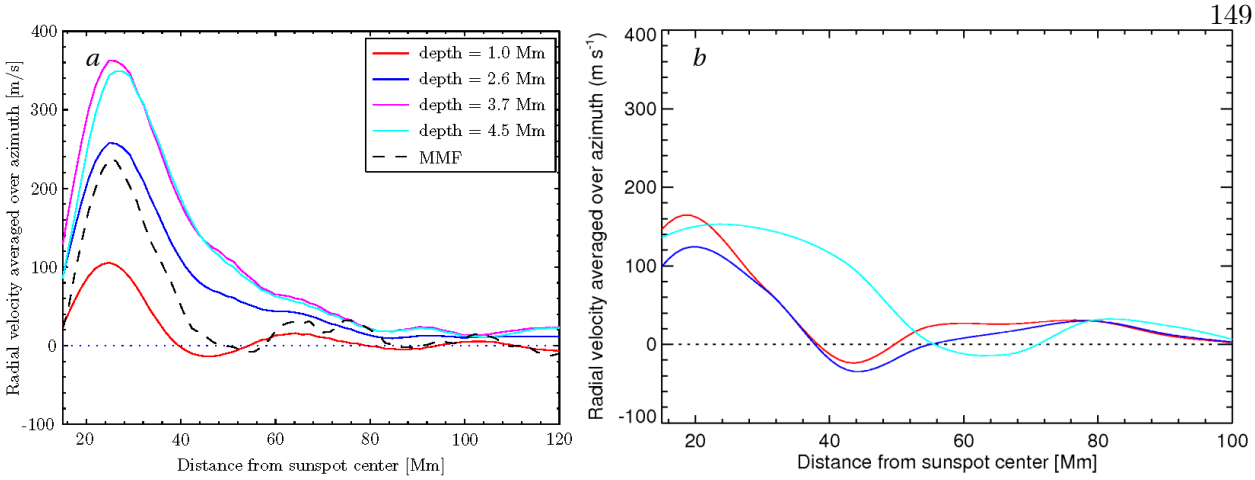

Figure 8.12: Comparison of outflows beneath NOAA AR 9787 as revealed through time-distance helioseismology and ring analysis. (*a*) Subsurface outflows measured with time-distance at various depths (indicated) in the upper 5 Mm of the convection zone. (Adapted from Gizon et al. 2009) (*b*) Outflows as measured with 3-D inversion of ring-analysis measurements using ARRDI. Coloring for the different depths is the same as in (*a*). Time-distance results indicate a steady increase in the strength of the outflow down to a depth of about 5 Mm, whereas results from ring-analysis indicate a diminishment of the outflow at 2.6 Mm before increasing again at 4.5 Mm.

ring analysis using ARRDI are displayed in Figure 8.12*b*. We see good agreement between the surface moat outflow (1 Mm, red line) as measured by both techniques. The moat flow in the surface layers peaks around a radius of 20 Mm and extends to about 40 Mm for both inversions. The inflows beyond 40 Mm are similar in strength at this depth, but the peak values of the moat flow are somewhat higher for the ring-analysis measurements than those achieved using time-distance.

Deep below the surface, there are considerable differences in the variation of the outflow with depth between these two approaches. At a depth of 2 Mm (dark blue), the time-distance results suggest that the moat outflow increases in strength relative to the surface, and the inflow at 40 Mm in radius disappears. Here, the ARRDI results differ and indicate that the outflow weakens in strength at this depth, while the inflow remains visible. An outflow persists to 4.5 Mm in depth in both sets of results, though the outflow as measured with ARRDI is still weak relative to its surface values. The time-distance results seem to indicate that the strength of the outflow increases with depth and do not hint at the presence of a two component outflow such as in the ARRDI inversions of NOAA AR 9787 and other sunspots from CR 1985. The ARRDI results thus agree

with those obtained from time-distance in that outflows are realized at all depths, but there are distinct differences in the depth dependence and amplitude of these outflows.

8.3 Further Reflections on 3-D Inversions with ARRDI

ARRDI holds distinct promise as a versatile tool for probing flows in the upper-convection zone. Flow maps obtained with ARRDI exhibit good agreement with those from previous ring analysis studies at depths where it is sensible to compare them. Particularly encouraging is the ability of ARRDI to compensate for missing data from one tile-size (usually the 2° tiles) through the use of lower resolution measurements when available. This is useful for establishing large-scale mean flows in the near surface layers where noisy high-resolution measurements and missing data (such as in regions of magnetic activity) can otherwise lead to artifacts in the inferred large-scale flows. As a "first light" application of ARRDI , we have examined the subsurface outflows around sunspots and found that many spots from CR 1985 possess subsurface outflows with a distinctive two-component structure.

The discovery of this structure is surprising in part for its disagreements with the time-distance results of Gizon et al. (2009), which suggest that the outflow should monotonically increase with depth. However, we are encouraged overall, rather than discouraged, by the comparison between ARRDI and the time-distance results. Both approaches show that some form of outflow persists to the 5 Mm depth, and we are not troubled by the overall amplitude differences between the two approaches (ring-analyses show weaker flows overall). Our RLS approach necessarily trades off between a good fit to the data and a smooth solution. By smoothing more or less (i.e. by varying the regularization parameters), the amplitude of our recovered solutions tends to vary as well. For instance, we have found qualitatively similar outflow structures, but with a velocity amplitudes more in accord with the time-distance results, by decreasing the vertical regularization from $\lambda_v = 0.1$ to $\lambda_v = 0.01$.

A detailed comparison between the time-distance and ARRDI inversions is difficult without knowledge of the averaging kernels realized in the time-distance inversions. These kernels were

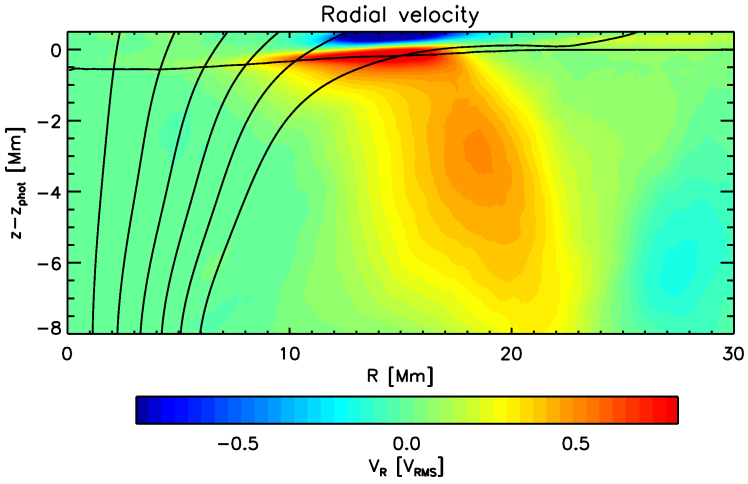

Figure 8.13: Sunspot outflow as realized through 3-D numerical simulations. Red tones indicate outflow from the sunspot, and blue tones indicate inflow. Black lines denote azimuthally averaged flux surfaces of the sunspot's magnetic field. The flow is seen to possess three components, the Evershed flow (red), a superficial moat flow (yellow-far upper right), and a deeper more extended outflow (orange) underlying the penumbra. The deeper outflow is reminiscent of those measured using ARRDI (see Fig. 8.8). Adapted from Rempel (2011).

not reported in Gizon et al. (2009), but averaging kernels obtained through time-distance with OLA are undoubtedly different from those obtained through ring analysis with RLS. Differences in the vertical widths alone could easily lead to differing outflow profiles. For instance, sufficiently broad (in the vertical) averaging kernels around the 2-3 Mm depth for the time-distance inversions could wipe out the two-component structure we have observed. Moreover, the presence of magnetic fields can confound the interpretation of results obtained using either ring-analysis or time-distance helioseismology through a tendency to absorb acoustic power and introduce phase shifts into the wavefield (e.g. Braun et al. 1987; Cally et al. 2003, Lindsey & Braun 2005*a*). The sensitivity kernels employed in ring analysis and time-distance methods do not account for these effects. Bearing these considerations in mind, we suggest that ARRDI yields results that are largely consistent with those deduced using time-distance helioseismology.

We conclude by noting that the two-component structure we observe in outflows beneath sunspots is remarkably reminiscent of sunspot outflows found through 3-D numerical MHD simu-

lations of a bundle of magnetic flux introduced into the near-surface convection and atmosphere of the Sun (Rempel 2011). These simulated outflows, which arise naturally from the blockage of heat transport by the magnetic field, are detailed in Figure 8.13 and appear to possess a multi-component flow structure of their own. The surface moat flow (light yellow region near 30 Mm) decays with depth before joining to a second outflow around 4 Mm. The depth variation of these simulated outflows is similar to that observed with ARRDI, but the deep outflow seen by Rempel (2011) seems to decay more quickly in radius from the spot than does the surface moat outflow. This contrasts with our observations of a deep outflow that extends further in radius than the surface inflow. We caution that we have only analyzed a handful of sunspots using ARRDI and that a much larger sample is needed to establish whether these two-component outflows truly are a robust feature of sunspots.

Chapter 9

Reflections and Future Directions

9.1 Convective Cores and Primordial Magnetic Fields in A stars

Our explorations of dynamos in A-type stars have revealed that the deep interior cores of these stars can attain two remarkably different dynamo states, characterized by equipartition magnetic field strengths on the one hand, and super-equipartition magnetic fields on the other. We have found that one route to transitioning from the first to the second state involves the presence of a large-scale ordered magnetic field in the radiative zone with some linkage to the core. The possible existence of a primordial magnetic field in the radiative zones of the Ap stars was our primary motivation for the inclusion of such a magnetic structure. Our initial field was thus twisted and largely toroidal in nature, but we found that the transition to a super-equipartition state did not require such a specific geometry. It appears instead that the transition between equipartition and super-equipartition behavior is a robust response to the presence of an organized poloidal field structure linking the radiative zone to the core. The existence of such a strong dynamo state in the cores of these stars raises a number of interesting questions regarding the limits of magnetic field strengths achievable, as well as the effects of such strong dynamo states on other stages of evolution of these stars.

9.1.1 Possible Magnetic Buoyancy Instabilities

The discovery of such strong magnetic fields in our simulations raises the question of whether magnetically buoyant fields might be achieved in the cores of the A stars. The super-equipartition

dynamo realized following the imposition of our fossil magnetic field has displayed a tendency for building strong toroidal bands of magnetic field which are roughly 300 kG in strength in some regions. We have not observed the buoyant rise of these magnetic fields, but there are diffusive limitations within our model which bear on the formation of strong magnetic fields in the radiative zone and their ability to rise.

As our models are large-eddy simulations, the magnetic diffusivities that we have adopted are quite high with respect to what might be expected in the deep interior of an A star. In particular, the diffusion times across the radiative envelope of the star in our simulations are several thousand days. This time is several orders of magnitude shorter than the realistic values. What might be the effect of substantially lower diffusivities in our system? The ramifications for the convective core dynamo are unclear.

Decreasing the magnetic diffusivity can certainly limit the diffusive destruction of magnetic energy in the core and permit the development of much finer structuring in the magnetic field topology than what is realized in our current simulations. However, the strength of the magnetic fields in our super-equipartition state appears to be set by a magneto-geostrophic balance within the core, in which the pressure, Coriolis, and Lorentz forces largely balance one another. Can magnetic fields strong enough to break this balance arise in the core? This may not be necessary to attain buoyant magnetic fields in the radiative zone.

Magnetic field strengths in the radiative zone are largely determined through a balance between the deposition of magnetic fields by overshooting motions and the slow decay of these fields through diffusive processes. The potential for our super-equipartition dynamo to generate magnetically buoyant fields in regimes with lower magnetic diffusivities may thus be interesting as a further avenue of study. Recent modifications to ASH have allowed us to begin simulating convection in stars while employing a slope-limited diffusion scheme. Such schemes permit much lower diffusivities than those achieved currently using ASH, but complicate things somewhat in that the diffusion is spatially variable, determined by the local gradients of the flow and magnetic field. Assessing a representative magnetic Prandlt number for such a system can thus be difficult. However, it would

be fascinating to observe magnetic buoyancy in the radiative envelopes of these stars, and we plan to pursue further simulations using lower diffusivities and more extensive radiative envelopes (to capture any buoyant rise of magnetic field) in the near future.

9.1.2 Convective Overshooting With and Without Primordial Fields

An interesting aspect of core convection is that the convective motions occur in the presence of nuclear burning. Convective overshooting into the overlying radiative envelope may then mix the products of nuclear burning from the core into the lower radiative zone, returning fresh hydrogen to the core in the process. Such a replenishment of the nuclear fuel supply holds potential for extending the main-sequence lifetimes of massive stars. The efficiency of the large-scale motions accessible to ASH in assisting such refueling might be assessed by adding a second chemical species to the ASH equations. This would constitute a straightforward modification to the ASH code, though large disparities between the diffusion rates of H and He may severely limit the time stepping. Nevertheless, an interesting extension of the mixing problem would be to compare the mixing efficiencies obtained by convective motions from an equipartition dynamo to those realized in the presence of the super-equipartition magnetic fields. *If* the presence of a strong primordial magnetic field (likely the distinguishing characteristic between the Ap and normal A stars) does lead to a large-scale dynamo in the convective core, then differences in the mixing effiencies might imply disparities in the main-sequence lifetimes of the Ap stars and the normal A stars.

In principle, such differences could be probed observationally by examining the relative ages of Ap and normal A stars in open clusters. Pinning down the ages of Ap stars has been difficult until recently since many of the known Ap stars are field stars, and the known cluster stars are typically very faint. However, serious progress has been made in recent years to identify and catalogue cluster Ap stars (Bagnulo et al. 2006; Landstreet et al. 2007; 2008). By constraining the ages of cluster Ap stars, these surveys have been able to demonstrate (for example) that Ap stars exhibit less surface magnetic flux as they near the end of their main-sequence lifetimes (Landstreet et al. 2007;2008). However, no comparison between the apparent ages of the normal A and the Ap stars

within a cluster has yet been conducted.

An alternative approach might be to assess the relative number of Ap-descended giant stars within a cluster. Distinguishing between the two can be difficult, but some red giants have been observed to possess chromospheric activity which is more intense than what might be expected for their mass and rotation rate (e.g., Strassmeier et al. 1999; Aurière et al. 2008), and it has been speculated that these inferred magnetic fields are primordial, rather than dynamo in origin. Abundance peculiarities, though of a different sort than in the main-sequence Ap stars, may provide a more reliable means for distinguishing between giants of peculiar and normal descent. As discussed in Charbonnel & Zhan (2007) the presence of strong magnetic fields in the 10^4 to 10^5 kG range might suppress thermohaline mixing in the descendants of Ap stars. This mixing mechanism, driven by a μ-gradient instability, is thought to link the deep hydrogen burning shell of red giants to the outer convective envelopes. Its absence in the giant descendants of the Ap stars (owing to their presumably strong magnetic fields) may lead to a perceived overabundance of C and Li on the surfaces of these stars.

9.1.3 Primordial Magnetism and Dynamos in Pre-Main Sequence Stars

One of the untouched questions of primordial magnetic fields inside massive stars concerns the effects of a fully convective Hayashi phase that these stars are thought to undergo on their journey to the main sequence. Does a dynamo operate during the fully convective phase, and if so, how does a pre-existing magnetic field alter its characteristics? Some sense of this is gained through the simulations presented in Chapter 2-4, but a fully convective sphere lacks the radiative envelope present in a main-sequence A star. The importance of the radiative envelope for attaining strong and global-scale magnetic fields in our simulations is difficult to discern, but it undoubtedly plays some role in the magnetic "memory" of the system. Overshooting motions deposit broad swaths of magnetic field into the lower radiative zone before diving back towards the deep core, revisiting their past works with each new overturning motion. The effects that a large-scale primordial magnetic field in the 10 kG range might have on a fully convective dynamo with no such reservoir for the

magnetic field are thus unclear.

The discovery that the Ae stars, the presumed pre-main sequence (PMS) progenitors of the Ap stars, exhibit a preference for slow rotation even before their arrival on the main sequence (e.g., Alecian et al. 2008; Wade et al. 2009) hints at the importance of the fully convective phase in understanding the angular momentum loss of these stars. The nature of the differential rotation and the convectively driven dynamo in this phase will undoubtedly impact the pre-main sequence spindown through their interaction with a stellar wind. Moreover, the magnetic field remaining after the convective envelope has receded will ultimately serve as the seed magnetic field for the convective-core dynamo. Does the primordial field maintain its twisted, toroidal shape throughout the fully convective phase? Is it amplified or augmented in some fashion, or is the role of turbulent convection in this regime instead to expedite the decay of the field? The destruction or amplification of a primordial field in this stage may bear on why only 10% of the A stars are magnetic (and peculiar).

Primordial magnetic fields may play a role in the early evolution of less massive stars as well, notably the the T Tauri stars. The majority of these stars are thought to be fully convective and exhibit surface fields of a few kG. Such strong magnetic fields are almost certainly generated by a dynamo operating in the midst of this convection as strong flaring observed on many of these stars suggests that magnetic fields are undergoing constant reordering at the stellar surface (e.g., Gregory et al. 2010). And yet, the observations of magnetic fields in the fully convective T Tauri stars suggests that they are predominantly large-scale and dipolar in nature. How are such strong coherent magnetic fields generated in the presence of vigorous convection?

Any attempt at modeling these stars with ASH would necessarily have to ignore the circumstellar accretion disk, and a possibly important contributor to the angular momentum balance within the star in the process. Nevertheless, it is interesting to ask what effects a primordial magnetic field may have on dynamos in other stars in the early stages of their evolution. In a broader sense, what sort of dynamos might operate in pre-main sequence stars? Are these fully convective objects characterized by the sweeping global-scale motions found in simulations of the A stars, or

are they more like the convective M-dwarfs, where vigorous small-scale convection occurs in the outer layers, with much weaker but larger scale motions comprising the deep interior (e.g., Browning et al. 2008). Models of pre-main sequence stars, both of the massive and less massive varieties, may be interesting to pursue with ASH. ASH provides the capability of pursuing dynamo calculations within the full spherical geometry and may be a useful tool for assessing how the global-scale magnetic fields observed on some PMS stars are generated. However, we acknowledge that certain complicating factors may arise when simulating convection in the early stages of stellar evolution. The presence of an accretion disk or the slow gravitational contraction of the star, for example, would certainly require some careful treatment if we are to assess the flavor of the dynamos in these stars using ASH.

9.2 Possible Further Improvements to 3-D Inversions with ARRDI

ARRDI was designed with implementation into the HMI data analysis pipeline in mind, and adapting the ARRDI algorithms to HMI data is straightforward in many respects. However, exploiting the full potential of ARRDI requires that similar assessments of the measurement errors and measurement success rates are performed using HMI data as were done with MDI. These assessments are crucial for deciding upon a sensible inversion grid. HMI has a fourfold increase in resolution over that currently achievable using MDI and will return Dopplergrams with a cadence of 45 s vs the 60 s used with MDI. This increased spatial and temporal resolution will undoubtedly affect the noise characteristics of the power spectra and the errors realized when performing ring analyses.

The increased horizontal resolution attainable with HMI may also allow ring analyses to be performed on smaller tile sizes such as 1° or possibly even 0.5° in horizontal extent. The radial orders accessible to ring-analysis fits of these smaller tiles (and hence the depths to which the inversions might reach) are currently unknown. Based on the success rates associated with fitting the 2° data, it seems safe to assume that at least a few f-modes might be fit, thus allowing us to probe the surface layers with a higher resolution. It remains unclear if HMI will permit the fitting

of modes with higher radial order (and thus more depth penetration) than is currently possible when using MDI data. However, efforts are now underway to develop a fitting procedure that measures the Doppler shifts of multiple ridges simultaneously (D. Haber, private communication). In particular, fitting in this manner may enable the measurement of modes beyond the p_1 ridge for the 2° tiles. Finer horizontal resolution, both near the surface and at depth, thus seems possible in the near future. There are a few adjustments that might be made to the ARRDI algorithms and to the sensitivity kernels in order to fully exploit this capability.

9.2.1 Obtaining Optimal Horizontal and Vertical Resolution

It is interesting to ask if the horizontal resolution of the ARRDI inversion grids (using 2°, 4°, and 16° measurements) might be improved. The effective horizontal resolution of the inversion grid, which is manifest in the narrowness of the averaging kernels obtained, is intimately related to the measurement tile size and the nature of the overlap between the tiles. What is the optimal tiling scheme? We have seen that for 4° measurements, ARRDI tends to produce averaging kernels with a width of about 2° and with small negative sidelobes. These sidelobes stem from the manner in which the inversion algorithm combines measurements. The solution at some target location is typically generated by subtracting measurements made at neighboring points from measurements centered on that target point. The resulting averaging kernel is constructed by adding and subtracting the associated sensitivity kernels in a similar fashion, yielding a central peak with small negative sidelobes in the horizontal.

A narrower central peak can in principle be produced by increasing the tiling density of the measurements. However, as the overlap of neighboring measurements is increased, the wavefields they sample are largely the same. These RLS inversions operate on the implicit assumption that the measurements and their errors are independent of one another. This overlap can lead to correlations in the errors which should be taken into account for the more densely packed measurements, and possibly for the current measurements which overlap by half of the analysis region size. In a similar vein, one might assess the optimal combination of tiling schemes and measurement resolutions.

Currently the 16° measurements are always centered on a 4° measurement, which is in turn centered on a 2° measurement. Are there advantages to be gained in the averaging kernels by staggering the different measurement grids with respect to one another? A study of these tiling scheme issues could be useful for optimizing both the time required to generate the measurements and the time required to perform the inversion.

Finally, we have yet to perform a systematic study of the optimal vertical gridding used in ARRDI. Such a task is accomplished much more easily in the horizontal direction, where each ring measurement has one of three distinct horizontal structures (corresponding to the 2°, 4° and 16° tiling sizes), and falls upon a regular grid. However, the situation is complicated in the vertical direction, where a continuum of eigenfunctions (associated with the different fitted modes) is available to construct a vertical averaging kernel. The details of how the vertical averaging function is constructed thus depend on the modes available and the vertical grid. We have performed some general testing of these issues and find that finer resolution than what was adopted in Chapter 8 yields no obvious benefits. However, we acknowledge that further exploration of the interplay between these two effects may enable us to establish a minimally acceptable vertical resolution, thereby increasing the efficiency of the 3-D inversion.

9.2.2 Further Possibilities for Improvements to the Sensitivity Kernels

Some work still lies ahead for the sensitivity kernels as well. Most notably, the effect of line-of-sight changes on measurements made near the limb needs to be accounted for in the kernels. As the centers of the analysis regions are extended toward the limb, measurements become increasingly sensitive to the horizontal components of the solar wavefield. In their current formulation, the sensitivity kernels assume that measurements are taken at the disk center. As a result, the kernel calculation is concerned with the effects of advection on only the vertical component of the wavefield. The inclusion of these effects will be vital, for instance, for the proper interpretation of outflows around sunspots close to the limb.

We note that it may be interesting to develop structure inversion kernels, such as sound

speed kernels. Conceptually there is no difficulty in using the existing kernel machinery to build sensitivity kernels for sound-speed perturbations. The ring-analysis measurement technique looks for anisotropic shifts in the mode frequencies and would need to be modified to account for the isotropic shifts induced by sound speed variations. The kernels would then need to be readjusted to reflect the new measurement procedure. Knowing both the temperature profile and outflow profiles beneath sunspots will help to further characterize their morphology. However, the effects of sunspot magnetic fields on the properties of acoustic waves can complicate the interpretation of the results.

Another limitation of the sensitivity kernels is the lack of any treatment of magnetism in their calculation. What effect the presence of magnetism may have on ring-analysis measurements is unclear at this time. Perhaps the most noticeable effect of a magnetic field is to absorb acoustic power. This absorption is largely frequency dependent, steadily increasing up to 3 mHz (e.g., Braun 1995). A power spectrum constructed for a region adjacent to a sunspot will exhibit a diminishment in power for waves travelling away from the sunspot relative to those travelling toward it. The sensitivity kernels assume that the power spectrum is isotropic in the absence of flows, and other anisotropies such as those introduced by a magnetic field remain unaccounted for. It is also difficult to say how a frequency dependent diminishment in power might alter the measurement procedure. It could modify the slope of the power spectrum in frequency, which is something the measurement procedure is sensitive to. We thus acknowledge that a magnetic field can certainly affect flow measurements, and that these effects are not accounted for in the kernels or by the measurement procedure.

9.3 Future Prospects for Ring Analysis with 3-D Inversions

Though some improvements are desirable, the ARRDI algorithms are now mature enough to warrant their application to a wide variety of phenomena in the upper convection zone. We expect ARRDI to find wide application in the analysis of HMI data, but note that the ARRDI algorithms can now be applied systematically to the vast existing archives of MDI Doppler data.

These archives span both quiet and active Sun periods and constitute an invaluable resource for long-term and statistical studies of various elements of dynamics in the upper convection zone that will complement ongoing observations with HMI.

9.3.1 Detailed Probing of Sunspot Outflows

The studies presented in Chapter 8 suggest that many sunspots possess a two-component structure to their outflows. This discovery is surprising in that it disagrees with earlier time-distance studies which suggest that sunspot outflows increase in strength monotonically down to a depth of 5 Mm (Gizon et al. 2009). We have only analyzed a handful of sunspots to date, and so the robustness of this two-component structure remains unclear. The ability to probe the subsurface flows in such detail allows us to ask other questions concerning the sunspot morphology as well. Are subsurface flows similar for all sunspots, or do they differ based on the magnetic field strength and the age of the spot? We have already seen some hints that the surface outflow decays before the deeper outflow (Fig. 8.11). Moreover, the deep flows around the sunspot in NOAA AR 9783 (Fig. 8.8) exhibit a strong vorticity at a depth of 13 Mm that is not seen in the other sunspots. Is such subsurface vorticity a common feature in many sunspots, and how does the depth dependence of the subsurface vorticity correlate with the outflows we observe? These questions are difficult to answer based on an examination of only a handful of sunspots. However, with ARRDI now operational, we are in a position to address such questions through the systematic study of sunspots in the MDI archives.

9.3.2 Probing Supergranulation in the Near-Surface Shear Layer

The subsurface mapping of supergranular motions is another interesting avenue which may be explored through the 3-D inversion of ring-analysis measurements. Supergranular convection occurs on scales of about 15-30 Mm, and are thought to be playing a role in the angular momentum transport responsible for the maintenance of the near-surface shear layer (e.g., DeRosa, Gilman & Toomre 2002). The depth to which supergranular motions persist, and how their properties

vary with depth, must determine their ability to influence dynamics in the near-surface shear layer. Time-distance analyses (e.g., Duval 1998; Zhao & Kosovichev 2003*b*) place the depth of supergranulation in the 8 to 15 Mm range. Frustratingly, current ring analysis inversions can extend studies of the supergranulation down to only depths of about 5 Mm, where the deepest 2° modes penetrate.

When using these 2° ring-analysis measurements, which overlap by about 1°, we are only just beginning to sample the horizontal structure of the largest supergranules. The increased horizontal resolutions accessible through HMI may allow measurements to be made at 1° or 0.5°, yielding a relatively coarse but still reasonable resolution across the profile of a supergranule. Alternatively, the possibility of fitting higher radial order modes in the 2° measurements using multi-ridge fitting with HMI data may allow for the deeper probing of supergranulation than that currently achievable using the f and p_1 modes. The application of ARRDI to supergranulation using HMI data may thus yield additional insights into the variation of solar supergranulation with depth.

9.3.3 Discerning the Surface Signal of the Solar Giant Cells

An interesting footnote to the subject of supergranulation is that motions at the supergranular scale may provide insights into the nature of the deep giant cells of convective motion thought to pervade the solar convection zone. These large-scale motions arise routinely in 3-D numerical simulations of the solar convection zone and are thought to play a key role in the establishment and maintenence of the solar differential rotation (e.g., Brun, Miesch & Toomre 2004; Miesch, Brun & Toomre 2006; Miesch et al. 2008; Bessolaz & Brun 2011). The surface signal of the giant cells is likely masked by the vigorous near-surface convection, but it has been suggested that these long-lived flows impose an organizing effect on the solar supergranulation.

The correlation tracking studies of Lisle, Rast & Toomre (2004) demonstrated that supergranular cells at low latitudes tend to align with one another in the north-south direction. More recent studies using time-distance helioseismology suggest that the north-south alignment persists in the polar regions as well (Nagashima et al. 2011). One theory concerning these supergranular

patterns is that they arise along the boundaries of giant cells, which are themselves thought to align in the north-south direction at low latitudes (though this may not explain the high-latitude component to the supergranular alignment). A more thorough probing of supergranular cells along these north-south lanes using ARRDI may provide further clues into the cause of this alignment. In particular, if improvements to the ring-fitting algorithms allow us to fit 2° modes that penetrate as deepy 10 Mm (roughly half a supergranule), we may be able to probe the transition between small-scale aligned flows and deeper organizing motions. ARRDI will find application to a variety of solar phenomena, and with HMI data now becoming available, it will soon allow us to exploit the capabilities of ring-analysis helioseismology in a manner which was not previously possible.

Bibliography

Abt, H.A. 2000, ApJ, 544, 933

Alecian, E., et al. 2008, A&A, 481, 99A

Aurière, M., et al. 2007, A&A, 475, 1053

Aurière, M., Konstantinova-Antova, P.P., Charbonnel, C., Dintrans, B., Lignières, F., et al., 2008, A&A, 491, 499

Babcock, H.W. 1947, ApJ, 105, 105

Bagnulo, S., Landstreet, J.D., Mason, E., Andretta, V., Silaj, J. & Wade, G.A. 2006, A&A, 450, 777

Baliunas, S.L., Donahue, R.A., Soon, W., Henry, G.W. 1998, *in The Tenth Cambridge Workshop on Cool Stars, Stellar Systems and the Sun*, eds. Donahue, R.A. & Bookbinder, J.A., ASP Conf. Ser., 154, 153

Barnes, J.R., Lister, T.A., Hilditch, R.W. & Collier Cameron, A. 2004, MNRAS, 348, 1321

Basu, S. & Antia, H.M. 2000, Solar Phys., 192, 469

Basu, S. & Antia, H.M. 2010, ApJ, 717, 488

Basu, S., Antia, H.M. & Bogart, R.S. 2004, ApJ, 610, 1157

Basu, S., Antia, H.M. & Tripathy, S.C. 1999, ApJ, 512, 458

Beck, J.G., Gizon, L. & Duvall, T.L. Jr 2002 ApJ, 575, L47

Bessolaz, N. & Brun, A.S. 2011, ApJ, 728, 115

Birch, A.C., Gizon, L., Hindman, B.W. & Haber, D.A. 2007, ApJ, 662, 730

Birch, A.C., Kosovichev, A.G. & Duvall, T.L., Jr 2004, ApJ, 608, 580

Borra, E.F., Landstreet, J.D., Mestel, L. 1982, ARA&A, 20, 191

Bouret, J.C., et al. 2008, MNRAS, 389, 75

Braithwaite, J. & Spruit, H.C. 2004, Nature, 431, 819

Braithwaite, J. & Nordlund, Å 2006, A&A, 450, 1077

Braithwaite, J. 2007, A&A, 469, 275

Braun, D.C. 1995 ApJ, 451, 859

Braun, D.C., Duval Jr, T.L., Labonte, B.J. 1987, ApJ, 319, L27

Braun, D.C., Duvall, T.L., Jr, Labonte, B.J., Jefferies, S.M., Harvey, J.W. & Pomerantz, M.A. 1992, ApJ, 391, L113

Braun, D.C. & Lindsey, C. 2001, ApJ, 560, L189

Brickhouse, N.S. & Labonte, B.J. 1988, Solar Phys., 115, 43

Brown, B.P., Browning, M.K., Brun, A.S., Miesch, M.S. & Toomre, J. 2010, ApJ, 711, 424

Brown, B.P., Browning, M.K., Brun, A.S., Miesch, M.S. & Toomre, J. 2011, ApJ, *in press*

Brown, S.F., Donati, J.-F., Rees, D.E., Semel, M. 1991, A&A, 250, 463

Browning, M.K. 2008, ApJ, 676, 1262

Browning, M.K., Brun, A.S., & Toomre, J. 2004, ApJ, 601, 512

Browning, M.K., Miesch, M.S., Brun, A.S. & Toomre, J. 2006, ApJ, 648, L157

Browning, M.K. & Basri, G. 2007, *in Unsolved Problems in Stellar Physics*, AIP Conf. Proc., 948, 157

Brun, A.S. & Toomre, J. 2002, ApJ, 570, 865

Brun, A.S., Browning, M.K. & Toomre, J. 2005, ApJ, 629, 461

Brun, A.S., Miesch, M.S. & Toomre, J. 2004, ApJ, 614, 1073

Brun, A.S. 2007, Astron. Nachr., 328, 1137

Busse, F.H. 2002, Phys. Fluids, 14, 1301

Cally, P.S., Crouch, A.D. & Braun, D.C., 2003, MNRAS, 346, 381

Catala, C., Donati, J.-F., Shkolnik, E., Bohlender, D., Alecian, E. 2007, MNRAS, 374, L42

Cattaneo, F. & Hughes, D.W. 1996, Phys. Rev. E, 54, 4534

Charbonneau, P. & MacGregor, K.B. 1997, ApJ, 486, 502

Charbonneau, P. & MacGregor, K.B. 2001, ApJ, 559, 1094

Charbonnel, C. & Zahn, J.-P. 2007, A&A, 476, L29

Christensen, U.R. & Aubert, J. 2006, Geophys. J. Int., 166, 97

Christensen-Dalsgaard, J., et al. 1996, Science, 272, 1286

Christensen-Dalsgaard, J. 2002, Rev. Mod. Phys., 74, 1073

Chou, D.-Y. & Dai, D.-C. 2001, ApJ, 559, L175

Clune, T.L., Elliott, J.R., Miesch, M.S., Toomre, J., & Glatzmaier, G.A. 1999 Parallel Comput., 25, 361

Clyne, J., Mininni, P., Norton, A. & Rast, M. 2007, New J. Phys., 9, 301

Craig, I.J.D. & Brown, J.C. 1986, *Inverse Problems in Astronomy*, (Bristol, England: Adam Hilger Ltd)

Collier Cameron, A., Robinson, R.D. 1989, MNRAS, 236, 57

Cowling, T.G. 1945, MNRAS, 105,166

DeRosa, M.L., Gilman, P.A. & Toomre, J. 2002, ApJ, 581, 1356

Deubner, F.-L. & Gough, D. 1984, ARA&A, 22, 593

Deutch, A.J. 1956, PASP, 68, 92

Dikpati, M. & Charbonneau, P. 1999, ApJ, 518, 508

Dobler, W., Stix, M. & Brandenburg, A. 2006, ApJ, 638, 336

Donati, J.-F.; Mengel, M.; Carter, B. D.; Marsden, S.; Collier Cameron, A.; Wichmann, R., 2000, MNRAS, 316, 699

Donati, J.-F., Babel, J., Harries, T.J., Howarth, I.D., Petit, P. & Semel, M., 2002, MNRAS, 333, 55

Donati, J.-F., et al. 2006, MNRAS, 379, 629

Donati, J.-F., et al. 2006*b*, MNRAS, 365, L6

Donati, J.-F., et al. 2006*c*, MNRAS, 379, 629

Donati, J.-F., et al. 2008, MNRAS, 386, 1234

Donati, J.-F., et al. 2010, MNRAS, 409, 1347

Donati, J.-F. & Landstreet, J.D. 2009, ARA&A, 47, 333

Donati, J.-F., Morin, J., Delfosse, X., Forveille, T., Farés, R., et al. 2009, *in 15th Cambridge Workshop on Cool Stars, Stellar Systems and the Sun*, AIP Conf. Proc. 1094, 130

Donati, J.-F., Moutou, C., Farés, R., Bohlender, D., Catala, C., et al. 2008, MNRAS, 385, 1179

Dorren, J.D. & Guinan, E.F. 1982, Astron. J., 87, 1546

Duez, V. & Mathis, S. 2009, ApJ, submitted

Duvall, T.L., Jr 1998, *in Structure and Dynamics of The Interior of the Sun and Sun-like Stars*, (eds.) Korzennik, S., Wilson, A., SOHO 6 GONG 98 Workshop, ESA Conf. Proc., 418, 581

Duvall, T.L., Jr, D'Silva, S., Jefferies, S.M., Harvey, J.W. & Schou, J. 1996, Nature, 379, 235

Duvall, T.L., Jr & Gizon, L. 2000, Solar Phys., 192, 177

Duvall, T.L., Jr, Jefferies, S.M., Harvey, J.W. & Pomerantz, M.A. 1993, Nature, 362, 430

Duvall, T.L., Jr, Kosovichev, A.G., Scherrer, P.H., Bogart, R.S., Bush, R.I., De Forest, C., Hoeksema, J.T., et al. 1997, Solar Phys., 170, 63

Featherstone, N.A., Hindman, B.W., Haber, D.A. & Toomre, J. 2004, *in Helio- and Asteroseismology: Towards a Golden Future*, Editor, D. Danesy, 559, 428

Featherstone, N.A., Hindman, B.W., Haber, D.A. & Toomre, J. 2006, *in Proceedings of SOHO 18/GONG 2006/HELAS I, Beyond the spherical Sun*, Editor, M. Thompson, 624, 131

Featherstone, N.A., Hindman, B.W., Thompson, M.J. 2011, *in GONG 2010 - SoHO 24: A new era of seismology of the Sun and solar-like stars*, *in press*

Flowers, E. & Ruderman, M.A. 1977, ApJ, 215, 302

Freyhammer, L.M., et al. 2008, MNRAS, 389, 441

Ghizaru, M., Charbonneau, P. & Smolarkiewicz, P.K. 2010, ApJ, 715, L133

Giles, P.M., 1999, *Time-Distance Measurements of Large-Scale Flows in the Solar Convection Zone*, Ph.D. Thesis, Stanford Univ.

Giles, P.M., Duvall, T.L., Jr, Scherrer, P.H. & Bogart, R.S. 1997, Nature, 390, 52

Giles, P.M., Duvall, T.L., Jr, T.L. & Scherrer, P.H. 1998, *in Structure and Dynamics of the Interior of the Sun and Sun-like Stars SOHO 6/GONG 98 Workshop*, eds., Korzennik, S. & Wilson, A., ESA, Noordwijk, Netherlands, 418, 775

Gilman, P.A. & Glatzmaier, G.A. 1980, ApJS, 45, 335

Gizon, L. 2003, *Probing Flows in the Upper Solar Convection Zone*, Ph.D. thesis, Stanford Univ.

Gizon, L. & Birch, A.C. 2002, ApJ, 571, 966

Gizon, L. & Birch, A.C. 2005, LRSP, 6, Local Helioseismology

Gizon, L., Birch, A.C. & Spruit, H.C. 2010, ARA&A, 48, 289

Gizon, L., Duvall, T.L., Jr & Larsen, R.M. 2000, J. Astrophys. Astr., 21, 339

Gizon, L., Duvall, T.L., Jr & Larsen, R.M. 2001, *in Recent Insights into the Physics of the Sun and Heliosphere: Highlights from SOHO and Other Space Missions*, Proc. of IAU Symposium 203, ed., P. Brekke, F. Bernhard & J.B. Gurman., 189

Gizon, L., et al. 2009, Space Sci. Rev., 144, 249

Gizon, L. & Rempel, M. 2008, Solar Phys., 251, 241

Glatzmaier, G.A., Coe, R.S., Hongre, L. & Roberts, P.H. 1999, Nature, 401, 885

Goldreich, P. & Keeley, D.A. 1977, ApJ, 212, 243

González Hernández, I., Hill, F. & Lindsey, C. 2007, ApJ, 669, 1382

González Hernández, I., Kholikov, S., Hill, F., Howe, R. & Komm, R.W. 2008, Solar Phys.

González, Hernández, I., Komm, R.W., Hill, F., Howe, R., Corbard, T. & Haber, D.A. 2006, ApJ, 638, 576

González, Hernández, I., Patrón, J., Bogart, R.S. & The SOI Ring Diagram Team 1999, ApJ, 510, L153

González, Hernández, I., Patrón, J., Cortés, T.R., Bogart, R.S., Hill, F. & Rhodes Jr., E.J. 2000, ApJ, 535, 454

Goode, P.R., Gough, D. & Kosovichev, A. 1992, ApJ, 387, 707

Gough, D.O. 1969, J. Atmos. Sci., 26, 448

Gough, D.O. & Toomre, J. 1991, ARA&A, 29, 627

Gregory, S.G., Jardine, M., Gray, C.G. & Donati, J.F. 2010, Rep. Prog. Phys. 73, 1

Haber, D.A., Hindman, B.W., Toomre, J., Bogart, R.S. & Hill, F. 2001, *in Proceedings of the SOHO 10/GONG 2000 Workshop: Helio- and asteroseismology at the Dawn of the Millennium*, Ed., A. Wilson, ESA SP-464, 209

Haber, D.A., Hindman, B.W., Toomre, J., Bogart, R.S., Larsen, R.M., & Hill, F. 2002, ApJ, 570, 855

Haber, D.A., Hindman, B.W., Toomre, J., Bogart, R.S., Thompson, M.J. & Hill, F. 2000, Solar Phys., 192, 335

Hale, G.E., Ellerman, F., Nicholson, S.B. & Joy, A.H. 1919, ApJ, 49, 153

Hale, G.E. & Nicholson, S.B. 1925, ApJ, 62, 270

Hindman, B.W., Haber, D.A. & Toomre, J. 2006, ApJ, 653, 725

Hindman, B.W., Haber, D.A. & Toomre, J. 2009, ApJ, 698, 1749

Hathaway, D.H. 1996, ApJ, 460, 1027

Harvey, J.W., Hill, F., Hubbard, R., Kennedy, J.R., Leibacher, J.W., et al. 1996, Science, 272, 1284

Henrichs, H.F., et al. 2000, *in Magnetic Fields of Chemically Peculiar and Related Stars*, Proc. Int. Meet., eds. YuV Glagolevskij, II Romanyuk, 57

Hindman, B.W., Gizon, L., Duvall, T.L., Jr, Haber, D.A. & Toomre, J. 2004, ApJ, 613, 1253

Howard, R. & LaBonte, B.J. 1980, ApJ, 239, L33

Howe, R., Christensen-Dalsgaard, J., Hill, F., Komm, R.W., Larsen, R.M., Schou, J., Thompson, M.J. & Toomre, J. 2000, ApJ, 533, L163

Hussain, G.A., et al. 2009, MNRAS, 398, 189

Hurlburt, N.E. & Rucklidge, A.M. 2000, MNRAS, 314, 793

Hurlburt, N.E. & DeRosa, M. 2008, ApJ, 684, L123

Johns-Krull, C.M., 1997, ApJ, 664, 975

Kochukhov, O., Drake, N.A., Piskunov, N. & de la Reza, R. 2004, A&A, 424, 935

Kochukhov, O., et al. 2004, A&A, 414, 613

Kochukhov, O. & Bagnulo, S. 2006, A&A, 450, 763

Komm, R., Corbard, T., Durney, B.R., González Hernández, I., Hill, F., Howe, R. Toner, C. 2004, ApJ, 605, 554

Komm, R., Howe, R. & Hill, F. 2009b, Solar Phys., 258, 13

Komm, R., Howe, R., Hill, F., González Hernández, I. & Toner, C. 2005, ApJ, 630, 1184

Komm, R., Howe, R., Hill, F., González Hernández, I. 2009a, Solar Phys., 254, 1

Komm, R.W., Howe, R., Hill, F., Miesch, M.S. Haber, D.A. & Hindman, B.W. 2007, ApJ, 667, 571

Komm, R., Morita, S., Howe, R. & Hill, F., 2008, ApJ, 672, 1254

Kosovichev, A.G., 1996, ApJ, 461, L55

Kosovichev, A.G. & Duvall, T.L., Jr 1997, *in SCORE '96 Solar Convection and Oscillation and Their Relationship*, eds. F.P. Pijpers, J. Christensen-Dalsgaard & C.S. Rosenthal, (Kluwer: Dordrecht), 241

Korzennik, S.G., Rabello-Soares, C. & Schou, J., 2004, ApJ, 602, 481

Kosovichev, A.G. & The HMI Science Team 2007, AN, 328, 339

Kosovichev, A.G. & Schou, J. 1997, ApJ, 482, L207

Krause, F. & Oetken, L. 1976, in Physics of Ap Stars, ed. W.W. Weiss, H. Jenkner, & H.J. Wood (Vienna: Univ. Wien), 29

Kuang, W. & Bloxham, J. 1999, J. Comput. Phys., 153, 51

Landstreet, J.D., Bagnulo, S., Andretta, V., Fossati, L., Mason, E., Silaj, J. & Wade, G.A. 2007, A&A, 470, 685

Landstreet, J.D., et al. 2008, A&A, 481, 465

Leibacher, J.W. & Stein, R.F. 1971, ApJ, 7, 191

Leroy, J.L. 1995, A&AS, 114, 79

Libbrecht, K.G., Popp, B.D., Kaufman, J.M. & Penn, M.J. 1986, Nature, 323, 235

Lindsey, C. & Braun, D.C. 1997, ApJ, 485, 895

Lindsey, C. & Braun, D.C. 2000, Science, 287, 1799

Lindsey, C. & Braun, D.C. 2005a, ApJ, 620, 1107

Lindsey, C. & Braun, D.C. 2005b, ApJ, 620, 1118

Lindsey, C., Braun, D.C., Jefferies, S.M., Woodard, M.F., Fan, Y., Gu, Y. & Redfield, S. 1996, ApJ, 470, 636

Lisle, J.P., Rast, M.P. & Toomre, J. 2004, ApJ, 608, 1167

MacDonald, J. & Mullan, D.J. 2004, MNRAS, 348, 702

MacGregor, K.B. & Cassinelli, J.P. 2003, ApJ, 586, 480

Markey, P., Tayler, R.J. 1973, MNRAS, 163, 77

Mason, D., Komm, R., Hill, F., Howe, R., Haber, D. & Hindman, B.W. 2006, ApJ, 645, 1543

Mathys, G., Hubrig, S., Landstreet, J.D., Lanz, T. & Manfroid, J. 1997, A&AS 123, 353

Mathys, G. 2001, *in Magnetic Fields Across the Hertzsprung-Russel Diagram*, ed. G. Mathys, S. K. Solanki, & D. T. Wickramasinghe (San Francisco: ASP), in ASP Conf. Ser. 248, 267

Maury, A.C. 1897, Harvard Ann., 28, 96

Maurya, R.A. & Ambastha, A. 2010, ApJ, 714, L196

Mestel, L. 1999, *Stellar Magnetism*, (Oxford: Clarendon Press)

Miesch, M.S., Brun, A.S. & Toomre, J. 2006, ApJ, 641, 618

Miesch, M.S., Brun, A.S., DeRosa, M.L. & Toomre, J. 2008, ApJ, 673, 557

Morel, P. 1997, A&AS, 124, 597

Moss, D.L. 2004, A&A, 414, 1065

Moss, D.L. 2001, *in Magnetic Fields Across the Hertzsprung-Russel Diagram*, ed. G. Mathys, S. K. Solanki, & D. T. Wickramasinghe (San Francisco: ASP), in ASP Conf. Ser. 248, 305

Nagashima, K., Zhao, J., Kosovichev, A.G. & Sekii, T. 2011, ApJ, 726, L17

Neiner, C., et al. 2003, A&A, 406, 1019

Noyes, R. W., Hartmann, L. W., Baliunas, S. L., Duncan, D. K., Vaughan, A. H. 1984, ApJ, 269, 763

Nye, A., Bruning, D. & Labonte, B.J. 1988, Solar Phys., 115, 251

Olson, P., Christensen, U. & Glatzmaier, G.A. 1999, J. Geophys. Res., 104, 10383

Parker, E.N. 1979, ApJ, 230, 905

Parker, E.N. 1992, ApJ, 390, 290

Parker, E.N. 1993, ApJ, 408, 707

Petit, P., Wade, G.A., Drissen, L., Montmerle, T., Alecian, E. 2008, MNRAS, 387, L23

Piskunov, N. & Kochukhov, O. 2002, A&A, 381, 736

Pizzolato, N., Maggio, A., Micela, G., Sciortino, S., Ventura, P. 2003, A&A, 397, 147

Power, J., Wade, G.A., Aurière, M., Silvester, J., & Hanes, D. 2008, Contrib. Astron. Obs. Skalnate Pleso, 38, 443

Prendergast, K.H. 1956, ApJ, 123, 498

Preston, G.W. 1967, ApJ, 150, 547

Preston, G.W. 1971, PASP, 83, 571

Radick, R.R., Mihalas, D., Hartmann, L., Worden, S.P., Africano, J.L., Klimke, A. & Tyson, E.T. 1982, PASP, 94, 934

Reiners, A., Basri, G. & Browning, M., 2009, ApJ, 692, 538

Rempel, M. 2011, ApJ, *submitted*

Rempel, M., Schüssler, M., Cameron, R.H. & Knölker, M., 2009, Science, 325, 171

Richards, M.T. 1990, ApJ, 350, 372

Roberts, P.H. & Glatzmaier, G.A. 2000, Rev. Mod. Phys., 72, 1081

Robinson Jr., R.D. 1980*a*, ApJ, 239, 961

Robinson, R. D., Worden, S. P. & Harvey, J. W. 1980*b*, ApJ, 236, L155

Royer, F., Zorec, J. & Gómez, A.E. 2007, A&A, 463, 671

Saar, S.H. 1988, ApJ, 324, 441

Saar, S.H. & Linskey, J.L. 1985, ApJ, 299, L47

Sakuraba, A. & Kono, M. 1999, Phys. Earth Planet. Interiors, 111, 105

Scherrer, P.H., Bogart, R.S., Bush, R.I., Hoeksema, J.T., Kosovichev, A.G., et al. 1995, Solar Phys., 162, 129

Schou, J. & Bogart, R.S. 1998, ApJ, 504, L131

Schou, J. 1999, ApJ, 523, L181

Schou, J. et al. 1998, ApJ, 505, 390

Schüssler, M. & Rempel, M. 2005, A&A, 441, 337

Semel, M. 1989, A&A, 225, 456

Sheeley Jr, N.R. 1969, Solar Physics, 9, 347

Sheeley Jr, N.R. 1972, Solar Physics, 25, 98

Shibahashi, H., 2004, *in Multi-Wavelength Investigations of Solar Activity*, IAU Symposium, 223, 23, Ed., A.V. Stepanov, E.E. Benevolenskaya & A.G. Kosovichev, Cambridge, UK: Cambridge University Press.

Shorlin, S.L.S., Wade, G.A., Donati, J.-F., Landstreet, J.D., Petit, P., et al. 2002, A&A, 392, 637

Solanki, S.K. 2003, Astron. Astr. Rev., 11, 153

Spiegel, E.A. & Zahn, J.-P. 1992, A&A, 265, 106

Spruit, H.C. 2002, A&A, 381, 923

Spruit, H.C. 2003, Solar Phys., 213,1

Stibbs, D.W.N. 1950, MNRAS, 110, 395

Strassmeier, K.G., Stepień, K., Henry, G.W. & Hall, D.S. 1999, A&A, 343, 175

Sun, M-T., Chou, D-Y., Lin, C-H. & the TON Team 1997, Solar Phys., 176, 59

Tayler, R.J. 1973, MNRAS, 161, 365

Thompson, M.J., Christensen-Dalsgaard, J., Miesch, M.S. & Toomre, J. 2003, ARA&A, 41, 599

Thompson, M.J., Toomre, J. et al., 1996, Science, 272, 1300

Title, A.M., Tarbell, T.D., Topka, K.P., Ferguson, S.H., Shine, R.A. & the SOUP Team 1989, ApJ, 336, 475

Ulrich, R.K. 1970, ApJ, 162, 993

Ulrich, R.K. 2010, ApJ, 725, 658

Valenti, J.A., Marcy, G.W. & Basri, G. 1995, ApJ, 439, 939

Wade, G.A., Alecian, E., Grunhut, J., Catala, C., Bagnulo, S., Folsom, C.P. & Landstreet, J.D. 2009, arXiv:0901.0347

Wilson, O.C. 1978, ApJ, 226, 279

Wittmann, A.D. & Xu, Z.T. 1987, A&AS, 70, 83

Wright, A.A.E. 1973, MNRAS, 162, 339

Zahn, J.-P, Brun, A.S. & Mathis, S. 2007, A&A, 474, 145

Zhao, J. & Kosovichev, A.G. 2003, ApJ, 591, 446

Zhao, J. & Kosovichev, A.G. 2003*b*, *in Local and Global Helioseismology: The Present and Future*, ed., H. Sawaya-Lacoste, ESA Conf. Proc., 517, 417

Zhao, J. & Kosovichev, A.G. 2004, ApJ, 603, 776

Zhao, J., Kosovichev, A.G. & Duvall, T.L., Jr 2001, ApJ, 557, 384

Zhao, J., Kosovichev, A.G., Duvall, T.L., Jr 2004, ApJ, 607, L135

Zhao, J., Kosovichev, A.G. & Sekii, T. 2010, ApJ, 708, 304